

National Academy of Sciences of Ukraine
Ministry of Education and Science of Ukraine
Institute for Scintillation Materials NASU
Gottfried Wilhelm Leibniz Universität Hannover
Kharkiv National University of Radio Electronics
V. N. Karazin Kharkiv National University
Odesa I.I. Mechnikov National University
National Technical University "Kharkiv Polytechnic Institute"
Ukrainian Physical Society

Collection of scientific works

**XII INTERNATIONAL SCIENTIFIC CONFERENCE
FUNCTIONAL BASIS
OF NANO-ELECTRONICS**

Kharkiv – Odesa
September, 2021

XII International Scientific Conference “Functional Basis of Nanoelectronics” Collection of scientific works. – XII.: September 2021. - 112 p.

Scientific works of the XII International Scientific Conference “Functional Basis of Nanoelectronics” are included in the collection

Program Committee of the Conference

Head of the Program Committee:

B.V. Grynyov Academician of NASU, Prof., Director of the Institute for Scintillation Materials of NAS of Ukraine, Kharkiv, Ukraine

Program Committee Co-Chairs:

Ya.I. Lepikh Prof., Dr., Odesa I.I.Mechnikov National University, Odesa, Ukraine

M.I. Slipchenko Prof., Dr., Leading researcher, Institute for Scintillation Materials of NAS of Ukraine, Kharkiv, Ukraine

Program Committee Members:

N.A. Azarenkov Academician of the NASU, Prof., Dr., V.N. Karazin Kharkiv National University, Kharkiv, Ukraine

A.E. Belyaev Academician of the NASU, Professor, Director of the V.E. Lashkaryov Institute of Semiconductor Physics NASU, Kyiv, Ukraine

I.N. Bondarenko Professor, Head of Dep. in Kharkiv National University of Radio Electronics, Kharkiv, Ukraine

B.N. Chichkov Prof., Dr., Gottfried Wilhelm Leibniz Universität / Institut für Quantenoptik, Hannover, Germany

V. Dyakonov Prof., Dr., Head of Experimental Physics VI, Julius-Maximilians Universität Würzburg, Germany

Yu.E. Gordienko Professor of Kharkiv National University of Radio Electronics, Kharkiv, Ukraine

V.O. Katrich Prof., Dr., Vice-Rector of the V.N. Karazin Kharkiv National University, Kharkiv, Ukraine

Yu. S. Kivshar Prof., Dr., Head of Nonlinear Physics Centre of The Australian National University, Canberra, Australia

V.P. Kladko Correspondent member of the NASU, Prof., Deputy. Director of the V.E. Lashkarev Institute of Semiconductor Physics NASU, Kyiv, Ukraine

O.A. Kordyuk Correspondent member NASU, Doctor, Prof., Director of Kyiv Academic University, Kyiv, Ukraine

V.P. Kostylyov Dr., Head. of the lab. of V.E. Lashkaryov Institute of Semiconductor Physics NASU, Kyiv, Ukraine

A.P. Kuznetsov Professor, Vice-Rector of the Belarusian State University of Informatics and Radioelectronics, Minsk, Belarus

- A. Medvids** Dr., Prof., Riga Technical University, Latvia
- K.M. Muzyka** Prof., Dr. Sci, Head of Laboratory, Kharkiv National University of Radio Electronics, Kharkiv, Ukraine
- A.M. Negriyko** Correspondent member of NASU, Deputy Director of the Institute of Physics of NASU, Kyiv, Ukraine
- I. Yu. Protsenko** Prof., Dr., Head of dep. of Electronics, General and Applied Physics of Sumy State University, Sumy, Ukraine
- F. Shan** Prof., Vice Dean of College of Microtechnology and Nanotechnology, China
- E. Sheregij** Dr., Prof., Rzeszow University, Poland
- O.C. Sidletskyi** Dr. Sci., Head of Department at Institute for Scintillation Materials of NAS of Ukraine, Kharkiv, Ukraine
- F.F. Sizov** Correspondent member of NASU, Prof., V.E. Lashkaryov Institute of Semiconductor Physics NASU, Kyiv, Ukraine
- V.A. Skryshevsky** Prof., Head. of dep. of the Institute of High Technologies, Taras Shevchenko National University, Kyiv, Ukraine
- Ye. I. Sokol** Prof., Dr. Sci., Rector of the National Technical University "Kharkiv Polytechnic Institute", Corresponding Member of NASU, Kharkiv, Ukraine
- O.V. Sorokin** Dr. Sci., Deputy Director of Science, Institute for Scintillation Materials National Academy of Sciences of Ukraine, Kharkiv, Ukraine
- S.I. Tarapov** Correspondent member of NASU, Prof., Dr., O.Ya. Usikov Institute of Radio Physics and Electronics NASU, Kharkiv, Ukraine
- Yu.I. Yakimenko** Academician of NASU, Professor, Vice-President of NTUU "KPI", Kyiv, Ukraine
- V.A. Yampolsky** Correspondent member of NASU, Prof of O.Ya. Usikov Institute of Radio Physics and Electronics NASU, Kharkiv, Ukraine
- I.V. Zavislyak** Professor of Taras Shevchenko National University, Kyiv, Ukraine
- A. Zayats** Prof., Dr., Head of the Photonics & Nanotechnology Group, King's College London, England
- Yu. Zorenko** Prof., Dr hab., Head of Chair for Optoelectronic Materials Institute of Physics Kazimierz Wielki University in Bydgoszcz, Poland

Laser Assisted Generation of Nanoparticles for Electrochemical and Electrochemiluminescent Applications

Yuriy Zholudov
Biomedical Engineering Department
Kharkiv National University of
RadioElectronics
Kharkiv, Ukraine
yuriy.zholudov@nure.ua

Boris Chichkov
Institute of Quantum Optics
Leibniz University of Hannover
Hannover, Germany
chichkov@iqo.uni-hannover.de

Kateryna Muzyka
Biomedical Engineering Department
Kharkiv National University of
RadioElectronics
Kharkiv, Ukraine
myzika_katya@ukr.net

Mykola Slipchenko
Institute for Scintillation Materials
of NAS of Ukraine
Kharkiv, Ukraine
<https://orcid.org/0000-0002-4242-4800>

Olena Slipchenko
National Technical University
"Kharkiv Polytechnic Institute"
Kharkiv, Ukraine
olena.slipchenko@kphi.edu.ua

Volodymyr Vasylykovskiy
Institute for Scintillation Materials
of NAS of Ukraine
Kharkiv, Ukraine
<https://orcid.org/0000-0002-1643-0027>

Abstract— Laser assisted generation method has numerous advantages for rapid and efficient production of ultrapure nanoparticles of various materials. The benefits of using such nanomaterials are not yet fully utilized in electroanalytical assay techniques. This work presents a brief review and own achievements in application of laser techniques for nanomaterials synthesis as well as achievements and prospects of their usage in electrochemical and electrochemiluminescent analytical applications.

Keywords— *quantum dots, nanomaterials, basis, nanotube, nanowires (key words)*

I. INTRODUCTION

Research on nanomaterials with specific and pre-programmed properties is one of the most expanding fields in nanotechnology, at the crossroad of physics and chemistry and biology. Material properties in this size range are mainly determined by the quantum confinement effects.

Nanoparticles (NPs) of different compositions and dimensions have become used in a variety of research and industrial areas. In particular, they are playing more and more important role for electroanalytical techniques – an important tool in modern analytical science due to inherent advantages like simplicity, versatility, efficiency, sensitivity, rapidness, etc. NPs of various materials can be employed in electrochemical and electrochemiluminescent assay techniques as versatile and sensitive tracers, redox mediators, light emitting centers, carriers of the reagents, for electrode surface modification, etc. They pave the way for creating electrochemical and ECL sensors with new distinguishing properties and analytical application [1]. Many kinds of NPs, including metal, metal-oxide, semiconductor, and even composite-metal NPs, have been used for constructing electrochemical sensors [2].

A wide variety of methods is available for nanoparticle synthesis, affording a broad spectrum of chemical and physical properties. Ultrapure nanoparticles can be obtained using laser irradiation of solid materials or suspended

microsols in liquid media. This green technology has become a reliable alternative to traditional chemical reduction method for obtaining diverse sorts of nanoparticles. The synthesis enables formation of highly stable nanocolloids, nanoparticle size and size distribution control, and direct surface conjugation during the synthesis using a great variety of raw materials [3].

This work is dedicated to reviewing recent advances of the use of NPs that are generated by laser assisted techniques for the development of new and efficient electroanalytical methods for the analysis of liquids as well as to presenting own achievements in generation of fluorescent nanoparticles of semiconductor materials (quantum dots, QDs) for ECL applications.

II. LASER GENERATION OF NANOPARTICLES

A. Laser Ablation and Fragmentation

Laser ablation is a method that utilizes laser as an energy source for ablating solid target materials. During this process, extremely high energy pulses are concentrated at a specific point for a few nanoseconds on a solid surface to evaporate light-absorbing material. Fig. 1 shows the scheme of nanoparticles formation by laser ablation. The laser systems for nanoparticle production consist of a pulsed laser, beam-handling optics, a target, and a substrate [4].

Targets required for the synthesis are less expensive than the metal salts and other chemicals required in the chemical routes, which makes this method cost-effective comparing to other methods. Laser ablation can generate high-purity nanoparticles because the purity of the particles is basically determined by the purity of the target and ambient media (gas or liquid) without contamination by the precursor chemicals and other reagents. Laser ablation demonstrates excellent suitability for the synthesis of a wide range of nanoparticles (QDs), carbon nanotubes, nanowires, core-shell nanoparticles, etc. in terms of the yield and size homogeneity of the produced nanomaterials [4]. Such

nanomaterials can be effectively used for detection applications [5].

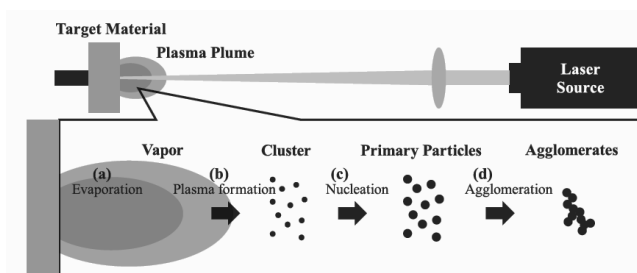


Fig. 1. Schematic of particle generation via laser ablation process [4]

Apart from laser ablation of bulk targets, laser fragmentation of microparticles (see Fig.2) has somewhat broader perspective allowing generation of colloidal nanocrystals of inorganic or organic compounds. This technique allows design of novel substances by combining molecular properties with tailored nanoparticle characteristics like electronic, optical, or solubility properties depending on the particle size. In the ultrashort pulse mode laser irradiation induces pressure buildup and the formation of an intense pressure wave within the exposed microparticle that leads to lower ablation thresholds compared to bulk materials. This results in a highly efficient nanoparticle generation process with almost negligible heat losses [6].

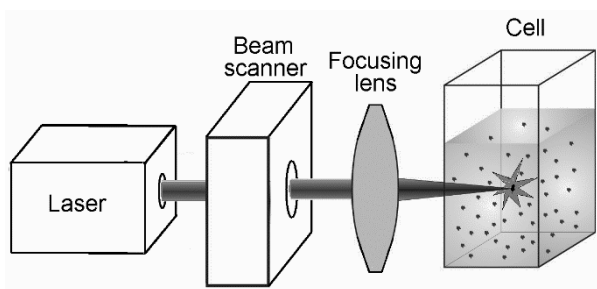


Fig. 2. Scheme of laser fragmentation experiment [7]

B. Laser dewetting

Self-assembly via laser dewetting of the heated thin metallic film is a cost-effective and environmentally-friendly approach for nanostructures fabrication. Moreover, this method can be applied for dielectric, semiconductor, and multilayer substrates, allowing them to precisely control their microscopic properties. Hence, dewetting can be an effective method to form nanoparticle arrays for electroanalytical applications [5].

Dewetting is a spontaneous phenomenon that refers to the decomposition of a film into droplets or other structures on an inert substrate. Its driving force is the minimization of the total energy of the free surfaces of the film and substrate, and of the film-substrate interface (see Fig. 3) [8].

III. ELECTROANALYTICAL APPLICATION OF LASER-GENERATED NANOPARTICLES

Modified electrodes are often used as a working electrode for electrochemical detection of a number of biomaterials, toxins, and other substances. Recently published articles on the usage of laser-fabricated

nanoparticles in the electrochemical methods of the analysis show their versatility and multifunctionality [5].

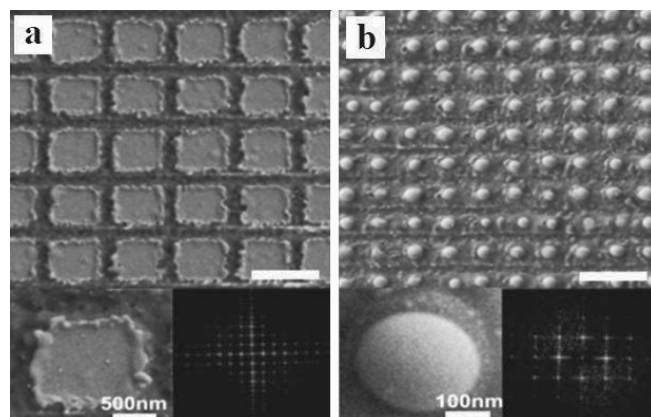


Fig. 3. Metal nanoparticles fabricated by laser dewetting a) SEM image of scribed Au film before laser treatment b) SEM image of an Au nanoparticle array on a SiO₂ substrate produced by laser dewetting [9]

The most common electrode materials for electrochemical detection are carbon (glassy carbon, carbon fiber), Indium tin oxide (ITO), graphene (graphene paper, graphene substrate), and silicon. ITO, graphene, and carbon electrodes are among the most widely used for electrochemical sensing of liquids. It is due to their high electrical conductivity, high chemical resistance, stable physical and electrochemical properties, wide range of available potentials in the solvents of interest, and the possibility of a variety of chemical functionalization [5].

Recently, a number of works have demonstrated that hybrid structures that include nanoparticles can offer unique physicochemical properties that are desirable for sensing applications by enhancing achievable sensitivity.

The analyzed articles show that the most usable laser-fabricated nanomaterials for electrochemical analysis are Au and Ni NPs that have drawn much attention in electrochemical fields because of their favorable properties which include: large surface-to-volume ratio, unique electronic properties, high chemical stability, biocompatibility, and ability to facilitate transfer between biomolecules and electrodes [5]. Correspondingly, such NPs were tested with the broadest range of detectable substances. Other types of laser generated NPs that have found analytical application include Pd and Cu NPs, whereas semiconductor NPs like CdSe QDs, TiO₂ and TiO₂/PbS NPs, ZnO NPs have demonstrated suitability for photoelectrochemical applications.

Shabalina et al. [10] have shown that usage of laser-fabricated Pd NPs and Cu NPs is possible for the detection of ascorbic acid. In case of Pd NPs, this nanomaterial has shown the best sensing efficiency of dopamine. Other analytes that were employed for demonstration of analytical applicability of laser generated nanoparticles include ascorbic acid, glucose, fructose, hydroquinone Aflatoxin B1, metal ions Cd²⁺, Pb²⁺, Cu²⁺, Hg²⁺ [5].

A. Potential of ECL applications

The method of electrogenerated chemiluminescence, also known as electrochemiluminescence (ECL) is a promising detection tool in the analytical chemistry of liquids. In ECL process, electrochemically generated intermediates undergo a highly exergonic reaction to

produce an electronically excited state that results in light emission. Currently, a number of substances are known as good co-reactants for exciting ECL emission in aqueous and nonaqueous media, thus making them good analytes for the detection using ECL method. Among such co-reactants are numerous amines, oxalate, peroxydisulfate, hydrogen peroxide and some others [11]. ECL has several attractive features (low background signal, precise control of reaction kinetics by the applied potential, compatibility with solution-phase and thin-film formats) that altogether make it a highly sensitive and selective analytical method.

In order to broaden the application area of ECL assays, it is promising to replace commonly used organic luminophores with new emitting species, such as semiconductor QDs and fluorescent nanocrystals. They have a number of advantages over conventional luminophores like broad absorption spectrum, narrow and size dependent luminescence spectrum (QDs), high resistivity towards photo bleaching, high quantum yield, thus making a future assay more efficient and sensitive. In this respect, the use of laser assisted synthesis techniques for production of fluorescent NPs of different nature has a great potential.

IV. FLUORESCENT NPS SUITABLE FOR ECL APPLICATIONS

A. Ruby NPs Synthesized by Laser Ablation

Recently a new unique type of fluorescent nanoparticles was reported by Edmonds et al. - fluorescent ruby nanoparticles, which were used for ultrasensitive fluorescent imaging. The developed fluorescent ruby probes have demonstrated enhanced optical properties: high brightness, contrast, and photostability as well as excellent biocompatibility, chemical and mechanical stability. This unique type of nanoparticles was produced by the method of laser ablation [12].

The NPs with the size of less than 100 nm (and 13.2 nm median) were produced by femtosecond laser ablation in air from a solid ruby target, with immediate dispersion in water (Fig. 4). They have demonstrated good colloidal stability in water and buffer solutions. The obtained NPs exhibit fluorescence at around 694 nm characteristic to ruby, or a broader band emission attributed to the γ - $\text{Al}_2\text{O}_3\text{:Cr}^{3+}$ allotrope. The emission was stable without any photobleaching or blinking with the estimated quantum yield of around 25% and was highly resistant to environmental influence. The produced NPs possessed millisecond scale fluorescence lifetime and were easily observable in the imaging mode at high contrast on the background of cell autofluorescence. Also ruby NPs possessed no detectable cytotoxicity and could be conjugated with antibodies by physisorption technique.

Thus conducted research demonstrate that nano ruby has significant potential as a molecular probe for high contrast bioimaging and biosensing and can also be suitable and valuable as light emitting species for certain ECL assay techniques where fluorophore redox activity is not desirable.

B. Synthesis of CdSe QDs using laser fragmentation

The fragmentation of CdSe nanoparticles was done using Trumpf TruMicro 5050 pulsed laser (<10 ps pulse duration, 250 μJ maximum energy, 1030 nm wavelength, 200 kHz maximum repetition rate). Ultrasonicated suspension of CdSe powder (99.99%, <50 μm particle size,

Sigma-Aldrich) in organic solvent was used as a fragmentation target. The target suspension was irradiated in 1cm spectroscopic quartz cuvette with the laser beam focused in the solution bulk. In order to prevent shooting into the cavitation bubbles and facilitate more efficient nanoparticles production the laser beam was spatially scanned along a spiral. The fragmentation process was accompanied by mixing of the suspension using laboratory pipette to prevent sedimentation of CdSe powder grains, thus creating vertical turbulent flow in the cell (see scheme in Fig. 2).

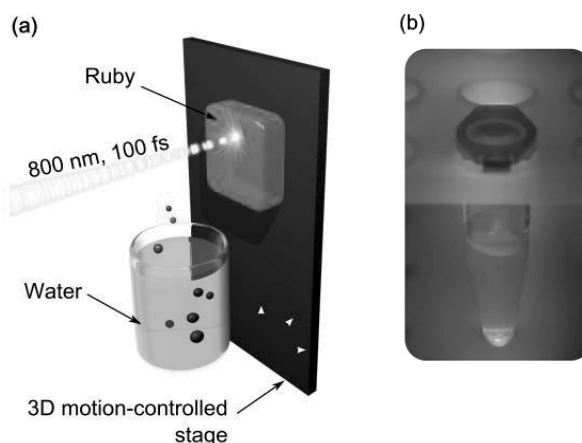


Fig. 4. a) Schematic representation of the experimental setup used for fs laser ablation of a bulk ruby sample. b) example nano-ruby colloid (in Eppendorf tube), displaying ruby-related fluorescence under excitation from a 532 nm laser [12]

The absorbance measurements were performed using Shimadzu UV-1650 UV-Vis-NIR spectrophotometer. Fluorescence spectra were recorded using OceanOptics HR4000 fiber optic spectrometer. Fluorescence was excited using 100 mW laser diode at 405 nm wavelength.

In order to choose appropriate media for laser fragmentation a number of solvents were first tested for their stability under laser irradiation. During preliminary studies several solvents were considered as potential media: nonpolar aprotic (toluene, chloroform, cyclohexane); lowpolar aprotic (dichloromethane); polar aprotic (dimethylformamide); polar protic (methanol, ethanol). These tests revealed that toluene, chloroform, cyclohexane and dichloromethane get very strong coloration in visible range, indicating essential degradation under strong laser irradiation. When excited by 405 nm light these laser treated solvents exhibited rather strong fluorescence indicating production of some fluorescent products, so they were not considered for further studies of CdSe nanoparticles synthesis. Dimethylformamide (DMF), methanol and ethanol showed raise of absorbance in the UV range without significant changes in the visible area. When excited by 405 nm laser diode only DMF showed weak fluorescence, while ethanol and methanol didn't give any measurable emission.

Preliminary testing of CdSe nanoparticles synthesis revealed that only in DMF a distinct absorbance peak positioned at about 405 nm is present. This absorbance peak was rather unstable and was decaying with time (it was almost disappearing in 2 hours). It was also noticed that depending on the concentration of fragmentation products (estimated from solution absorbance) there was different tendency towards aggregation. Samples having peak absorbance less than 1 unit were relatively stable without

any visible aggregation within hours. Flocculation of CdSe nanoparticles was only starting at relatively high concentrations when absorbance peak had value above 1.5 units.

Considering presence of fluorescent products of DMF degradation after laser irradiation in all further studies the fragmentation products were removed from the original solution by centrifugation and redispersed in a new DMF solvent. Obtained quantum dots possess weak broadband fluorescence with the peak position at about 660 nm (see Fig. 5). The position of absorption peak (~400nm) is characteristic for core-type CdSe quantum dots with the diameter below 2 nm [13].

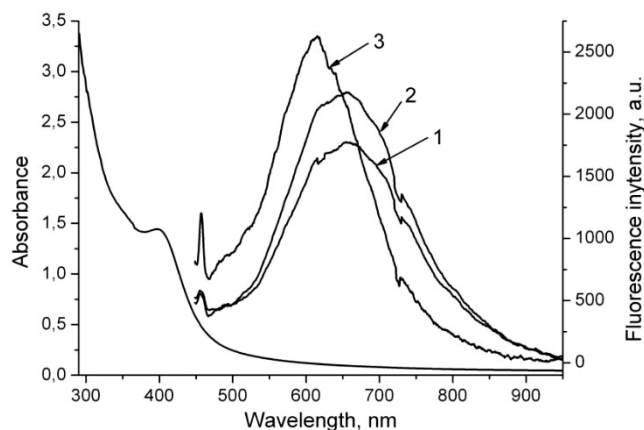


Fig. 5. Absorption and fluorescence spectra of freshly synthesized CdSe nanoparticles in DMF (1), the same particles after 1 day of storage (2) and after 6 days of storage (3), excitation at 405 nm [7]

The stability and fluorescent activity of CdSe nanoparticles in DMF is attributed to their surface stabilization with dimethylamine which is commonly present in DMF as its synthesis reagent and main product of decomposition during storage [39]. At the same time it is well known that amines belong to the group of capping ligands that efficiently passivate CdSe surface and block nonradiative recombination centers [40]. The storage of nanoparticles in fresh DMF was causing enhancement of their fluorescent activity and some blue shift of fluorescence spectrum/ probably due to further passivation of surface defects by dimethylamine (Fig. 5).

In order to stabilize the properties of produced nanocrystals their surface modification was applied. Substances, commonly used for such purpose, mostly belong to the classes of phosphines and amines. In this study the modification of CdSe quantum dots was performed by trimethylolphosphine and oleylamine to provide their solubility on polar and nonpolar solvents accordingly. The reaction with trimethylolphosphine and oleylamine was performed in DMF. The reaction was performed at room temperature during 24 hours. After that quantum dots were separated by centrifugation and redispersed in appropriate solvent. Nanoparticles covered with oleylamine showed good solubility in toluene whereas those covered by trimethylolphosphine are well soluble in DMF.

The coverage of nanoparticles significantly enhanced their fluorescence efficiency due to blocking of surface defects. This is common behavior considering extremely high surface to volume ratio of nanoparticles of this size scale when surface states essentially contribute to the overall energetic structure of the nanoparticle. In all cases there was

observed a shift of fluorescence maxima towards shorter wavelengths comparing to unmodified samples, especially in the case of modification with oleylamine.

Fig. 6 shows fluorescence and absorbance spectra of CdSe/ trimethylolphosphine. An essentially stronger influence on both fluorescence and absorbance was found when oleylamine was used as a surfactant. Fig. 7 shows fluorescence and absorbance spectra of CdSe/ oleylamine quantum dots in toluene. As it is seen from the figure, the absorbance spectra exhibits well resolved narrow peaks corresponding to different energy levels of quantum dot. Also the shift of the fluorescence maxima due to surface passivation in this sample is the highest and emission peak occurs at 565 nm.

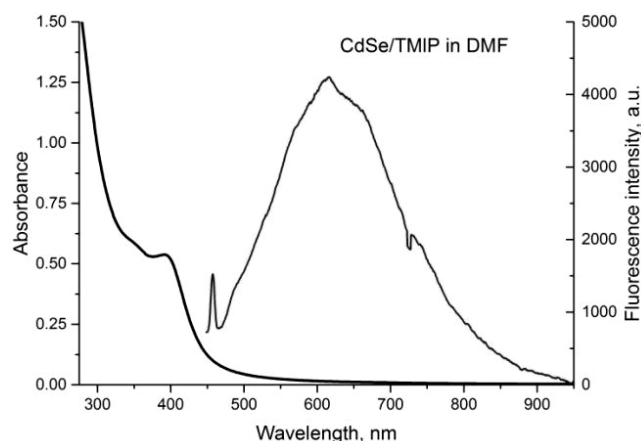


Fig. 6. Fluorescence and absorbance spectra of CdSe quantum dots modified with trimethylolphosphine in DMF excited at 405 nm [7]

Due to rather small expected size of obtained CdSe nanoparticles the task of their visualization was rather challenging. Fig. 8 presents a TEM image of particles modified with oleylamine. Due to pretty low contrast and resolution at the limit of microscope capabilities there are only well seen structures of the order of 2-3 nanometers in diameter, whereas diameter calculated on the base of the position of first absorbance peak corresponds to 1.5-1.6 nm.

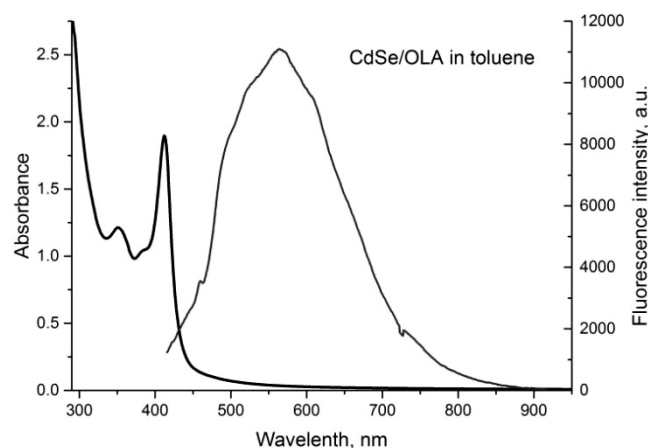


Fig. 7. Fluorescence and absorbance spectra of CdSe quantum dots modified with trimethylolphosphine in DMF excited at 405 nm [7]

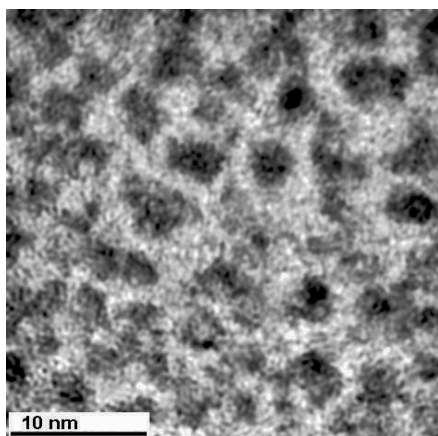


Fig. 8. Fluorescence and absorbance spectra of CdSe quantum dots modified with trimethylolphosphine in DMF excited at 405 nm [7]

V. CONCLUSION

Observed research works indicate that the utilization of the nanoparticles obtained by laser methods and the modification of electrodes by these modifiers are promising for electrochemical, electrochemiluminescent, and photoelectrochemical assays. Also, it has been demonstrated the effectiveness of the detection of organic substances, toxins, and heavy metal ions in liquids by the use of these electrodes in electroanalytical methods.

We have also demonstrated that laser fragmentation is a new promising method for the rapid and efficient production of new kinds of fluorescent nanoparticles for imaging and ECL applications. Among them are ruby NPs (a member of fluorescent inorganic crystal NPs) and shell-free semiconductor QDs with high monodispersity and purity. Those laser generated NPs possess unique optical properties and can find broad applications in electroanalytical techniques.

ACKNOWLEDGMENT

This work was partly supported by the National Research Fund of Ukraine project 2020.02/0390, DAAD grant A/14/02402 and Federal Ministry of Education and Research (Germany) initiative for the establishment of German-Ukrainian centers of excellence in Ukraine.

REFERENCES

- [1] S. Sharma, N. Singh, V. Tomar, and R. Chandra, "A review on electrochemical detection of serotonin based on surface modified electrodes," *Biosensors and Bioelectronics*, vol. 107, pp. 76–93, Jun. 2018.
- [2] W. Siangproh, W. Dungchai, P. Rattanarat, and O. Chailapakul, "Nanoparticle-based electrochemical detection in conventional and miniaturized systems and their bioanalytical applications: A review," *Analytica Chimica Acta*, vol. 690, no. 1, pp. 10–25, Mar. 2011.
- [3] F. Mafuné, J. Kohno, Y. Takeda, T. Kondow, and H. Sawabe, "Formation of gold nanoparticles by laser ablation in aqueous solution of surfactant," *The Journal of Physical Chemistry B*, vol. 105, pp. 5114–5120, 2001.
- [4] M. Kim, S. Osone, T. Kim, H. Higashi, and T. Seto, "Synthesis of Nanoparticles by Laser Ablation: A Review," *KONA Powder and Particle Journal*, vol. 34, pp. 80–90, 2017.
- [5] V. Vasylykovskiy, M. Slipchenko, O. Slipchenko, K. Muzyka, Y. Zholidov, "Laser-induced nanoparticles in electroanalysis: Review," *Functional Materials*, vol. 28, no. 2, Jun. 2021.
- [6] P. Wagener and S. Barcikowski, "Laser fragmentation of organic microparticles into colloidal nanoparticles in a free liquid jet," *Applied Physics A*, vol. 101, no. 2, pp. 435–439, Jun. 2010.
- [7] Y. T. Zholidov, C. L. Sajti, N. N. Slipchenko, and B. N. Chichkov, "Generation of fluorescent CdSe nanocrystals by short-pulse laser fragmentation," *Journal of Nanoparticle Research*, vol. 17, no. 12, Dec. 2015.
- [8] H. Oh, A. Pyatenko, and M. Lee, "Laser dewetting behaviors of Ag and Au thin films on glass and Si substrates: Experiments and theoretical considerations," *Applied Surface Science*, vol. 475, pp. 740–747, May 2019.
- [9] L. Yang, J. Wei, Z. Ma, P. Song, J. Ma, Y. Zhao et al. "The Fabrication of Micro/Nano Structures by Laser Machining," *Nanomaterials*, vol. 9, no. 12, p. 1789, Dec. 2019.
- [10] A. V. Shabalina, I. N. Lapin, K. A. Belova, and V. A. Svetlichnyi, "Carbon electrodes modified by metal nanoparticles obtained by laser ablation method in organic substances determination," *Russian Journal of Electrochemistry*, vol. 51, no. 4, pp. 362–367, Apr. 2015.
- [11] W. Miao, "Electrogenerated Chemiluminescence and Its Biorelated Applications," *Chemical Reviews*, vol. 108, no. 7, pp. 2506–2553, Jul. 2008.
- [12] A. Edmonds, M. Sobhan, V. Sreenivasan, E. Grebenik, J. Rabeau, E. Goldys, and A. Zvyagin, "Nano-Ruby: A Promising Fluorescent Probe for Background-Free Cellular Imaging," *Particle & Particle Systems Characterization*, vol. 30, no. 6, pp. 506–513, Feb. 2013.
- [13] W. W. Yu, L. Qu, W. Guo, and X. Peng, "Experimental Determination of the Extinction Coefficient of CdTe, CdSe, and CdS Nanocrystals," *Chemistry of Materials*, vol. 15, no. 14, pp. 2854–2860, Jul. 2003.

Laser-based Nanostructuring of Carbon Materials

Kateryna Muzyka
Department of Biomedical
Engineering,
Kharkiv National University of
RadioElectronics
Kharkiv, Ukraine
kateryna.muzyka@nure.ua

Dmytro Snizhko
Department of Biomedical
Engineering,
Kharkiv National University of
RadioElectronics
Kharkiv, Ukraine
dmytro.snizhko@nure.ua

Yuriy Zholudov
Department of Biomedical
Engineering,
Kharkiv National University of
RadioElectronics
Kharkiv, Ukraine
yurets.zh@gmail.com

Volodymyr Vasylykovskyi
Institute for Scintillation Materials
of NAS of Ukraine
Kharkiv, Ukraine
<https://orcid.org/0000-0002-1643-0027>

Iaroslav Gnilitzkiy
LLC Novinanolab,
Lviv, Ukraine
iaroslav.gnilitzkiy@novinano.com

Olena Slipchenko
National Technical University
“Kharkiv Polytechnic Institute”
Kharkiv, Ukraine
Olena.Slipchenko@khpi.edu.ua

Abstract — This work reviews different laser-based methods used to fabricate nanostructured carbon materials, including our recent achievement related to the fabrication, characterization, and electrochemical investigation of self-organized periodic nanostructures, known as laser-induced periodic surface structures.

Keywords— laser-induced periodic surface structures, nanomaterials, laser-induced graphene, glassy carbone, electroanalysis

I. INTRODUCTION

Until now, carbon materials continue to show great potential for potential applications in analytical detection and electrochemical energy conversion. In order to expand the portfolio of accurate traditional electrode materials such as graphite, glassy carbon, new carbon materials, and ways to modify traditional carbon materials are being actively studied. Interest in these materials for sensor applications arises from the possibility of tuning their analytical characteristics by controlling morphology and surface since all of the above physicochemical parameters directly affect the electron transfer rate (ET). [1]. In order to develop carbon-based electrodes with advanced architecture, conventional carbon materials have been modified with nanocarbon materials such as carbon nanotubes (CNTs) and graphene. CNTs and graphene-modified glassy carbon electrodes (GCE) have improved electrocatalytic signals for a wide variety of electrochemical reactions compared to signals obtained using GCE [2]. One of the advantages of GCE modified with CNTs is a larger effective electroactive surface area with obvious analytical benefits [3].

II. LASER INDUCED GRAPHENE

A. Laser-induced graphitization

Laser-induced graphitization (LIG) converts a carbon-rich precursor into a highly conductive graphite-like carbon by laser scribing.

In this regard, laser-induced technology has been pointed out as a promising method, allowing to obtain laser-derived graphene as a distinct electrode patterned on a non-conducting flexible substrate. Thus, it presents an

opportunity to print a new generation of disposable electrochemical sensors [4].

Laser processing of graphene is of great interest for cutting, patterning, and structural engineering purposes.

Since laser-derived graphene (LDG) is a graphene-like pure carbon material that can be made inexpensively in any chosen two-dimensional shape, it seems an obvious candidate for disposable electrodes used in electrochemical sensing. This area is dominated by screen-printed carbon electrodes at the time.

However, currently, laser induction of graphene is still in its infancy. So, the fit is of great significance to understand and evaluate the performance of LDG in the context of electroanalysis.

B. Two types of direct-write laser technologies and a short history of milestones towards fabrication laser-derived graphene

In 2012 Strong et al. [5] introduced a facile, inexpensive, solid-state method for generating, patterning, and electronic tuning graphene-based materials.

Laser scribed graphene (LSG) is successfully produced and selectively patterned from the direct laser irradiation of graphite oxide films under ambient conditions. In the same year, El-kady et al. [5] have demonstrated using a standard LightScribe DVD optical drive to make the direct infrared (IR) laser reduction of graphite oxide films to LSG, as a new member of the graphene family that be used directly as EC electrodes without the need for any additional binders or conductive additives. In 2014 Griffiths et al. [6] used the same technology to produce LSG electrodes for electrochemical sensor applications. However, this technique requires multi-step chemical processing before patterning.

Lin and his colleagues introduced another method for the rapid and straightforward production of graphene-based materials in the same year. They have developed a one-step and scalable approach to the preparation of porous graphene from commercial polymer Kapton sheets (a polyimide (PI) film developed by DuPont in the late 1960s) using CO₂ (IR) laser irradiation under ambient conditions for the production of highly efficient supercapacitors. In these studies, the resulting product, laser-induced graphene (LIG), contained few-layer graphene with high electrical

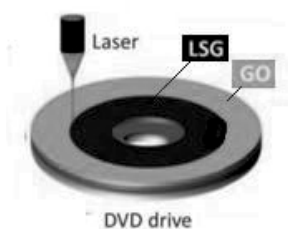
conductivity, high thermal stability, high thermal conductivity, and outstanding electrochemical performance.

TABLE 1. TWO TYPES OF DIRECT-WRITE LASER TECHNOLOGIES THAT CAN BE USED TO PATTERNS LDG DIRECTLY ON SUBSTRATES

Laser scribed graphene (via conversion of GO into reduced GO using IR laser similar to those found in DVD) (introduced by El-Kady MF²⁴ et al. in 2012)

Main features

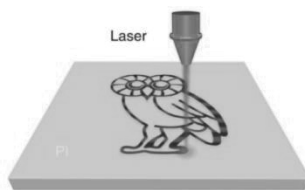
- Apply GO film supported on flexible substrate
- direct laser reduction of GO films to graphene.
- using an CO₂ IR laser beam ($\lambda = 788$ nm).
- DVD drive as a support. • **conductivity:** 1738 S/m.
- **specific surface area** (1520 m²/g).
- \uparrow mechanical flexibility with only ~1% change in the electrical resistance after 1000 bending cycles
- **multistep processing**



Laser induced graphen (via conversion of polymers (polyimide) or natural carbon sources using IR laser) (introduced by Lin²⁵ et al. in 2014)

Main features

- a direct-write laser scribing (10.6 μm CO₂).
- ambient conditions.
- **specific surface area** (≈ 340 m²/g),
- **conductivity:** 500-2500 S/m
- **a thickness:** 20 to hundreds of micrometers,
- **one-step approach**



In 2016 Nayak et al. [8] adopted a direct writing process to fabricate flexible LIG-based electrochemical sensors. The available edge-plane sites on the surface of the LSG pattern are expected to enhance electron transfer behavior, whereas the intact 3D morphology offers high accessible electrochemical surface area.

Currently, the LIG technique is an innovative technique for preparing 3D porous graphene and various shapes by directly laser-inducing polymer precursors (not only PI).

Moreover, after emerging LIG by using a CO₂ laser, researchers attempted to apply other types of lasers, including a UV laser, visible laser, and ultra-short pulse laser, to generate LIG.

III. LASER-INDUCED PERIODIC SURFACE STRUCTURES

Nano and micro-level surface morphology determine its mechanical, chemical, wetting, and physical properties. Traditional methods of morphology management, in particular lithography and chemical etching, have several disadvantages: low processing speed and process control,

insufficient reproducibility over large areas. Among the new promising methods of surface functionalization of materials are technologies of laser-nanostructuring. They allow a controlled change in many materials' optical, mechanical, and chemical properties, which are often impossible using «non-laser» technologies [9].

Femtosecond laser-based machining has been proven to be a highly efficient tool for microstructuring due to the inherent characteristics of the process, such as distinct and sharp laser energy density threshold for ablation significantly lower than that of nanosecond or longer pulses, minimization of heat- and shock-affected areas due to the energy delivery within a short period, and multiphoton absorption processes. It has created possibilities for machining high conductivity materials, e.g., gold films and bulk modification of transparent glass and aerogel materials, not possible with pulsed lasers of longer duration.

Laser-induced periodic surface structures (LIPSS, ripples) are universal phenomena and can be generated on almost any material upon irradiation with linearly polarized radiation. With the availability of ultrashort laser pulses, LIPSS has gained an increasing attraction during the past decade. These structures can be generated in a simple single-step process, allowing surface nanostructuring for tailoring optical, mechanical, and chemical surface properties. However, the study and electrochemical application of LIPSS as electrode material are limited by only a few works [10].

Here we reported an electrochemical characterization of GC electrode nanostructured with LIPSS under different conditions. Standard redox couples, ferrocyanide, and ruthenium hexamine in an aqueous solution were employed. Moreover, standard cyclic voltammetry (CV) measurements to derive essential electrode parameters and quantitative figures for the electron-transfer kinetics were performed. The electrochemical investigation is complemented by morphological characterization of the laser-textured GCE, performed by atomic force microscopy, and surface characterizations by contact angle measurement. Moreover, we analyzed the effect of fabrication parameters on the morphology and electrochemical performance of LIPSS GC electrodes and discussed the potential use of laser-textured GC electrodes.

The AFM images concluded that the nanostructured GC electrodes were successfully fabricated by femtosecond laser.

The spatial period of the femtosecond LIPSS is 680 nm that is smaller than the irradiation wavelength ($\lambda=1030$ nm). Thus, these structures are termed a high spatial frequency LIPSS (HSFL), or sometimes nanoripples, and must clearly be distinguished from the classical near-wavelength sized LIPSS, called low spatial frequency LIPSS.

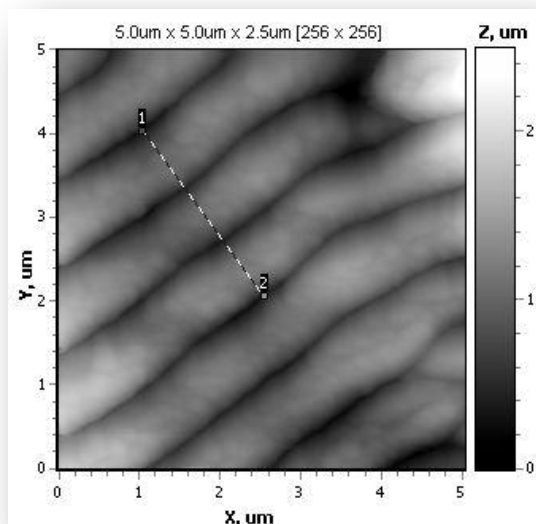


Fig. 1. 3D AFM scan of the LIPSS on glassy carbon

The presence of LIPSS on GC is attributed to an increase of the genuine part of the effective index of the air-carbon interface when surface roughness developed and affected the electrochemical properties.

Controlling the adhesion of water on the glassy carbon electrode surface could play a significant role since the adhesive property ultimately determines the dynamic performance of GC electrodes. For GCs surfaces, the wettability control is helpful in order to improve its performance as the electrode. In order to analyze the effect of the fabricated LIPSS nanopatterns, wettability tests have been performed.

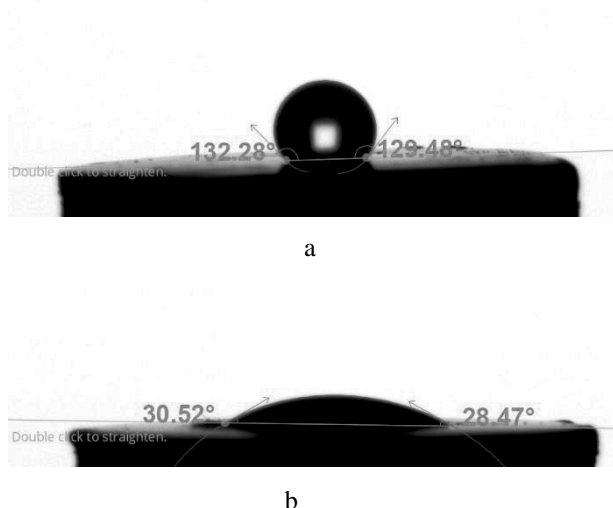


Fig. 2. Wettability test results: (a) glassy carbone; (b) galssy carbone nanostructured with LIPSS

From Fig. 1 can be concluded that LIPSS could be a simple alternative for the fabrication of surface-enhanced glassy carbon electrodes with improved surface and wettability properties.

CONCLUSIOINS

LIPSS could be a simple alternative for fabricating surface enhanced glassy carbon electrodes with improved surface and wettability properties.

Hexaamineruthenium is presentative for molecules that undergo outer-sphere electron transfer, which was just as easily detected on LIPSS GC electrode as ferrocyanide, which is classified as a more surface-dependent redox species.

LIPSS may be extended to prepare novel nanostructures of other electrode materials for potential chemical development applications, including electrochemiluminescent sensors.

ACKNOWLEDGMENT

This work was supported by the National Research Fund of Ukraine (project #2020.02/0390).

REFERENCES

- [1] K. Nemčėková and J. Labuda, "Advanced materials-integrated electrochemical sensors as promising medical diagnostics tools: A review," *Materials Science and Engineering: C*, vol. 120, p. 111751, Jan. 2021
- [2] H.-W. Chang, C.-W. Cheng, C.-Y. Lin, P.-H. Wu, and Y.-C. Tsai, "Femtosecond laser forming of nanostructured glassy carbon: Improved electrocatalytic behavior for electrooxidation of biomolecules," *Electrochemistry Communications*, vol. 15, no. 1, pp. 38–41, Feb. 2012.
- [3] G. G. Wildgoose, H. C. Leventis, I. Streeter, N. S. Lawrence, S. J. Wilkins, L. Jiang, T. G. J. Jones, and R. G. Compton, "Abrasively Immobilised Multiwalled Carbon Nanotube Agglomerates: A Novel Electrode Material Approach for the Analytical Sensing of pH," *ChemPhysChem*, vol. 5, no. 5, pp. 669–677, May 2004.
- [4] K. Griffiths, C. Dale, J. Hedley, M. D. Kowal, R. B. Kaner, and N. Keegan, "Laser-scribed graphene presents an opportunity to print a new generation of disposable electrochemical sensors," *Nanoscale*, vol. 6, no. 22, pp. 13613–13622, 2014.
- [5] V. Strong, S. Dubin, M. F. El-Kady, A. Lech, Y. Wang, B. H. Weiller, and R. B. Kaner, "Patterning and Electronic Tuning of Laser Scribed Graphene for Flexible All-Carbon Devices," *ACS Nano*, vol. 6, no. 2, pp. 1395–1403, Jan. 2012.
- [6] M. F. El-Kady, V. Strong, S. Dubin, and R. B. Kaner, "Laser Scribing of High-Performance and Flexible Graphene-Based Electrochemical Capacitors," *Science*, vol. 335, no. 6074, pp. 1326–1330, Mar. 2012.
- [7] J. Lin, Z. Peng, Y. Liu, F. Ruiz-Zepeda, R. Ye, E. L. G. Samuel, M. J. Yacaman, B. I. Yakobson, and J. M. Tour, "Laser-induced porous graphene films from commercial polymers," *Nature Communications*, vol. 5, no. 1, Dec. 2014.
- [8] P. Nayak, N. Kurra, C. Xia, and H. N. Alshareef, "Highly Efficient Laser Scribed Graphene Electrodes for On-Chip Electrochemical Sensing Applications," *Advanced Electronic Materials*, vol. 2, no. 10, p. 1600185, Aug. 2016.
- [9] Vasylykovskiy V.S., Zholidov Yu. T, Snizhko D.V., Muzyka K.M. Laser-based Nanostructured Materials for Electroanalysis // International research and practice conference "Nanotechnology and nanomaterials", 25-27 August, 2021. – P.355.
- [10] Muzyka K., Gnilitzky Ya, Zholidov Yu, Snizhko D., Vasylykovskiy V. Laser-induced Periodic Surface Structures on Glassy Carbon for Electrode Applications // The eighteenth International Symposium on Electroanalytical Chemistry, August 24-27, 2021, Changchun, Jilin, CHINA

Research of electrochemiluminescence of cesium lead halide perovskite nanocrystals

Volodymyr Vasylykovskyi

*Institute for Scintillation Materials
of NAS of Ukraine
Kharkiv, Ukraine*
<https://orcid.org/0000-0002-1643-0027>

Yuriy Zholudov

*Department of Biomedical
Engineering,
Kharkiv National University of
RadioElectronics
Kharkiv, Ukraine*
yurets.zh@gmail.com

Iryna Bespalova

*Yu.V. Malyukin Department of
Nanostructured Materials
Institute for Scintillation Materials of
NAS of Ukraine
Kharkiv, Ukraine*
<https://orcid.org/0000-0002-9923-7563>

Mykola Slipchenko

*Institute for Scintillation Materials
of NAS of Ukraine
Kharkiv, Ukraine*
<https://orcid.org/0000-0002-4242-4800>

Alexander Sorokin

*Yu.V. Malyukin Department of
Nanostructured Materials
Institute for Scintillation Materials of
NAS of Ukraine
Kharkiv, Ukraine*
<https://orcid.org/0000-0001-5990-4416>

Olena Slipchenko

*National Technical University
"Kharkiv Polytechnic Institute"
Kharkiv, Ukraine*
Olena.Slipchenko@khp.edu.ua

Abstract — In this work, it was shown the possibility of achieving a stable state of cesium lead halide perovskite nanocrystals (CsPbBr_3) in an aqueous solution and obtaining the electrochemiluminescent signal of the stabilized nanoparticles in combination with tripropylamine (TPrA) as a coreactant. The estimated wavelength of the ECL signal was investigated.

Keywords — halide perovskites, electrochemiluminescence, nanocrystals, tripropylamine

I. INTRODUCTION

Electroanalytical techniques have a broad application for the chemical analysis of various samples because of their advantages such as versatility and high sensitivity.

In the field of the research of the electrochemiluminescent (ECL) method of analysis, there is a task to find new stable luminophores with effective light output and which do not degrade after several measurements. That is why ECL assay can benefit from electrode modification with various functional structures and films that have great potential for the development of cheap, reliable, and reusable analytical ECL devices – ECL sensors.

The use of various nanoparticles of fluorescent materials for the functionalization of ECL sensors' electrodes is widely exploited to enhance their analytical performance. So, in this work, it is proposed to apply cesium lead halide perovskite nanocrystals (PeNCs) as a light emitter in the ECL method of analysis of liquids.

II. CESIUM LEAD HALIDE PEROVSKITE NANOPARTICLES

The use of nanoparticles of different materials — a relatively new form of matter — for electrode modification can offer further enhancement of the performance of modified working electrodes for electroanalytical applications.

Nanoparticles (NPs) of different compositions and dimensions have become used as versatile and sensitive

tracers. The creation of NPs for enhanced sensitivity in electroanalytical applications greatly benefits from their nanoscale size, where their properties are strongly influenced by increasing their surface area to volume ratio. Also, NPs are one of the most exciting areas in modern electroanalytical chemistry because they offer excellent prospects for creating highly sensitive and selective electrodes. Many kinds of NPs, including metal, metal-oxide, semiconductors, and even composite-metal NPs, have been used for constructing electrochemical sensors. [1]

At the moment, perovskite nanoparticles are popular and promising material that is studied by scientists from many fields of science. PeNCs have been extensively explored due to their unique properties and various application prospects.

A. Properties

Recently, cesium lead halide perovskite nanoparticles have emerged as new potential materials and show promising results for a number of applications. It has been previously reported that cesium (Cs)-based lead halide perovskite nanocrystals (Cs-LHNCs) have replaced the II–VI group semiconductor materials as potential candidates for many applications including LEDs, lasing, photodetectors, nonlinear, solar cells, and spectrochemical probes to detect the ions [2]. It is due to their broadband light absorption, near-unity photoluminescence quantum yield, and union-tunable optical properties.

However, the structural and optical stability of PeNCs remains the foremost practical challenge. There are numerous reports about the disintegration of CsPbX_3 NPs ($X = \text{Cl, Br, I}$), accompanied by the photoluminescence (PL) quenching, which is accelerated by polar organic solvents and water or under ultraviolet irradiation [4]. That is why this work is relevant where the perovskite nanoparticles show stable electrochemiluminescent signal with tripropylamine coreactant in aqueous phosphate buffer solution.

B. Synthesis

In this work CsPbBr₃ NPs ($D = 25 \pm 5$ nm) have been synthesized by the Ligand Assisted Reprecipitation (LARP) method. The LARP technique is both simple and versatile for the synthesis of halide perovskite NPs and other nanostructures. The synthesis method is based on mixing the perovskite precursor solution with insoluble nonpolar solvent [5]. After the synthesis, a yellow colloidal solution was obtained. (Fig. 1)



Fig.1. Colloidal solution of CsPbBr₃ nanocrystals under the under daylight and UV irradiation

Two types of PeNCs samples were stored in different surfactants: one sample in toluene, another one in chloroform. The sample of perovskite NPs, stored in toluene, showed the impossibility of its usage because in combination with PVB polymer the precipitation of nanoparticles was observed. Therefore, it was decided to work with nanoparticles stored in chloroform. In addition, the polymethyl methacrylate (PMMA) polymer dissolves in chloroform, that is why chloroform has been chosen as a suitable solvent.

III. ELECTROGENERATED CHEMILUMINESCENCE

Electrochemistry is the branch of chemistry concerned with the interrelation of electrical and chemical effects. A large part of this field deals with the study of chemical changes caused by the passage of an electric current and the production of electrical or optical energy by chemical reactions in the solution. Namely, the measurement of electrical quantities, such as current, potential, or charge, as well as optical quantities and their relationship to chemical parameters. Measurement of these parameters gives data on the concentration of certain substances in a solution.

Electrogenerated chemiluminescence is a phenomenon where light-emitting species are produced during the electrochemical reaction. During ECL measurements a light-emitting excited state of luminophore species is formed by highly energetic electron transfer reactions in the solution near the surface of the working electrode from the electrochemically generated precursors. ECL-method has a broad application for the chemical analysis of various substances in liquids because of its ultra-sensitivity and high selectivity.

A. ECL setup

The classical electrochemical cell for ECL measurements for this work has consisted of a working electrode, counter electrode, and reference electrode. (Fig. 2) One of the electrodes, termed the reference electrode, is independent of the properties of the solution. The second

one responds to the target analyte(s) and is thus termed the working electrode.

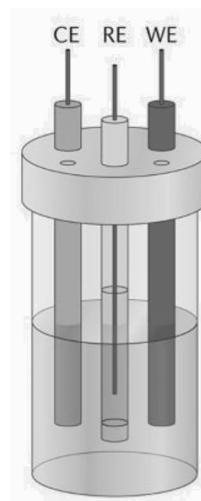


Fig.2. Schematic of the electrochemical cell for the ECL measurements [6]

For the ECL measurements, all three electrodes are injected in liquid solution and connected to the potentiostat. The ECL light signal is measured by a photomultiplier tube that is located under the electrochemical cell.

B. Working electrode modification

Modification of the working electrode surface is a way of creating electrochemical sensors — elements with new properties. Modification of the electrode surface can enhance the performance of an electrode as a sensor device suitable for biological and environmental samples in many ways.

Glassy carbon electrodes (Fig. 3) that have been used in this work are widely applied as a working electrode for electrochemical detection of the analytes. The solution of nanoparticles with the polymer for the electrode modification is applied to the electrode surface in the form of electroactive thin films via the spin-coating method.

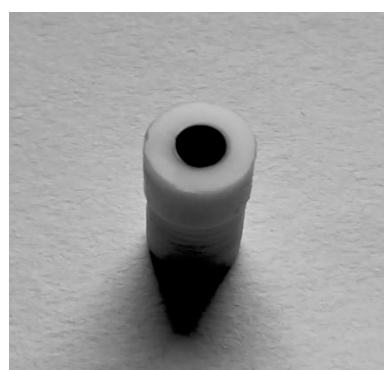


Fig.3. Glassy carbon working electrode

IV. ECL MEASUREMENTS

A. Stabilization of PeNCs

The technique of stabilizing of NPs by polymer as well as transferring them from a thin film into an aqueous phosphate buffer solution (pH = 6.6) has been studied. Firstly, it was decided to use polyvinyl butyral (PVB) dissolved in ethanol as a stabilizing polymer, but the experiment has shown that ethanol negatively affects the

luminescence of perovskites and leads to the aggregation of nanoparticles into microclusters. That is why that a stabilizing polymer polymethyl methacrylate (PMMA) has been chosen, because of its ability to dissolve in chloroform and absence of negative phenomena like aggregation, precipitation, and luminescence quenching.

B. ECL measurements

The ECL research has been conducted in an aqueous phosphate buffer solution (PBS) in the voltage span between 0V and 1.8V. During the experiment, it was noticed that ECL signal occurs only with nanoparticles that had been previously irradiated by the UV light for some amount of time (15-20 seconds) and it is enough to irradiate them once to observe a stable light signal during ECL measurements. The mechanism of such ECL signal amplification new and needs further research.

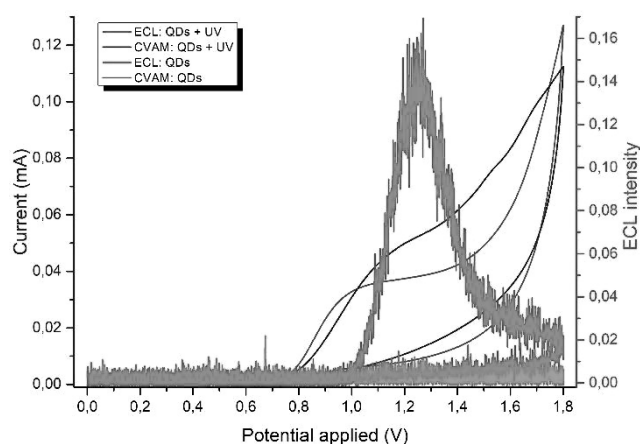


Fig.4. EC and ECL-signal with TPrA coreactant of CsPbBr₃ QDs after preliminary UV irradiation of the solution with polymer and QDs without preliminary UV irradiation

In addition, the spectrometry measurements have shown that the irradiation of PeNCs for more than 3 minutes leads to the decrease and offset of the absorbance spectrum by about 100 nm in the UV region of the spectrum.

ECL and spectrometry measurements showed that perovskite nanoparticles deposited on the glassy carbon are washed out of the thin polymer film and remain in phosphate buffer solution, where they react with tripropylamine (TPrA) and emit light in the course of oxidation reaction at the glassy carbon electrode. Spectroscopic measurements of the solution before and after ECL measurements, as well as measurements of the nanoparticle solution, prove the above-mentioned observations. Subsequent ECL measurements showed that nanoparticles in solution remain relatively stable and have an ECL intensity proportional to the amount of coreactant in the solution.

C. ECL spectra

The approximate range of the electrochemiluminescent signal was estimated. The spectrum was determined using optical filters that were placed between the electrochemical cell and the photomultiplier tube. As a result of the

experiment, it was found that the spectrum of the light signal during the electrochemical reaction is in the range from 600 to 650 nm. (Fig.5)

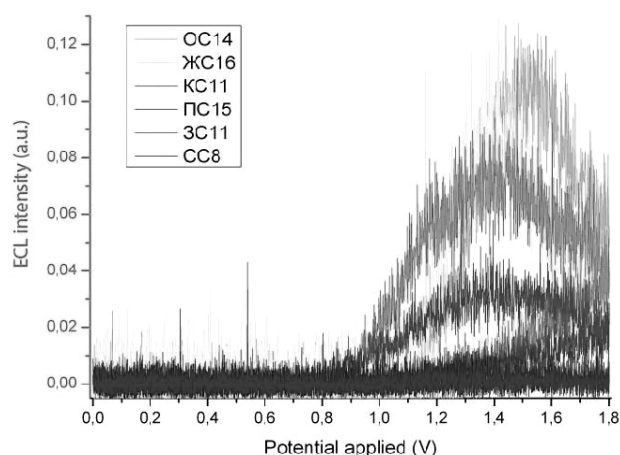


Fig.5. ECL signal through the optical filters

V. CONCLUSIONS

It can be argued that the combination of CsPbBr₃ nanocrystals with polymethylmethacrylate polymer and preliminary UV irradiation allows obtaining a state of perovskite nanocrystals that are stable in the aqueous buffer solution and have a stable ECL signal during multiple measurements. The obtained results open up prospects for the application of perovskite NPs in the ECL method, as well as for studying the process of increasing the ECL intensity by the UV irradiation of mixed perovskites colloid solution and PMMA polymer.

ACKNOWLEDGMENT

Part of this work was supported by the National Research Foundation of Ukraine project 2020.02/0390.

REFERENCES

- [1] Laser-induced nanoparticles in electroanalysis: Review/ V.S. Vasylykovskiy, M.I. Slipchenko, O.V. Slipchenko, K.M. Muzyka, Yu.T. Zholudov // J. Functional Materials, 28 (2), pp. 210 - 216
- [2] Cesium lead halide (CsPbX₃, X=Cl, Br, I) perovskite quantum dots-synthesis, properties, and applications: a review of their present status / Ananthakumar S., Kumar J. R., Babu S. M. // J. of Photonics for Energy, 6(4), 2016, pp. 042001
- [3] Recent Advances in Electrochemiluminescence of Halide Perovskites / Kong, Y., Zhang, B.-H., Zeng, Z.-H., Zhang, Y.-W., Niu, L. // Chinese Journal of Analytical Chemistry, 2020, 48(2), pp. e20021-e20031
- [4] Highly luminescent and stable CsPbBr₃ perovskite quantum dots modified by phosphine ligands / Li, Y., Wang, X., Xue, W., Wang, W., Zhu, W., Zhao, L. // Nano Research, 2019, pp. 1-5.
- [5] High-quality CsPbBr₃ perovskite nanocrystals for quantum dot light emitting diodes/ X. Du, G. Wu, J. Cheng, H. Dang, K. Ma, Y.-W. Zhang, P.-F. Tana, S. Chen// RSC Adv., 2017, 7, pp. 10391-10396.
- [6] Electrochemical characterization of modified glassy carbon based nanosensor with polyaniline nanoparticles / graphene using cyclic voltammetry / A. N. Lafta, A. Moosa, M.M Radhi // AdvNanoBioM&D, 2020, pp. 603-616

DC magnetron sputtering method for obtaining nanoscale semiconductor films

Yevgen Sokol
Department of Industrial and
Biomedical Electronics
National Technical University
"Kharkiv Polytechnic Institute"
Kharkiv, Ukraine
0000-0003-1370-1482

Andrii Dobrozhan
Department of
Natural Science
National Technical University
"Kharkiv Polytechnic Institute"
Kharkiv, Ukraine
doabr.ubs@gmail.com

Andrey Meriuts
Department of Materials for
Electronics and Solar Cells
National Technical University
"Kharkiv Polytechnic Institute"
Kharkiv, Ukraine
meriuts@ukr.net

Alina Khrypunova
Department of
Natural Science
National Technical University
"Kharkiv Polytechnic Institute"
Kharkiv, Ukraine
khripalina22@gmail.com

Abstract — It has been carried out the experimental studies of the process of semiconductor direct current magnetron sputtering, and the impact of a magnetron sputtering mode on optical properties of solar cell functional layers. In order to create thin-film solar cells based on CdTe, thin films for the base layers of thin film solar cells was obtained on flexible polyimide and glass substrates by direct current magnetron sputtering. It has found that obtained by DC magnetron sputtering method ZnO and CdS nanoscale thin films and CdTe layers have optimal optical properties for obtaining thin film solar cells based on CdS/CdTe heterosystem.

Keywords—solar cells, cadmium sulfide, cadmium telluride, direct current magnetron sputtering

I. INTRODUCTION

Thin film solar cells (SC), based on cadmium sulfide and telluride, represent an alternative to the most widespread silicon crystalline solar cells in the capacity of autonomous sources of electric energy in terrestrial and space conditions. Modern high efficiency film SC based on CdS/CdTe are produces in the back configuration on the glass substrate through which solar radiation enters the base layer [1]. In terrestrial conditions, SC based on CdS/CdTe, in accordance with the optimum band gap of cadmium telluride, have the greatest efficiency – 29%. In space applications, due to the nature of the chemical bonds of CdTe such SC are the most resistant to radiation [2]. In addition, lower material and energy consumption of manufacturing process of film photovoltaic converters based on CdS/CdTe provides a lower cost compared to crystalline silicon photovoltaic converters. For example, in the conditions of industrial production, First Solar company which manufactures photovoltaic converters based on CdS/CdTe said about reaching "grid parity" when the cost of electricity produced by photovoltaic converters equals the cost of electricity produced by conventional power sources [3]. It should be note that conventional SC based on CdTe essentially concedes to SC based on crystalline silicon in power density (value of electric power generated per unit weight of a SC).

Substitution of glass substrates, which are conventional for SC based on CdS/CdTe to a flexible substrate, allows the reduced power to increase by several orders of magnitude, and to surpass by this parameter not only silicon-based SC, but also SC based on A_3B_5 . However, in addition, due to the lower thermal stability of the polyimide substrate it is necessary to reduce the deposition temperature of the cadmium telluride films below 400 °C what is impossible for methods of close space sublimation [4] and vapor phase transport deposition [5] which are conventionally used to produce high performance SC based on CdS/CdTe. When implementing these methods forming the base layer of cadmium telluride has carried out at a deposition temperature of 550°C.

Low temperature techniques for production of cadmium telluride films that can be realize in mass production includes magnetron sputtering method [6]. The main technological challenge of getting the semiconductor films by magnetron sputtering with direct current is a low rate of film growth. This is because during sputtering, a low-conducting substrate accumulation of positive charge takes place, and this charge does not have time to drain off. This creates a counter field inhibiting the argon ions which bombard the substrate what causes a decrease in the discharge current. Also for materials with a high work function of electrons, which include most semiconductors and dielectrics, a low electron emission is characteristic. Accordingly, when the DC sputtering method was implement for semiconductor materials, low ion current densities are observes that do not allow the realization of the production of thin films of semiconductors in industrial scale.

This problem can be solved by increasing the discharge current density during direct current (DC) magnetron sputtering of cadmium sulfide and telluride due to the use of the phenomenon of thermionic emission providing enhanced ionization of the working gas.

Therefore, obtaining of CdTe, CdS and ZnO films for flexible SC base layers by direct current magnetron sputtering is an urgent technological problem. In this work obtaining semiconductors films by DC magnetron sputtering

method and the impact of the magnetron sputtering modes on thin films optical properties was studied.

II. EXPERIMENTS

The mentioned problem can be solved due to the intensification of thermionic emission when the cadmium telluride target surface is preheated up to a 166°C and then maintained in the range from 156°C to 166°C . For this temperature interval, the increase of discharge current due to thermionic emission exceeds the effect of reducing the discharge current due to the growth of working gas ions with the target surface atoms elastic collisions probability. The heating of the target was carry out by the heater combined with a substrate heater placed above magnetron surface using an automated negative feedback based on a microcontroller controlling the heater and providing stabilization of the discharge current with an accuracy of ± 2 mA with constant voltage on the magnetron and argon pressure.

In the work, we have used deposition of CdTe, CdS and ZnO films by DC magnetron sputtering. We used an experimental vacuum plant VUP-5M with original magnetron systems what important design feature was their cooling circuit which includes only a magnetic system. The manufacturing of target provided by cold pressing from semiconductor powder and with diameter - 76 mm, and thickness - 2 mm. Target cold pressing pressure was 100 MPa. The dwell time of the target at this pressure was 15 hours. After pressing the target its vacuum annealing has performed at a residual pressure of at least 10^{-4} mmHg and a

temperature of 80°C . For obtaining CdTe, CdS, ZnO layers as a substrate used thermostable polyimide film manufactured by Uplex firm or soda-lime glass. The flexible or glass substrate has positioned in a movable substrate holder of VUP-5M vacuum chamber in close contact with the front surface of the thermocouple. Before the process of applying the cadmium telluride layers pumping in the working volume to a pressure of 10^{-5} Pa has carried out. Argon puffing in the capacity of a working gas has carried out using an automated puffing system SNO.

To realize the effect of thermionic emission in the DC magnetron sputtering of cadmium telluride, we used a heated cathode, which produce additional electrons mainly by thermionic rather than secondary emission.

During studying the process of DC magnetron sputtering to produce CdTe, CdS, ZnO films, different obtaining modes were realize. These regimes differed by argon pressure (P_{arg}), voltage on the magnetron (V), and the heating modes of the substrate and target also, we measured the dependence of the discharge current of the magnetron (I) on the sputtering time (t).

III. RESULTS AND THEIR DISCUSSION

Based on the analysis of the process of direct current magnetron sputtering semiconductors films we have selected deposition modes what provide intensive sputtering of a target. For this purpose, we pre-heated the substrate up to $300\text{-}420^{\circ}\text{C}$ for different films obtaining processes (Fig. 1a).

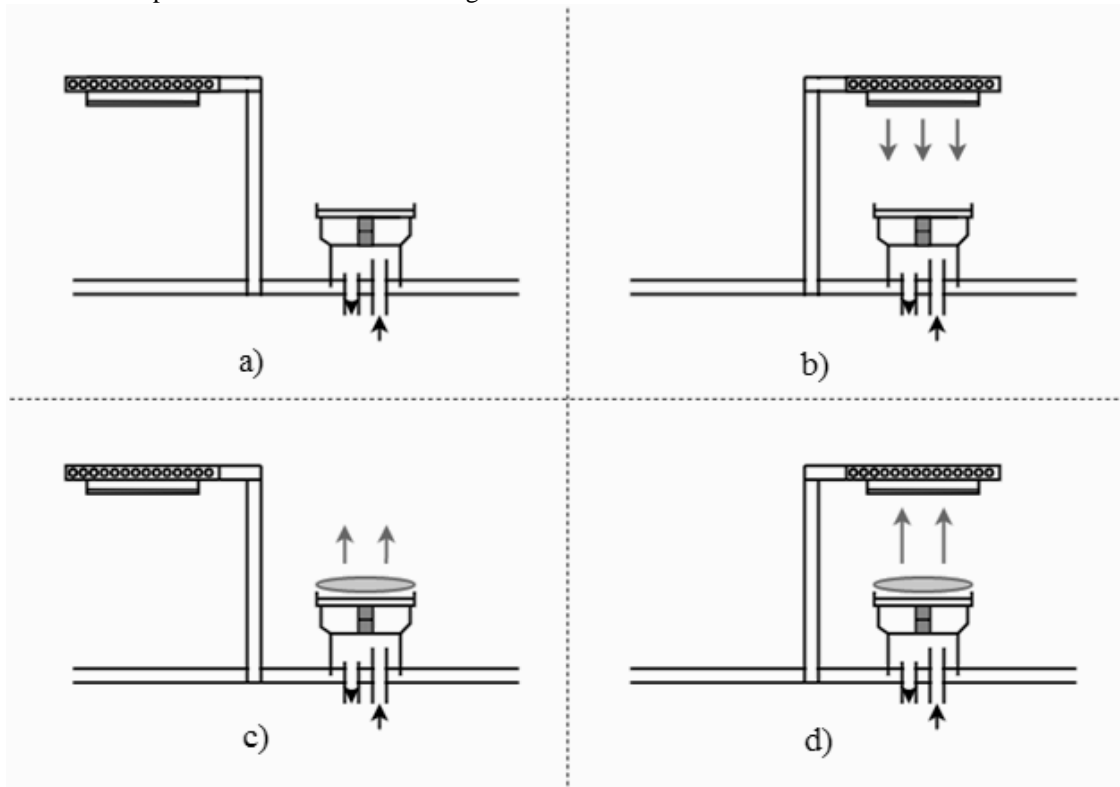


Fig. 1. Schematic representation of the mutual orientation of the magnetron system with a semiconductor target and a movable substrate holder with a built-in heater and substrate at different stages of obtaining semiconductor films by DC magnetron sputtering method: a) heating the substrate; b) heating the semiconductor target; c) the process of training a semiconductor target; d) the process of sputtering semiconductor material on the substrate

After reaching this temperature, the movable substrate holder has transferred to the mode above the target; as a result, the target has also heated for 5-8 minutes (Fig. 1b).

From our point of view, heating up of the target surface causes increase in the intensity of the thermal emission of secondary electrons from the target surface in the magnetron

discharge zone and reducing the electric resistance of the target because of the thermal generation of the main charge carriers (Fig. 2). Increase in the concentration of the secondary electrons increases the probability of ionization of the argon molecules what in turn causes increase in the intensity of the argon ion bombardment of the target surface and therefore the target sputtering rate. Generation of main carriers lowers the target resistivity and decreases the intensity of the accumulation of positive charge that leads to formation of the electric counter field retarding accelerated argon ions, which bombard the target. Availability of a charge accumulation process is confirming by experimentally observed decrease in the discharge current. The experimentally observed stabilization of the discharge current irrespective of the technological process of magnetron sputtering indicates the occurrence of the heat balance mode in the target. A voltage was applying to the magnetron, and the previous preparation process - target training process (Fig. 1c). It is necessary for cleaning target surface before semiconductors films deposition process has started. Upon that, the discharge current varied within the range of 40 mA to 100 mA for different samples by variation of the magnetron power ranging from 600 V to 650V, and of an argon partial pressure from 1 Pa to 0.8Pa. Thus, discharge current has almost not changed in the process of sputtering. The substrate temperature during the deposition was also virtually unchanged and was 300°C. The time of the films deposition process ranged from 5 to 25 minutes (Fig. 1).

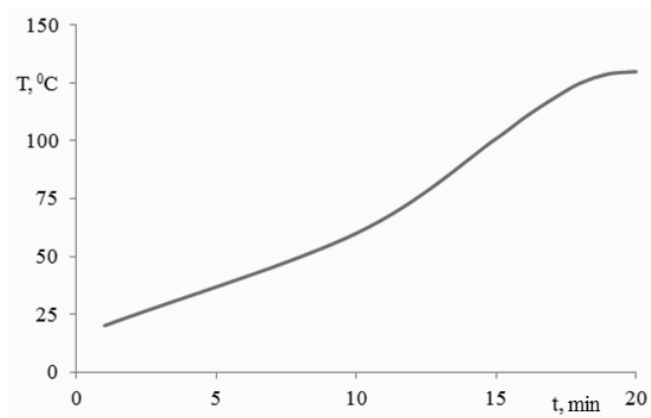


Fig. 2. Temperature dependence of the semiconductor target during preheating before the magnetron sputtering process

It has found that in the process of magnetron sputtering of a cadmium telluride target the change of discharge current has observed. The carried out research of the magnetron sputtering process with direct current of the cadmium telluride target has shown that changing the magnetron sputtering current in the process of CdTe film deposition has related to target material surface heating. Experiments show that this can occur due to thermal radiation from the substrate surface. Indeed, it has experimentally demonstrated that with increasing of substrate temperature and, particularly, its heating time over the target surface, an increase of the initial discharge current of 1.2 mA to 75 mA has observed. The temperature of the target surface also increases with magnetron sputtering time due to the bombardment of the target by ions of the working gas [7].

CdS thin films were condensed on soda-lime glass substrates at following physical and technological mode:

substrate temperature $T_{\text{sub}}=130^{\circ}\text{C}$, pressure of inert gas Ar $P_{\text{arg}}=0.9\text{-}1\text{ Pa}$, magnetron discharge current density $J=1.1\text{ mA/cm}^2$, the voltage on magnetron $V=470\text{-}500\text{ V}$, deposition time 10-15 min.

ZnO thin films were condensed on a soda-lime glass substrates at following physical and technological mode: substrate temperature $T_{\text{sub}}=210^{\circ}\text{C}$, pressure of inert gas Ar $P_{\text{arg}}=0.9\text{-}1\text{ Pa}$, magnetron discharge current density $J=2.2\text{ mA/cm}^2$, the voltage on magnetron $V=310\text{-}340\text{ V}$, deposition time 3-16 min.

Spectral dependences of transmission coefficient of obtained FTO/ZnO layers are presented in fig. 3. According to results of optical studies there is a absorption of radiation in the wavelength range 300-500 nm, while in visible ($\lambda>500\text{ nm}$) and infrared spectral ranges the FTO/ZnO films transparense is up to 70%.

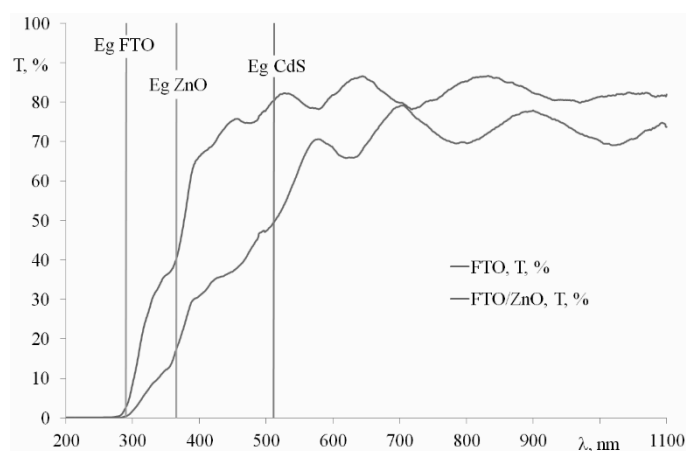


Fig. 3. Spectral dependences of FTO and FTO/ZnO transmission coefficient samples with marks of optical bandgap E_g for FTO, ZnO and CdS material

Spectral dependences of transmission coefficient of obtained CdS layers are presented in fig. 4. Spectral dependences of transmission coefficient of obtained CdS layers are presented in fig. 3. According to results of optical studies there is a strong absorption of radiation in the wavelength range 400-500 nm, while in visible and infrared spectral ranges the CdS films transparense is up to 80%. Calculation of their thickness showed that the deposition rate of CdS layers is 18-20 nm/min.

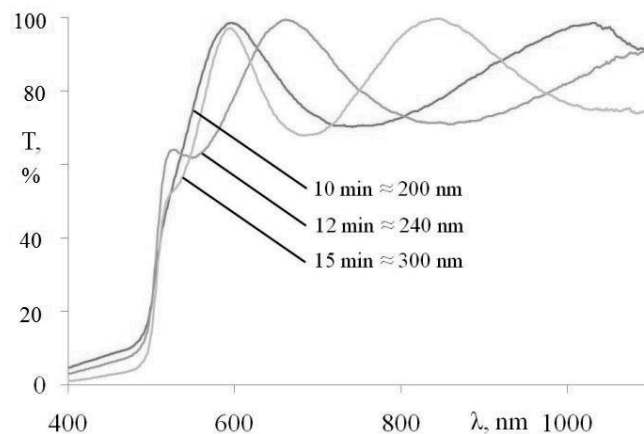


Fig. 4. Spectral dependences of transmission coefficient of CdS samples for calculate the sputtering rate and the thickness of the nanolayers.

Spectral dependences of transmission coefficient of obtained CdTe layers with 4-5 μm thickness are presented in fig. 5. According to results of optical studies there is a strong absorption of radiation in the wavelength range 400-800 nm, while in infrared spectral ranges the CdTe films transperance is up to 40-45%.

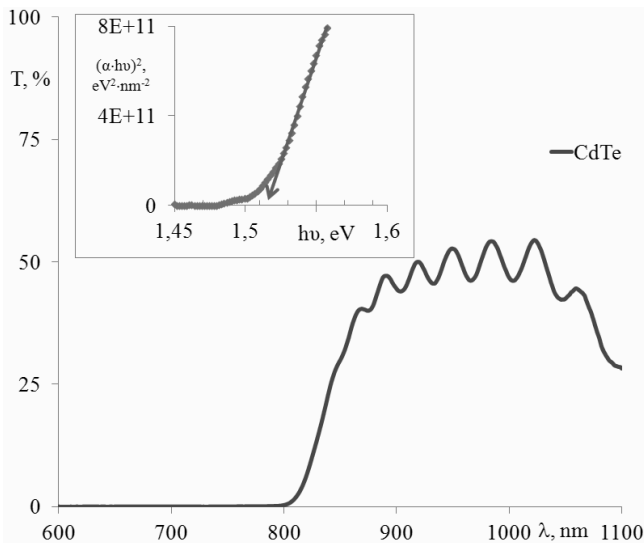


Fig. 5. Spectral dependence of typical CdTe samples transmission coefficient and dependence of the $(\alpha \cdot hv)^2 = f(hv)$ curve

Obtained by DC magnetron sputtering method ZnO, CdS nanoscale thin films and CdTe layers have optimal crystal structure [8] and optical properties for obtaining thin film solar cells based on CdS/CdTe heterosystem.

IV. CONCLUSIONS

The CdTe, CdS and ZnO films have been produce on flexible polyimide substrates and soda-lime glass by direct current magnetron sputtering. This process realized due to heating the target surface to intensify the thermal emission of the secondary electrons in the magnetron discharge zone and to reduce the electrical resistance of the target as a result of thermal generation of main charge carriers.

The obtained experimental data make it possible to propose the following method for the realization of deposition of these or other semiconductor materials films by the method of direct current magnetron sputtering. The surface of magnetron target, whose design allows the target

to be cools, is heating up to a temperature of 166 $^{\circ}\text{C}$, which corresponds to the maximum discharge current.

To heat the target, a substrate heater placed above the magnetron's surface. After reaching a temperature of 166 $^{\circ}\text{C}$ is supplied with a discharge voltage and the process of sputtering the target begins during of which the automated feedback system maintains the target temperature in the range from 156 $^{\circ}\text{C}$ to 166 $^{\circ}\text{C}$ in which the thermionic emission effect increases the discharge current and intensify the process of cadmium telluride sputtering.

The proposed method makes it possible to obtain high quality films with a high growth rate by a well-developed industry and an economical method of magnetron sputtering with direct current and does not require making significant changes to the design of typical magnetron sputtering plants.

The practical realization of proposed method in industrial scales will be allow to increase the values of thin film solar cells production, especially the solar cells based on glass or flexible polyimide substrates.

REFERENCES

- [1] M. Hädrich, C. Heisler, U. Reislöhner, C. Kraft, H. Metzner, "Back contact formation in thin cadmium telluride solar cells," *Thin Solid Films*, vol. 519, no. 21, pp. 7156-7159, 2011.
- [2] J. Han, C. Spanheimer, G. Haindl, G. Fu, V. Krishnakumar, J. Schaffner, C. Fan, K. Zhao, A. Klein, W. Jaegermann, "Optimized chemical bath deposited CdS layers for the improvement of CdTe solar cells," *Solar Energy Materials and Solar Cells*, vol. 95, no. 3, pp. 816-820, 2011.
- [3] FirstSolar [Official website]. – URL: www.firstsolar.com. Accessed: 5.09.2021.
- [4] N. Romeo, A. Bosio, R. Tedeschi, A. Romeo, V.Canevari, "Highly efficient and stable CdTe/CdS thin film solar cell," *Solar Energy Materials and Solar Cells*, vol. 58, no. 1-4, pp. 209-218, 1999.
- [5] R.W. Birkmire, E. Elser, "Polycrystalline thin film solar cells," *Journal of Materials Research*, vol. 27, pp. 625-653, 1997.
- [6] A. Gupta, V. Parikh, A.D. Compaan, "High efficiency ultra-thin CdTe solar cells," *Solar Energy Materials and Solar Cells*, vol. 90, no. 6, pp. 2263-2271, 2006.
- [7] G.S. Khrypunov, G.I. Kopach, R.V. Zaitsev, A.I. Dobrozhan, M.M. Harchenko, "Flexible Solar Cells are Based on Underlying Layers of CdTe Obtained by Magnetron Sputtering", *J. Nano- Electron. Phys.*, no. 9, p. 02008, 2017.
- [8] Kopach G.I., R.P. Mygushchenko, G.S. Khrypunov, A.I. Dobrozhan, M.M. Harchenko "Structure and optical properties CdS and CdTe films on flexible substrate obtained by DC magnetron sputtering for solar cells", *J. of Nano- and Electron. Phys.*, vol. 9., no. 5, p. 05035-1 - 05035-6, 2017.

Determination of Longitudinal Sizes of Carbon Nanotubes at the Fundamental Resonant Frequency

Sergey Berdnik
*Department of Radiophysics,
Biomedical Electronics and Computer
Systems*
V. N. Karazin Kharkiv National
University
Kharkiv, Ukraine
berdnik@karazin.ua

Oleksandr Dumin
*Department of Radiophysics,
Biomedical Electronics and Computer
Systems*
V. N. Karazin Kharkiv National
University
Kharkiv, Ukraine
dumin@karazin.ua

Victor Katrich
*Department of Radiophysics,
Biomedical Electronics and Computer
Systems*
V. N. Karazin Kharkiv National
University
Kharkiv, Ukraine
vkatrich@karazin.ua

Mikhail Nesterenko
*Department of Radiophysics,
Biomedical Electronics and Computer
Systems*
V. N. Karazin Kharkiv National
University
Kharkiv, Ukraine
mikhail.v.nesterenko@gmail.com

Svetlana Pshenichnaya
*Department of Radiophysics,
Biomedical Electronics and Computer
Systems*
V. N. Karazin Kharkiv National
University
Kharkiv, Ukraine
s.v.pshenichnaya@gmail.com

Sergey Shulga
*Department of Radiophysics,
Biomedical Electronics and Computer
Systems*
V. N. Karazin Kharkiv National
University
Kharkiv, Ukraine
sergeyshulga@karazin.ua

Abstract—This communication substantiates the possibility of using the diffraction method to determine the longitudinal dimensions of long carbon nanotubes. This method, being a non-destructive testing method, is based on the asymptotic solution of the inverse problem of scattering of a plane electromagnetic wave by a thin impedance vibrator located in a medium at a finite distance above a screen of finite dimensions, parallel to its ideally conducting surface. As a result of solving this problem for the infinitesimal losses in the medium, the length of the carbon nanotube can be found unambiguously at the frequency of the fundamental resonance response. The frequency (wavelength) of the fundamental resonance of the vibrator is preliminarily determined experimentally by one of the diffraction spectroscopic methods.

Keywords—carbon nanotube, electromagnetic wave, impedance vibrator

I. INTRODUCTION

In modern scientific literature [1-8] carbon nanotubes (CNT) are defined as extended cylindrical structures with a diameter of one to several tens of nanometers and a length of up to several centimeters, consisting of one or more graphene planes rolled into a tube and usually ending in a hemispherical head, which can be considered as half of a fullerene molecule. Studies have shown that CNT have a number of physical and mechanical properties that are promising from the point of view of the development of new unique devices. So, for example, single-wall CNT (SWCNT) are characterized by very high values of Young's modulus, thermal conductivity, electronic conductivity, etc. Therefore, the development of nanometric methods that make it possible to measure and control the CNT dimensions is an important task both for finding new practical applications of CNT and for providing their further fundamental research.

Originally obtained in practice, CNT (multilayer and single-walled) had transverse and longitudinal dimensions from units to several hundred nanometers, which could be measured within the framework of known high-resolution electron microscopy methods. In connection with the rapid progress in technologies for growing SWCNT (for example, in [2], the fact of growing CNT with a record length of 18.5 cm is reported), a significant gap was determined between the scale of CNT diameters and their linear longitudinal dimensions. This has led to the fact that the direct application of electron microscopy methods for measuring the longitudinal dimensions of CNT has become extremely difficult. Moreover, a feature of the methods of transmission electron microscopy, scanning tunneling and atomic force microscopy is the need for spatial manipulation with the measurement objects, which often leads to damage of CNT samples [3].

In this communication, the authors propose a non-contact diffraction method for assessing the longitudinal dimensions of long SWCNT, devoid of these disadvantages. This method is based on the asymptotic solution of the inverse problem of scattering of a plane electromagnetic wave on a thin impedance vibrator located at a finite distance above the screen, parallel to its ideally conducting surface, and makes it possible to unambiguously determine the length of SWCNT at the frequency of the main resonant response.

II. RESONANT PROPERTIES OF IMPEDANCE VIBRATORS

To analyze the resonance properties of long SWCNT, let us consider the model problem of diffraction of a plane electromagnetic wave by a horizontal impedance vibrator located in a semi-infinite material medium above an ideally conducting plane. This choice of the model problem is determined by the fact that, in practice, the growth of long SWCNT is possible only in the presence of a dielectric

substrate base [2], which is easiest to implement in the form of a dielectric layer on a metal screen from a technological point of view. The investigated structure of the model and the designations adopted in the problem are shown in Fig. 1. Here $\{x, y, z\}$ is the Cartesian coordinate system associated with an ideally conducting plane and a cylindrical vibrator of length $2L$ and radius r , respectively. The axis $\{0s\}$ is directed along the axis of the vibrator located in a medium with material parameters (ϵ_1, m_1) at a distance h from the plane.

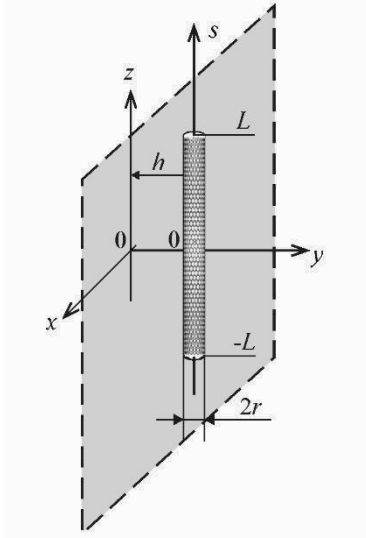


Fig. 1. The geometry of the impedance vibrator model above the screen.

It is assumed that the impedance scatterer SWCNT is excited by an external harmonic field $\vec{E}_0(\vec{r})$, where \vec{r} is the radius-vector of the observation point, the time t dependence has the form $e^{i\omega t}$, ω is the angular frequency. Its geometric dimensions satisfy the following inequalities, the conditions of a thin vibrator: $r/(2L) \ll 1$, $|r/l_1| \ll 1$,

where l_1 is the wavelength in environment. In the case of SWCNT, it is known [1, 9] that a nanovibrator can be characterized by a constant distributed normalized surface impedance, if the condition $m_1 = 1$ is met:

$$\bar{Z}_s = \bar{R}_s + i\bar{X}_s = \frac{i\pi\hbar^2(\omega - i\nu)}{240e^2v_F}, \quad (1)$$

where v_F is the Fermi velocity (for CNT $v_F \gg 9.71\tau \cdot 10^5$ m/s), ν is the relaxation frequency (for CNT $\nu = 3.33\tau \cdot 10^{11}$ Hz), e is the electron charge, \hbar is the Planck constant. It should be noted that according to [2], the value of the internal impedance (1) is retained when changing the accumulated length of the SWCNT.

As a starting point, we use the analytical solution of the integral equation for the electric current in a thin impedance vibrator, obtained in monograph [9] by the averaging method. Under the condition of vanishingly small losses in the medium on the basis of this solution, taking into account the definition of resonance as equality to zero of the

imaginary part of the input impedance of the vibrator, we write the transcendental equation for finding the resonant electrical length of the impedance vibrator in our case [10]:

$$\operatorname{Re} \left\{ \tilde{k} \frac{\cos(\tilde{k}L_{res}) + \alpha \operatorname{Re} P^{Hs}[k_1 r + h, (\tilde{k}L_{res})]}{\sin(\tilde{k}L_{res})} \right\} = 0, \quad (2)$$

where $\operatorname{Re} P^{Hs}[k_1 r + h, (\tilde{k}L_{res})]$ is the real part of the function

$$P^{Hs}[k_1(h+r), \tilde{k}L] \Big|_{\frac{r}{2L} \ll 1} \approx P^{Fs}(k_1 r, \tilde{k}L) - \frac{1}{2} \left\{ \begin{array}{l} \cos \tilde{k}L \left[\ln \frac{B+2k_1L}{B-2k_1L} + \operatorname{Cin}(B-2k_1L) - \operatorname{Cin}(B+2k_1L) \right] \\ -i[\operatorname{Si}(B+2k_1L) - \operatorname{Si}(B-2k_1L)] \\ + \sin \tilde{k}L \left[\operatorname{Si}(B+2k_1L) + \operatorname{Si}(B-2k_1L) - 2\operatorname{Si}(A) \right] \\ -i[\operatorname{Cin}(B+2k_1L) + \operatorname{Cin}(B-2k_1L) - 2\operatorname{Cin}(A)] \end{array} \right\}$$

$$P^{Fs}(k_1 r, \tilde{k}L) \Big|_{\frac{r}{\lambda_1} \ll 1} \approx \frac{1}{2} \left\{ \begin{array}{l} \cos \tilde{k}L \left[2 \ln(4L/r) - \operatorname{Cin}(2\tilde{k}L + 2k_1L) - \operatorname{Cin}(2\tilde{k}L - 2k_1L) \right] \\ -i[\operatorname{Si}(2\tilde{k}L + 2k_1L) - \operatorname{Si}(2\tilde{k}L - 2k_1L)] \\ + \sin \tilde{k}L \left[\operatorname{Si}(2\tilde{k}L + 2k_1L) + \operatorname{Si}(2\tilde{k}L - 2k_1L) \right] \\ -i[\operatorname{Cin}(2\tilde{k}L + 2k_1L) - \operatorname{Cin}(2\tilde{k}L - 2k_1L)] \end{array} \right\}$$

$\operatorname{Si}(x)$ and $\operatorname{Cin}(x)$ are the integral sine and cosine of the complex argument, $A = k_1(2h+r)$, $B = \sqrt{(2k_1L)^2 + A^2}$, $k_1 = 2\pi/\lambda_1$ is the wavenumber in the medium, $\tilde{k} = k_1 + i(\alpha/r)\bar{Z}_s$, $\alpha = \frac{1}{2 \ln[r/(2L)]}$ is the small parameter. We emphasize that equation (2) turns out to be valid both for symmetric excitation of the vibrator by a point voltage generator in the form of the Dirac delta function $\delta(s-0) = \delta(s)$, and in the case of its excitation by a plane wave.

Fig. 2 shows the results of comparative calculations of functions from [8] $P^{Fs}(k_1 r, \tilde{k}L)$ and $P^{Hs}[k_1(h+r), \tilde{k}L]$ both by numerical integration and by the approximate relations presented above. As can be seen, the coincidence of the numerical and analytical values is quite satisfactory, especially at relatively small values of the surface impedance of the vibrator.

The general transcendental equation (2) with respect to the sought-for vibrator length L_{res} is correct for an arbitrary wavelength of the exciting field when the conditions for the fineness of the vibrator are met. It can be successfully solved by numerical methods for a given wavelength. It should be understood that for the case of centimeter and millimeter wavelength ranges (in which resonant frequencies for long SWCNT will be observed) in formula

(1) $w = v$ and the complex impedance \bar{Z}_s will be characterized by a real part that significantly exceeds the value of its imaginary part $\bar{R}_s \gg \bar{X}_s$. Since, according to the general theory [9], the presence of a purely active impedance in the vibrator does not lead to a change in the resonant frequency of the impedance vibrator with respect to the ideally conducting one, when numerically solving the transcendental equation (2) as an initial approximation $L_{res}^{(0)}$, it is optimal to use the value:

$$\cos(k_1 L_{res}^{(0)}) = 0, L_{res}^{(0)} \gg l_1/4. \quad (3)$$

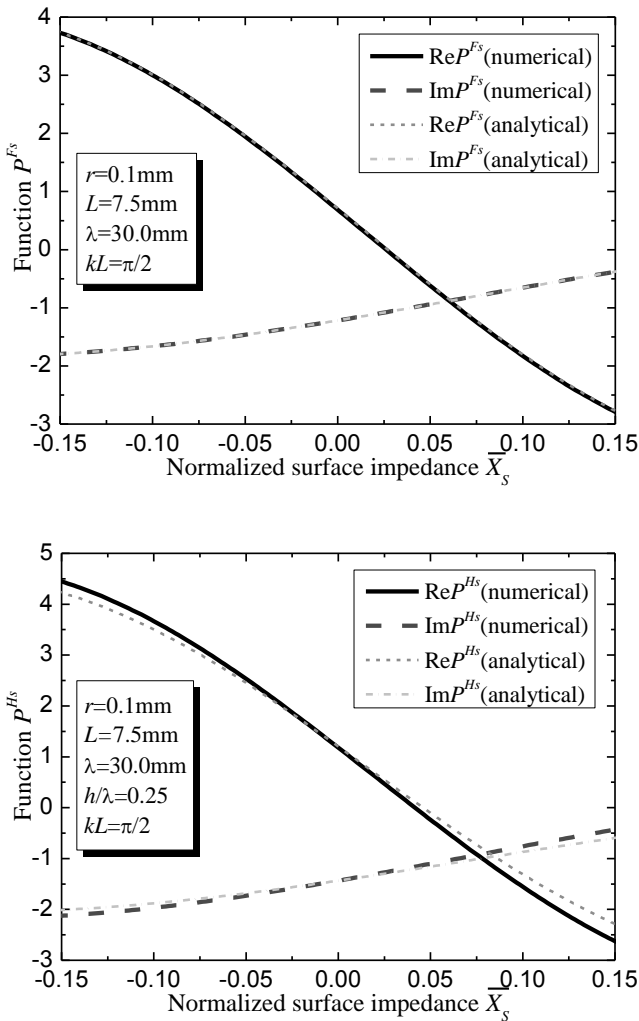


Fig. 2. The functions $P^{Fs}(k, r, \frac{l}{\lambda})$ and $P^{Hs}[k_1(h+r), \frac{l}{\lambda}]$ depending on vibrator surface impedance.

It also follows from (1) that in the frequency range from 1 THz to 100 THz the imaginary part of the normalized impedance is much larger than its real part (that is, $\bar{X}_s \gg \bar{R}_s$). Therefore, in this frequency range, carbon tubes can be modeled as thin vibrator scatterers with a distributed surface impedance of a purely inductive type. In this case, the transcendental equation (2) is somewhat simplified, taking into account that $k\bar{L}$ becomes a purely real quantity

$$\cos(\tilde{k}L_{res}) + \alpha \operatorname{Re} P^{Hs}[k_1 r + h, (\tilde{k}L_{res})] = 0. \quad (4)$$

Its approximate solution can be found by expanding the unknown quantity in a series in powers of a small parameter

$$(\tilde{k}L_{res}) = (\tilde{k}L_{res}^{(0)}) + \alpha(\tilde{k}L_{res}^{(1)}) + \alpha^2(\tilde{k}L_{res}^{(2)}) + \dots \quad (5)$$

and $(\tilde{k}L_{res}^{(0)}) \approx \pi/2$.

III. CONCLUSION

Thus, having previously determined experimentally the frequency (wavelength) of the main resonance of the impedance vibrator, the length of the carbon nanotube can be found unambiguously from the transcendental equation (2). Since in this case there is a need to determine the frequency of the main resonant response in a wide frequency band, diffraction spectroscopic methods should be used here, for which modern equipment and techniques allow using electromagnetic pulses as exciting fields. Of course, the frequency of the resonant response will be determined here by Fourier analysis of the SCWNT pulses supplied and reflected from the sample. Note that the nature of the impedance SCWNT (its large real part) allows us to assume at the resonant frequency for the vibrator the implementation of the resonant absorption mode of the incident power.

REFERENCES

- [1] G. W. Hanson, "Radiation efficiency of nano-radius dipole antennas in the microwave and far-infrared regimes," *IEEE Antenn. Propag. Mag.*, vol. 50, pp. 66–77, 2008.
- [2] X. Wang, Q. Li, J. Xie, Z. Jin, J. Wang, Y. Li, K. Jiang, and S. Fan, "Fabrication of ultralong and electrically uniform single-walled carbon nanotubes on clean substrates," *Nano Letters*, vol. 9, pp. 3137–3141, 2009.
- [3] A. I. Vorobyova, "Equipment and methods for studying carbon nanotubes," // *Advances in Physical Sciences*, vol. 180, pp. 265–288, 2010 (in Russian).
- [4] G. W. Hanson, and J. A. Berres, "Multiwall carbon nanotubes at RF-THz frequencies: scattering, shielding, effective conductivity, and power dissipation," *IEEE Transactions on Antennas and Propagation*, vol. 59, pp. 3098–3103, 2011.
- [5] Y. N. Jurn, M. F. Malek, and H. A. Rahim, "Mathematical analysis and modeling of single-walled carbon nanotube material for antenna applications," *Progress In Electromagnetics Research M*, vol. 45, pp. 59–71, 2016.
- [6] Y. N. Jurn, S. A. Mahmood, and I. Q. Habeeb, "Performance prediction of bundle double-walled carbon nanotube-composite materials for dipole antennas at TeraHertz frequency range," *Progress In Electromagnetics Research M*, vol. 88, pp. 179–189, 2020.
- [7] Y. Antonenko, S. Berdnik, V. Katrich, M. Nesterenko, Y. Penkin, and S. Shulga, "Estimation of wave pressure on scattering carbon nanotubes in THz range," *Proc. of XI International Scientific Conference "Functional Basis of Nanoelectronics"*, Kharkiv-Odesa (Ukraine), pp. 44–47, 2020.
- [8] A. V. Melnikov, P. P. Kuzhir, S. A. Maksimenko, G. Y. Slepyan, A. Boag, O. Pulci, I. A. Shelykh, and M. V. Shuba, "Scattering of electromagnetic waves by two crossing metallic single-walled carbon nanotubes of finite length," *Phys. Rev. B*, vol. 103, No. 3, 2021.
- [9] M. V. Nesterenko, V. A. Katrich, Yu. M. Penkin, V. M. Dakhov, and S. L. Berdnik, *Thin Impedance Vibrators: Theory and Applications*, Springer Science+Business Media, New York, 2011.
- [10] N. P. Yeliseyeva, S. L. Berdnik, V. A. Katrich, and M. V. Nesterenko, "Electrodynamic characteristics of horizontal impedance vibrator located over a finite-dimensional perfectly conducting screen," *Progress In Electromagnetics Research B*, vol. 63, pp. 275–288, 2015.

High-sensitive combined gamma detector

Andrey Boyarintsev
Deputy Director of Science
Institute for Scintillation Materials of
NAS of Ukraine
Kharkiv, Ukraine
boyarintsev@isma.kharkov.ua

Alexandr Kolesnikov
Research-and-Development
Applications Division
Institute for Scintillation Materials of
NAS of Ukraine
Kharkiv, Ukraine
kolesnikov@isma.kharkov.ua

Sergii Kovalchuk
Research-and-Development
Applications Division
Institute for Scintillation Materials of
NAS of Ukraine
Kharkiv, Ukraine
kovalchuk@isma.kharkov.ua

Tatiana Nepokupnaya
Engineering and technology
department
Institute for Scintillation Materials of
NAS of Ukraine
Kharkiv, Ukraine
nepokupnaya@isma.kharkov.ua

Igor Nevliudov
Department of Computer-Integrated
Technologies, Automation and
Mechatronics
Kharkiv National University of Radio
Electronics
Kharkiv, Ukraine
igor.nevliudov@nure.ua

Vladimir Tarasov
Scintillation Radiometry and
Radiochemical Testing Methods
Department
Institute for Scintillation Materials of
NAS of Ukraine
Kharkiv, Ukraine
tarasov@isma.kharkov.ua

Abstract— The task of increasing of sensitivity of detectors of gamma-ray photons was solved in work by developing of technological processes of manufacturing of large area combined detectors based on organic and inorganic metamaterials with size of input window from 1000 cm². The sensitivity of gamma combined detectors based on CsI:Tl composite scintillator and scintillation polystyrene was 22% higher under ¹³⁷Cs irradiation and 78% higher under ²⁴⁰Am irradiation than that of scintillation polystyrene detector.

Keywords — sensitivity, combined gamma detector, metamaterials, composite materials

I. INTRODUCTION

High-efficient detectors for radiation portal monitors with higher sensitivity compare to NaI:Tl or plastic scintillators detectors are required now to detect ultra-low doses of gamma-ray photons. Advantages of plastic scintillators are high registration efficiency of gamma-ray photons with energy more than 300 keV. Main disadvantage of detectors based on plastic scintillators are low registration efficiency of gamma-ray photons with energy less than 100 keV. NaI:Tl detectors provide spectrometry and high sensitivity to low-energy gamma-ray photons. But this type of detectors is very expensive compare to plastic scintillators. Large area combined gamma detectors based on organic and inorganic materials are promising solution that allow to produce devices with high sensitivity to low-energy gamma radiation. Using such metamaterials as composite scintillators consisting of granules and optical medium allows to produce large area cost-efficient gamma detectors.

In general, combined radiation detector includes scintillation sandwich, reflector, protective housing and photodetector. Scintillation sandwich of any combined detector consists of scintillation layer makes of inorganic single crystal or composite scintillators and organic or inorganic light-conducting layer. Both sandwich layers are optically coupled by transparent glue.

Main requirements for large area scintillation sandwich and combined detectors are high sensitivity of small streams of ionizing radiation, input window from 1000 cm² and stability of scintillation characteristics of detectors at temperatures from - 50°C to +70°C.

Technological process of manufacturing of combined detectors with mention parameters is difficult task due to high cost of technology of crystals growth if we need crystals with one of linear dimensions more than 500 mm. Therefore, in order to fabricate large area scintillation layers it is necessary to use layers made of several crystall segments as mosaic. Other decision is using of composite scintillators based on crystal granules, mixed with optically transparent glue. Composite scintillators are new type of metamaterials that are suitable for manufacture of scintillation layers with high sensitivity of gamma-ray photons with energies less than 100 keV.

To enhance sensitivity of combined gamma detectors, it is necessary to increase transparency of composite layers. Light collection in composite layers depends on many factors, main of them are surface treatment of scintillation granules (degree of roughness, its shape), difference between refractive indices of crystal granules and optical medium, transparency of granules and number of granular layers in composite scintillator [1].

In this work CsI:Tl crystal granules were selected for production of scintillation layers of counting combined gamma detectors. This material was chosen because of such advantages as light output about 55,000 photons / MeV, decay time 1 μm and low hygroscopicity [2, 3]. Also it possible to use CsI:Tl crystal chips for production of corresponding granules. CsI:Tl crystal chips are formed during machining of single crystals, so production cost of CsI:Tl composite layers is lower than that of single crystal.

II. IMPROVING OF TRANSPARENCY OF COMPOSITE LAYER FOR COMBINED GAMMA DETECTOR PRODUCTION

Sensitivity of combined detector based on composite layer depends on transparency of heterogeneous medium. There are different ways to improve light collection in composite scintillation layer. One of them decreasing of difference between refractive indices of granules and optical medium. Other way is increasing of transparency of scintillation granules surface. Both methods were considered in work.

Mathematical simulation using Monte Carlo method was performed to predict processes of scintillation light transmission in weakly transparent composite layers. Composite scintillation layer is heterogeneous medium in which size of granules significantly exceeds wavelength of scintillation light, so approximations of geometric optics were used during simulation [4]. Dependence of light attenuation after its passage through composite layer was described by Bouguer-Lambert-Beer and expressed in terms of light collection coefficients k :

$$k = I / I_0 \cdot \exp(-\alpha \cdot h) \quad (1)$$

where I – number of photons came out of scintillator, I_0 – number of photons generated in scintillator, α – light collection coefficient, h – thickness of composite scintillation layer.

To register gamma rays photons, it is necessary to use scintillation layers based on granules with size of 100 - 500 μm and with maximum possible thickness to ensure absorption of significant part of radiation. Results of mathematical simulation allow estimating dependence of light collection coefficients on refractive indices of granules and optical medium.

During simulations, refractive index of granules was 1.80. It corresponds to data of CsI:Tl. Refractive indices of optical medium were 1.80 and 1.40, respectively. When refractive indices of granules and optical medium were equal, ideal case of structure of composite layer was simulated. When refractive index of optical medium was 1.4, simulation was performed for real contents of composite layers, because polysiloxane adhesives with such values of refractive index commonly use in manufacturing of composite scintillators [5, 6, 7]. Number of granule layers in composite scintillator varied from 1 to 10.

Simulated dependence of light collection coefficients on effective thickness of scintillation layer made of granules with size of 200 μm and optical mediums with refractive index of 1.80 and 1.40 are presented at Fig. 1, 2. If refractive indices of granules (n_{granule}) and optical medium ($n_{\text{optical medium}}$) were equal, then difference in light collection coefficients near input and output surfaces of composite layer was quite big and it increased with increasing of layer thickness (Fig. 1).

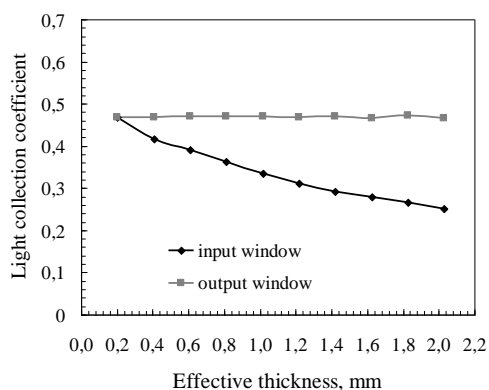


Fig. 1. Light collection coefficients of scintillation layers: granule size 200 μm ; $n_{\text{granule}} = 1.8$; $n_{\text{optical medium}} = 1.8$

If refractive index of optical medium was 1.40, then difference between light collection coefficients near input and output surface becomes smaller (Fig. 2.). This effect is due to fact that in thick composite layers (in this case 2 mm), consisting of 10 layers of granules with size of 200 μm transparency of composite layer is lower if ratio of refractive indices of granules and optical medium is 1.80 - 1.4. But in this case light collection coefficients increase due to diffuse reflection of light in part of composite layer remote from photodetector. If refractive indices ratio was 1.80 - 1.80, then transparency of composite layer increases, but light collection got worth due to increase of total thickness of layer and light scattering in volume of composite scintillator.

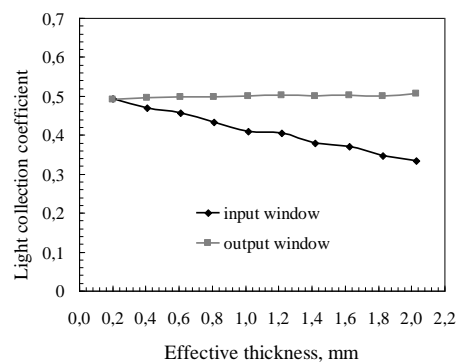


Fig. 2. Light collection coefficients of scintillation layers: granule size 200 μm ; $n_{\text{granule}} = 1.8$; $n_{\text{optical medium}} = 1.4$

So for composite scintillation layers with thickness from 1 mm, consisting of granules with size of 100 - 500 μm , light collection coefficients increases by 17% if refractive index of optical medium is 30% lower than that one of granules.

CsI:Tl granules for manufacturing of scintillation layer of combined detector were obtained from crystal chips producing after machining of single crystals. But in this case surface of CsI:Tl granules was opaque due to presence of broken crystal layer and remnants of coolant residues. Also shape of granules was close to scales with angles (Fig. 3).

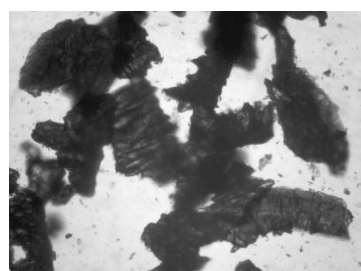


Fig. 3. Shape of surface of CsI:Tl granules before polishing

In order to increase transparency of granule surface chemical polishing of CsI:Tl crystal granules was used. Polishing process was based on treatment of granules surface with polar solvent containing OH- group. It is known that CsI:Tl is well soluble in water, ethanol, and poorly soluble in methanol and ethylene glycol [8, 9]. When choosing polishing solvent, determining criteria was its high chemical purity and low dissolution rate of CsI:Tl. Last parameter is important to prevent decrease of thallium activator concentration in CsI granules due to precipitation

of insoluble in ethylene glycol thallium iodide. As result of chemical polishing, surface of CsI:Tl granules became more spherical, and its transparency increased (Fig.4).

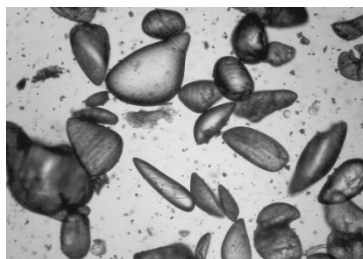


Fig. 4. Shape of surface of CsI:Tl granules after polishing

Technological process of polishing included stages of obtaining of crystal chips, screening of granules through calibrated metal sieves, selection of granules fraction with desired dimensions, stirring mixture of CsI:Tl granules with ethylene glycol for 1 minute, drying of granules in oven at 100 °C and relative humidity of 0 - 3% for 4 hours with periodic stirring until complete evaporation of solvent, screening of CsI: Tl granules through calibrated sieves and finally selection of granule fraction with sizes 63 - 300 μm for manufacturing of combined gamma detectors.

To study effect of surface treatment of CsI:Tl granules on optical and scintillation characteristics of composite layers, prototypes of CsI:Tl composite scintillators were fabricated. Test samples consisted of granules with size of 63 - 300 μm (80 wt.%) and polysiloxane rubber SKTN-med (20 wt. %). Size of granules 63-300 μm was chosen due to optimal utilization factor of material. Dimension of test samples were 20x20x0.98 mm³.

Transmission spectra of CsI: Tl scintillation composite layers before and after treatment by ethylene glycol are presented at Fig. 5. Spectra were measured on Shimatzu UV-2450 spectrophotometer using integrating sphere. Test samples were installed in measuring channel and fixed on outer surface of sphere. Measurement error was ± 0.5%.

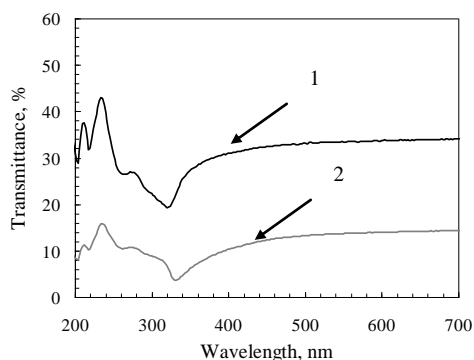


Fig. 5. Transmittance of CsI:Tl composite layers (granules 63 - 300 μm, thickness 0.98 mm): 1 - polished granules, 2 - untreated granules

As can be seen from figure 5, improvement of transparency and shape of CsI:Tl granules after polishing process has led to increasing of transmittance of CsI: Tl composite scintillators in 2.5 - 3 times in wavelength region 400 - 800 nm.

Dependence of light output of CsI:Tl composite scintillators on treatment of granule surface was also

investigated. Amplitude spectra of test samples under ¹³⁷Cs and ²⁴¹Am irradiation are presented at Fig. 6, 7. Measurements were performed on CANBERRA analyzer using Hamamatsu R1307 photodetector. Radiation source was placed at distance of 50 mm from the composite layer.

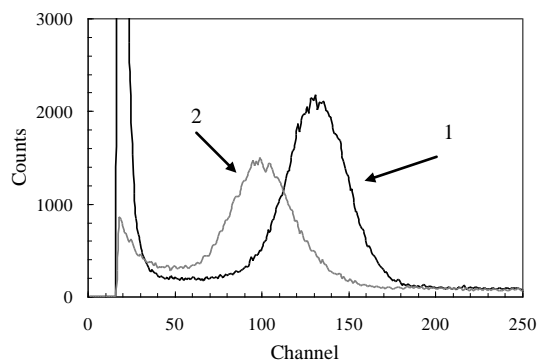


Fig. 6. Amplitude spectra of CsI: Tl composite layers (granules 63 - 300 μm, thickness 0.98 mm) under ¹³⁷Cs irradiation
1- polished granules, 2 - untreated granules

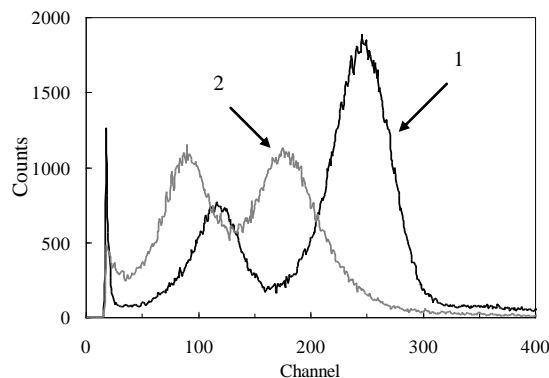


Fig. 7. Amplitude spectra of CsI:Tl composite layers (granules 63 - 300 μm, thickness 0.98 mm) under ²⁴¹Am irradiation
1- polished granules, 2 - untreated granules

It was shown that in case of using polished granules light output of CsI:Tl composite layers increased on 20 - 30% when gamma-radionuclides with energy 7 - 59.6 keV were identified.

Optimal thickness of composite layer based on polished CsI:Tl granules with size of 63 - 300 μm was determined (Fig 8).

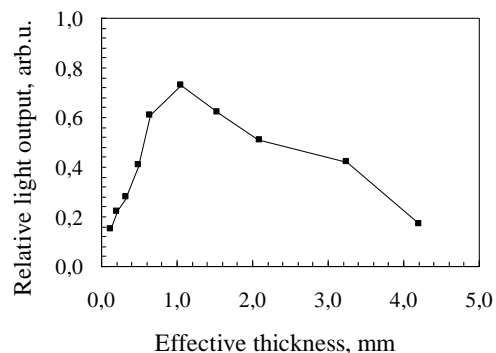


Fig. 8. Dependence of relative light output of composite layer CsI: Tl (granules 63 - 300 μm) on its thickness (E_γ = 59.6 keV)

The highest relative light output under ^{241}Am irradiation provided when thickness of layer was 1 mm.

III. SENSITIVITY OF COMBINED GAMMA DETECTORS BASED ON CsI:Tl COMPOSITE LAYER AND SCINTILLATION POLYSTYRENE

Scintillation characteristics of combined gamma detectors based on composite scintillator CsI:Tl and scintillation polystyrene with dimensions of 51x100x1000 mm² were studied (Fig. 9).

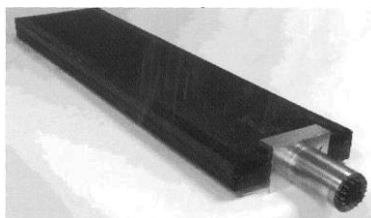


Fig. 9. Counting combined gamma-detector based on CsI:Tl composite scintillator and scintillation polystyrene

Scintillation polystyrene with dimensions of 50x100x1000 mm³ was used as reference detector. Counting rate of the combined and reference detectors was measured on a CANBERRA pulse analyzer. Radiation sources ^{241}Am (activity 4600 kBq), ^{137}Cs (activity 140 kBq) and ^{232}Th (activity 2800 kBq) were located in center of composite scintillator CsI:Tl at distance of 100 cm from detector. Hamamatsu R1306 was used as photodetector. The registration threshold was 20 keV.

Sensitivity of detectors η was determined by the formula:

$$\eta = (N_{det} - N_{bg}) / A \quad (2)$$

where N_{det} – count rate of combined detector, N_{bg} – count rate of background, A – source activity.

Calculated values of sensitivity are presented in Table I.

TABLE I Sensitivity of gamma-ray detectors

Detector type	Sensitivity, pulse/s·kBq	
	^{241}Am	^{137}Cs
Scintillation polystyrene 50x500x1000 mm ³	7,64	28,59
CsI:Tl - Scintillation polystyrene 51x100x1000 mm ³	13,65	35,03

Shape of amplitude spectra of combined detectors based on CsI:Tl composite layer and scintillation polystyrene indicated that such type of detectors register gamma-ray photons only in counting mode. When it was irradiated with ^{232}Th source difference between count rate of combined detector and scintillation polystyrene was not more than 2% due to fact that thickness of the composite layer was too small to register high energy particles.

Sensitivity of combined detector based on CsI:Tl composite layer and scintillation polystyrene was 22%

higher when irradiated with ^{137}Cs source and 78% higher when irradiated with ^{241}Am source if compare with corresponding values of scintillation polystyrene detector.

IV. CONCLUSIONS

Physical and technical parameters that allow to increase sensitivity of gamma ray photons of counting combined detectors with input window from 1000 cm² based on optically coupled CsI:Tl composite layer and scintillation polystyrene plate were determined.

It was determined that for manufacturing of composite scintillation layers based on CsI:Tl granules with size of 100–500 μm and with thickness from 1 mm, light collection coefficient increases by 17% if refractive index of optical medium is 30% lower than that of granules. This is due to diffuse reflection of light in part of the scintillation layer that removed from photodetector.

It was shown that after chemical polishing of surface of CsI:Tl granules with ethylene glycol, light output of CsI:Tl composite layer with thickness from 1 mm based on granules with size of 63–300 μm , increases by 30%.

It was determined that presence of scintillation layer based on 1-2 mm thick CsI:Tl composite layer from 63-300 μm granules on surface of scintillation polystyrene plate provides improving of sensitivity of combined gamma detector.

It was shown that sensitivity of gamma-ray photons with energy of 20-3000 keV increased by 22-78% if compare with scintillation polystyrene detectors.

REFERENCES

- [1] A.Yu. Boyarintsev, T.A. Nepokupnaya, Yu.D. Onufriyev, V.A. Tarasov, "Composite scintillator". Springer proceedings in Physics, 2017. vol. 200, pp. 167-194.
- [2] M.E. Globus, B.V. Grynyov, "Inorganic scintillators. New and traditional materials". Kharkov, Acta. 2000, 409 p.
- [3] P. Dorenbos, J.T. de Haas, C.W.E. van Eijk, "Non-Proportionality in the Scintillation Response and the Energy Resolution Obtainable with Scintillation Crystals", IEEE Transaction of Nuclear Science, 1995, vol. 42, pp. 2190-2202.
- [4] T.E Gorbacheva, V.A. Tarasov, N.Z. Galunov, "Light collection simulation when determining light yield of single crystal and polycrystalline organic scintillators", Functional Materials, 2015, vol. 22., pp. 408 – 415.
- [5] V. Litichevskiy, V. Tarasov, S. Galkin, O. Lalaian, E. Voronkin, "Scintillation panels based on zinc selenide for detection of alpha radiation", Functional materials, 2012, vol. 19, pp. 546 – 550.
- [6] A. Boyarintsev, A. Bobovnilov, A. Gektin, S. Kovalchuk, T. Nepokupnaya, Yu. Onufriyev, V. Tarasov, "Composite detector $^6\text{Li(Eu)}$ for thermal neutron registration", Functional Materials, Aspects of scintillation technics, Kharkov, 2017. pp. 132 – 140.
- [7] A. Boyarintsev, T. Nepokupnaya, Yu. Onufriyev, "Radiation-resistant scintillation element", Patent 119798 Ukraine, 2017.
- [8] W. Wang H. Si, F. Li, H. Meng, J. Cai, S. Xu, S. Jing, F. Hong, Y. Zhu, H. Xu, R. Xu, J. Lai, F. Xu, L. Wang, "Approaching the Theoretical Light Yield Limit in CsI (Tl) Scintillator Single Crystals by a Low-Temperature Solution Method", Crystal Growth and Design, 2020, vol. 20 pp. 3474 – 3481.
- [9] V.A. Rabinovich, Z.Ya. Havin, Brief chemical reference book, Chemistry, 1977, p. 392.

Iron-impurities-activated kinetics of the light-induced processes in silicon solar cells

Viktor Vlasjuk

*Physical and Technical Fundamentals
of Semiconductor Photovoltaics*

*V. Lashkaryov Institute
of Semiconductor Physics
of NAS of Ukraine
Kyiv, Ukraine
viktorvlasjuk@gmail.com*

Roman Korkishko

*Physical and Technical Fundamentals
of Semiconductor Photovoltaics*

*V. Lashkaryov Institute
of Semiconductor Physics
of NAS of Ukraine
Kyiv, Ukraine
romkin.ua@gmail.com*

Vitaliy Kostylyov

*Physical and Technical Fundamentals
of Semiconductor Photovoltaics*

*V. Lashkaryov Institute
of Semiconductor Physics of NAS of
Ukraine
Kyiv, Ukraine
vkost@isp.kiev.ua*

Oleg Olikh

*Faculty of Physics
Taras Shevchenko National University
of Kyiv*

*Kyiv, Ukraine
olikh@univ.kiev.ua*

Abstract—An approach is proposed that allows to extend the existing techniques of studying the behaviour and properties of iron in silicon wafers to ready-made silicon solar cells (SC) and in case of arbitrary level of injection of excess electron-hole pairs. The kinetics of light-induced processes, namely the kinetics of open circuit voltage and short-circuit current, the kinetics of the effective lifetime and the kinetics of changes in the interstitial iron concentration during iron-boron pair dissociation reactions and their reverse association into pairs were studied.

The total iron concentration in the studied SCs was determined, as well as the time constants of photodissociation the pairs and the inverse association into pairs. It was found that the processes observed experimentally on silicon SC samples are due to iron impurities, because the photodissociation of pairs at room temperatures and the obtained value of the association time constant of the pairing kinetics is the "fingerprint" of iron in silicon.

Keywords — silicon, solar cells, iron, iron-boron pairs, pair dissociation, recombination

I. INTRODUCTION

The main task of research in the field of photovoltaics is to increase the efficiency of photoconversion. This task is primarily related to the need to reduce the level of losses in silicon SC. One of the most significant losses for both laboratory and mass-produced SCs is the loss associated with the recombination of nonequilibrium electron-hole pairs. The determining factor that directly affects the level of recombination losses is the impurity composition and its concentration. Heavy metal impurities in silicon act as recombination centers, thus reducing the lifetime of excess current carriers. One of the most common and at the same time the most harmful impurities in silicon are iron (Fe) atoms.

A large number of works have been devoted to the study of the behavior of iron impurities in silicon and its influence on the recombination characteristics of silicon and SC made on its basis. In particular, various methods for determining the concentration have been proposed [1–6].

Most of the work on the study of the behaviour of iron impurities in silicon was performed on silicon wafers.

In all these works, the parameters of the centers due to iron, and their transformation were determined, as a rule, on silicon wafers, from which were then made of SC. This circumstance was due to the use of appropriate methods for determining the concentration of iron by changing the lifetime (diffusion length) after the operations of dissociation-association of FeB pairs—surface photovoltage (SPV) [1, 2]—and quasi-steady-state photoconductivity (QSSPC) [4–6]. These techniques are suitable for wafers and are not suitable for determining the concentration of iron and its behaviour in finished SC. However, the behaviour of iron in the finished structures of SC may have features compared to wafers, because SC is a multilayer multi-barrier structure in contrast to the wafers, and iron diffusion processes can be affected by potential barriers at the boundaries of regions with different type and level doping. In addition, in the technological process of manufacturing SC, which contains several high-temperature operations, there may be an effect of contamination by impurities (including iron) from technological equipment and equipping, chemical reagents, etc., and the effect of impurities gettering [6]. Thus, the study of the processes caused by iron impurities in finished SCs is important and relevant.

It is known that Fe in silicon can be in two states [1–3, 7–10]:

- in the form of FeB pair (energy level $E_C - 0.27$ eV [10]);
- in the interstitial state Fe_i (energy level $E_C - 0.735$ eV [10])—is formed during the dissociation of FeB pair.

At room temperature and boron concentration $>10^{14}$ cm⁻³, all Fe bound in FeB pairs is in equilibrium, whereas at temperatures above 200°C and boron concentration $<10^{16}$ cm⁻³, most Fe is in the interstitial state. Fe_i with its relatively deep energy level is a more efficient recombination center than FeB with an energy level close to the edge of the valence band. The decay of FeB pairs can be caused by external factors: temperature, irradiation with a quantum energy greater than the silicon band gap, etc.

Issues of understanding the behavior of defects and research aimed at developing and implementing methods

for converting such defects into a recombination-inactive state are fundamental to improving the performance of SC.

Therefore, the purpose of this work was to develop a research technique aimed at determining the concentration of impurity iron atoms in ready-made silicon SCs, their effect on the characteristics of silicon SCs, as well as to study the kinetics of the light-induced dissociation reaction of FeB onto interstitial iron Fe_i and boron B and the kinetics of the reverse association reaction Fe_i and B into pairs.

II. DESCRIPTION OF THE TEST SAMPLES

Experimental studies were performed on samples of silicon SC with geometric dimensions of 1.52 x 1.535 cm², made on the basis of single-crystal *p*-type silicon wafers KDB-10 with a resistivity of about 10 Ohm·cm (doping level ~1.4·10¹⁵ cm⁻³). The thickness of the wafers was 380 μm. On the front surface, the SCs had a separating *n*⁺-*p* junction formed by phosphorus diffusion. In addition, to reduce recombination losses and increase the conductivity of the contact layer on the rear surface an isotype *p*⁺-*p* barrier was formed by diffusion of boron. Electrical contacts were formed by applying a solid layer of aluminum on the rear surface and a layer in the form of a grid—on the front surface. Layers of 30 nm thick SiO₂ and 40 nm thick Si₃N₄ silicon nitride were formed on the surface of the SC to passivate the surface and reduce optical reflectance.

The choice for experimental studies of SC samples made on the basis of *p*-type silicon wafers is not accidental and is due to the fact that in silicon SCs with *n*-type base, the presence of iron, even with a high concentration does not affect recombination. At the same time, in silicon SCs with a *p*-type base, iron impurities lead to a significant reduction in the lifetime of excess current carriers with an increase in the doping level [11].

III. RESEARCH METHODS

For the first time, a technique for determining the concentration of iron in silicon was proposed in [1]. The authors, using the method of deep level transient spectroscopy (DLTS), have shown that heat treatment of silicon in the dark at a temperature of 210°C for 3 minutes leads to the decomposition of FeB pairs and the transition of iron to the interstitial state of Fe_i. In this case, the parameters of the iron recombination center change. To record these changes, it was proposed to use measurements of the diffusion length of excess current carriers by the method of spectral dependences of surface photovoltage. The technique was calibrated using DLTS spectra and a formula for calculating the iron concentration in silicon was obtained:

$$N_{Fe} = \frac{D_n}{f} \left(\frac{1}{L_1^2} - \frac{1}{L_0^2} \right) \cdot \left[C_n(Fe_i) - \frac{C_n(FeB)}{\exp\left(\frac{E_F - 0.1}{kT}\right)} \right]^{-1}, \quad (1)$$

where D_n is the electron diffusion coefficient at room temperature, L_0 , L_1 are the diffusion lengths of minority current carriers before and after heat treatment, respectively, $C_n(Fe_i)$, $C_n(FeB)$ are the electron capture

coefficients of Fe_i, FeB, respectively, f is the coefficient, takes into account incomplete dissociation of FeB pairs, k is the Boltzmann constant, T is the temperature. Formula (1) is still relevant and is used both when conducting research on iron in silicon and in industry, in particular, it is implemented in the Semilab SDI PV-2000 instrument equipment in the form of:

$$N_{Fe} = 1.05 \cdot 10^{16} \left(\frac{1}{L_1^2} - \frac{1}{L_0^2} \right), \quad (2)$$

where the coefficient $1.05 \cdot 10^{16}$ has the dimension μm²/cm³, and the diffusion length of minority current carriers is expressed in μm.

Subsequently it was proposed to use light with a quantum energy exceeding the width of the band gap of silicon (1.124 eV) [7] for the dissociation of FeB pairs [7], as well as a combination of light + heat treatment [8, 9]. This combined treatment makes it possible to discriminate the contributions to changes in the lifetime of nonequilibrium electron-hole pairs in silicon SCs from the transformation of iron centers and activation-deactivation of boron-oxygen complexes. Below is table 1, which shows the effect of various combinations of light and heat treatment on the light-induced processes in silicon, in accordance with [9].

To develop a technique for studying the kinetics of light-induced processes caused by iron impurities in silicon SCs, we performed theoretical calculations of the dependences of the lifetime of minority current carriers on the excitation level according to the Shockley-Reed-Hall (SRH) model. For solar cells with a *p*-type base:

$$\tau_{SRH}^p = \frac{\tau_{p0} \cdot (n_1 + \Delta n) + \tau_{n0} \cdot (N_A + p_1 + \Delta n)}{N_A + \Delta n}, \quad (3)$$

where N_A —is the level of doping, Δn —is the concentration of excess nonequilibrium electron-hole pairs (excitation level), $\tau_{p0} = (N_t \sigma_p v_{th})^{-1}$, $\tau_{n0} = (N_t \sigma_n v_{th})^{-1}$, N_t —is the concentration of recombination centers, σ_n , σ_p —is the cross sections of the recombination center for electrons and holes, respectively, v_{th}^n , v_{th}^p —is the average thermal velocities of electrons and holes were calculated according to [12],

$n_1 = N_C \cdot \exp(-(E_C - E_i)/kT)$, $p_1 = N_V \cdot \exp(-(E_i - E_V)/kT)$, N_C , N_V —is the effective densities of states near the bottom of the conduction band and the top of the valence band, respectively [12], E_C , E_V —is the energy positions of the bottom of the conduction band and the ceiling of the valence band, E_i —is the energy position of the recombination level due to defect.

TABLE I. INFLUENCE OF DIFFERENT COMBINATIONS OF LIGHT-HEAT TREATMENT ON LIGHT-INDUCED PROCESSES IN SILICON

Processing modes			Effect
Temperature	Light	Time	
Heat treatment			
≥ 200°C	no	≥ 2 min.	Fe _i B → Fe _i + B BO ₂₁ → B + O ₂₁
FeB Recovery			
90°C	no	≥ 3 min.	Fe _i + B → Fe _i B B state does not change
Light Induced Degradation Activation			
120°C	1 Sun	≥ 5 min.	Fe _i B → Fe _i + B B + O ₂₁ → BO ₂₁

The results of the calculations are shown in Fig. 1. During the calculations, the values of the level of doping and the concentration of recombination centers due to iron varied.

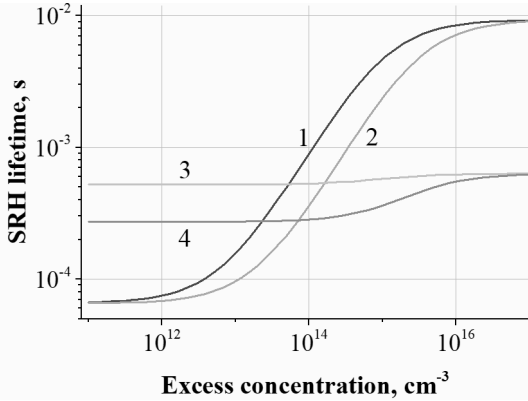


Fig. 1. Dependences of SRH lifetime in the SC base on the excitation level: curves 1, 2—in the case of the Fe_i recombination center, $E_C - E_i = 0.735$ eV, $\sigma_n = 3.47 \cdot 10^{-11} \cdot T^{-1.48}$, $\sigma_p = 4.54 \cdot 10^{-16} \exp(-0.05/kT)$ [10], curves 3, 4—in the case of the FeB recombination center, $E_C - E_i = 0.27$ eV, $\sigma_n = 5.1 \cdot 10^{-9} \cdot T^{-2.5}$, $\sigma_p = 3 \cdot \exp(-0.262/kT)$ [10]. $N_i = 3 \cdot 10^{11} \text{ cm}^{-3}$, $N_A = 10^{15} \text{ cm}^{-3}$ (1, 3) and $3 \cdot 10^{15} \text{ cm}^{-3}$ (2, 4), $T = 298\text{K}$.

As can be seen from Fig. 1, with increasing excitation level, the lifetime of SRH associated with the recombination level of Fe_i (curves 1 and 2) increases rapidly with the range of doping levels $2 \cdot 10^{12} - 3 \cdot 10^{15} \text{ cm}^{-3}$ and remains constant at doping levels of $10^{16} < \Delta n < 10^{12} \text{ cm}^{-3}$. While in the case of recombination levels of FeB (curves 3 and 4), the lifetime of SRH remains constant or increases slightly. In addition, as the doping level increases, the dependence of the lifetime of the SRH on the level of excitation in the case of the recombination level of FeB becomes more rapid. So, as can be seen from Fig. 1, there are two basic possibilities for the study of kinetic dependences due to iron impurities: the first is to use excitation levels $< 10^{12} \text{ cm}^{-3}$, the second is to use excitation levels $> 10^{16} \text{ cm}^{-3}$, because in these cases the SRH lifetime dependence in the case of recombination via Fe_i levels are quite gentle, which allows for high accuracy of the experiment. However, excitation levels $> 10^{16} \text{ cm}^{-3}$ are difficult to provide, especially in samples with short lifetimes. Also, such levels of excitation lead to heating of the sample, which in turn strongly affects its characteristics. In addition, as can be seen from table 1, light treatment with an intensity of even 1 Sun leads to a redistribution of concentrations between FeB and Fe_i , i.e. the use of high levels of irradiation to achieve high levels of excitation will lead to dissociation of FeB complexes during the experiment, thereby complicating analysis of kinetic dependences. Therefore, the study of the kinetics of light-induced processes due to iron impurities in silicon SC should be performed at a level of excitation not exceeding 10^{12} cm^{-3} . Also for measurements it is better to choose SC with a doping level of $10^{15} - 3 \cdot 10^{15} \text{ cm}^{-3}$, because in this case the dependences of the lifetime of the SRH for the recombination level of FeB are more gentle in the whole range of excitation levels.

To study the kinetics of light-induced processes due to iron impurities, the measurement of light $I-V$ characteristics of the studied silicon SCs was performed. In order to ensure excitation levels not exceeding $\Delta n = 10^{11} \text{ cm}^{-3}$, these

characteristics were measured by illuminating the test samples with an LED. An infrared LED with a radiation wavelength of 950 nm was chosen to ensure uniform in thickness generation of nonequilibrium electron-hole pairs and which created an irradiation level of 0.4 mW/cm^2 . By varying the LED current, the $I-V$ characteristics for several excitation levels are obtained. To study the kinetics of light-induced dissociation of FeB pairs, these characteristics were measured in stages, namely, on the initial SC samples, then after each stage of sequential illumination of the samples with a halogen lamp ($1 \text{ Sun} = 100 \text{ mW/cm}^2$), which leads to dissociation of FeB pairs. This rearrangement of the defective structure leads to a decrease in the effective lifetime of nonequilibrium current carriers (Fig. 1), which can be registered in the study of $I-V$ characteristics.

The time constant τ_p of the association reaction into FeB pairs is determined by the formula [1, 3]:

$$\tau_p = \frac{4.3 \cdot 10^5 T}{N_A} \exp\left(\frac{E_A}{kT}\right) \quad (4)$$

where N_A is the level of boron doping, $E_A = 0.68$ eV is the activation energy of the association reaction $Fe_i + B \rightarrow FeB$. For room temperature, the value of τ_p is more than 8 hours, so the study of the kinetics of the association of interstitial iron Fe_i with an boron doping impurity was performed at a temperature $T = 90^\circ\text{C}$, when τ_p decreases to 315 sec. according to (4). The sample was heated to $T = 90^\circ\text{C}$, then a halogen lamp (100 mW/cm^2) was turned on and the dissociation of FeB pairs was performed for 10 minutes. After switching off the light, the association kinetics into FeB pairs were recorded by measuring the light $I-V$ characteristics similar to that described above. It should be noted that the correspondence of the time constant of the association kinetics of formula (4) with the activation energy of the association reaction $E_A = 0.68$ eV [1], as well as photodissociation of pairs at room temperatures [2] is a "fingerprint" of iron impurities. Thus, the dependences of the open-circuit voltage and short-circuit current on the duration of SC illumination by a halogen lamp (open-circuit voltage and short-circuit current kinetics) was obtained during dissociation ($FeB \rightarrow Fe_i + B$) and association ($Fe_i + B \rightarrow FeB$) reactions. Using the equation of the generation-recombination balance for the open circuit conditions (5), the kinetics of the effective lifetime of nonequilibrium electron-hole pairs is obtained.

$$J_{sc} = q \frac{d}{\tau_{eff}} \Delta n_{oc}, \quad (5)$$

where J_{sc} is the short-circuit current density, q is the elementary charge, d is the thickness of the SC, τ_{eff} is the effective lifetime of nonequilibrium electron-hole pairs, Δn_{oc} is the excess concentration of electron-hole pairs in the open circuit, which is given by the equation:

$$\Delta n_{oc} = -\frac{n_0}{2} + \sqrt{\frac{n_0^2}{4} + n_i^2 \cdot \exp\left(\frac{V_{oc}}{kT}\right)}, \quad (6)$$

where n_0 is the equilibrium concentration of electron-hole pairs, for the studied SC it is determined by the doping level, V_{oc} is the open circuit voltage, n_i is the intrinsic concentration of electron-hole pairs in silicon, the temperature dependence of which is given by the expression [13]:

$$n_i(T) = 2.9135 \cdot 10^{15} \cdot T^{1.6} \cdot \exp\left(-\frac{E_g(T)}{kT}\right), \quad (7)$$

here $E_g(T) = 1.206 - 2.73 \cdot 10^{-4} \cdot T$ —the temperature dependence of the silicon band gap [12].

From (5) we have:

$$\tau_{eff} = \frac{qd\Delta n_{OC}}{J_{SC}} \quad (8)$$

In addition, using formula (2), the kinetics of the change in the concentration of interstitial iron Fe_i due to the dissociation of FeB pairs under the illumination of SC with a halogen lamp and the kinetics of the change in the concentration of FeB in the reverse reaction of the association were obtained. The diffusion length of the minority current carriers L_d was determined from the ratio:

$$L_d = \sqrt{D\tau}, \quad (9)$$

where $D = 32 \text{ cm}^2/\text{s}$ —diffusion coefficient of minority carriers (electrons).

IV. ANALYSIS OF THE RESULTS

The kinetics of open circuit voltage and short-circuit current for several levels of excitation were obtained from measurements of light $I-V$ characteristics first at the initial SC and then after each stage of light processing (halogen lamp lighting, energy illumination $100 \text{ mW}/\text{cm}^2$). Both dependences have a decreasing character, increasing the duration of light treatment leads to a decrease in both the open circuit voltage and short circuit current. Depending on the level of excitation, the maximum value of the voltage drop of the open circuit as a result of light treatment is greater the lower the excitation level. While the maximum reduction of short-circuit current does not depend on the level of excitation. When the values of the light processing time $>1000 \text{ sec.}$ dependence of the open circuit voltage and short-circuit current go to the shelf and subsequent light processing does not actually lead to a decrease in these values. Having the values of open circuit voltage and short-circuit current obtained from the $I-V$ characteristics and using formulas (5–7), the effective lifetime of nonequilibrium electron-hole pairs was determined, and hence the kinetics of the effective lifetime of excess current carriers was obtained (Fig. 2).

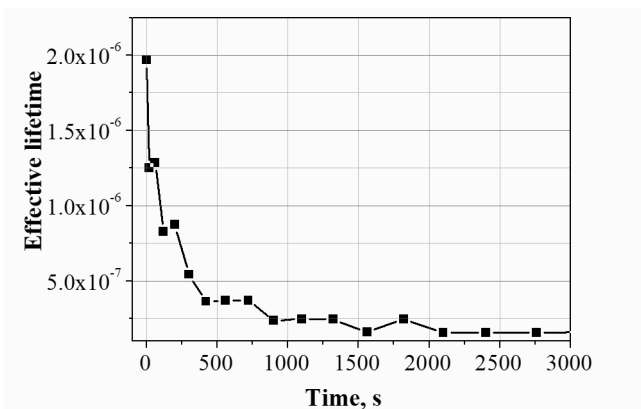


Fig. 2. Kinetics of the effective lifetime of non-equilibrium current carriers under the illumination of a SC with a halogen lamp ($100 \text{ mW}/\text{cm}^2$). Excess pairs concentration (injection level) $\Delta n = 3 \cdot 10^{10} \text{ cm}^{-3}$.

As in the case of open-circuit voltage kinetics and short-circuit current, the obtained dependences are decreasing

and have an exponential character. The maximum τ_{eff} values obtained at the original SC are in the range from $2.5 \cdot 10^{-7}$ to $2.0 \cdot 10^{-6} \text{ sec.}$ depending on the excitation level. The minimum values are in the range from $1.37 \cdot 10^{-8}$ to $1.9 \cdot 10^{-7}$ depending on the level of excitation. That is, the maximum decrease in the lifetime of nonequilibrium electron-hole pairs as a result of light treatment is $\sim 100\%$ and decreases slightly with increasing excitation level.

The obtained values of the lifetime were recalculated according to formula (8) into the values of the diffusion length of minority current carriers on the initial SC, and at each stage of research. Using formula (2), the concentration of iron atoms in the Fe_i state was estimated at different stages of processing. The calculation results are shown in Fig. 3.

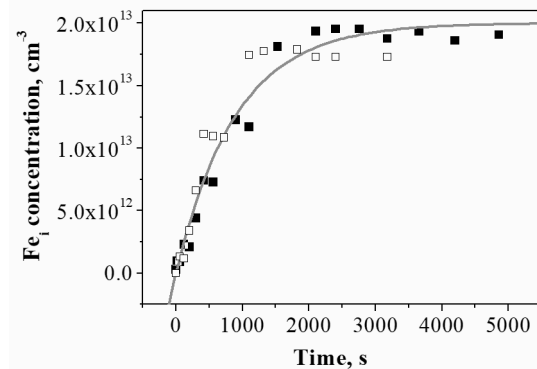


Fig. 3. Kinetics of changes in the concentration of interstitial iron Fe_i during the dissociation of FeB pairs induced by the light of a halogen lamp ($100 \text{ mW}/\text{cm}^2$). Points—experimental values, line—exponential approximation. Excess vapor concentration (injection level) $\Delta n = 2 \cdot 10^{10} \text{ cm}^{-3}$ (open squares) and $3 \cdot 10^{10} \text{ cm}^{-3}$ (squares).

In the same Fig.3 the line shows the approximation of the obtained experimental data by an exponential dependence with a time constant of 900 sec. One can see a good agreement between the experimental and theoretical dependences, especially for the first half of the kinetic curve. Almost complete dissociation of FeB pairs occurs in 3000 sec. (50 min.). The obtained value correlates with the time of complete dissociation given in [2]: 15 sec. at an illumination level 100 times higher— $10 \text{ W}/\text{cm}^2$ for p -Si wafers. With a linear approximation up to $100 \text{ mW}/\text{cm}^2$, we get 1500 sec., which is two times less than what we obtained. The reason for this may be the superlinear effect of the illumination level on photodissociation, as well as the influence of potential barriers in SC. The stationary value of the concentration of interstitial iron $N_{Fe_i} = 2 \cdot 10^{13} \text{ cm}^{-3}$ is equal to the total concentration of iron in the case of complete dissociation of FeB pairs. Photodissociation at room temperature according to [2] is a characteristic feature of FeB pairs, in contrast to other metals, in particular CrB. To further verify that the obtained kinetic dependences are due precisely to iron impurities, we studied the kinetics of the reverse association reaction in the $Fe_i + B \rightarrow FeB$ pair in SC as a “fingerprint” of iron in silicon [1]. The kinetics of association in pairs was observed at a temperature of 90°C [2, 8, 9] after photodissociation at the same temperature. The results obtained by the previously described method are shown in Fig. 4, which also shows the approximation of the experimental data by an exponential dependence with the association time constant

$\tau_p = 315$ sec. Note that formula (4) gives exactly the same value τ_p for the experimental conditions $T = 90^\circ\text{C}$, that is, the kinetics of the association reaction of iron with boron in pairs in the studied SC occurs with an activation energy $E_a = 0.68$ eV, which is a "fingerprint" of iron in silicon. Thus, it can be argued that in experiments on the study of the kinetics of the pairs association-dissociation in silicon SCs, processes were observed that were caused precisely by an iron impurity.

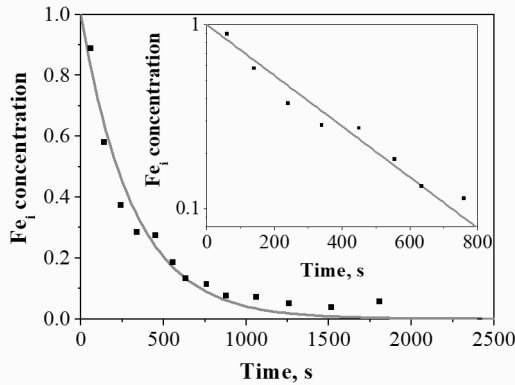


Fig. 4. Kinetics of changes in the concentration of interstitial iron Fe_i due to its association with B in FeB pairs. Points—experimental values, line—approximation by an exponential dependence with a time constant of 315 sec. Inset—a graph on a semi-log scale.

V. CONCLUSIONS

An approach is proposed that makes it possible to extend the existing methods of studying the behaviour and properties of iron in silicon wafers to ready-made silicon SCs even in the case of an arbitrary level of injection of excess electron-hole pairs. Using the proposed approach, the kinetics of light-induced processes, namely the kinetics of the open-circuit voltage and short-circuit current, the kinetics of the effective life time and the kinetics of changes in the concentration of iron Fe_i in the reactions of dissociation of FeB pairs to Fe_i and B and their reverse association into pairs, have been investigated. The total concentration of iron in the studied SCs, as well as the time constants of the kinetics of photodissociation of pairs (3000 sec. at 100 mW/cm^2) and reverse association in pairs (315 sec. at $T = 90^\circ\text{C}$) were determined. It was found that observed experimentally on silicon SC samples processes are caused precisely by iron impurities, since the photodissociation of pairs at room temperatures and the obtained value of the association kinetics time constant is a "fingerprint" of iron in silicon. It is shown that in SCs made on the basis of p -type silicon wafers, iron impurities can

lead to a significant decrease in the effective lifetime of excess current carriers, which in turn causes a decrease in the open-circuit voltage and short-circuit current.

ACKNOWLEDGMENT

This work was supported by National Research Foundation of Ukraine by the state budget finance (project 2020.02/0036 "Development of physical base of both acoustically controlled modification and machine learning-oriented characterization for silicon solar cells").

REFERENCES

- [1] G. Zoth, W. Bergholz, "A fast, preparation-free method to detect iron in silicon," *J. Appl. Phys.*, vol. 67, No. 11, 1990, pp. 6764–6771.
- [2] J. Lagowski, P. Edelman, A. M. Kontkiewicz, O. Milic, W. Henley, M. Dexter, L. Jastrzebski, A. M. Hoff, "Iron detection in the part per quadrillion range in silicon using surface photovoltage and photodissociation of iron-boron pairs," *Appl. Phys. Lett.*, vol. 63, No. 22, 1993, pp. 3043–3045.
- [3] W. Wijaranakula, "The Reaction Kinetics of Iron-Boron Pair Formation and Dissociation in P-Type Silicon," *J. Electrochem. Soc.*, vol. 140, No. 1, January 1993, pp. 275–281.
- [4] D. H. Macdonald, L. J. Geerligs, A. Azzizi, "Iron detection in crystalline silicon by carrier lifetime measurements for arbitrary injection and doping," *Journal of Appl. Phys.*, vol. 95, No. 3, 2004, pp. 1021–1028.
- [5] J. Tan, D. Macdonald, F. Rougieux and A. Cuevas, "Accurate measurement of the formation rate of iron–boron pairs in silicon," *Semicond. Sci. Technol.*, vol. 2, No. 5, 2011, P. 055019.
- [6] D. Macdonald, H. Mäckel, and A. Cuevas "Effect of gettered iron on recombination in diffused regions of crystalline silicon wafers," *Appl. Phys. Lett.*, vol. 88, 2006, pp. 092105 1–4.
- [7] D. Walz, J.-P. My, G. Kamarinos, "On the recombination behaviour of iron in moderately boron-doped p-type silicon," *Appl. Phys. A: Mater. Sci. Process.*, vol. 62, No. 4, 1996, pp. 345–353.
- [8] M. Wilson, P. Edelman, A. Savtchouk, J. D'Amico, A. Findlay, J. Lagowski, "Accelerated light-induced degradation (ALID) for monitoring of defects in PV silicon wafers and solar cells," *J. Electron. Mater.*, vol. 39, 2010, pp. 642–647.
- [9] M. Tayyib, J. Theobald, K. Peter, J.O. Odden, T.O. Sætre, "Accelerated light-induced defect transformation study of Elkem solar grade silicon," *Energy Procedia*, vol. 27, 2012, pp. 21–26.
- [10] B. B. Paudyal, K. R. McIntosh, D. H. Macdonald, "Temperature dependent electron and hole capture cross sections of iron-contaminated boron-doped silicon," 34th IEEE Photovoltaic Specialists Conference (PVSC), USA, Philadelphia, 7–12 June 2009.
- [11] A.V. Sachenko, V.P. Kostylyov, M.V. Gerasymenko, R.M. Korkishko, M.R. Kulish, M.I. Slipchenko, I.O. Sokolovskiy, V.V. Chernenko, "Analysis of the silicon solar cells efficiency. Type of doping and level optimization," *Semiconductor Physics, Quantum Electronics & Optoelectronics*, vol. 19, No. 1, 2016, pp. 67–74.
- [12] M.A. Green, "Intrinsic concentration, effective densities of states, and effective mass in silicon," *J. Appl. Phys.*, vol. 67, No. 6, 1990, pp. 2944–2954.
- [13] T. Trupke, M. Green, P. Wurfel, P. P. Altermatt, A. Wang, J. Zhao, and R. Corkish, "Temperature dependence of the radiative recombination coefficient of intrinsic crystalline silicon," *J. Appl. Phys.*, vol. 94, No. 8, 2003, pp. 4930–4937.

Luminescent solar concentrator with nano-scale absorber: the form-factor

Mykola Kulish
*V. Lashkaryov Institute
of Semiconductor Physics of NAS of
Ukraine*
Kyiv, Ukraine
n_kulish@yahoo.com

Vitaliy Kostylyov
*V. Lashkaryov Institute
of Semiconductor Physics of NAS of
Ukraine*
Kyiv, Ukraine
vkost@isp.kiev.ua

Anatoly Sachenko
*V. Lashkaryov Institute
of Semiconductor Physics of NAS of
Ukraine*
Kyiv, Ukraine
sach@isp.kiev.ua

Anatoly Shkrebtiy
*Ontario Tech University
Oshawa, Canada*
Anatoli.Chkrebtiy@uoit.ca

Igor Sokolovskiy
*V. Lashkaryov Institute
of Semiconductor Physics of NAS of
Ukraine*
Kyiv, Ukraine
I.O.Sokolovskiy@gmail.com

Abstract— The analytical model for the propagation of QD-emitted light through the LSC plates of different form-factors is developed. The difference between square and round form factors is shown to be weak and not decisive in the luminescent concentrator construction. The influence of matrix absorption coefficient on the losses amplitude the form-factors relation is shown.

Keywords— luminescent solar concentrator, photon transport, reabsorption, escape cone, form-factor

I. INTRODUCTION

The latest technological advances allowed reaching the photoconversion efficiency of the silicon and gallium arsenide based solar cells of 26.7% and 29.1%, respectively [1], almost reaching the theoretical limit of 31% [2]. However, this does not apply to the luminescent solar concentrator (LSC) photoconverters. A photoconverter with luminescent solar concentrator is a system, containing a plate of dielectric host matrix, transparent to sunlight, which is doped with luminophores (we consider quantum dots (QDs)). At the plate edges peripheral solar cells (SCs) are attached, which convert the concentrated light to electricity. QDs absorb incoming solar photons in a wide spectral range and re-emit luminescent photons in a narrow spectral band. Due to the complete internal reflection inside the plate, the luminescent photons are transported to the plate edges, where the SCs are located [3].

In LSCs, the area of the matrix edges is much smaller than the front surface of the matrix plate area. Since a cost of the plate, doped with luminophores is small compared to the SCs price, especially with highly efficient multijunction SCs, while the area of the SC attached to the edges is small, a lower cost of LSCs is expected, compared to the cost panels of traditional silicon photoconverters [4]. It is expected that the LSC efficiency can reach 21.3%, 29.5% and 33.6%, respectively, in single, double and triple structures [5]. However, the experimentally achieved LSC efficiencies are below 10% [4]. The main reasons for low LSC efficiency are (i) reabsorption, (ii) low quantum yield of luminescence and (iii) a presence of the so-called "dead layer" in the matrix. While the modern QDs synthesis technology has already been developed to provide close to unity quantum yield of the luminescence [6] the reabsorption and the dead

layer factors are still posing challenges on the way of increasing the LSC efficiency. The last two factors severely limit the efficiency of the standard concentrator.

To convert the sunlight energy into electricity in LSCs, several types of luminophores have already been tested: (i) rare-earth atoms or complexes, (ii) dyes, and (iii) semiconductor quantum dots (QDs). The most promising luminophores are nano-scaled QDs, because by changing their radius, the spectral position of the luminescent band can be matched with the region of maximum sensitivity of the SCs, attached to the plate edges [7]. Such nano-scaled structures as quantum wires and quantum wells can make obstacles for the light propagation to the solar cells. However, experimentally the efficiency of the LSCs with QDs does not exceed a few percent [8], reaching maximum of only 8.71% [15]. From the most important limiting factors of the LSC efficiency, namely (1) relaxation losses; (2) low quantum yield of luminescence; (3) reabsorption; and (4) presence of a "dead layer" [9]. Here we focus on the efficiency of optical transport of luminescent photons to the edges [10]. It is schematically shown in Fig. 1.

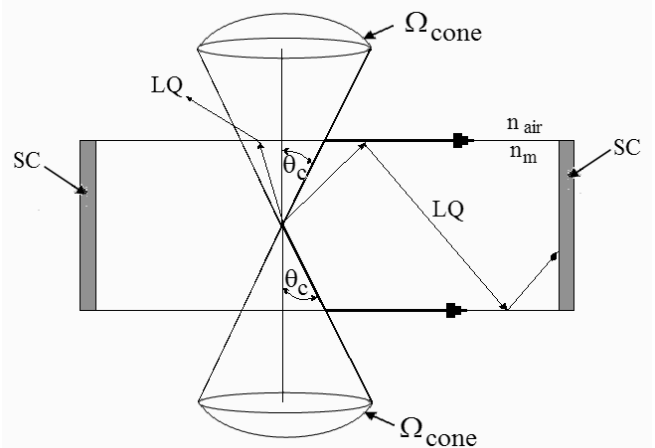


Fig. 1. Typical geometry of the FLC matrix. The sunlight is absorbed by quantum dots (not shown in the figure). Luminescent quanta LQs can radiate in an arbitrary direction. When they fall to the matrix-space separation at angles $\theta < \theta_c$, they leave the matrix (θ_c is the critical angle to which the refracted beam propagates along the matrix surface, Ω_{cone} is the solid angle of the cone of leakage). When luminescent photons fall to the matrix-air separation boundary (n_m and n_{air} are respectively the refractive index of the matrix and air) at angles $\theta \geq \theta_c$ they are transported to the side

face plate of the matrix through the full internal reflection and the photons fall to the entrance surface of the solar cell (SC), where their energy is converted into electrical energy.

After a standard preparation technology of the top and back surfaces of the LSC slab, a damage of a near-surface region is always present. Such a layer with the damage is often called the dead layer, since a presence of numerous defects causes nonradiative recombination of the carriers, which is dominant source of the LSC losses. To the best of our knowledge, we are not aware of literature sources where the effect of the dead layer on the LSC efficiency is analyzed. In this paper, we attempt to fill this gap.

In the ideal LSC (no absorption in the matrix material, and quantum efficiency of the QDs equals to unity) the solar photons first are absorbed only by the QDs. Next, the luminescent photons, emitted by the QDs, are transported through the total internal reflection to the solar cells at the matrix edges, where their energy is converted into electricity. To minimize the luminescent photons losses during their transport through the the internal reflections, the top and back surfaces of the matrix are polished.

II. MODEL

The absorption coefficient of the matrix of fused quartz $\alpha_m = 10^{-5} \text{ cm}^{-1}$, which is practically wavelength

$$\int_{\theta_c}^{\pi/2} \left[\int_{-\arctan\left(\frac{d/2+y}{d/2-x}\right)}^{\arctan\left(\frac{d/2-y}{d/2-x}\right)} \exp\left(-\alpha \frac{d/2-x}{\sin(\theta) \cos(\beta)}\right) d\beta + \int_{-\arctan\left(\frac{d/2-x}{d/2-y}\right)}^{\arctan\left(\frac{d/2+x}{d/2-y}\right)} \exp\left(-\alpha \frac{d/2-y}{\sin(\theta) \cos(\beta)}\right) d\beta + \int_{-\arctan\left(\frac{d/2+y}{d/2+x}\right)}^{\arctan\left(\frac{d/2+y}{d/2+x}\right)} \exp\left(-\alpha \frac{d/2+x}{\sin(\theta) \cos(\beta)}\right) d\beta + \int_{-\arctan\left(\frac{d/2+x}{d/2+y}\right)}^{\arctan\left(\frac{d/2-x}{d/2+y}\right)} \exp\left(-\alpha \frac{d/2+y}{\sin(\theta) \cos(\beta)}\right) d\beta \right] d\theta \times \frac{1}{2\pi \left(\frac{\pi}{2} - \theta_c\right) \frac{d^2}{4}}$$

More accurate calculation requires to consider the light dispersion by integration through QD emission spectra, this effect will be considered when further improving the formalism. The first term in the equation corresponds to the photon paths from QD to the right side of the square, the second one to the top side, the third to the left side and the fourth to the bottom side.

Since the quadrants of the plate are equal, it is sufficient to average the attenuation by the one quadrant (see Fig. 2a).

$$k_{ws} = 1 - \int_0^{d/2} \int_0^{d/2} \int_{\theta_c}^{\pi/2} \left[\int_{-\arctan\left(\frac{d/2+y}{d/2-x}\right)}^{\arctan\left(\frac{d/2-y}{d/2-x}\right)} \exp\left(-\alpha \frac{d/2-x}{\sin(\theta) \cos(\beta)}\right) d\beta + \int_{-\arctan\left(\frac{d/2-x}{d/2-y}\right)}^{\arctan\left(\frac{d/2+x}{d/2-y}\right)} \exp\left(-\alpha \frac{d/2-y}{\sin(\theta) \cos(\beta)}\right) d\beta + \int_{-\arctan\left(\frac{d/2+y}{d/2+x}\right)}^{\arctan\left(\frac{d/2+y}{d/2+x}\right)} \exp\left(-\alpha \frac{d/2+x}{\sin(\theta) \cos(\beta)}\right) d\beta + \int_{-\arctan\left(\frac{d/2+x}{d/2+y}\right)}^{\arctan\left(\frac{d/2-x}{d/2+y}\right)} \exp\left(-\alpha \frac{d/2+y}{\sin(\theta) \cos(\beta)}\right) d\beta \right] d\theta dy dx \times \frac{1}{2\pi \left(\frac{\pi}{2} - \theta_c\right) \frac{d^2}{4}}$$

As for the circle, the distance w can be found from the law of cosines and written as

independent. After the sunlight photons are absorbed by QDs, they emit luminescence photons in an arbitrary direction. If the QDs are embedded in a transparent dielectric matrix (for example, of squared shape), luminescent photons are transmitted through the total internal reflection to the edges of the matrix with solar cells attached. The SCs convert the energy of the luminescence photon into electricity (Fig. 1). During the transport of luminescent photons to the SCs, some of them are lost due to absorption by the matrix.

To estimate losses of the emitted by the QDs light on its way from the luminophore to the solar cell, we calculate first the mean attenuation of the light, travelling to the edge of the structure considered. The optical path increases by a factor of $1/\sin(\theta)$ due to the light reflection (θ is the incidence angle). Therefore, on the way to the matrix edge the light intensity is attenuated by a factor of $\exp(-\alpha_m w/\sin(\theta))$, where α_m is the light absorption coefficient of the matrix and w is the distance the photon propagates to the edge.

For every QD position (x,y) in the square plate with side d , the light attenuation should be averaged by four angles, corresponding to four sides of the square plate (see Fig. 2a):

Escape cone losses do not depend on the depth of the QD position, so there is no need to average QD emission by the depth. It should be noted, that the sunlight absorption by QDs is depth-dependent. Neglecting the reflection of the emitted light on the subcritical angles, we define the factor for the light attenuation on the photons way to the plate edge for QD emission as:

$$w = \sqrt{R^2 - [r \sin(\beta)]^2} - r \cos(\beta),$$

where r is the distance from the center and β is the planar angle. This way, averaged by r and β light attenuation factor is

$$k_{wc} = \int_{\theta_c}^{\pi} \int_0^{2\pi R} \int_0^R \exp\left(-\alpha \frac{\sqrt{R^2 - [r \sin(\beta)]^2} - r \cos(\beta)}{\sin(\theta)}\right) d\theta d\beta dr \frac{1}{2\pi(\pi/2 - \theta_c)R}$$

The absorption coefficient for the homogeneously doped

plate can be set as $\alpha = \alpha_m + \alpha_q$, where α_m is the absorption coefficient for the matrix material and α_q is the absorption coefficient in the luminophore in its emission band, namely the reabsorption coefficient. Therefore, for QD luminescence quantum yield k_l the fraction of absorbed-emitted by the luminophore photons is:

$$k_r = \frac{\alpha_q}{\alpha_m + \alpha_q} k_l (1 - k_w).$$

This fraction of photons is also attenuated on the way to the plate's edge. Therefore, the final quantum optical efficiency can be set as the sum of infinite geometric progression (for the consideration of every reabsorption act with its losses) and equals to

$$k_{pl} = \frac{k_w k_\theta}{1 - k_r k_\theta}.$$

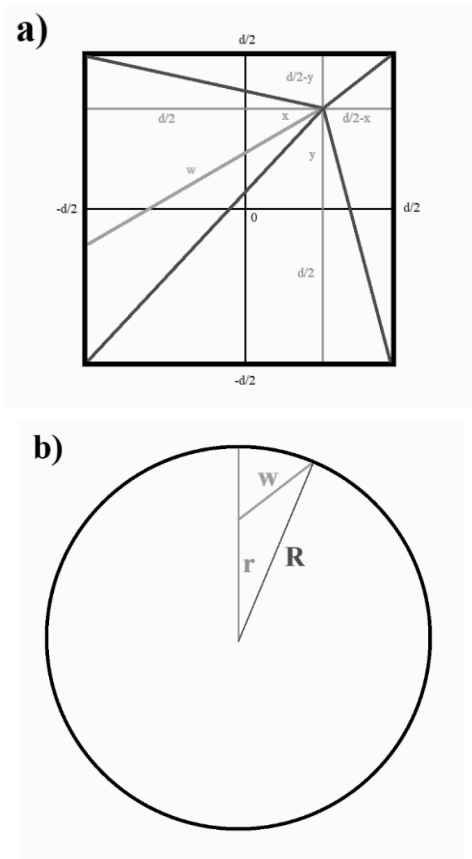


Fig. 2. The geometry of the light propagation in the sample, top view for a) square plate and b) round plate.

Here $k_\theta = (1 - 1/n_m^2)^{1/2}$ is the factor for the losses due to escape cone, n_m is the refractive index of the matrix for the photon average wavelength of QD emission.

III. RESULTS

Fig. 3 shows the matrix size dependence of the transport efficiency for overall absorption of 10^{-5} cm^{-1} . This case corresponds to the fused quartz matrix without reabsorption by the luminophore. One can see that the difference for all three cases is not too big and form-factor can be selected for such technical reasons as the convenience of solar cells disposition and optimal area coverage by the concentrators.

The dependence of transport efficiency on the overall absorption coefficient is shown in Fig. 4. This dependence is predictably strong and should be accurately considered in the technical implementation of the luminescent concentrator. A more accurate estimate of the transport efficiency requires consideration of the infinite (until the last photon) geometric progression of the reflections from the frontal and back surfaces on subcritical angles.

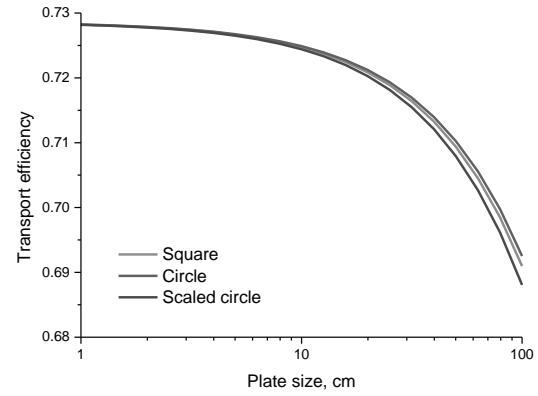


Fig. 3. The transport efficiency k_{pl} vs. size of the plate for different matrix form-factors. Red line is plotted for the square plate of the corresponding side, green line for the round matrix of corresponding diameter and blue line for the round matrix of the same area as for the square.

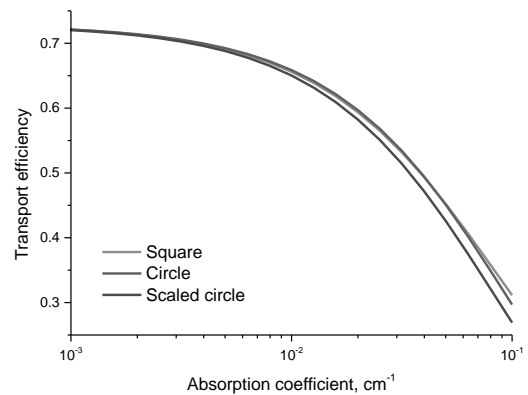


Fig. 4. The transport efficiency k_{pl} vs. the absorption coefficient for different matrix form-factors.

IV. CONCLUSIONS

The analytical model for the propagation of QD-emitted light through the LSC plates of different form-factors is developed.

It is shown that the difference for square and round plates is not too strong and form-factor can be selected for such technical reasons as the convenience of solar cells disposition and optimal area coverage by the concentrators. On the other hand, the matrix absorption coefficient influences not only losses amplitude but the relation between the efficiency of form-factors too.

ACKNOWLEDGMENT

This work was partially supported by dedicated program of basic research of the National Academy of Sciences of Ukraine "Prospective basic research and innovative development of nanomaterials and nanotechnologies for the need of industry, health care and agriculture".

REFERENCES

- [1] M. Green, E. Dunlop, J. Hohl-Ebinger, M. Yoshita, N. Kopidakis, and X. Hao, *Prog Photovoltaics Res Appl*, vol. 29, pp. 3–15, January 2021.
- [2] W. Shockley and H. J. Queisser, *J. Appl. Phys.*, vol. 32, pp. 510-519, March 1961.
- [3] M. Wei, de Arquer, F. Pelayo García, G. Walters, Z. Yang, et al., *Nature Energy*, vol. 4, pp. 197-205, March 2019.
- [4] A. Louwen, W. van Sark, R. Schropp, and A. Faaij, *Solar Energy Mater. Solar Cells*, vol. 147, pp. 295-314, December 2016.
- [5] H. Hernandez-Noyola, D. H. Potterveld, R. J. Holt, and S. B. Darling, *Energy Environ. Sci.*, vol. 5, pp. 5798-5802, February 2012.
- [6] P. Samokhvalov, P. Linkov, J. Michel, M. Molinari, and I. Nabiev, [SPIEDigitalLibrary.org/conference-proceedings-of-spie](https://www.spiedigitallibrary.org/conference-proceedings-of-spie), pp. 8955-8954, September 2014.
- [7] M. R. Kulish, V. P. Kostilyov, A. V. Sachenko, I. O. Sokolovskyi, D.V. Khomenko, and A. I. Shkrebti, *Semicond. Phys, Quantum Electronics & Optoelectronics*, vol. 19, pp. 229-247, October 2016.
- [8] C. Li, W. Chen, D. Wu, D. Quan, Z. Zhou, et al., *Scientific Reports*, vol. 5, pp. 17777-17788, January 2016.
- [9] M. Kulish, A. Shkrebti, V. Kostilyov, I. Sokolovskyi and A. Sachenko, "Minimizing Reabsorption in Multilayered Luminescent Solar Concentrators with Quantum Dots," *2021 IEEE 48th Photovoltaic Specialists Conference (PVSC)*, 2021, pp. 0687-0692.
- [10] Ilya Sychugov, "Geometry effects on luminescence solar concentrator efficiency: analytical treatment," *Appl. Opt.* 59, 2020, 5715-5722.

Dispersion of nanoparticles in optically transparent polymer matrices

V. Borshchov
LLC «Research and Production
Enterprise «LTU»
Kharkiv, Ukraine
info@ltu.ua

O. Listratenko
LLC «Research and Production
Enterprise «LTU»
Kharkiv, Ukraine
info@ltu.ua

Oleksandr Kravchenko
LLC «Research and Production
Enterprise «LTU»
Kharkiv, Ukraine
info@ltu.ua

O. Suddia
LLC «Research and Production
Enterprise «LTU»
Kharkiv, Ukraine
info@ltu.ua

Mykola Slipchenko
Institute for Scintillation Materials of
NAS of Ukraine
Kharkiv, Ukraine
<https://orcid.org/0000-0002-4242-4800>

Boris Chichkov
Institute of Quantum Optics, Leibniz
Universität Hannover
Hannover, Germany
chichkov@iqo.uni-hannover.de

Abstract – The data and recommendations have been summarized for the development of methods for dispersing nanoparticles into polymer matrices when creating optically transparent nanocomposites for use in many fields of science and technology. The analysis of the results of the reviewed works makes it possible to conclude that in order to successfully create optically transparent hybrid organic/inorganic nanocomposites with a high level of dispersion of the inorganic components, many difficult problems related to the compatibility of the components and the stabilization of nanoparticles of fillers in polymer matrices have to be solved.

Keywords - nanoparticles, nanocomposites, polymers.

I. INTRODUCTION

Currently, there is a great interest in optical nanomaterials. However, despite the variety of studies, there is practically no data on optical materials in which a high concentration of nanoparticles is combined with good optical properties.

The high concentration of structural additives can, and usually is accompanied by, significant light scattering on them or fluctuations in their concentration. Therefore, the creation of materials combining optical properties with a high concentration of nanoparticles is a very difficult task. The introduction of metal nanoparticles and their oxides into polymer matrices in recent years has been an intensively developed field of nanoscale physical chemistry. The structural organization of such nanoscale particles is a serious problem, without which it is difficult to determine and optimize the areas of their practical use.

The stabilization of nanoparticles by polymers is considered as shielding by a protective colloid. It is created due to the fact that the spatial dimensions of low-molecular polymers are commensurate with the range of action of Van der Waals forces (dispersion interaction) or exceed it. The need to increase the stability of nanocomposites and the control of reversible transitions in such systems attracts increasing attention of researchers to find ways to manage their morphology, structural organization, and architecture.

The purpose of the work was to search and analyze data and results of theoretical and experimental studies, dissertation materials, literary sources and patents in the

field of optical and optical-electronic instrument making. Generalizations of the obtained data and recommendations for the development of methods for the dispersion of nanoparticles into polymer matrices when creating optically transparent nanocomposites for use not only in optical devices but also for products in scintillation technology, lighting, photovoltaic and many other fields of science and technology.

II. PROPERTIES OF NANOPOLYMER MATERIALS

The synthesis of new materials with improved properties and operational qualities is constantly supplemented by new methods in chemistry and materials science [1]. During the synthesis process, the ability to control the molecular structure at the atomic and macroscopic level is one of the key parameters in the design of materials for special applications.

A significant step forward in this area is the synthesis of nanocomposites, when it is possible to control the structural order in the material on nanometer or submicron scales. Despite the fact that materials with such a complex structure are widespread in nature, reliable and versatile methods for preparing synthetic nanocomposites remain an interesting problem that is being solved by research groups around the world [2].

Nanoparticles synthesized by various methods can have different internal structures that affect the properties of materials made from them. It is quite difficult to achieve full processing of nanoparticles in practice, it is difficult to maintain the nanometer scale of their sizes, to avoid the formation of agglomerates. Because of their high specific surface area, nanoparticles have high reactivity and there is a high probability of agglomeration. A large number of boundary grains in nanocrystalline materials is critical for maintaining the microstructure on a nanometer scale during the consolidation process in such materials.

To achieve a low level of light scattering in transparent nanopolymers, the effects of self-organization of a quasi-lattice having an ordered arrangement of nanoparticles are needed. In this case, the homogeneity of the medium and the absence of distortion of light passing through it can be obtained. This medium will be described in the

approximation of a homogeneous rather than dispersed medium. Thus, in order to reduce the level of light scattering, it is necessary to create an ordered system of nanoparticles in the volume of the polymer material (Figure 1 a).

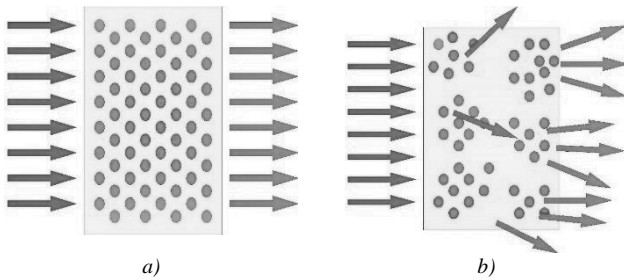


Fig. 1 - a) Light scattering in an ordered system of nanoparticles in the volume of polymer material. b) Light scattering on nanoparticle concentration microfluctuations.

At the same time, nanoparticles in the nanocomposite tend to coagulate or form an irregular arrangement at which the concentration of nanoparticles will fluctuate according to the statistical distribution. Such material will have high light scattering at a high concentration of nanoparticles (Figure 1b).

Thus, the properties of nanoparticles and nanocomposites based on them are highly dependent on the size, concentration, chemical composition of the nanoparticles used and many other factors. But unlike conventional optical materials, the properties of nanocomposites can be improved by varying the above-mentioned nanoparticle parameters [3].

III. METHODS OF DISPERSION OF NANOPARTICLES INTO POLYMER MATRICES

Interfacial interaction is a key point in the creation of organic/inorganic composites and it is on this basis that the conditional division of hybrid materials into two main classes is currently accepted. The first class of hybrid materials includes nanopolymers with a weak interaction between organic and inorganic parts. The second includes materials in which organic and inorganic components are bonded by chemical bonds. In this case, the organic components may have two different roles, the net-forming agents or the inorganic component modifiers.

First-class nanocomposites are produced by direct mixing of nanoparticles with polymer matrix. At the same time, the interaction between the polymer matrix and the inorganic component is relatively weak and is based on hydrogen bonds, as well as Van der Waals interactions. A low degree of interfacial interaction of hydrophobic polymer matrix and hydrophilic filler particles leads to aggregation of inorganic particles, their non-uniform distribution in the volume of polymer matrix. Thus, poor adhesion at the phase boundary results from deterioration of the claimed properties of the polymer nanocomposites and limits their effective use.

To solve the problem, various stabilizing and modifying additives are introduced during the synthesis of

nanocomposites of the second class, which reduce surface energy at the interfacial boundary and increase the compatibility of the polymer and the inorganic component. Nanostructuring, as a method of producing transparent nanocomposites, is carried out by a chemical synthesis reaction in a diluted solution of nanocrystals of fixed dimensions (about 20-50 nm) due to the introduction of an organic substance with surface-active properties into the synthesis zone, which allows obtaining crystals of the desired dimensions isolated from each other and stable in time. In this case, the surface-active properties (shell of nanocrystals) and the matrix can be from one or different organic materials. The most stable and optically uniform compositions are obtained using polyvinyl alcohol and polyvinyl pyridine as a protective medium, as well as photographic gelatin [4, 5, 6].

Among a large number of nanodisperse polymer matrix fillers, titanium dioxide (TiO_2) and zinc oxide (ZnO) are of great importance in the preparation of composite materials. The use of hydrophilic polymer matrices in the synthesis of nanocomposites with TiO_2 greatly facilitates the production of hybrid organ-inorganic materials. The advantage of this method is the good compatibility of the two components and the absence of the need for modifiers. One of the simplest ways to obtain these composites is to synthesize them from a common solvent. In [7], nanocomposites with hydrophilic polymer TiO_2 (polyvinyl alcohol, partially hydrolyzed polyvinyl acetate, polyvinylpyrrolidone, polyvinylpyridine) were prepared by mixing polymer solutions and finely dispersed TiO_2 particle solution. To obtain a finely dispersed solution of TiO_2 , TiCl_4 was used as a precursor, which was hydrolyzed in a strong acid medium. The particle size (D_p) was TiO_2 2.5 nm. The TiO_2 content of the polymer composites varied from 2 to 35% by weight. The resulting nanocomposites containing more than 24% TiO_2 were used as UV - filters (up to 360 nm).

Recently, nanocomposites based on biopolymers have attracted great interest from researchers, since such materials are functional analogues of natural materials. The authors of [8] obtained nanocomposites based on a graft copolymer of chitosan (15 wt%) with polyvinyl alcohol and nanodispersed TiO_2 (D_p - 4,5 - 5 nm). The films containing the 25 and 8 wt. % TiO_2 , were prepared by the method of watering of water solutions of copolymer and nanoparticles of TiO_2 . The formation of particles TiO_2 occurred during the hydrolysis of titanium tert-butoxide.

For most electronic devices, the main task is to obtain a sufficiently high level of conductivity, which is achieved by doping electrically conductive polymers and creating composites. It is known that composites combining TiO_2 (n-type semiconductor) in the nanostate and conductive polymer are widely used in optoelectronics. In [9], nanocomposites with TiO_2 (D_p - 21 nm) based on a polyphenylenevinylene matrix from a common solvent (CHCl_3) were obtained. For the synthesis of nanocomposites, an industrial TiO_2 (Degussa P25) of 70% consisting of the crystalline phase of anatases was used. Another example [10] is the synthesis of organo-inorganic hybrid systems based on a polyaniline matrix and TiO_2 particles (D_p - 9 nm) with a mass content of 17, 18, 30 and

39 wt%. Synthesis of composites was carried out from a common solvent, titanium isopropoxide was used as a precursor.

Using hydrophobic matrices to create nanocomposites with TiO_2 is more challenging. The addition of fillers thermodynamically incompatible with the polymer matrix can be accompanied by the formation of large aggregates that degrade the properties of the final nanocomposite. The problem of aggregation can be overcome by modifying the particles of the TiO_2 or polymer matrix, as well as adding various stabilizers to the system. The surface of the inorganic component can be modified with surfactants and binders by adsorption or covalent bonding of the inorganic particles on the surface (Figure 3). In [11], methods were proposed for preparing composites with different contents of TiO_2 (0.25; 0.5; 1; 2; 5; 10 and 13 wt%) based on a copolymer of ethylene-vinyl alcohol and polypropylene (0, 5; 1; 2; 5 wt%) by mixing the melt with TiO_2 particles. To form polypropylene-based composites, a graft copolymer of polypropylene with maleic anhydride was used, the latter acted as a binding agent to stabilize TiO_2 particles in the polymer matrix and prevent their possible aggregation. The result of the polymer modification was the production of hybrid composites containing TiO_2 particles, the size of which was ~ 10 nm.

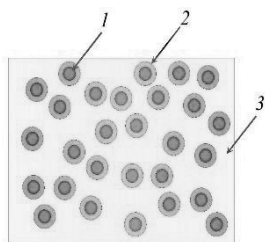


Fig. 2. Structural model of nanocomposite: 1 - nanocrystal of inorganic semiconductor; 2 - a shell of organic material; 3 - organic (liquid or solid) matrix

In order to improve the compatibility between the inorganic material and the polymer matrix and to prevent particle aggregation, a method of chemically modifying the surface of the inorganic component is used. As TiO_2 particle modifiers, various silane agents are often used that are capable of chemically binding to their surface, while the presence of hydrophobic radicals in their molecules improves the compatibility of inorganic particles with the polymer matrix. One method of forming organo-inorganic hybrid systems is to polymerize the monomer on the surface of the TiO_2 particles (in the presence or absence of modifiers). In [12], a method is described for preparing nanocomposites by polymerizing styrene chemically bonded to the surface of modified TiO_2 particles. The content of TiO_2 particles in polystyrene-based composites ranged from 0.5 to 2.0% by weight. The authors of [13], by polymerizing methyl methacrylate, obtained composites with a structure similar to a nut, when a core of modified TiO_2 particles ($D_p - 260$ nm) was enclosed in a "shell" of polymethyl methacrylate.

Thus, by chemically modifying the surface of the particles TiO_2 , the thermodynamic incompatibility of the

components of the nanocomposite can be solved. The use of this method makes it possible to prevent the process of aggregation of particles and to obtain polymer nanocomposites with a high level of dispersion of the inorganic component.

In one version of nanopolymer manufacture, the introduction of ZnO nanoparticles into polysiloxane-containing epoxyurethane polymers was carried out by intercalation: powdered nanoparticles were ZnO dissolved in a mixture of solvents (30 wt% ethyl alcohol + 70 wt% xylene) at a weight ratio of 8:2 to cause swelling of nanosized particles in a solvent. The solution was then magnetically stirred at 800 rpm for 30 minutes, then sonicated for 15 minutes. The dissolved nanoparticles were added to the polymer and stirred for 20 minutes at 1000 rpm, then sonicated for 15 minutes before adding the hardener.

The study of the developed coatings based on polysiloxane-containing epoxyurethane oligomers modified with ZnO nanoparticles showed that they have high hydrophobicity, environmental resistance and anticorrosive properties [14].

In [15], in one example from the field of nanomaterials for scintillation techniques, namely for plastic scintillators, a method of creating a three-component plastic scintillators (polymer base, primary phosphor, secondary phosphor) is described. The plastic scintillators consist of a polymer base that contains primary and secondary phosphors connected by silicon atoms into nanoscale branched macromolecules. Any polymer from the group of vinylaromatic polymers, for example, polystyrene, can be used as the polymer base. The primary phosphor is selected from the group of compounds in which the maximum of the long-wavelength band of the absorption spectrum is in the range from 270 to 350 nm. In this case, the quantum yield of fluorescence is at least 5%.

The secondary phosphor is selected from the group of compounds in which the maximum wavelength of the absorption spectrum is in the range of 330 to 400 nm. In this case, the quantum yield of fluorescence is at least 30%. Increase of light output of scintillator and reduction of the duration of scintillation is achieved due to the fact that in nanoscale branched macromolecule with claimed parameters efficiency of radiation-free transfer of electron excitation energy from units of primary to units of secondary phosphor can reach 100%.

The scintillator blank is prepared by mixing a nanostructured filler with a polymer selected as a base in a double screw mixer with a return channel (at a temperature of 180°C and a screw speed of 600 rpm).

The work [16] describes an organosilicon composition for connecting optical elements and a method for creating an organosilicon lubricant composition that provides maximum light transmission in contact with optical devices and is stable in the temperature range of minus 70°C plus 200°C . For connection and sealing of optical elements on the basis of a plastic base and a thickener, a new

composition is proposed, consisting of a base - a mixture of polydimethylsiloxane and polymethylphenylsiloxane liquid with viscosity from 3000 to 40,000 mm²/s at a temperature of 20 ° C and a thickener of silicon dioxide. To provide such a composition in a vessel provided with a heater, a stirring device and a thermometer; loading 180-270 g of PMS liquid with viscosity 1000 - 20000 mm²/s and 270-180 g of PFMS liquid with viscosity 10000-20000 mm²/s; the contents of the vessel were mixed to give 450 g of a mixture having a viscosity of 3000-20000 mm²/s; a base composition, then 50-20 g of silica powder is added; the mass was heated to 40-60 C and stirred for 3-4 hours.

One of the most common and effective methods of protecting polymers from ultraviolet radiation is the use of various dispersed materials (fillers). For example, zinc oxide powders with a particle size of 0.5 to 20 μm are part of a large number of cosmetic preparations and light stabilizers used in the polymer industry. One of the most important functions of these powders is to protect the polymer from ultraviolet radiation. Replacing ZnO microparticles with nanometer-range particles is of great practical interest, since it allows to significantly reduce the content of light stabilizers simultaneously with maintaining or improving the necessary properties. Thus, the development of methods for controlling the physicochemical parameters and optical properties of dispersions based on zinc oxide nanoparticles during their synthesis allows not only to create effective light stabilizers for use in polymer, as well as cosmetic, industries, but also to reduce the economic damage from the destruction of polymer materials under the influence of solar radiation. The development of such systems is therefore of considerable scientific and practical interest.

There are many methods for the synthesis of nanoparticles of ZnO with various shapes and sizes, including the laser ablation method, which is a convenient and versatile method for producing nanosuspensions of solid-phase materials in a liquid. In this case, by varying the technological modes of ϕ laser action, the target material and the liquid medium, it is possible to obtain nanodispersed products of various composition, size, and properties in the liquid. In [17, 18, 19], the results of studying the characteristics of the products of pulsed laser ablation of zinc oxide in liquid media are presented. The interaction of pulsed laser radiation with a zinc target creates a plasma region above the surface of the target, which consists of zinc atoms and clusters. The plasma expands adiabatically and creates a shock wave at the interface, increasing pressure and temperature. At high pressures and temperatures, zinc oxidizes with water and coagulates. The formed clusters induce further growth of nanoparticles. After the plasma region that is supported by laser radiation disappears, the particle size increases relatively slowly due to the surface of the nanoparticles being coated with surface-active properties molecules. Nanoparticles can be polycrystalline or almost amorphous due to the development of coagulation and coalescence processes. It should be noted that the nanoparticles are resistant to coalescence to a certain level, which is close to 20 nm. Since ZnO nanoparticles in aqueous solution are positively charged due to incomplete oxidation, charged

surfaces can become the main factor in overcoming Van der Waals forces between nanoparticles.

The main advantages of laser ablation in a liquid are technical simplicity and chemical purity. However, the use of surface-active properties to limit the coalescence of nanoparticles often results in large size dispersion. The introduction of surface-active properties molecules can lead to the loss of one of the main advantages of laser ablation in aqueous solution, since the specific surface area of nanoparticles is reduced. In [19], nanoparticles ZnO were obtained by pulsed laser ablation from a zinc target in an aqueous solution. By this method, nanoparticles of ZnO with a very narrow size distribution are obtained. The authors found that ZnO nanoparticles obtained in a NaCl solution strongly coalesce. It is noted that the exciton emission value in the green radiation region gradually increases with a decrease in the average particle size. This means that over a larger surface area, smaller nanoparticles form more oxygen defects. The results of the experiments presented in the above work demonstrate that after passivation of the nanoparticles with a surfactant (laurylbetaindimethylamic acid) and reduction of surface charge, the nanoparticles can ZnO radiate in the green region due to oxygen defects on the surface. The medium in which ZnO nanoparticles are synthesized by laser ablation has a strong effect on the absorption spectrum. The absorption of ZnO nanoparticles obtained in HCl and NaOH is much higher in the UV range than that of nanoparticles obtained in deionized water. The high absolute surface charge of nanoparticles obtained in HCl or NaOH solution leads to an increase in the repulsion force between the nanoparticles and suppression of their growth due to coagulation. The spectra show strong absorption in the wavelength range up to 400 nm.

However, recently, laser ablation under a layer of the liquid has become a promising technology for the synthesis of nanoparticles. Advantages over other methods of nanoparticle synthesis, such as simplicity of the method, environmental friendliness, low cost, made laser ablation in a liquid medium very popular among researchers. Also of great importance, this method allows the preparation of cleaner colloidal solutions without the use of surfactants and other impurities.

IV. CONCLUSIONS

The analysis of the reviewed works allows us to conclude that to create hybrid organo-inorganic composites with a high level of dispersion of the inorganic component, problems related to the compatibility of the components and the stabilization of filler nanoparticles in the polymer matrix have to be solved. Due to the limited range of hydrophilic polymers capable of forming composites with nanoparticles without stabilizers, the main approaches to preparing hybrid composites are the use of modifying additives of surfactants, as well as complex chemical reactions on the surface of inorganic filler nanoparticles. These production methods of nanocomposites with nanoparticles are laborious, associated with the formation of by-products and additional purification. At the same time, due to the differences in the chemical nature of the

polymers, each of them requires an individual approach in choosing a modifying additive and a stabilization method.

At the same time, the use of nanoparticles in polymers should not be considered as an unambiguous positive solution to all problems. Their practical use in polymer matrices should be considered carefully, taking into account the final research goals. In this regard, research planning to select priority properties of nanocomposites and the search for new approaches to improve the qualities of hybrid composites for optical and optoelectronic devices based on a wide range of polymers and nanoparticles are becoming relevant.

REFERENCES

- [1] Shaporev A.S., Vanetsev A.S., Kiryukhin D.P., Sokolov M.N., Buznik V.M. "Synthesis of polymer composites based on ZnO, CeO₂ and Gd₂O₃ sols." Condensed media and interphase boundaries, V. 13, № 3, P. 374-380. (in Russian)
- [2] Trofimchuk E.S., Nikonorova N.I., Nesterova E.A., Muzafarov A.M., Meshkov I.B., Volynsky A.L., Bakeev N.F. "Obtaining film composites based on crazed polymers and silica sol nanoparticles". Russian nanotechnologies. - 2009. - V. 4. - № 9. - P. 164-166. (in Russian)
- [3] Pozdnyakova S.A. "Structuring and self-organization of nanocomposites in the field of a light wave": dis. Ph.D. Sciences. - 2014. - P. 120. (in Russian)
- [4] Polyanskaya V.V. "Organo-inorganic nanocomposites based on metal oxides and polyolefins deformed by the crazing mechanism": dis. Ph.D. Sciences. - 2015. - P. 138 p. (in Russian)
- [5] Serova V.N. "Optical and other materials based on transparent polymers." Serov: monograph; Feder. Education Agency, Kazan. State Technol. Univ. - Kazan: KSTU, 2010. - P. 540 (in Russian)
- [6] Burunkova, Yu.E., Denisyuk, I.Yu., Shekhanova E.B., Fokina, M.I. "Optical polymer nanocomposites." - SPb: ITMO University, 2017. - P. 80 (in Russian)
- [7] Nussbaumer R. J., Caseri W. R., Smith P., Th Tervoort. "Polymer-TiO₂ nanocomposites: a route towards visually transparent broadband UV filters and high refractive index materials", Macromol. Mater. Eng. - 2003. - V. 288. - № 1. - P. 44-49.
- [8] Ozerin A.N., Perov N.S., Zelenetsky A.N., Akopova T.A., Ozerina L.A., Kechekian A.S., Surin N.M., Vladimirov L.V., Yulovskaya V D. "Hybrid nanocomposites based on graft copolymer of chitosan with polyvinyl alcohol and titanium oxide." Russian nanotechnology. - 2009. - Vol. 4. - № 5-6. - P. 76-79. (in Russian)
- [9] Baratonny M.-I., Merhariz L., Wangx J., Gonsalves K. E. "Investigation of the TiO₂/PPV nanocomposite for gas sensing applications", Nanotechnology. - 1998. - V. 9. - № 4. - P. 356-359.
- [10] Shnitzler D.C., Zabrin J.G. J. "Organic/Inorganic hybrid materials formed from TiO₂ nanoparticles and polyaniline", Braz. Chem. Soc. - 2004. - V. 15. - №3. - P. 378-384.
- [11] Jimenez Rioboo R.J., De Andres A., Kubacka A., Fernandez-Garcia M., Cerrada M.L., Serrano C. "Influence of nanoparticles on elastic and optical properties of a polymeric matrix: Hypersonic studies on ethylene-vinyl alcohol copolymer-titania nanocomposites", Europ. Polym. J. - 2010. - V. 46. - P. 397-403.
- [12] Rong Y., Chen H.-Z., Wu G., Wang M. "Preparation and characterization of titanium dioxide nanoparticle /polystyrene composites via radical polymerization", Materials Chemistry and Physics. - 2005. - V. 91. - № 2-3. - P. 370-374.
- [13] Caris C. H. M., Van Elven L. P. M., Van Herk A. M., A. L. German. "Polymerization of MMA at the surface of inorganic submicron particles", British Polymer Journal. - 1989. - V. 21. - № 2. - P. 133-140.
- [14] Nguyen Van Ngan. "Development of composite materials based on epoxy-containing oligomers with increased chemical and biological resistance": dis. Ph.D. Sciences. - 2019 - 139 p.
- [15] Patent RF № 2380726 "Plastic scintillator with nanostructured phosphors". Patent publication: 01.27.2010 (in Russian)
- [16] Patent RF № 2505569 "Organosilicon composition". Patent publication: 27.01.2014 (in Russian)
- [17] N.G. Semaltianos, S. Logothetidis, N. Frangis, I. Tsiaoussis, W. Perrie, G.Dearden, K.G. Watkins, Chem. Phys. Lett. 496 - 2010 - P. 113.
- [18] K.K. "Kim et al. Formation of ZnO nanoparticles by laser ablation in neat ", Chemical Physics Letters 511 - 2011 - P. 116-120.
- [19] Ch. He, T. Sasaki, H. Usui, Y. Shimizu, N. Koshizaki. "Fabrication of ZnO nanoparticles by pulsed laser ablation in aqueous media and pH-dependent particle size: An approach to study the mechanism of enhanced green photoluminescence", Journal of Photochemistry and Photobiology A: Chemistry 191 - 2007 - P. 66-73.

Ab initio Electronic-Structure Calculations for Cd_{1-x}Fe_xS Semimagnetic Semiconductors

M.A. Mehrabova
Institute of Radiation Problems,
Azerbaijan National Academy of
Sciences
Baku, Azerbaijan
m.mehtabova@svience.az

N.H. Hasanov
Baku State University, Department of
Physics
Baku, Azerbaijan

S.N. Huseynli
Institute of Radiation Problems,
Azerbaijan National Academy of
Sciences
Baku, Azerbaijan

Abstract— Ab initio calculations have been carried out for calculations of electronic band structure, density of states, band gap of supercells Cd_{1-x}Fe_xS of 16 atoms ($x=0.14$) and 8 atoms ($x=0.25$) by using the Functional Density Theory. It was defined that band gap value decreases upon increasing Fe concentration, which is attributed to the interaction of CdS band electrons with Fe²⁺ ions d electrons.

Keywords — semimagnetic semiconductors, ab initio, band gap, band structure, supercells

I. INTRODUCTION

Cadmium sulfide is one of the important II-VI semiconductor compounds with band gap 2.44 eV which makes it an interesting material for use in solar cell devices, thin film transistors, optoelectronic devices, etc. Thin cadmium sulfide films have attracted much attention as making electronic devices, photovoltaic cells and optical detectors too. During the last few years, some studies in the field of magnetic materials have been focused with the aim of achieving semiconductors having ferromagnetic properties at room temperature. II-VI semiconductor compounds containing Mn, Fe and Co ions have been thoroughly studied due to their diluted magnetic semiconductors or semimagnetic semiconductors (SMSC) properties.

Semimagnetic semiconductors of II–VI are a new class of materials where semiconductors are doped with magnetic impurities. SMSC play an important role in the future of electronic science because of the combined elements of semiconductors (charge) and magnetism (spin) into a single material, known as spintronics. The existence of the strong exchange interactions between s - p band electrons and d -electrons associated with magnetic ion leads to use optical and electrical properties [1,2]. SMSC have attracted extensive research interests due to their unique magnetic and optical properties and potential applications [3]. Among these materials Mn and Fe doped II–VI semiconductors have been well studied [4,5]. However, theoretical studies of the band structure of Cd_{1-x}Fe_xS are very few. Therefore the objective of this investigation is to report on the ab initio calculations of band structure and density of states of the Cd_{1-x}Fe_xS ($x=0.14; 0.25$) SMSC.

For a basic understanding of the related phenomena and an optimization of materials for relevant processes ("band-structure engineering"), a quantitative knowledge of electronic and structural properties of these compounds,

their surfaces, and interfaces is needed. In recent years, a number of local-density approximation (LDA) calculations of bulk and surface properties of II-VI semiconductors have been reported. They are very demanding because of the cationic d electrons. If the d electrons are treated as core electrons, calculated lattice constants badly underestimate the experimental values, while inclusion of the d electrons in the valence shell yields very accurate lattice constants. But even if the d electrons are properly taken into account, the results of standard LDA calculations show distinct shortcomings. Not only is the band gap strongly underestimated, but even worse, the occupied cationic d bands reside roughly 3 eV too high in energy as compared to experiment. In consequence, their interactions with the anion p valence bands are artificially enlarged, falsifying the dispersion and bandwidth of the latter and shifting them unphysically close to the conduction bands. As a result, the LDA band-gap underestimate for the II-VI compounds is even more severe than in elemental or III-V semiconductors. For CdS, e.g., we obtain $E_g = 0.23$ eV in LDA, as opposed to $E_g = 2.44$ eV.

In this paper, we suggest an alternative approach to treat II-VI semiconductor compounds, which approximately incorporates correction Hibbard U potential. It is capable of overcoming the above-mentioned shortcomings. Correction Hibbard U to the LDA can be very important for a quantitative description of systems with strongly localized states such as 3d electrons.

II. AB INITIO CALCULATIONS OF ELECTRONIC BAND STRUCTURE

Ab initio calculations are performed in Atomistix Toolkit (ATK) program within the Density Functional Theory (DFT) and Local Spin Density Approximation (LSDA) on Double Zeta Double Polarized (DZDP) basis by using Hubbard U potential. Supercells of CdS were constructed and band structures were calculated (fig.1).

Cd_{1-x}Fe_xS supercells of 16 atoms ($x=0.14$) and 8 atoms ($x=0.25$) were constructed, atom relaxation and optimization of the crystal structure were carried out. Electronic band structure (EBS), density of states (DOS), total energy have been calculated in both ferromagnetic (FM) and antiferromagnetic (AFM) phases. Fig.2 and fig.3 show crystal bulk configuration, ab initio calculated band structure, and DOS of Cd_{1-x}Fe_xS ($x=0.14; 0.25$).

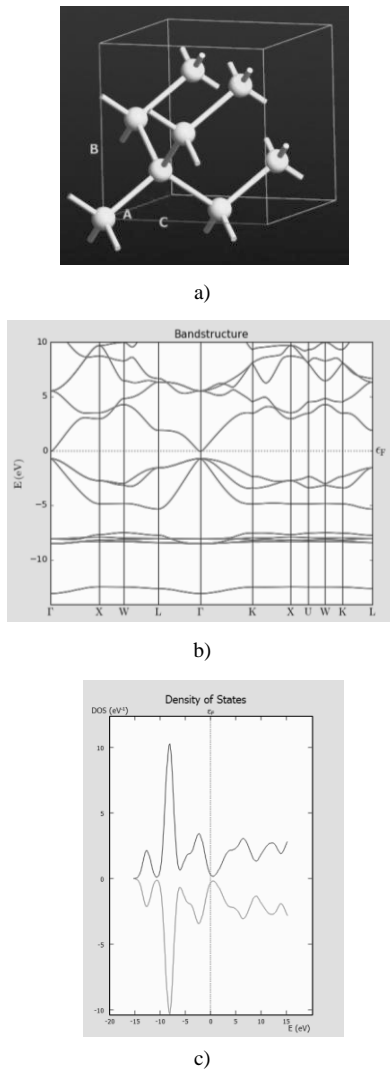


Fig.1. CdS supercell of 8 atoms in FM phase a) bulk configuration b) electronic band structure c) DOS

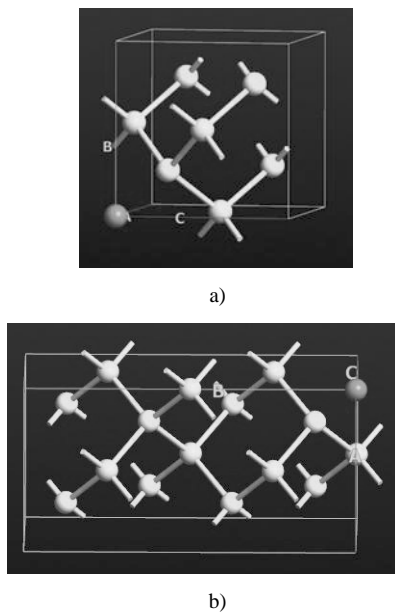


Fig.2. Bulk configuration of $Cd_{1-x}Fe_xS$ in FM phase a) $x = 0.25$, b) $x = 0.14$

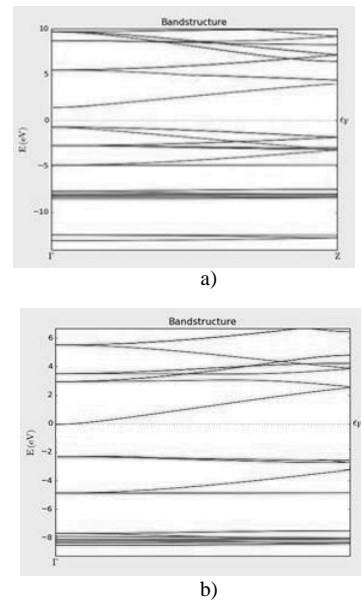


Fig.3. Band structure of $Cd_{1-x}Fe_xS$ in FM phase a) $x = 0.25$, b) $x = 0.14$

The calculated band gap value was found to be $E_g = 0.5$ eV, while the literature date shows 2.44 eV [6], this difference in value is connected with DFT theory. We corrected this band gap value for $Cd_{1-x}Fe_xS$ by using Hubbard U potential. This study performed ab initio calculations based on density functional theory with Hubbard U correction to evaluate the crystal structure, Fe impurity formation energy, and electronic structure. We adopted the effective Hubbard U potential values of $U_{Fe} = 6.4$ eV for Fe 3d atoms [7].

The calculated band gap E_g value of the $Cd_{1-x}Fe_xS$ SMSC for $x = 0.25$ and $x = 0.14$ was found to be $E_g = 2.15$ eV and $E_g = 2.21$ eV, respectively. As can be seen, E_g value decreases upon increasing Fe concentration. This was attributed to the interaction of CdS band electrons with Fe^{+2} ions d electrons (Table 1).

TABLE II. THE BAND GAP DATA

No	Material	x	E_g (300 K), eV (theoretical)	E_g (300 K), eV (experimental)
1	CdS	0	0.5	2.44
2	$Cd_{1-x}Fe_xS$	0.14	2.21	2.20
3	$Cd_{1-x}Fe_xS$	0.25	2.15	2.14

The obtained theoretical results are consistent with experimental data where reported the same observations about $Cd_{1-x}Fe_xS$ with different Fe concentrations prepared by electrodeposition technique [6].

In our previous works, we have calculated electronic band structure, density of states by ab-initio method and defined band gap, total energy, magnetic moments of some SMSC [8-10]. It was defined that in $Cd_{1-x}Mn_xTe$ and $Cd_{1-x}Fe_xTe$ SMSC, band gap value increases upon increasing transition metals Mn, Fe concentration, but in $Cd_{1-x}Mn_xSe$ and $Cd_{1-x}Fe_xS$ SMSC, band gap value decreases upon increasing transition metals Mn, Fe concentration.

III. CONCLUSION

Ab initio calculations have been carried out for supercells $Cd_{1-x}Fe_xS$ of 16 atoms ($x=0.14$) and 8 atoms

($x=0.25$). It has been calculated the electronic band structure, density of states, band gap, by the ab initio method using the Functional Density Theory. It was defined that band gap value decreases upon increasing Fe concentration, which is attributed to the interaction of CdS band electrons with Fe^{+2} ions d electrons.

ACKNOWLEDGMENT

This work was supported by the SOCAR grant 2019.

REFERENCES

- [1] Agarwal R.L., Furdyna J.K., Vonmolnar S., DMS MRS. Sym. Proc. 89 MRS, 1987, Pittsburgh.
- [2] Mycielski A., Mycielski J., Phys J. Soc. Jpn. 1980, 49, 809.
- [3] Willardson P.K., Beer A.C. (Eds.), Semimetals and Semiconductors, 1988, 25, Academic Press, New York.
- [4] Twardowski A., J. Appl. Phys. 1990, 67, 5108.
- [5] Han S.J., Song J.W., Yang C.H., Park S.H., Jeong J.H., Appl. Phys. Lett. 2002, 81, 4212.
- [6] Dizaji H.R., Ghasemian M., Ehsani M.H. Structural and optical characterization of CdS:Fe thin films prepared by flash evaporation method. Surface Review and Letters, 2012, 19, 2, 1250012-1-6
- [7] Hsuan-Chung Wu, Sheng-Hong Li, Syuan-Wei Lin. Effect of Fe Concentration on Fe-Doped Anatase TiO₂ from GGA + U Calculations. International Journal of Photoenergy, 2012, 1- 6
- [8] Mehrabova M. A., Orujov H.S., Hasanov N.H., Kazimova A.I., Abdullayeva A. A. Ab initio calculations of defects in CdMnSe semimagnetic semiconductors. Mechanics of Solids, 2020, 55, 1, 108–113
- [9] Mehrabova M.A., Nuriyev H.R., Orujov H.S., Nazarov A.M., Sadigov R.M., Poladova V.N. Defect formation energy for charge states and electrophysical properties of CdMnTe // SPIE Photonics, Devices and Systems VI, 2015, 9450, 94500Q-(1-10)
- [10] M.A. Mehrabova H.S.Orujov, H.R. Nuriyev N.H.Hasanov, A.A. Abdullayeva Z.I.Suleymanov. Ab-initio calculations of electronic structure of CdFeTe and optical properties. Conference proceedings Modern Trends in Physics. 2019, 01-03 May, 39-42, Baku.

The surface plasmonic resonance in the metallic 1D-structures with the elliptic cross-section

Yan Karandas

Department of Micro- and
Nanoelectronics

National University "Zaporizhzhia
Politechnic"
Zaporizhzhia, Ukraine

Andrii Korotun

Department of Micro- and
Nanoelectronics

National University "Zaporizhzhia
Politechnic"
Zaporizhzhia, Ukraine
andko@zp.edu.ua

Abstract—The expressions for the diagonal components of the polarizability tensor of the nanocylinder with the elliptic cross-section have been obtained to the dipole approximation. The frequencies of the surface plasmonic resonance in such system have been determined. The evolution of the extremums of the real and imaginary parts of the diagonal components of the polarizability tensor under the variation of the eccentricity of the cross-section has been analyzed. The splitting of the frequencies of the surface plasmonic resonance has been estimated.

Keywords — polarizability tensor, nanocylinder, elliptic cross-section, surface plasmonic resonance, eccentricity.

I. INTRODUCTION

The main trends in the development of the applied optics are determined by the necessity for the miniaturization of the optical devices. In addition, along with the miniaturization of the devices, the problem connected with the increasing of the speed of the computing devices arises, for which one proposes to use the plasmonic structures [1]. In particular, it is necessary to create a new element base [2,3], since the transition from the optical elements to the plasmonic ones results in the essential decrease in the characteristic size of the system [4]. In this regard, the active researches are carried out in this direction [5–7].

The localized plasmons form the important class of the plasma waves. Such plasmons are localized with respect to all three coordinates, and the region of the localization can be subwavelength. This effect is used to construct many optical schemes that operate with the subwavelength spatial resolution, which contradicts Rayleigh criterion. This possibility is associated with the use of the near fields. Rayleigh criterion can not be applied to such fields. For example, such focusing of the field near the metallic needle made it possible to construct the scanning optical apertureless near-field microscope with the extremely high spatial resolution [8]. The high degree of the localization of the modes of the field near the metallic nanoobjects gives an opportunity to vary essentially the rates of the spontaneous emission of atoms and molecules [9,10] and enhance the effects of birefringence and dichroism [11]. The high intensity of the electromagnetic field along with the high ohmic losses give an opportunity to heat nanoobjects with the help of the optic methods, which can potentially find an application in medicine for the thermal destruction of the malignant neoplasms [12]. The nonhomogeneity of the field of plasmon can be used for the creation of the plasmonic optical tweezers [13–15].

In addition to the areas listed above, the plasmonic phenomena are used under the creation of the sensors [16–

18]. In this connection, 1D-structures have much higher spectral sensitivity in comparison with the spherical nanoparticles. Thus, the maximum of the absorption band for the rod-like particles is situated in the long-wavelength part of the spectrum, which makes them attractive for use in the sensors in the near IR range. An influence of the shape of the cross-section on the spectral sensitivity of the nanowires with the triangular, trapezoidal and rectangular cross-section has been studied in the work [19].

However, the production of the nanowires with the mentioned above shapes of the cross-sections seems to be more complicated than with the elliptic cross-section from the technological point of view, since the effect of small transverse stresses is sufficient for this. The optical response of the metallic nanocylinders with the elliptic cross-section has been studied in the work [20], an influence of the deformation of the cross-section on the variance of the surface plasmons in the achiral carbon nanotubes has been studied in the work [21, 22].

Therefore, the aim of this article is the study of the optical properties of 1D-structures with the elliptic cross-section with small value of eccentricity.

II. THE BASIC RELATIONS

A. The polarizability of the nanowire

Let us consider the metallic nanowire with the length l with the elliptic cross-section, the effective radius of which ρ_0 ($\rho_0 = (a+b)/2 \ll l$, where a and b – semimajor and semiminor axes of ellipse), and the eccentricity of the cross-section $\varepsilon = \sqrt{1 - (a/b)^2} \ll 1$. Let us assume, that the indicated 1D-structure is situated in the homogeneous isotropic dielectric medium with the permittivity ϵ_m , and its axis is directed along z -axis of the Cartesian coordinate system (Fig. 1).

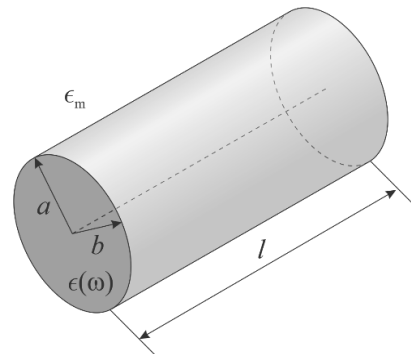


Fig. 1. The geometry of the problem

As is known, the particularities of the interaction between the electromagnetic waves and the metallic nanostructures can be characterized based on the frequency variance of their dipole polarizability. The components of the polarizability tensor can be obtained from the solution of the electrostatic problem connected with the determination of the scalar potential. As long as the explicit solution of such problem exists only for the spherical and ellipsoidal particles, including the particular cases of prolate spheroid and oblate spheroid, let us use the expression for the diagonal components of the polarizability tensor of ellipsoid [23].

$$\alpha_{ii} = V \frac{\tau_{jj}(\omega) - \tau_m}{\tau_m + \mathcal{L}_j (\tau_{jj}(\omega) - \tau_m)}, \quad (1)$$

where $V = \pi a b l$ – the volume of the ellipsoidal nanoparticle; \mathcal{L}_j – depolarization factors ($j = x, y, z$); $\tau_{jj}(\omega)$ – dielectric tensor of the material of the nanoparticle

$$\tau_{jj}(\omega) = \tau^\infty - \frac{\omega_p^2}{\omega(\omega + i\gamma_{jj}^{\text{eff}})}, \quad (2)$$

Here τ^∞ – the contribution of ion core into the dielectric function of metal; $\omega_p = \sqrt{e^2 n_e / \tau_0 m^*}$ – the frequency of bulk plasmons, e , n_e and m^* – the charge, the concentration and the effective mass of electron ($n_e^{-1} = 4\pi r_s^3 / 3$, r_s – the mean distance between the conduction electrons), and the diagonal components of the tensor of the effective relaxation rate are determined as follows

$$\gamma_{jj}^{\text{eff}} = \gamma^{\text{bulk}} + \gamma_{jj}^{\text{surf}} + \gamma_{jj}^{\text{rad}}, \quad (3)$$

where γ^{bulk} – bulk relaxation rate, and the expressions for the diagonal components of the surface relaxation rates $\gamma_{jj}^{\text{surf}}$ and the radiation attenuation γ_{jj}^{rad} have the form [24,25]

$$\gamma_{jj}^{\text{surf}} = \frac{\mathcal{L}_j \sigma_{jj}(\omega)}{\tau_0 (\tau_m + \mathcal{L}_j (1 - \mathcal{L}_j))}, \quad (4)$$

$$\gamma_{jj}^{\text{rad}} = \frac{2\pi}{3\tau_0 \sqrt{\tau_m}} V \left(\frac{\omega_p}{c} \right)^3 \frac{\mathcal{L}_j \sigma_{jj}(\omega)}{\sqrt{\tau^\infty + \left(\frac{1}{\mathcal{L}_j} - 1 \right) \tau_m}}, \quad (5)$$

Due to the fact that the depolarization factors for the elliptic cylinder at $\rho_0 \ll l$ have the form [26]

$$\mathcal{L}_x = \frac{a}{a+b}, \quad \mathcal{L}_y = \frac{b}{a+b}, \quad \mathcal{L}_z = 0. \quad (6)$$

then

$$\alpha_{kk}(\omega) = 2V \tilde{\alpha}_{kk} \left(1 \pm \frac{\varepsilon^2}{4} \tilde{\alpha}_{kk} \right); \quad (7)$$

$$\alpha_{zz}(\omega) = V \frac{\tau_{zz}(\omega) - \tau_m}{\tau_m},$$

where $k = x, y$; one uses the sign «+» under $k = x$, and the sign «-» - under $k = y$;

$$\tilde{\alpha}_{kk} \equiv \frac{\tau_{kk}(\omega) - \tau_m}{\tau_{kk}(\omega) + \tau_m}. \quad (8)$$

The transverse components of the conductivity tensor for the nanowire have the following form to the weak ellipticity approximation

$$\sigma_{xx}(\omega) = \frac{27}{64} T_0 \left(\frac{\omega_p}{\omega} \right)^2 \frac{v_F}{a} \left(\frac{\pi}{2} + \frac{a}{l} \right); \quad (9)$$

$$\sigma_{yy}(\omega) = \frac{27}{64} T_0 \left(\frac{\omega_p}{\omega} \right)^2 \frac{v_F}{b} \left(\frac{\pi}{2} + \frac{b}{l} \right).$$

Thus, the diagonal components of the tensors of the surface relaxation rates and the radiation attenuation have the form

$$\gamma_{xx}^{\text{surf}} = \frac{27}{64(\tau_m + 1)} \left(\frac{\omega_p}{\omega} \right)^2 \frac{v_F}{a} \left(\frac{\pi}{2} + \frac{a}{l} \right); \quad (10)$$

$$\gamma_{yy}^{\text{surf}} = \frac{27}{64(\tau_m + 1)} \left(\frac{\omega_p}{\omega} \right)^2 \frac{v_F}{b} \left(\frac{\pi}{2} + \frac{b}{l} \right); \quad (11)$$

$$\gamma_{xx}^{\text{rad}} = \frac{9\pi V}{64\sqrt{\tau_m}(\tau^\infty + \tau_m)} \left(\frac{\omega_p}{c} \right)^3 \left(\frac{\omega_p}{\omega} \right)^2 \frac{v_F}{a} \left(\frac{\pi}{2} + \frac{a}{l} \right); \quad (12)$$

$$\gamma_{yy}^{\text{rad}} = \frac{9\pi V}{64\sqrt{\tau_m}(\tau^\infty + \tau_m)} \left(\frac{\omega_p}{c} \right)^3 \left(\frac{\omega_p}{\omega} \right)^2 \frac{v_F}{b} \left(\frac{\pi}{2} + \frac{b}{l} \right); \quad (13)$$

$$\gamma_{zz}^{\text{surf}} = \gamma_{zz}^{\text{rad}} = 0. \quad (14)$$

The presented concepts are going to be used in the next subsection for the determination of the frequencies of the surface plasmonic resonances.

B. The frequencies of SPR for the long nanowire

As long as $a, b \ll l$, $\mathcal{L}_z = 0$ for 1D-structure with the big length, then $\omega_z^{\text{sp}} = 0$ and the longitudinal surface plasmonic resonance is absent.

The expressions for the frequencies of the transverse surface plasmonic resonances can be obtained from the conditions

$$\text{Re}\tau(\omega_k^{\text{sp}}) = -\frac{1 - \mathcal{L}_k}{\mathcal{L}_k} \tau_m = -\left(\frac{b}{a} \right)^{\delta_k} \tau_m, \quad (15)$$

where

$$\delta_k = \begin{cases} 1, & k = x; \\ -1, & k = y, \end{cases}$$

and

$$\left(\frac{b}{a}\right)^{\delta_k} = 1 - \delta_k \frac{\varepsilon^2}{2}. \quad (16)$$

Thus, one can obtain the following relation from the expressions (3) and (14) taking into account (15)

$$\left(\omega_k^{sp}\right)^2 + \left(\gamma^{\text{bulk}} + \frac{\mathcal{K}_{pp}}{\left(\omega_k^{sp}\right)^2}\right)^2 = \frac{\omega_p^2}{\tau^\infty + \left(1 - \delta_k \frac{\varepsilon^2}{2}\right)\tau_m}, \quad (17)$$

where

$$\begin{aligned} \mathcal{K}_{xx} &= \frac{9}{64} \omega_p^2 \frac{v_F}{a} \left(\frac{\pi}{2} + \frac{a}{l}\right) \times \\ &\times \left[\frac{3}{\tau_m + 1} + \frac{\pi V}{\sqrt{\tau_m(\tau^\infty + 2\tau_m)}} \left(\frac{\omega_p}{c}\right)^3 \right]; \\ \mathcal{K}_{yy} &= \frac{9}{64} \omega_p^2 \frac{v_F}{b} \left(\frac{\pi}{2} + \frac{b}{l}\right) \times \\ &\times \left[\frac{3}{\tau_m + 1} + \frac{\pi V}{\sqrt{\tau_m(\tau^\infty + 2\tau_m)}} \left(\frac{\omega_p}{c}\right)^3 \right], \end{aligned} \quad (18)$$

We are going to solve the equation (17) using the method of the successive approximations

$$\left(\omega_k^{sp}\right)^2 = \omega_k^{sp(0)} + \omega_k^{sp(1)} + \dots, \quad (19)$$

where

$$\omega_k^{sp(0)} = \sqrt{\frac{\omega_p^2}{\tau^\infty + \left(1 - \delta_k \frac{\varepsilon^2}{2}\right)\tau_m} - \left(\gamma^{\text{bulk}}\right)^2}. \quad (20)$$

We obtain the first order correction to the frequency of the surface plasmonic resonance after the substitution of (19) into the equation (17)

$$\omega_k^{sp(1)} = -\frac{\mathcal{K}_{kk} \left(2\gamma_{\text{bulk}} \left(\omega_k^{sp(0)}\right)^2 + \mathcal{K}_{kk}\right)}{2\omega_k^{sp(0)} \left[\left(\omega_k^{sp(0)}\right)^4 + 2\gamma_{\text{bulk}} \mathcal{K}_{kk}\right]}. \quad (21)$$

It should be pointed out that the frequencies of the transverse SPR in the case of the weak ellipticity differ insignificantly from each other, since the splitting is proportional to the squared eccentricity

$$\begin{aligned} \Delta\omega_{sp} &= \omega_y^{sp} - \omega_x^{sp} = \sqrt{\frac{\omega_p^2}{\tau^\infty + \tau_m} - \left(\gamma^{\text{bulk}}\right)^2} \times \\ &\times \frac{1}{1 - \frac{\left(\gamma^{\text{bulk}}\right)^2 \left(\tau^\infty + \tau_m\right)}{\omega_p^2}} \frac{\tau_m}{\tau^\infty + \tau_m} \frac{\varepsilon^2}{2}. \end{aligned} \quad (22)$$

Let us compare the obtained results with the results presented in the work [27] for the case when the attenuation is ignored. According to this work, the formulae for the upper and lower branches of the plasmonic resonances have the form

$$\omega_{sp}^{(+)} = \frac{\omega_p}{\sqrt{\tau^\infty + \frac{b}{a}\tau_m}}, \quad \omega_{sp}^{(-)} = \frac{\omega_p}{\sqrt{\tau^\infty + \frac{a}{b}\tau_m}}. \quad (23)$$

Taking into account that the ratio of the semiaxes of the ellipse $b/a = (1 - \varepsilon^2)^{1/2}$, we obtain for the splitting of the frequencies of SPR to the first nonvanishing with respect to ε approximation

$$\left(\frac{\Delta\omega_{sp}}{\omega_p}\right)_{\gamma=0} = \frac{1}{2} \frac{\tau_m}{\left(\tau^\infty + \tau_m\right)^{3/2}} \varepsilon^2. \quad (24)$$

It should be pointed out that the following relation can be obtained from the formula (22) for the case $\gamma^{\text{bulk}} \neq 0$

$$\begin{aligned} \left(\frac{\Delta\omega_{sp}}{\omega_p}\right)_{\gamma^{\text{bulk}} \neq 0} &= \sqrt{\frac{1}{\tau^\infty + \tau_m} - \left(\frac{\gamma^{\text{bulk}}}{\omega_p}\right)^2} \times \\ &\times \frac{1}{1 - \left(\tau^\infty + \tau_m\right) \left(\frac{\gamma^{\text{bulk}}}{\omega_p}\right)^2} \frac{\tau_m}{\tau^\infty + \tau_m} \frac{\varepsilon^2}{2}, \end{aligned} \quad (25)$$

which coincides with (24) in the limit $\gamma^{\text{bulk}} \rightarrow 0$.

III. THE RESULTS OF THE CALCULATIONS AND THE DISCUSSION

The calculations have been performed for the isolated metallic cylinders ($\tau_m = 1$) with the different effective radius under the different values of the eccentricity. The parameters of metals are given in Table 1.

TABLE III. PARAMETERS OF METALS [28]

Value	Metals			
	Al	Cu	Au	Ag
r_s / a_0	2.07	2.11	3.01	3.02
m^* / m_e	1.06	1.49	0.99	0.96
τ^∞	0.7	12.03	9.84	3.70
$\gamma_{\text{bulk}}, 10^{14} \text{ s}^{-1}$	1.25	0.37	0.35	0.25

Figure 2 shows the frequency dependencies for the real and imaginary parts of the diagonal components of the polarizability tensor. It should be pointed out that

$\max(\text{Re}(\text{Im})\alpha_{yy}) > \max(\text{Re}(\text{Im})\alpha_{xx})$ for all values of the eccentricity which are under the consideration. The increase of the eccentricity results in the increase of $\max(\text{Re}(\text{Im})\alpha_{yy})$, while $\max(\text{Re}(\text{Im})\alpha_{xx})$ decreases. This is due to the facts that $b > a$ and the response in the direction of y -axis is stronger than in the direction of x -axis. In addition, the spectral location of the maximums of the imaginary parts α_{xx} and α_{yy} remains the same.

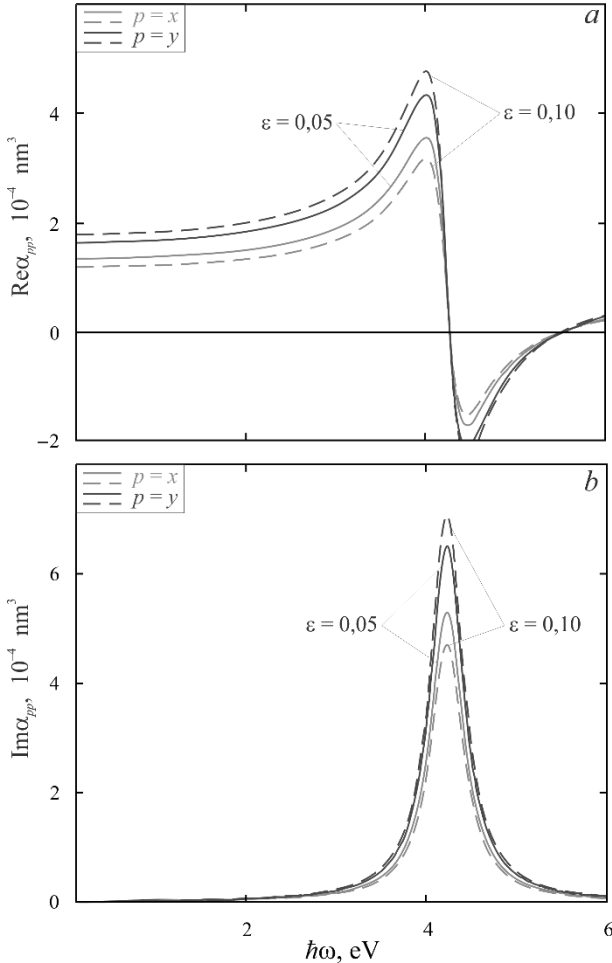


Fig. 2. The frequency dependencies for the real (a) and imaginary (b) parts of the components of the polarizability tensor of the nanocylinders Ag with the different values of the eccentricity.

The frequency dependencies for the real and imaginary parts of the diagonal components of the polarizability tensor α_{xx} and α_{yy} for the nanocylinders of different metals are given in Figure 3 and 4 respectively. It should be pointed out that the spectral locations of the maximums and minimums of the real parts and of the maximums of the imaginary parts are independent of the fact which component it is (α_{xx} or α_{yy}) for specific metal, but depend on the type of metal itself. So, $\max(\text{Im}\alpha_{pp}(\omega))$ experiences the "blue" shift in the sequence of metals $\text{Au} \rightarrow \text{Cu} \rightarrow \text{Ag} \rightarrow \text{Al}$. It is explained exceptionally by the differences in the values of the frequency of bulk plasmons ω_p and by the contribution of ion core τ^∞ into the dielectric function of metal.

In conclusion let us point out that the splitting of the frequency of SPR is proportional to the square of the eccentricity both with and without taking into consideration the attenuation and, therefore, is insignificant. The results of the calculations show that taking account of the attenuation for the case of the nanocylinders with the weakly elliptic cross-section has practically no effect on the splitting of the frequencies of SPR and, therefore, the use of the nondissipative approximation is justified in such problems. In this connection, the geometric factor makes the main contribution into the splitting.

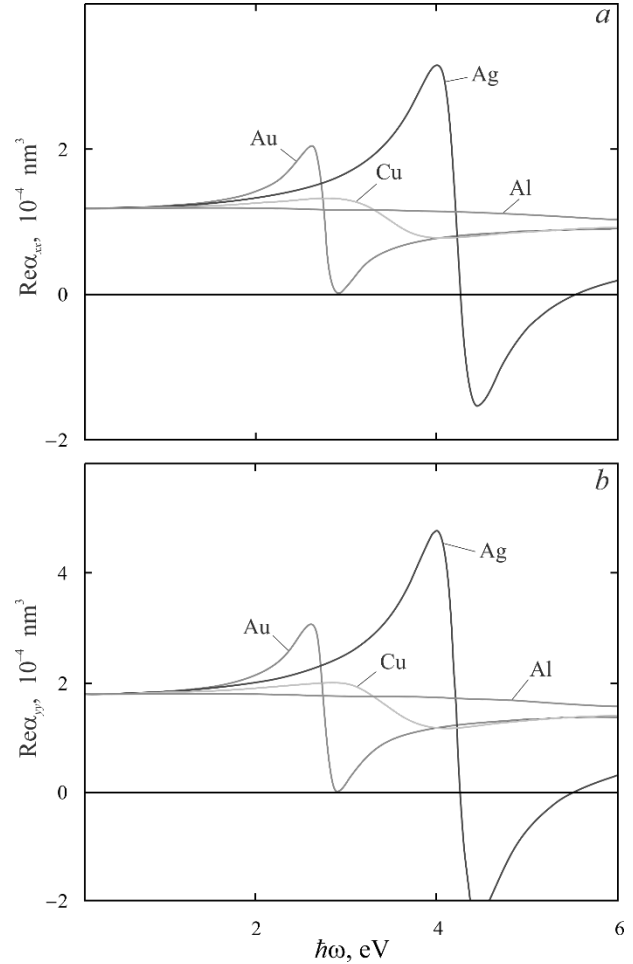


Fig. 3. The frequency dependencies for the real parts of the components α_{xx} (a) and α_{yy} (b) of the polarizability tensor of the nanocylinders of different metals under $\epsilon = 0.1$.

IV. CONCLUSIONS

The expressions for the diagonal components of the polarizability tensor of the nanocylinder with the elliptic cross-section under the small values of the eccentricity have been obtained using the passage to the limit from the case of the ellipsoidal nanoparticle.

It has been established that the increase of the eccentricity results in the increase of the extreme values of the real and imaginary parts of the component α_{yy} and in the decrease of the components α_{xx} , which is explained by the big lateral size of the nanostructure in y -direction.

It has been shown that the shift of the maximums and the minimums of the real part and the maximums of the

imaginary part of the diagonal components of the polarizability of the cylinders of different metals is associated with their optical properties – the frequency of bulk plasmons and the contribution of the crystal lattice into the dielectric function of metal.

It has been proved that the splitting is proportional to the square of the eccentricity in the case of the weakly deformed cross section of the nanocylinder, which means that it is small and is determined, first of all, by the geometric factor, and not by the scattering processes.

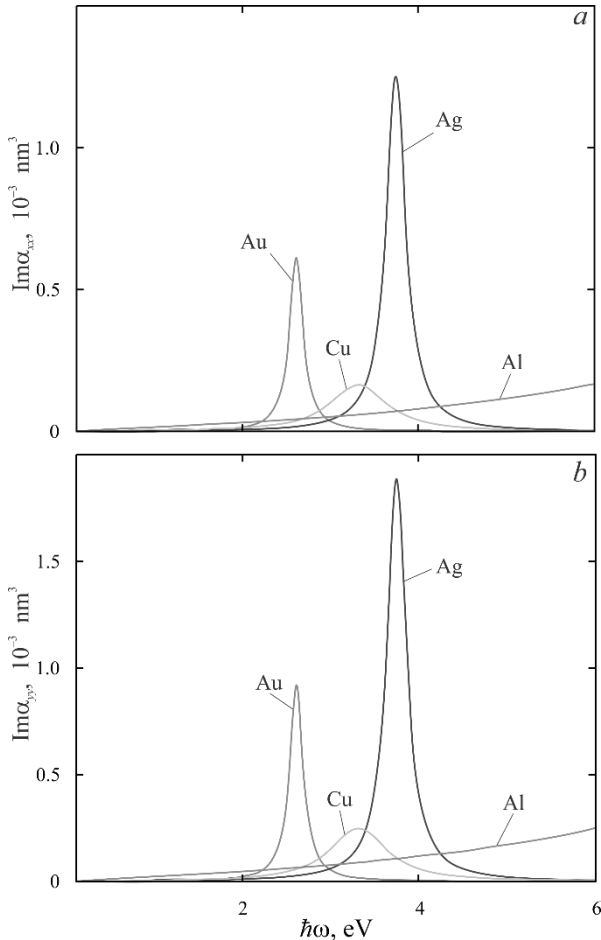


Fig. 4. The frequency dependencies for the imaginary parts of the components α_{xx} (a) and α_{yy} (b) of the polarizability tensor of the nanocylinders of different metals under $\epsilon = 0.1$.

REFERENCES

[1] Andrianov, A. P. Vinogradov, A. V. Dorofeenko, A. A. Zyablovskij, A. A. Lisyanskiy, A. A. Pukhov, *Kvantovaya nanoplazmonika*. Moskva: Intellekt, 2015 [in russian].
 [2] S. Bozhevolnyi, *Plasmonic nanoguides and circuits*. Singapore: Pan Stanford, 2009.
 [3] J. T. Kim, J. J. Ju, S. Park, M.-S. Kim, S. K. Park, and M.-H. Lee, “Chip-to-chip optical interconnect using gold long-range surface plasmon polariton waveguides,” *Opt. Express*, vol. 16, pp. 13133–13138 August 2008.
 [4] E. Andrianov, A. Pukhov, A. Dorofeenko, A. Vinogradov, and A. Lisyanskiy, “Forced synchronization of spaser by an external optical wave,” *Opt. Express*, vol. 19, pp. 24849–24857, December 2011.
 [5] S. A. Maier, *Plasmonics: Fundamentals and Applications*. New York, Springer, 2007.
 [6] T. V. Shahbazyan, M. I. Stockman, *Plasmonics: Theory and Applications*. New York, Springer, 2013.
 [7] *Plasmonics and Its Applications* / Ed. by G. Barbillon. Basel, 2019

[8] T. Kalkbrenner, M. Ramstein, J. Mlynek, and V. Sandoghdar, “A single gold particle as a probe for apertureless scanning near-field optical microscopy,” *J. Microsc.*, vol. 202, pp. 72–76, April 2001.
 [9] K. Okamoto, I. Niki, A. Scherer, Y. Narukawa, T. Mukai, and Y. Kawakami, “Surface plasmon enhanced spontaneous emission rate of InGaN/GaN quantum wells probed by time-resolved photoluminescence spectroscopy,” *App. Phys. Lett.*, vol. 87, p. 071102, June 2005.
 [10] K. Y. Yang, K. C. Choi, and C. W. Ahn, “Surface plasmon-enhanced spontaneous emission rate in an organic light-emitting device structure: Cathode structure for plasmonic application,” *App. Phys. Lett.*, vol. 94, p. 173301, April 2009.
 [11] M. R. Shcherbakov, P. P. Vabishchevich, M. I. Dobynde, T. V. Dolgova, A. S. Sigov, C. M. Wang, D. P. Tsai, and A. A. Fedyanin, “Plasmonic enhancement of linear birefringence and linear dichroism in anisotropic optical metamaterials,” *JETP Lett.*, vol. 90, pp. 433–437, November 2009.
 [12] X. Huang, P. K. Jain, I. H. El-Sayed, and M. A. El-Sayed, “Determination of the minimum temperature required for selective photothermal destruction of cancer cells with the use of immunotargeted gold nanoparticles,” *Photochem. Photobiol.*, vol. 82, pp. 412–417, April 2006.
 [13] M. L. Juan, M. Righini, and R. Quidant, “Plasmon nano-optical tweezers,” *Nature Photonics*, vol. 5, pp. 349–356, May 2011.
 [14] L. Novotny, R. X. Bian, and X. S. Xie, “Theory of nanometric optical tweezers,” *Phys. Rev. Lett.*, vol. 79, p. 645, July 1997.
 [15] M. Righini, G. Volpe, C. Girard, D. Petrov, and R. Quidant, “Surface plasmon optical tweezers: tunable optical manipulation in the femtonewton range,” *Phys. Rev. Lett.*, vol. 100, p. 186804, May 2008.
 [16] H. Kano and S. Kawata, “Surface-plasmon sensor for absorption-sensitivity enhancement,” *App. Opt.*, vol. 33, pp. 5166–5170, August 1994.
 [17] K. Kurihara, and K. Suzuki, “Theoretical understanding of an absorption-based surface plasmon resonance sensor based on Kretschmann’s theory,” *Anal. Chem.*, vol. 74, pp. 696–701, January 2002.
 [18] V.V. Klimov, “*Nanoplasmonics*,” Boca Raton, FL: CRC Press, Taylor and Francis Group, 2014, 581 p.
 [19] M.V. Sosnova, N.L. Dmitruk, A.V. Korovin, S.N. Mamykin, V.I. Mynko, and O.S. Lytvyn, “Local plasmon excitations in one-dimensional array of metal nanowires for sensor applications,” *Appl. Phys. B*, vol. 99, pp. 493–497, November 2009.
 [20] A. V. Korotun, A.A. Koval', “Dielectric Tensor of a Metal Nanowire with an Elliptical Cross Section,” *Phys. Met. and Metallogr.*, vol. 120, pp. 621 – 625, July 2019.
 [21] A. V. Korotun, I. M. Titov, A. O. Koval', “Surface plasmons in carbon nanotubes with elliptical cross section,” *J. Nano- Electron. Phys.*, vol. 9, id. 01017.
 [22] A. Korotun, Y. Karandas, D. Demianenko, and I. Titov, “The long-wavelength surface plasmons in the single-wall carbon nanotubes with the elliptic cross section,” *CAOL*, pp. 387–391, September 2019 [IEEE 8th International Conference on Advanced Optoelectronics and Lasers Sozopol, Bulgaria, p. 301, 2019].
 [23] C. F. Bohren and D. R. Huffman, *Absorption and Scattering of Light by Small Particles*. John Wiley & Sons, 2008.
 [24] N. I. Grigorochuk and P.M. Tomchuk, “Optical and transport properties of spheroidal metal nanoparticles with account for the surface effect,” *Phys. Rev. B*, vol. 84, p. 085448, August 2011.
 [25] N. I. Grigorochuk “Radiative damping of surface plasmon resonance in spheroidal metallic nanoparticle embedded in a dielectric medium,” *J. Opt. Soc. Am. B*, vol. 29, pp. 3404–3411, December 2012.
 [26] J. A. Osborn, “Demagnetizing Factors of the General Ellipsoid,” *Phys. Rev.*, vol. 67, pp. 351–357, June 1945.
 [27] D. V. Guzatov and V. V. Klimov “Spontaneous emission of an atom placed near a nanobelt of elliptical cross section,” *Phys. Rev. A*, vol. 75, p. 052901, Mar 2007.
 [28] A. V. Korotun and N. I. Pavlyshche, “Cross-sections of Absorption and Scattering of Electromagnetic Radiation by Ensembles of Metal Nanoparticles of Different Shapes,” *Phys. Met. Metallogr.*, in press.

The size thermal effects in the neighborhood of the plasmonic bimetallic nanoparticle

Andrii Korotun

Department of Micro- and
Nanoelectronics

National University "Zaporizhzhia
Politechnic"

Zaporizhzhia, Ukraine

andko@zp.edu.ua

Abstract—The thermal phenomena, which are caused by the excitation of the surface plasmons in the two-layer spherical nanoparticles, have been studied in the work. The frequency and size dependencies for the heating of the neighborhood of the bimetallic nanoparticles with the different composition of the elements have been calculated. The possibility of the heating control with the help of the variation of the morphology of the nanoparticles has been demonstrated.

Keywords—heating, bimetallic nanoparticle, light absorption, relaxation time, surface plasmon resonance

I. INTRODUCTION

The significant progress in the construction of the systems with the nanoscale elements in recent years results in the improvement of the technologies of the synthesis of the bimetallic nanostructures.

Such systems are of special interest due to their optical properties, which are the subject of the intensive theoretical and experimental studies [1–7]. It is well-known that the plasmonic resonances – the maximums of the absorption cross-sections dominate in the electromagnetic response of the metallic nanostructure. If photon interacts with the metallic nanoparticle, the size of which is less than or comparable to the wavelength of light, then it can cause the collective coherent oscillations of electrons in metal. In the case of the nanoparticle, these oscillations take place at the definite frequency which is called the frequency of the localized surface plasmonic resonance (SPR) [1,2]. The result of this interaction is the following. First, the strong scattering of photons takes place, which makes the plasmonic nanoparticles very important for the applications connected with the redirection of photons, such as waveguide; for the capturing of light inside the thin-film solar cells and under the optical calculations which require an effective light deflection in small volumes [3]. Secondly, the plasmonic resonances are also associated with the increase of the absorption inside the nanoparticle. The further transformation of this absorbed energy for the generation of the charge carriers and photons have been considered in such applications as photocatalysis, photothermal visualization, plasmonic heating and the heated magnetic recording [3,8].

The photothermal heating is the well-known physical phenomenon which manifests itself as a rise of the temperature in the micrometric domain around the interface metal – environment [4]. It is known that the metallic nanostructures generate the heat under the interaction with

the electromagnetic radiation at the frequency of their plasmonic resonance. The heat release process depends on the morphology of the metallic structure and on the incident wavelength [5]. The heat release takes place due to the losses, faced by the surface plasmons which propagate along the interface metal – environment [8]. As known, these losses restrict the pathlength of the surface plasmons, hence, making these plasmons the localized ones and heating the medium. The heating of the plasmonic structures is the rapidly expanding field of research which is known as thermoplasmonics [9]. Recently, the various studies tried to use thermoplasmonics for the different applications. These applications include photoelectrical [10], liquid heating [11], gene therapy [12], thermobiology [13], photothermal cancer therapy [14], visualization and spectroscopy [15] and plasmofluidics [16]. Some of the thermoplasmonic studies use the thermally induced shift of SPR as the temperature measuring mechanism [17], while in [18], the highly-sensitive method which analyses the deformation of the shape of the protein molecule by virtue of the fact that it is adsorbed on the surface of metal at the different temperatures, has been developed using SPR. However, the majority of the works, which associate SPR with the temperature of the matter under the consideration, refer to the bulk temperature and do not take into account the variation of the temperature near the plasmonic structure.

It is known [10] that the degree of the heating of the domains, adjacent to the nanoparticle, depends on its absorption cross-section which can be varied by means of changing of the shape and morphology of the nanoparticle. Recently, there has been considerable interest in use of the bimetallic nanoparticles in the form of the alloys and the other segregated structures such as core-shell, the multilayer discs and the particles with Janus surface [20–24]. The use of such structures allows more flexible regulation of the plasmonic properties in comparison with the monometallic nanoparticles.

In this context, the determination of the size dependence for the domain of heating, adjacent to the bimetallic nanoparticle, is the actual problem.

II. THE BASIC RELATIONS

Let us consider the bimetallic spherical nanoparticle with the total radius R , which is situated in the dielectric medium with the permittivity ϵ_m (fig. 1). The core with the radius R_c ($R = R_c + t$) is situated under the shell of thickness t .

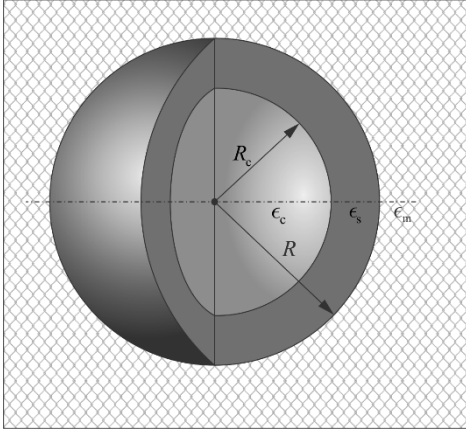


Fig. 1. The geometry of the problem

After the external pumping of light, the average temperature increases by the value [10]

$$\Delta T \approx \frac{I_0 R}{4\kappa} Q_{\oplus}^{\text{abs}}, \quad (1)$$

where I_0 – an incident light intensity; κ – the thermal conductivity of the environment; Q_{\oplus}^{abs} – an absorption efficiency, which is determined as

$$Q_{\oplus}^{\text{abs}} = \frac{\omega}{\pi c R^2} \sqrt{T_m} \text{Im} \alpha_{\oplus}. \quad (2)$$

Here ω – the frequency of the incident electromagnetic wave; c – light velocity, a α_{\oplus} – the dipole polarizability of the bimetalllic nanoparticle

$$\alpha_{\oplus} = R^3 \frac{(\tau_s - \tau_m)(2\tau_s + \tau_c) - (2\tau_s + \tau_m)(\tau_s - \tau_c)\beta_c}{(\tau_s + 2\tau_m)(2\tau_s + \tau_c) - 2(\tau_s - \tau_m)(\tau_s - \tau_c)\beta_c}, \quad (3)$$

where τ_c and τ_s are the functions of the frequency of light, and $\beta_c = (R_c/R)^3$ – the volumetric “fraction” of material of the core of the bimetalllic spherical nanoparticle.

In the frameworks of Drude theory, the dielectric functions of material of the core (shell) are determined by the expressions

$$\tau_{c(s)}(\omega) = \tau_{c(s)}^{\infty} - \frac{\omega_{p,c(s)}^2 (\tau_{\oplus}^{\text{eff}})^2}{1 + \omega^2 (\tau_{\oplus}^{\text{eff}})^2} + i \frac{\omega_{p,c(s)}^2 \tau_{\oplus}^{\text{eff}}}{\omega (1 + \omega^2 (\tau_{\oplus}^{\text{eff}})^2)}. \quad (4)$$

Here $\tau_{c(s)}^{\infty}$ – the contribution of ion core into the dielectric function of metal of the core (shell); $\omega_{p,c(s)} = \sqrt{e^2 n_{e,c(s)} / \tau_0 m_{c(s)}^*}$ – the frequency of bulk plasmons, e , $n_{e,c(s)}$ and $m_{c(s)}^*$ – the charge, the concentration and the effective mass of electron ($n_{e,c(s)}^{-1} = 4\pi r_{s,c(s)}^3 / 3$, $r_{s,c(s)}$ – the mean distance between conductivity electrons in metal of the core (shell); $\tau_{\oplus}^{\text{eff}}$ – an effective electron relaxation time in the bimetalllic nanoparticle.

As shown in [25], the value $\tau_{\oplus}^{\text{eff}}$ can be expressed in terms of the average values

$$\frac{1}{\tau_{\oplus}^{\text{eff}}} = \frac{1}{\langle \tau_{\oplus}^{\text{bulk}} \rangle_R} + \frac{1}{\langle \tau_{\oplus}^{\text{surf}} \rangle_R} + \frac{1}{\langle \tau_{\oplus}^{\text{rad}} \rangle_R}. \quad (5)$$

In addition, all the addends in the expression (5) are a kind of “cross” and create an effect of “internal mixing” of the dielectric functions τ_c and τ_s similarly as it happens with “external mixing” of the dielectric functions according to the formula (4). They can not be referred entirely to either the core or the shell.

The expressions for $\langle \tau_{\oplus}^{\text{bulk}} \rangle_R$, $\langle \tau_{\oplus}^{\text{surf}} \rangle_R$ and $\langle \tau_{\oplus}^{\text{rad}} \rangle_R$ have been obtained in [25].

The bulk relaxation time:

$$\frac{1}{\langle \tau_{\oplus}^{\text{bulk}} \rangle_R} = \left\{ \tau_s^{\text{bulk}} \left(2 - \sqrt{1 - \beta_c^{2/3}} \right) + \tau_c^{\text{bulk}} \left(1 - \sqrt{1 - \beta_c^{2/3}} \right) \right\}^{-1}, \quad (6)$$

where $\tau_{c(s)}^{\text{bulk}}$ – the bulk relaxation time in the core (shell).

The expression for the surface relaxation time has the form

$$\frac{1}{\langle \tau_{\oplus}^{\text{surf}} \rangle_R} = \mathcal{A} \frac{v_{F,s}}{R}, \quad (7)$$

where

$$\mathcal{A} = \left[1 + \left(\frac{v_{F,s}}{v_{F,c}} - 1 \right) \left(\beta_c^{1/3} + \frac{1}{2} (1 - \beta_c^{2/3}) \ln \frac{1 - \beta_c^{1/3}}{1 + \beta_c^{1/3}} \right) \right]^{-1}, \quad (8)$$

and $v_{F,c(s)}$ – Fermi electron velocity in metal of the core (shell).

The time of the radiation attenuation is determined as follows:

➤ under the conditions $\ell_c^{\text{bulk}} > 2R_c$, $\ell_s^{\text{bulk}} > 2(R - R_c)$

$$\begin{aligned} \langle \tau_{\oplus}^{\text{rad}} \rangle_R &= \frac{9 \sqrt{T_m}}{2} \frac{R}{V_0} \frac{c^3}{v_{F,s} \omega_{p,s}^3} \left\{ \frac{1}{1 - \beta_c} \times \right. \\ &\times \left[1 - \beta_c^{1/3} - \frac{1}{2} (1 - \beta_c^{2/3}) \ln \frac{1 - \beta_c^{1/3}}{1 + \beta_c^{1/3}} \right] \\ &\left. + \frac{v_{F,s}}{v_{F,c}} \frac{\omega_{p,s}^3}{\omega_{p,c}^3} \frac{1}{\beta_c} \left[\beta_c^{1/3} + \frac{1}{2} (1 - \beta_c^{2/3}) \ln \frac{1 - \beta_c^{1/3}}{1 + \beta_c^{1/3}} \right] \right\}; \end{aligned} \quad (9)$$

➤ under the conditions $\ell_c^{\text{bulk}} \leq 2R_c$, $\ell_s^{\text{bulk}} \leq 2(R - R_c)$

$$\begin{aligned} \langle \tau_{\oplus}^{\text{rad}} \rangle_R &= \frac{9 \sqrt{T_m}}{2} \frac{c^3}{V_0 \omega_{p,s}^3} \left\{ \frac{\tau_s^{\text{bulk}}}{1 - \beta_c} \left(2 - \sqrt{1 - \beta_c^{2/3}} \right) + \right. \\ &\left. + \frac{\omega_{p,s}^3}{\omega_{p,c}^3} \frac{\tau_c^{\text{bulk}}}{\beta_c} \left(1 - \sqrt{1 - \beta_c^{2/3}} \right) \right\}, \end{aligned} \quad (10)$$

where $\ell_{c(s)}^{\text{bulk}}$ is the mean free path of electrons in the core (shell).

One can calculate the frequency and size dependencies for the heating of the neighborhood of the bimetallic nanoparticle by means of the successive substitution of the formulas (2) – (8), (9) or (10) into the relation (1).

III. THE RESULTS OF THE CALCULATIONS AND THE DISCUSSION

The calculations have been performed for the spherical nanoparticles Au@Ag, Ag@Au and Au@Pt which are situated in teflon ($\tau_m = 2.3$, $\kappa = 0.25$ W/m·K) under the incident light intensity $I_0 = 1$ mW/ μm^2 .

The parameters of metals are given in the table 1.

TABLE I. PARAMETERS OF METALS [25]

Value	Metals		
	Au	Ag	Pt
r_s / a_0	3.01	3.02	3.27
m^* / m_e	0.99	0.96	0.54
τ^∞	9.84	3.70	4.42
$\tau_{\text{bulk}}, 10^{-15}$ s	29	40	9.5

The figure 2 shows the frequency dependencies for the heating for the particles Au@Ag. It should be pointed out that the dependence $\Delta T(\omega)$ has two maximums in the visible and ultraviolet regions of the spectrum. The increase of the size of the core (the curves in sequence 1 \rightarrow 2 \rightarrow 3) results in the increase of the maximum value of the heating and in the "red" shift of its maximum. With the increase in the shell thickness (the curves in sequence 2 \rightarrow 4 \rightarrow 5) the increase of ΔT_{max} also takes place, but the maximums themselves shift to the "blue" region of the spectrum. Such spectral shifts of the maximums of the heating are associated with the properties of metals of the core and the shell, and correspond to the maximums of the absorption efficiency [25].

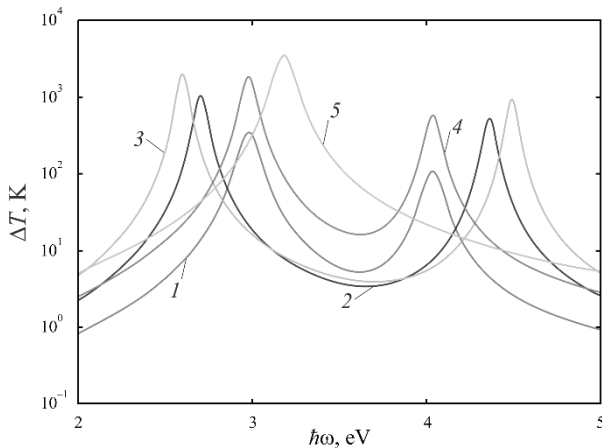


Fig. 2. The frequency dependencies for the heating of the neighborhood of the nanoparticle under the different radii of the core and the thicknesses of the shell: 1 – $R_c = 10$ nm, $t = 5$ nm; 2 – $R_c = 20$ nm, $t = 5$ nm; 3 – $R_c = 30$ nm, $t = 5$ nm; 4 – $R_c = 20$ nm, $t = 10$ nm; 5 – $R_c = 20$ nm, $t = 20$ nm.

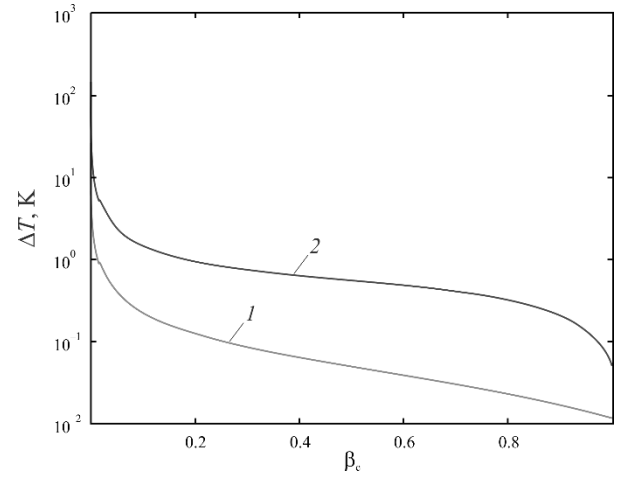


Fig. 3. The dependence of the nanoparticle neighborhood heating on the volumetric content of metal of the core under the frequencies $\omega = \omega_{sp}^{*@(+)}$ (1) and $\omega = \omega_{sp}^{*@(-)}$ (2)

The figures 3 and 4 show the dependencies of the heating of the nanoparticle neighborhoods on the volumetric content of metal of the core under the frequencies $\omega_{sp}^{*@(\pm)}$. The indicated frequencies correspond to the frequencies of SPR for the "idealized" case when $\tau_{\text{eff}}^\infty = \infty$, $\tau_c^\infty = \tau_s^\infty = \tau_m = 1$. In this case the dependence of the frequency on the volumetric content of metal of the core has the form [25]

$$\left(\omega_{sp}^{*@(\pm)}\right)^2 = \frac{1}{6} \left\{ \omega_{p,c}^2 + 3\omega_{p,s}^2 \pm \left[\left(\omega_{p,c}^2 + \omega_{p,s}^2 \right)^2 - 8\beta_c \omega_{p,s}^2 \left(\omega_{p,c}^2 - \omega_{p,s}^2 \right) \right]^{1/2} \right\}. \quad (11)$$

The values of $\omega_{sp}^{*@(\pm)}$ under the different β_c for the bimetallic nanoparticles Au@Ag, Ag@Au and Au@Pt are given in the table 2.

For the nanoparticles Au@Ag the increase of β_c results in the decrease of the heating by two orders of magnitude both for $\omega = \omega_{sp}^{*@(\pm)}$, and for $\omega = \omega_{sp}^{*@(-)}$, moreover $\Delta T|_{\omega=\omega_{sp}^{*@(-)}} > \Delta T|_{\omega=\omega_{sp}^{*@(\+)}}$ (fig. 3). The values $\Delta T(\beta_c)$ are essentially different from $\Delta T(\omega)$, given in fig. 2, because $\hbar\omega_{sp}^{*@(-)} > 5$ eV, and $\hbar\omega_{sp}^{*@(\pm)} > 9$ eV. This fact indicates that the frequencies of SPR for the "idealized" case are approximately twice as much as the actual frequencies of SPR for the nanoparticles Au@Ag.

TABLE II. THE “IDEALIZED” FREQUENCIES OF SPR UNDER THE DIFFERENT VALUES OF THE VOLUMETRIC CONTENT OF MATERIAL OF THE CORE

β_c	$\hbar\omega_{sp}^{*(-)}$, eV			$\hbar\omega_{sp}^{*(+)}$, eV		
	Au @ Ag	Ag @ Au	Au @ Pt	Au @ Ag	Ag @ Au	Au @ Pt
0	5.286	5.242	8.390	9.137	9.099	13.745
0.1	5.281	5.248	8.013	9.141	9.096	13.968
0.2	5.275	5.253	7.653	9.144	9.093	14.169
0.3	5.270	5.259	7.303	9.147	9.090	14.353
0.4	5.264	5.264	6.960	9.150	9.087	14.522
0.5	5.259	5.270	6.620	9.153	9.084	14.680
0.6	5.253	5.275	6.281	9.156	9.080	14.828
0.7	5.248	5.281	5.939	9.159	9.077	14.969
0.8	5.242	5.286	5.592	9.163	9.074	15.102
0.9	5.237	5.292	5.237	9.166	9.071	15.228
1.0	5.232	5.297	4.871	9.169	9.068	15.349

The figure 4 shows the dependencies $\Delta T(\beta_c)$ under $\omega = \omega_{sp}^{*(+)}$ and $\omega = \omega_{sp}^{*(-)}$ for the bimetallic nanoparticles of the different composition. It should be pointed out that the indicated curves have the different kind depending on the content of the nanoparticle and on the frequency, at which the calculations are performed. Thus, $\Delta T(\beta_c)$ for the nanoparticles Ag@Au immediately decreases with the growth of β_c , and then weakly increases both under $\omega = \omega_{sp}^{*(+)}$ and under $\omega = \omega_{sp}^{*(-)}$. Again, there is the maximum ΔT under $\beta_c \approx 0.54$ for the nanoparticles Au@Pt. This is due to the fact that the values of the frequencies $\omega_{sp}^{*(+)}$ and $\omega_{sp}^{*(-)}$ are close for the particles Au@Pt.

IV. CONCLUSIONS

The model for the determination of the frequency and the size dependencies for the heating of the neighborhoods of the plasmonic bimetallic nanoparticle has been constructed.

It has been established that the spectral shifts of the maximums of the heating under the increase of the radius of the core and the thickness of the shell correspond to the spectral shifts of the maximums of the absorption efficiency.

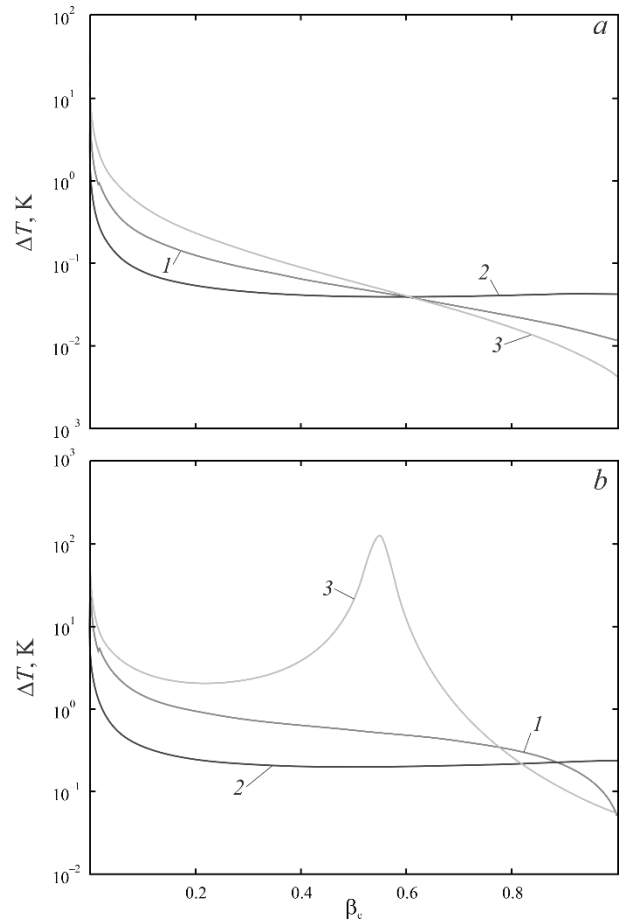


Fig. 4. The size dependence of the heating for the nanoparticles of the different elemental composition on the volumetric content of metal of the core under the frequencies $\omega = \omega_{sp}^{*(+)}$ (a) and $\omega = \omega_{sp}^{*(-)}$ (b): 1 – Au @ Ag; 2 – Ag @ Au; 3 – Au @ Pt.

It has been demonstrated that the dependencies of the heating on the volumetric content of material of the core for the nanoparticles Au@Ag at the upper and lower “idealized” frequencies of SPR are qualitatively similar but quantitatively differ by an order of magnitude. As for the particles of the other elemental composition (Ag@Au and Au@Pt) the qualitative nature of such curves is different, which demonstrates the possibility of the controlling of the thermal effects in the neighborhood of the bimetallic nanoparticle by means of the variation of their geometric parameters (the radius of the core and the thickness of the shell) and the elemental composition.

REFERENCES

- [1] S. A. Maier, Plasmonics: Fundamentals and Applications. New York, Springer, 2007.
- [2] M. Pelton and G. W. Bryant, Introduction to Metal-Nanoparticle Plasmonics. A Wiley-Science Wise Co-Publication, 2013.
- [3] P. K. Jain, X. Huang, I. H. El-Sayed, and M. A. El-Sayed, “Noble metals on the nanoscale: Optical and photothermal properties and some applications in imaging, sensing, biology, and medicine,” Acc. Chem. Res., vol. 41, pp. 1578–1586, May 2008.
- [4] A. Lalis, G. Tessier, J. Plain, and G. Baffou, “Quantifying the Efficiency of Plasmonic Materials for Near-Field Enhancement and Photothermal Conversion,” J. Phys. Chem. C, vol. 119, pp. 25518–25528, October 2015.
- [5] Y. Ren, Q. Chen, H. Qi, and L. Ruan, “Experimental comparison of photothermal conversion efficiency of gold nanotriangle and nanorod

- in laser induced thermal therapy," *Nanomaterials*, vol. 7, p. 416, November 2017.
- [6] A. V. Korotun, A. A. Koval', V. I. Reva, I. N. Titov, "Optical Absorption of a Composite Based on Bimetallic Nanoparticles. Classical Approach," *Phys. Met. Metallogr.*, vol. 120, pp. 1040–1046, December 2019.
- [7] M. Shabaninezhad, A. Kayani, and G. Ramakrishna, "Theoretical investigation of optical properties of embedded plasmonic nanoparticles," *Chem. Phys.*, vol. 541, id. 111044, January 2021.
- [8] G. Baffou, *Thermoplasmonics Heating Metal Nanoparticles Using Light*. Cambridge University Press, 2017.
- [9] A. Elkalsh, A. Vukovic, P. D. Sewell, and T. M. Benson, "Electro-thermal modelling for plasmonic structures in the TLM method," *Opt. Quantum Electron.*, vol. 48, p. 263, March 2016.
- [10] G. Baffou and R. Quidant, "Thermo-plasmonics: Using metallic nanostructures as nano-sources of heat," *Laser Photonics Rev.*, vol. 7, pp. 171–187, March 2013.
- [11] B. Paci, G. Kakavelakis, A. Generosi, J. Wright, C. Ferrero, E. Stratakis, and E. Kymakis, "Improving stability of organic devices: A time/space resolved structural monitoring approach applied to plasmonic photovoltaics," *Sol. Energy Mater. Sol. Cells*, vol. 159, pp. 617–624, January 2017.
- [12] Z. Fang, Y.-R. Zhen, O. Neumann, A. Polman, F. J. Garcia de Abajo, P. Nordlander, and N. J. Halas, "Evolution of light-induced vapor generation at a liquid-immersed metallic nanoparticle," *Nano Lett.*, vol. 13, pp. 1736–1742, March 2013.
- [13] P. Ghosh, G. Han, M. De, C. K. Kim, and V. M. Rotello, "Gold nanoparticles in delivery applications," *Adv. Drug Deliv. Rev.*, vol. 60, pp. 1307–1315, August 2008.
- [14] M. Zhu, G. Baffou, N. Meyerbröcker, and J. Polleux, "Micropatterning thermoplasmonic gold nanoarrays to manipulate cell adhesion," *ACS Nano*, vol. 6, pp. 7227–7233, July 2012.
- [15] X. Jin, J. He, and J. Ye, "Nanotriangle-based gap-enhanced Raman tags for bioimaging and photothermal therapy," *J. Appl. Phys.*, vol. 125, p. 073102, February 2019.
- [16] C. Kim, E. C. Cho, J. Chen, K. H. Song, L. Au, C. Favazza, Q. Zhang, C. M. Cobley, F. Gao, Y. Xia, and L. V. Wang, "In vivo molecular photoacoustic tomography of melanomas targeted by bioconjugated gold nanocages," *ACS Nano*, vol. 4, pp. 4559–4564, July 2010.
- [17] J. Kim, "Joining plasmonics with microfluidics: From convenience to inevitability," *Lab Chip*, vol. 12, pp. 3611–3623, August 2012.
- [18] G. K. Joshi, K. A. Smith, M. A. Johnson, and R. Sardar, "Temperature-controlled reversible localized surface plasmon resonance response of polymer-functionalized gold nanoprisms in the solid state," *J. Phys. Chem. C*, vol. 117, pp. 26228–26237, December 2013.
- [19] J. A. Jackman, A. R. Ferhan, B. K. Yoon, J. H. Park, V. P. Zhdanov, and N. J. Cho, "Indirect Nanoplasmonic Sensing Platform for Monitoring Temperature-Dependent Protein Adsorption," *Anal. Chem.*, vol. 89, pp. 12976–12983, November 2017.
- [20] G. Baffou, R. Quidant, and F. J. García De Abajo, "Nanoscale control of optical heating in complex plasmonic systems," *Proc. ACS Nano*, vol. 4, pp. 709–716, January 2010.
- [21] D. Meneses-Rodríguez, E. Ferreira-Vila, P. Prieto, J. Anguita, M. U. Gonzalez, J. M. Garcia-Martin, A. Cebollada, A. Garcia-Martin, and G. Armelles, "Probing the electromagnetic field distribution within a metallic nanodisk," *Small*, vol. 7, pp. 3317–3323, October 2011.
- [22] G. A. Sotiriou, A. M. Hirt, P. Y. Lozach, A. Teleki, F. Krumeich, and S. E. Pratsinis, "Hybrid, silica-coated, janus-like plasmonic-magnetic nanoparticles," *Chem. Mater.*, vol. 23, pp. 1985–1992, March 2011.
- [23] Y. Sato, S. Naya, and H. Tada, "Anewbimetallic plasmonic photocatalyst consisting of gold(core)-copper(shell) nanoparticle and titanium(IV) oxide support," *APL Mater.*, vol. 3, p. 104502, June 2015.
- [24] B. N. Khlebtsov, Z. Liu, J. Ye, and N. G. Khlebtsov, "Au@Ag core/shell cuboids and dumbbells: Optical properties and SERS response," *J. Quant. Spectrosc. Radiat. Transfer*, vol. 167, pp. 64–75, December 2015.
- [25] A. V. Korotun and V. V. Pogosov, "On the Calculation of Optical Characteristics and Dimensional Shifts of Surface Plasmons of Spherical Bimetallic Nanoparticles," *Phys. Sol. St.*, vol. 63, pp. 122–133, January 2021.

The spectral Q-factor of the metallic nanodiscs

Nazar Pavlyshche
Department of Micro- and
Nanoelectronics
National University "Zaporizhzhia
Politechnic"
Zaporizhzhia, Ukraine

Andrii Korotun
Department of Micro- and
Nanoelectronics
National University "Zaporizhzhia
Politechnic"
Zaporizhzhia, Ukraine
andko@zp.edu.ua

Vitalii Reva
Department of Micro- and
Nanoelectronics
National University "Zaporizhzhia
Politechnic"
Zaporizhzhia, Ukraine

Igor Titov
UAD Systems
Zaporizhzhia, Ukraine

Abstract—The size dependencies for the frequencies of the surface plasmonic resonance and for the components of the tensor of spectral Q-factor for the metallic nanodiscs with the small aspect ratio have been studied. An aspect ratio interval, in which the simultaneous excitation of two surface plasmonic resonances takes place, has been established. The practical recommendations as for the choice of the sizes and the material of the sensory elements of the sensor and the type of the dielectric environment have been given.

Keywords— spectral Q-factor, nanodisc, aspect ratio, surface plasmonic resonance, relaxation rate

I. INTRODUCTION

The achievements in the field of plasmonics and the technology of the nanostructure forming let the researches start developing the optical sensors on the surface plasmonic resonance [1].

The phenomenon of the surface plasmonic resonance (SPR) is associated with the existence of the surface electromagnetic waves at the metal-dielectric interface, which decay exponentially as one moves away in both directions from the interface. In addition, the wavevector depends both on the dielectric permittivity of metal and on the environment. The production of the effective sensors, which register the changes in the surface layer of metal, is based on this phenomenon. In recent times, one pays a great attention to the study of SPR in the metallic nanoparticles, the size of which is less than or comparable to the penetration depth of the electromagnetic wave into metal [2]. The principle of this phenomenon is the resonance between the internal collective oscillations of electrons in metal with the oscillations which are stimulated by the propagating electromagnetic wave.

Hence, the study of SPR in the metallic nanostructures is of fundamental interest because its position, shape and intensity can be controlled in the wide spectral range by means of the variation of the size, the shape and the content of the nanoparticle [3–5] or by means of the variation of the environment.

The possibility to measure the optical effects, using the changing of the refractive index, is frequently used for the determination of the chemical sensibility and under the studying of the dynamics of the biological molecules [6–8].

In order to make full use of the unique properties of the plasmonic materials in the practical applications, the detailed knowledge of the plasmonic modes is required. The optical properties of the plasmons in the nanodiscs have own features. Thus, the volumetric attenuation in the nanodiscs plays more significant role in comparison with the nanorods [9]. As a result, the spectral widths of the individual modes become big and the overlaps between the plasmonic resonances are observed [10,11]. The study of the nanodiscs for the sensor applications has been performed in the work [12], the device based on the array of the nanodiscs, operating as the plasmonic sensor in the near infrared range, has been experimentally demonstrated in [13].

In this context, the study of the physical and technical characteristics of the sensors on the surface plasmonic resonance, based on the metallic nanodiscs, is actual.

II. THE BASIC RELATIONS

Let us consider the metallic nanodisc with the diameter D and the height H ($H \ll D$), which is situated in the medium with the dielectric permittivity ϵ_m (Fig. 1).

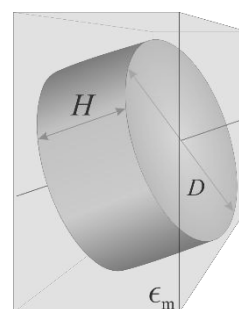


Fig. 1. The geometry of the problem

The most widely used characteristics of the performance of the plasmonic sensors is the ability to detect the changes of the refractive index \bar{n} . This characteristic can be determined quantitatively as the volumetric sensibility:

$$S_\lambda = \frac{\partial \lambda_{sp}}{\partial \bar{n}}, \quad (1)$$

or in frequency units

$$S_{\omega} = \frac{\partial \omega_{sp}}{\partial \bar{n}}, \quad (2) \quad \text{where } \gamma_{\text{bulk}} \text{ — the relaxation rate of electrons in 3D-metal, and}$$

where λ_{sp} (ω_{sp}) — the wavelength (frequency) of the surface plasmonic resonance.

Taking into account $\bar{n}^2 = \tau_m$, one can rewrite the expression (2) as

$$S_{\omega} = 2\sqrt{\tau_m} \frac{\partial \omega_{sp}}{\partial \tau_m}, \quad (3)$$

Hence, the sensibility depends essentially on the frequency of SPR, on the geometry of the excitation and on the properties of the substrate.

The plasmonic excitation can break apart due to the various attenuation mechanisms [3–5], which is responsible for the natural width of the resonance line γ_{eff} (the total width on the half of the maximum). The parameter γ_{eff} is considered to be the main parameter in such applications as the sensors [14,15], surface enhanced Raman scattering (SERS) [16], the concentration of the field by 1D-structures [17], plasmonic nanolithography [18], nanooptics [19], etc.

The ability of the plasmonic sensor to measure the small changes of the refractive index is directly proportional to the sensibility S_{ω} and inversely proportional to the width of the observed resonance characteristics. The combination of these parameters gives such characteristics as spectral Q-factor or the figure of merit (figure of merit – FOM):

$$\text{FOM} = \frac{S_{\omega}}{\gamma_{\text{eff}}}. \quad (4)$$

As long as the directions of the polarization vectors and the external electric field do not coincide, the spectral Q-factor of the nanodiscs is the diagonal second-rank tensor.

$$\text{FOM} = \begin{pmatrix} \text{FOM}_{\perp} & 0 & 0 \\ 0 & \text{FOM}_{\perp} & 0 \\ 0 & 0 & \text{FOM}_{\square} \end{pmatrix}, \quad (5)$$

the elements of which

$$\text{FOM}_{\perp(l)} = \frac{2\sqrt{\tau_m} \partial \omega_{sp}^{\perp(l)}}{\gamma_{\text{eff}}^{\perp(l)} \partial \tau_m}. \quad (6)$$

Here $\gamma_{\text{eff}}^{\perp(l)}$ — the effective relaxation rates of electrons under their transverse (longitudinal) movement, which are determined by the relations [20]

$$\gamma_{\text{eff}}^{\perp} = \gamma_{\text{bulk}}; \quad \gamma_{\text{eff}}^{\square} = \gamma_{\text{bulk}} + \frac{\mathcal{K}_{\square}}{\omega^2}, \quad (7)$$

$$\mathcal{K}_{\square} = \frac{1}{2} \omega_p^2 \frac{v_F}{H} \left(\frac{H}{D} \right)^{-1} \left\{ \frac{9}{4} \left(1 + (\tau_m - 2) \frac{\pi H}{2 D} \right) + \frac{V}{2\sqrt{\tau_m^{\infty} \tau_m}} \left(\frac{\omega_p}{c} \right)^3 \left(1 + \left(\frac{\tau_m}{2\tau_m^{\infty}} - 1 \right) \frac{\pi H}{2 D} \right) \right\}. \quad (8)$$

Here V – the volume of the nanodisc; c – light velocity; v_F – Fermi electron velocity; τ^{∞} – the contribution of ion core into the dielectric function of metal; $\omega_p = \sqrt{e^2 n_e / \tau_0 m^*}$ – the frequency of bulk plasmons, e , n_e and m^* – the charge, the concentration and the effective mass of electron ($n_e^{-1} = 4\pi r_s^3 / 3$, r_s – the mean distance between the conduction electrons).

The frequencies of the transverse and longitudinal surface plasmons are determined by the expressions [20]

$$\omega_{sp}^{\perp} \left(\frac{H}{D} \right) = \sqrt{\frac{\omega_p^2 \frac{\pi H}{4 D}}{\left(1 - \frac{\pi H}{4 D} \right) \tau_m + \frac{\pi H}{4 D} \tau^{\infty}} - \gamma_{\text{bulk}}^2}; \quad (9)$$

$$\omega_{sp}^{\square} \left(\frac{H}{D} \right) = \sqrt{\frac{\omega_p^2 \left(1 - \frac{\pi H}{2 D} \right)}{\frac{\pi H}{2 D} \tau_m + \left(1 - \frac{\pi H}{2 D} \right) \tau^{\infty}} - \gamma_{\text{bulk}}^2} \times \left[1 - \frac{\gamma_{\text{bulk}} \mathcal{K}_{\square}}{\left(\frac{\omega_p^2 \left(1 - \frac{\pi H}{2 D} \right)}{\frac{\pi H}{2 D} \tau_m + \left(1 - \frac{\pi H}{2 D} \right) \tau^{\infty}} - \gamma_{\text{bulk}}^2} \right)^2} \right]. \quad (10)$$

By this means, using (9), one obtains for the transverse component of spectral Q-factor of the nanodisc

$$\text{FOM}_{\perp} = \frac{\pi}{4\tau_m^{3/2}} \frac{\omega_p^2}{\gamma_{\text{bulk}}} \frac{H}{D} \left\{ \frac{\pi H}{4 D} \frac{\omega_p^2}{\tau_m} - \gamma_{\text{bulk}}^2 \right\}^{-1/2}. \quad (11)$$

One obtains for the longitudinal component of Q-factor

$$\text{FOM}_{\square} = \frac{2\sqrt{\tau_m} \partial \omega_{sp}^{\square}}{\gamma_{\text{bulk}} + \frac{\mathcal{K}_{\square}}{(\omega_{sp}^{\square})^2}}, \quad (12)$$

where

$$\frac{\partial \omega_{sp}^{\square}}{\partial \tau_m} = \left(1 + \frac{3\gamma_{\text{bulk}} \mathcal{K}_{\square}}{\left(\omega_{sp}^{\square(0)}\right)^4} \right) \frac{\partial \omega_{sp}^{\square(0)}}{\partial \tau_m} + \frac{\gamma_{\text{bulk}}}{\left(\omega_{sp}^{\square(0)}\right)^3} \frac{\partial \mathcal{K}_{\square}}{\partial \tau_m}. \quad (13)$$

In the formulas (12) and (13), \mathcal{K}_{\square} and ω_{sp}^{\square} are determined by the expressions (8) and (10), while

$$\omega_{sp}^{\square(0)} = \sqrt{\frac{\omega_p^2 \frac{\pi H}{4 D}}{\left(1 - \frac{\pi H}{4 D}\right) \frac{H}{D} \tau_m + \frac{\pi H}{4 D} \tau_m^{\infty}} - \gamma_{\text{bulk}}^2}; \quad (14)$$

$$\frac{\partial \omega_{sp}^{\square(0)}}{\partial \tau_m} = - \frac{\frac{\omega_p^2 \pi H}{\tau_m^{\infty 2} 2 D}}{2 \sqrt{\frac{\omega_p^2}{\tau_m^{\infty 2}} \left(1 - \frac{\pi H}{2 D} \tau_m\right) - \gamma_{\text{bulk}}^2}}; \quad (15)$$

$$\frac{\partial \mathcal{K}_{\square}}{\partial \tau_m} = \frac{1}{8} \omega_p^2 \frac{v_F}{H} \left(\frac{H}{D}\right)^{-1} \left\{ \frac{9\pi H}{2 D} + \frac{V}{2\tau_m^{\infty 1/2} \tau_m^{3/2}} \left(\frac{\omega_p}{c}\right)^3 \left(\frac{\pi H}{2 D} - 1\right) \right\}. \quad (16)$$

Thereafter, the relations (9) – (12) are used for the study of the size dependencies for the frequencies of the transverse and longitudinal surface plasmonic resonances and the components of the spectral Q-factor tensor.

III. THE RESULTS OF THE CALCULATIONS AND THE DISCUSSION

The calculations of the frequency and size dependencies for Q-factor have been performed for the nanodiscs of different metals, which are situated in teflon ($\tau_m = 2.3$). The parameters of metals are given in Table 1.

TABLE I. PARAMETERS OF METALS [20]

Value	Metals			
	Al	Cu	Au	Ag
r_s / a_0	2.07	2.11	3.01	3.02
m^* / m_e	1.06	1.49	0.99	0.96
τ_m^{∞}	0.7	12.03	9.84	3.70
$\gamma_{\text{bulk}}, 10^{14} \text{ s}^{-1}$	1.25	0.37	0.35	0.25

Figure 2 shows the size dependencies for the frequencies of the transverse and longitudinal surface plasmonic resonance in the nanodiscs of different metals. It should be pointed out that the frequency of the transverse SPR increases with the increase of the aspect ratio H/D according to the root law (Fig. 2, *a*), and the location of the curves is determined by such parameters of metal as the

frequency of bulk plasmons and the contribution of the ion subsystem into the dielectric function.

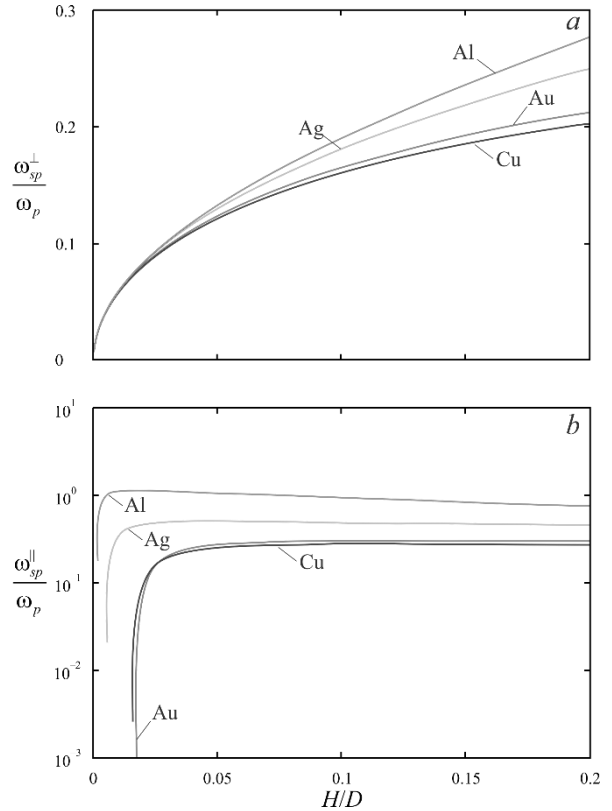


Fig. 1. The size dependencies for the transverse (*a*) and longitudinal (*b*) frequencies of SPR for the nanodiscs of different metals.

The frequency of the longitudinal SPR, in turn, increases essentially under small H/D , reaching the saturation (Fig. 2, *b*), which indicates the strong size dependence ω_{sp}^{\square} under $H/D \leq 0.02$. This fact results from the manifestation of the classical size effects in the metallic nanodiscs with the small thickness.

It should be pointed out that the interval of the aspect ratios, at which the excitation of the transverse and longitudinal SPR is possible, can be obtained from the nonnegativity constraint for the radical expressions in the formulas (9) and (10). The minimum and maximum values H/D , taking into account that $\tau_m, \tau_m^{\infty} \ll \omega_p^2 / \gamma_{\text{bulk}}^2$, are determined by the expressions

$$\left(\frac{H}{D}\right)_{\perp}^* = \frac{4\tau_m \gamma_{\text{bulk}}^2}{\pi \omega_p^2}; \quad (17)$$

$$\left(\frac{H}{D}\right)_{\square}^* = \frac{2}{\pi} \left(1 - \frac{\tau_m \gamma_{\text{bulk}}^2}{\omega_p^2}\right). \quad (18)$$

Hence, the transverse and longitudinal SPR are excited simultaneously only in the interval of the aspect ratios

$$\left(\frac{H}{D}\right)_{\perp}^* \leq \frac{H}{D} \leq \left(\frac{H}{D}\right)_{\square}^*. \quad (19)$$

For example, for Au $(H/D)_{\perp}^* = 1.8 \cdot 10^{-5}$, while $(H/D)_{\parallel}^* = 0.64$. Since this work deals with the case of the nanodiscs with small aspect ratio ($H/D \ll 1$), then it is clear that one should consider the transverse and longitudinal SPR which are excited simultaneously.

Figure 3 shows the size dependencies for the longitudinal component of spectral Q-factor. This value reaches its minimum under the aspect ratios $H/D \leq 0.02$, and it increases with the increase of H/D . This fact indicates that, in practice, it is reasonable to use the sensors with the sensory element in the form of the nanodisc made of aluminum with the aspect ratio $H/D \approx 0.2$, since spectral Q-factor for such sensory elements is the greatest.

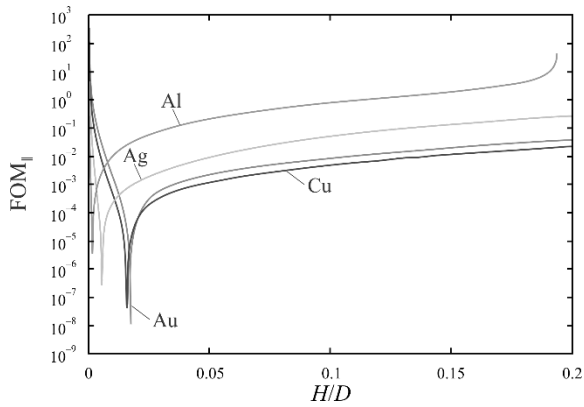


Fig. 2. The size dependence for the longitudinal component of spectral Q-factor for the nanodiscs of different metals.

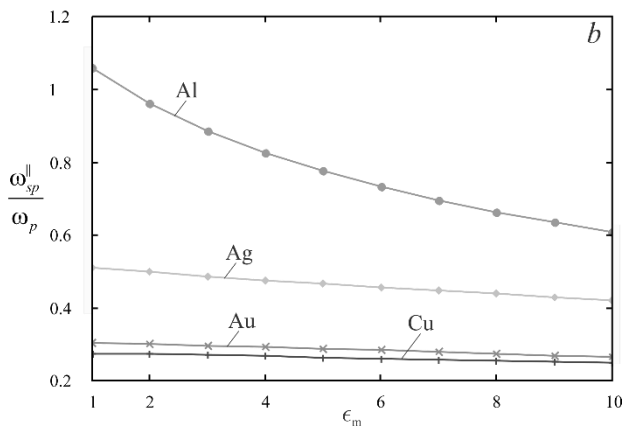
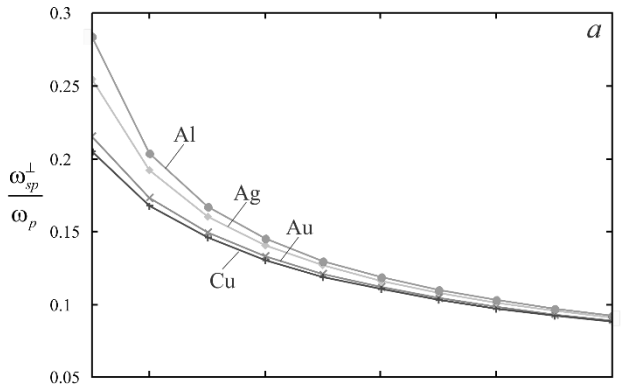


Fig. 3. The dependence of the longitudinal (a) and transverse (b) SPR on the dielectric permittivity of the environment for the nanodiscs of different metals.

Figures 4 and 5 show the dependence of the frequencies of the transverse and longitudinal SPR and the corresponding FOM for the nanodiscs of different metals on the dielectric permittivity of the environment. Moreover, if both frequencies of SPR decrease under the increase τ_m (Fig. 4), then FOM_{\perp} and FOM_{\parallel} behave differently. Thus, $FOM_{\parallel}(\tau_m)$ increases with the increase τ_m (Fig. 5, a), while $FOM_{\perp}(\tau_m)$, on contrary, decreases (Fig. 5, b), and most of all in the interval $1 \leq \tau_m \leq 4$.

Since the value FOM_{\perp} increase with the decrease of τ_m , the optimal dielectric environment for the sensory element of the sensor is air with $\tau_m = 1$.

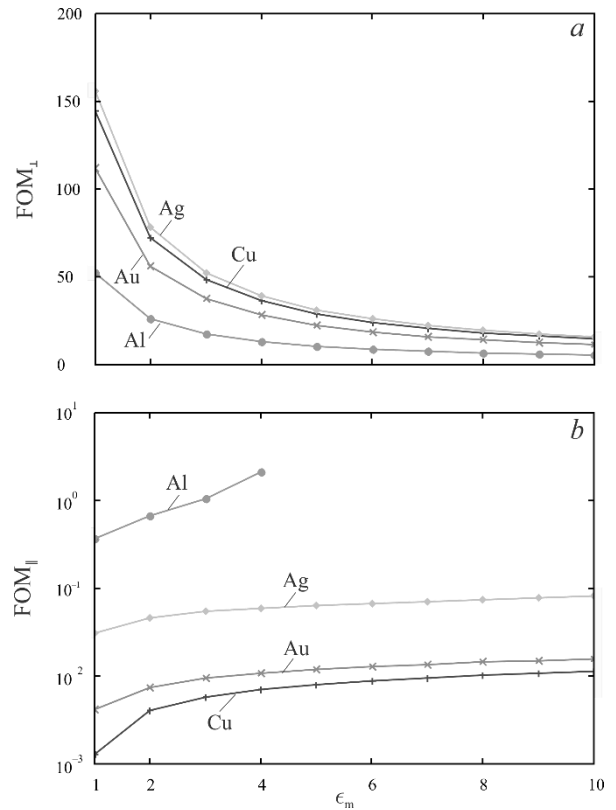


Fig. 4. The dependence of the longitudinal (a) and transverse (b) components of the spectral Q-factor tensor on the dielectric permittivity of the environment for the nanodiscs of different metals.

IV. CONCLUSIONS

The size dependencies for the frequencies of the transverse and longitudinal SPR and for the components of the spectral Q-factor tensor for the metallic nanodiscs with small aspect ratio have been obtained. An interval of the aspect ratios, in which the longitudinal and transverse SPR are excited simultaneously, has been determined.

It has been established that the essential increase of the frequency of the longitudinal SPR, in the case when the height of the disc is less than 2% of its diameter, is the manifestation of the classical size effect in the metallic nanodiscs with the thickness, which is small in comparison with the diameter.

The calculations of the longitudinal component of spectral Q-factor indicate that the use of the nanodiscs of

aluminum, the height of which is 20 % of its diameter, as the sensory elements of the sensors is optimal.

It has been shown that air is preferred as the environment of the sensory element, because, in this case (all other things being equal), the values of spectral Q-factor are the greatest.

REFERENCES

- [1] L. C. Oliveira, A. M. N. Lima, C. Thirstrup, H. F. Neff, *Surface Plasmon Resonance Sensors: A Materials Guide to Design, Characterization, Optimization, and Usage* (Springer Series in Surface Sciences, 70), 2019.
- [2] S. A. Maier, *Plasmonics: Fundamentals and Applications*. New York, Springer, 2007.
- [3] C. F. Bohren and D. R. Huffman, *Absorption and Scattering of Light by Small Particles*. Moscow: Mir, 1986.
- [4] U. Kreibig and M. Vollmer, *Optical Properties of Metal Clusters*. Berlin: Springer-Verlag, 1995.
- [5] H.C. Van De Hulst, *Light Scattering by Small Particles*. New York: Dover Publication, 2000.
- [6] A. J. Haes, S. Zou, G. C. Schatz, and R. P. Van Duyne, "A nanoscale optical biosensor: The long range distance dependence of the localized surface plasmon resonance of noble metal nanoparticles," *J. Phys. Chem. B*, vol. 108, pp. 109-116, September 2003.
- [7] J. Becker, A. Trügler, A. Jakab, U. Hohenester, and C. Sönnichsen, "The optimal aspect ratio of gold nanorods for plasmonic biosensing," *Plasmonics*, vol. 5, pp. 161-167, March 2010.
- [8] K. M. Mayer, J. H. Hafner, "Localized surface plasmon resonance sensors," *Chem. Rev.*, vol. 111, pp. 3828-3857, June 2011.
- [9] C. Sönnichsen, T. Franzl, T. Wilk, G. von Plessen, J. Feldmann, O. Wilson, and P. Mulvaney, "Drastic reduction of plasmon damping in gold nanorods," *Phys. Rev. Lett.* vol. 88, p. 077402, January 2002.
- [10] P. Hanarp, M. Käll, and D. S. Sutherland, "Optical properties of short range ordered arrays of nanometer gold disks prepared by colloidal lithography," *J. Phys. Chem. B*, vol. 107, pp. 5768-5772, May 2003.
- [11] C. Langhammer, B. Kasemo, and I. Zorić, "Absorption and scattering of light by Pt, Pd, Ag, and Au nanodisks: Absolute cross sections and branching ratios," *J. Chem. Phys.* Vol. 126, p. 194702, March 2007.
- [12] A. Abumazwed and A. G. Kirk, "Plasmonic properties of suspended nanodisc structures for enhancement of the electric field distributions," *Proc. of SPIE*, vol. 9288, p. 92880Z, September 2014.
- [13] N. Liu, M. Mesch, T. Weiss, M. Hentschel, and H. Giessen, "Infrared Perfect Absorber and Its Application As Plasmonic Sensor," *Nano Lett.*, vol. 10, pp. 2342-2348, June 2010.
- [14] K. A. Willets and R. P. Van Duyne, "Localized surface plasmon resonance spectroscopy and sensing," *Annu. Rev. Phys. Chem.*, vol. 58, pp. 267-297, May 2007.
- [15] C.-D. Chen, S.-F. Cheng, L.-K. Chau, and C.R.C. Wang, "Sensing capability of the localized surface plasmon resonance of gold nanorods," *Biosensors and Bioelectronics*, vol. 22, pp. 926-932, January 2007.
- [16] S. Nie, and S.R. Emory, "Probing single molecules and single nanoparticles by surface-enhanced Raman scattering," *Science*, vol. 275, pp. 1102-1106, February 1997.
- [17] D. Li, and Y. Xia, "Welding and patterning in a flash," *Nature materials*, vol. 3, pp. 753-754, November 2004.
- [18] W. Srituravanich, N. Fang, C. Sun, Q. Luo, and X. Zhang, "Plasmonic nanolithography," *Nano Lett.*, vol. 4, pp. 1085-1088, May 2004.
- [19] S. Lal, S. Link, and N. J. Halas, "Nano-optics from sensing to waveguiding," *Nature Phot.*, vol. 1, pp. 641-648, November 2007.
- [20] A. V. Korotun and N. I. Pavlyshche, "Cross-sections of Absorption and Scattering of Electromagnetic Radiation by Ensembles of Metal Nanoparticles of Different Shapes," *Phys. Met. Metallogr.*, in press.

Effect of Zinc on CdS QD surface modification

V.M. Skobeeva
Research Institute of Physics
Odessa I.I.Mechnikov National
University
Odesa, Ukraine
v_skobeeva@ukr.net

V.A. Smyntyna
Odessa I.I.Mechnikov National
University)
Odesa, Ukraine
smyntyna@onu.edu.ua

M. I.Kiose
Odessa I.I.Mechnikov National
University
Odesa, Ukraine
mihail20032015@gmail.com

N.V. Malushin
Research Institute of Physics
Odessa I.I.Mechnikov National
University
Odesa, Ukraine
malushinnv@gmail.com

Abstract - *The paper presents the results effect zinc on the cadmium sulfide quantum dots surface modification. A non-monotonic dependence of the luminescence intensity on zinc salt concentration, which was introduced into the solution with grown quantum dots has been established. It is shown that the increasing in the luminescence intensity occurs with the growth of a thin zinc sulfide shell, at which the mismatch of their lattice constants is leveled.*

Keywords - *CdS quantum dots, ZnS shell, luminescence, absorption spectra.*

I. INTRODUCTION

Quantum dots (QDs) or nanocrystals (NCs) of A_2B_6 compounds are promising for practical using in electronics as light-emitting devices and diode lasers [1], as well as in medicine for biological fluorescent labeling [2,3]. In these areas, the efficiency of QDs luminescence is the main characteristic that determines the success of the creation of light-emitting and immunosensor devices based on them. Despite the fact that semiconductor NCs have shown great promise as a new class of fluorophores in biological imaging, the intensity of their luminescence is often insufficient or degrades over time. This is due to the fact that in NCs, the surface plays a decisive role in comparison with the volume. As a result of uncompensated torn valence bonds are formed the without radiative centers of recombination and trapping centers of carries on the NCs surface.

In addition, due to the absence or insufficient height of the potential barrier between the QD and the external water-soluble environment, a leak of excitons from the bulk can be observed, which also reduce the luminescence efficiency.

Thus, the issues of synthesizing semiconductor NCs with a high quantum yield and increasing the efficiency of their luminescence are urgent. In literature are described numerous ways to solve this problem, the purpose of which is to search for both ways of surface passivation by processing it and the development of methods for covering the surface with a shell with a band gap more than have NCs [4-7].

To observe luminescence in the visible region of the spectrum, semiconductor materials such as sulfides and selenides of the metals cadmium and zinc are used. For NCs cadmium sulfide and selenide, the most suitable shell is the semiconductor ZnS, which have the band gap $E_g = 3.7$ eV, which is more than, for example, CdS ($E_g = 2.4$ eV). In addition, the using of zinc sulfide can contribute the more stability and lower toxicity of CdS (Se) NCs .

In [5, 9], besides of the observation strengthen the fluorescence CdSe / CdS nanostructures in the form of core – shell, is the strong dependence of the optical density and luminescence on surface modification was noted. This may depend on the environment in which the synthesis of colloidal nanomaterials is carried out, on organic and biological environment that surround and interact with the nanostructures. The latter means that the properties of colloidal heterogeneous structures will depend on the specific methods of their preparation, namely, on the type and chemical composition of the stabilizer of the NC size, the stoichiometry of the surface, the nature of the interaction of the stabilizer with the surface, depending on the pH of the environment, etc.

The zinc influence on the luminescence of CdS NCs was studied in works in which zinc salts were added during the synthesis NCs. The results obtained indicated the formation of a solid solution [9], as well as doping of cadmium sulfide with zinc [10]. The authors didn't observe the formation of a shell in this technology.

Thus, the study of physicochemical and technological methods aimed at increasing the quantum efficiency of CdS NC are little studied and has of scientific and practical interest.

This paper presents a study of zinc influence on the optical and luminescent properties CdS NCs. This process was carried out by introducing a zinc salt into gelatinous solution with grown nanocrystals. In this case, the growth of the ZnS shell on the CdS surface can be expected.

II. MATERIALS AND METHODS

Cadmium nitrate $Cd(NO_3)_2$ and sodium sulfide Na_2S were used as precursors in the synthesis of NC CdS. An

aqueous solution of gelatin was used to stabilize the size of the NC.

To measure the optical density spectra, SF-26 spectrophotometer with a spectral range from 186 to 1100 nm was used. The luminescence spectra were measured using an LCS-DTL-374QT solid-state laser with pumping, semiconductor diodes operating in the optoacoustic modulation mode.

A. Synthesis of QDs and Nanocomposites

In aqueous solution of gelatin (5%), was added 2.5 ml. of aqueous solution of Cd (NO₃)₂ (0.25 mol / L), followed by stirring for 10 min., after which, was added 2.5 ml. of aqueous solution of Na₂S (0.25 mol \ L). The synthesis reaction took place within 20 minutes at the temperature of 40°C with continuous stirring. As the reaction proceeded, the color of the solution changed from clear to orange.

Without interrupting the process, (1.5; 2.5; 3.5; 5; 7.5) ml. of aqueous solution of ZnCl₂ (0.25 mol / L) and 2.5 ml. aqueous solution of Na₂S (0.25 mol / L) were added to the colloidal solution of gelatin containing CdS nanoparticles. While stirring the solution for 10 minutes, the color of the solution changed from orange to light yellow.

III. RESULTS AND ITS DISCUSSION

A. Optical and luminescent properties of the core-shell structure of CdS / ZnS.

Analysis of the luminescence spectra revealed the following regularities. The luminescence spectrum of freshly grown CdS QDs contains a broad luminescence band with a maximum at $\lambda_{max} = 630$ nm. The intensity of this band changed upon the addition of zinc chloride to the solution. It was found that at a low concentration, the luminescence intensity of the obtained nanostructure increases, and at a higher ZnCl₂ concentration, the luminescence intensity decreases (Fig. 1). The increase in the luminescence CdS intensity whiskers can be explained by the formation of a zinc sulfide shell, which is confirmed by the data of the absorption spectra plotted in the coordinates: optical density $(D \cdot hv)^2 = f(hv)$ (Fig. 2). Extrapolation of the rectilinear part of the absorption curve to the abscissa axis gives the value of the band gap of the CdS NCs. The average size of the NCs is determined by the formula (1)

$$R = \frac{h}{\sqrt{8\mu\Delta E_g}} \quad (1)$$

where h - Planck's constant $\mu = ((m_e^*)^{-1} + (m_h^*)^{-1})^{-1}$, where $m_e^* = 0.19m_e$, $m_h^* = 0.8m_e$ - respectively, the effective masses of electron and a hole in cadmium sulfide, m_e - free electron mass; ΔE_g is the difference between the band gap in nanoparticle and a bulk CdS crystal (2.4 eV). The calculated values are summarized in Table 1.

TABLE I. CALCULATED VALUES OF THE WIDTH OF THE FORBIDDEN AREA AND THE AVERAGE RADIUS OF THE STUDIED SAMPLES.

Testsamples	E _g , eV	r, nm
CdS(freshlygrown)	2.75	2.6
CdS+ZnCl ₂ (1,5 ml.)	2.75	2.6
CdS+ZnCl ₂ (2,5 ml.)	2.75	2.6
CdS+ZnCl ₂ (3,5 ml.)	2.68	2.94
CdS+ZnCl ₂ (5,0 ml)	2.66	3.2

It could be seen that at low values of ZnCl₂ concentrations, the band gap and radius of CdS don't

change, which may indicate a small shell thickness, on the order of ZnS monolayer, and this value is within the experimental error. With a further increase in the concentration of zinc salt, the size of the NC increases, that is, the growth of the next layers of the shell occurs. However, at these values, a decrease in the luminescence intensity of the nanostructure is observed.

The fact that the emission intensity of the CdS / ZnS QD nanostructure decreases with increasing shell thickness is explained by the appearance of defects at the interface as a result of the mismatch between the lattice constants of CdS and ZnS.

In order to exclude the influence of ZnS NCs, which could form in the bulk of the solution, they were synthesized using a technology similar to the synthesis of CdS NCs. Figure 1 shows the emission spectrum of ZnS NCs. It is seen that a low-intensity zinc sulfide impurity band with a maximum $\lambda = 470$ nm is excited, which can't affect the luminescence intensity of nanostructures with shell. This is confirmed by the fact that, in the investigated wavelength range, no absorption bands of zinc sulfide were found in the absorption spectrum of CdS / ZnS nanostructures (Fig. 2).

Based on the above facts, it follows that ZnS nanoparticles that could be formed during the synthesis don't affect the luminescence spectra of CdS / ZnS nanostructures.

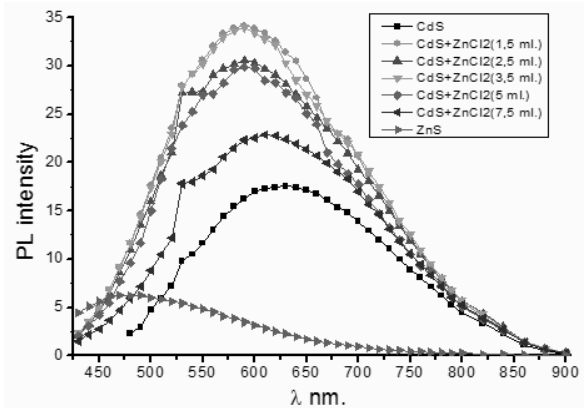


Fig. 1. Photoluminescence spectra of CdS, ZnS QDs and CdS / ZnS nanostructures.

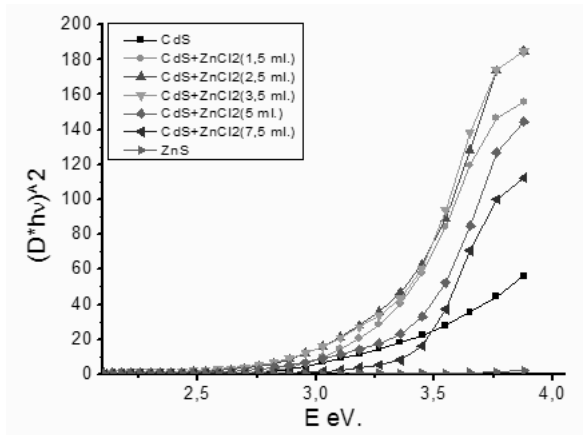


Fig. 2. Absorption spectra of CdS, ZnS QDs and CdS / ZnS nanostructures.

CONCLUSION

It is shown that the introduction of a zinc salt into a solution with grown CdS NCs increases the luminescence intensity due to the formation of a thin ZnS shell. With an increase in the shell thickness, the emission intensity of the CdS / ZnS nanostructure decreases due to the formation of defects caused by the mismatch between the lattice constants of CdS and ZnS. The results of optical and luminescence studies of ZnS NCs grown using a technology similar to the synthesis of CdS NCs and under identical luminescence excitation conditions showed that there is no possible effect of ZnS NCs on the luminescence of CdS / ZnS nanostructures. The studied CdS / ZnS nanostructures obtained in the one-stage process can be promising for use in biomedicine.

REFERENCES

- [1] AL Rogach, N Gaponik, JM Lupton, C Bertoni, DE Gallardo, S Dunn, ... Alexander Eychmüller. Light-Emitting Diodes with Semiconductor Nanocrystals. *Angewandte Chemie International Edition* 47 (35), 6538-6549. DOI: 10.1002/anie.200705109
- [2] Jonathan S. Steckel, John P. Zimmer, Seth Coe-Sullivan, Nathan E. Stott, Vladimir Bulovic', and Mounqi G. Bawendi. Blue Luminescence from (CdS)ZnS Core-Shell Nanocrystals. *Angew. Chem. Int. Ed.* 2004, 43, 2154–2158. DOI: 10.1002/anie.200453728
- [3] Quantum dot bioconjugates for imaging, labelling and sensing Medintz, I.L., Uyeda, H.T., Goldman, E.R. & Mattoussi, H. Quantum dot bioconjugates for imaging, labelling and sensing *Nature Materials* 2005 4(6):435-446. DOI: 10.1038/nmat1390
- [4] Fábio Pereira Ramanery, Alexandra Ancelmo Piscitelli Mansur, Herman Sander Mansur* Synthesis and Characterization of Water-dispersed CdSe/CdS Core-shell Quantum Dots Prepared via Layer-by-layer Method Capped with Carboxylic-functionalized Poly(Vinyl Alcohol). *Materials Research*. 2014; 17(Suppl. 1): 133-140 DOI: D <http://dx.doi.org/10.1590/S1516-14392014005000060>
- [5] Adolfas K. Gaigalas, Paul DeRose, Lili Wang, and Yu-Zhong Zhang. Optical Properties of CdSe/ZnS Nanocrystals. *Journal of Research of the National Institute of Standards and Technology*. Volume 119 (2014). P. 609-628. <http://dx.doi.org/10.6028/jres.119.026>
- [6] Bonghwan Chon, Sung Jun Lim, Wonjung Kim, Jongcheol Seo, Hyeonggon Kang, Taiha Joo, Jeeseong Hwang and Seung Koo Shin. Shell and ligand-dependent blinking of CdSe-based core/shell nanocrystals. *Phys. Chem. Chem. Phys.*, 2010, 12, 9312-9319 DOI: 10.1039/b924917f
- [7] Synthesis and Characterization of Zinc-Blende CdSe-Based Core/Shell Nanocrystals and Their Luminescence in Water. *J. Phys. Chem. C*, Vol. 112, No. 6, 2008 Sung Jun Lim, Bonghwan Chon, Taiha Joo, and Seung Koo Shin* 2008, 112, 1744-1747 10.1021/jp710648g CCC: \$40.75
- [8] Dmitri V. Talapin, Andrey L. Rogach, Andreas Kornowski, Markus Haase, and Horst Weller Oxide-Trioctylphosphine Mixture Highly Luminescent Monodisperse CdSe and CdSe/ZnS Nanocrystals Synthesized in a Hexadecylamine-Trioctylphosphine. *Nano Letters* 2001, 1, 4, 207–211. <https://doi.org/10.1021/nl0155126>
- [9] Yu.A. Nitsuk, M.I. Kiose, Yu.F. Vaksman, V.A. Smyntyn, I.R. Yatsunsky. Optical properties of CdS nanocrystals doped with zinc and copper. *Physics and technology of semiconductors*, 2019, volume 53, no. 3.
- [10] D.V. Korbutyak, S.V. Tokarev, S.I. Budzulyak, A.O. Couric, V.P. Kladko, Yu.O. Polishchuk, O.M. Shevchuk, G.A. Ilchuk, V.S. Tokarev. Optical and structurally defective characteristics of nanocrystals CdS: Cu and CdS: Zn synthesized in polymer matrices. *Solid State Physics and Chemistry* Vol. 14, №1 (2013) p. 222-227

Electrodynamic fundamentals of designing a highly localized resonator probe with adjustable sensitivity for microwave diagnostics of nanoelectronic objects

Yu.Ye. Gordienko
Kharkiv National University of Radio
Electronics
Kharkiv, Ukraine

I.M. Shcherban
Kharkiv National University of Radio
Electronics
Kharkiv, Ukraine
ihor.shcherban@nure.ua

Abstract — The report discusses the prospects for expanding the sensitivity range of microwave diagnostics of small objects using resonator aperture sensors. To change the degree of inclusion of the object in the electromagnetic field of the aperture coaxial resonator sensor in order to expand the range of values ϵ and $\text{tg}\delta$ controlled by it, it is proposed to change the position of the probe tip relative to the edge of the waveguide plane.

A new functional diagram of measurements was used. Instead of modulating the frequency of the master microwave generator, the resonator sensor was modulated, which had a positive effect on the signal-to-noise ratio and the registration of rather small signals.

Quantitative data are presented that characterize the operation of a tunable sensor within each of the two considered modes of operation.

The invariance of the hybrid signal $(\Delta Q/Q) / (\Delta f/f)$ to the influence of interfering factors caused by changes in the geometry of the sensor aperture unit and the degree of inclusion of the object in the electromagnetic field of the resonator was obtained.

The possibility of theoretical calibration of a tunable sensor, similar to the previously proposed and studied resonator sensor with a classical coaxial aperture, has been substantiated.

Keywords — local microwave diagnostics, electrodynamic properties, resonator probe, tunable sensitivity, quarter-wave resonator near-field, evanescent electromagnetic field.

I. INTRODUCTION

Small-sized microwave diagnostics has been widely developed in many modern fields related to the study of the structure of materials, their electrophysical properties, crystallographic structure, and the presence of inhomogeneities. This is primarily the biomedical field, which has recently been closely related to nanoelectronics. Topical tasks in this area include studies of bone implants, nanocomposites, directed drug delivery devices, etc.

Diagnostic tools that allow solving such problems should not only provide high information content of the results obtained during the study of the internal structure of objects, but also be very universal. This is primarily determined by a fairly wide range of electrophysical parameters of objects, the study of which is quite promising in nanoelectronics. Such a toolkit in small-size microwave diagnostics can be represented by well-developed hardware tools for scanning microwave microscopy (SMM).

Special attention is paid to the development of aperture sensors based on the open end of a coaxial waveguide [1] in local microwave sensors and SMM, in view of achieving ultra-high locality with insignificant loss of sensitivity. It is advisable to optimize the metrological properties of such sensors separately for their resonator and waveguide versions. Resonator sensors have high sensitivity, while waveguide sensors have a wider range in terms of dielectric properties of controlled objects. Their common property is non-invasiveness due to the external location of the aperture region and the near-surface nature of interaction with the object under study. However, it should be noted that the classic quarter-wave cone-type resonator sensor, even due to the higher achievable sensitivity, cannot be called wide-range. As shown in a number of works [2, 3], the development of simultaneously highly local and highly sensitive microwave sensors, the problems are diametrically opposite, which are quite difficult to solve.

The report theoretically investigates the issue of expanding the high-sensitivity range of microwave diagnostics of small-sized objects using resonator aperture sensors due to the optimal location of the end of the inner conductor of the coaxial relative to the plane of the aperture.

II. MAIN PART

When considering this issue, we will proceed from the provisions of the theory of these sensors, which were developed for the SMM [1, 3]. First of all, we will focus on the selection of fundamental signals of measurement information (change in the resonant frequency $\Delta f/f$ and the Q-factor $\Delta Q/Q$ of the resonator) using the AFC system, as described in [4]. This approach will eliminate the influence of various interfering factors [5] and make the sensor theoretically calibrated regardless of the shape of the object and variations in the operating modes of the elements of the microwave path, including the microwave generator.

In order to reduce the effect of modulation in the AFC system on the noise level in both channels for separating signals $\Delta f/f$ and $\Delta Q/Q$, it is proposed to modulate the resonant frequency of the probe, in contrast to the previously used modulation of the operating frequency of the microwave generator. In this case, the functional diagram of the microwave sensor as a whole will have the form shown in Fig. 1.

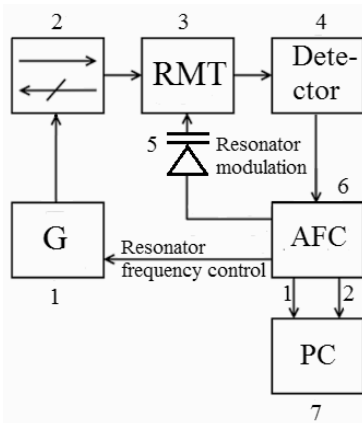


Fig. 1 - Functional diagram of the microwave sensor. 1 - microwave generator; 2 - ferrite valve; 3 - resonator measuring transducer; 4 - detector; 5 - variable capacitance; 6 - AFC; 7 - personal computer

Modulation of the resonant frequency of the probe (3) is performed here using a varicap (5) built into the probe and powered by a generator. Accordingly, a reference signal is supplied to the synchronous detector (4) from this generator through a phase shifter and an attenuator. In the figure, the modulation generator, phase shifter and attenuator are not shown separately, since they are part of the AFC system (6). The measuring signals $\Delta Q/Q$ and $\Delta f/f$ will be determined by the voltage level at the frequency F_m (for the $\Delta f/f$ signal) and at the frequency $2F_m$ (for the $\Delta Q/Q$ signal) taken from the outputs 1 and 2 of the AFC, respectively.

As shown in [1, 4], these levels will depend not only on the main informative signals $\Delta Q/Q$ and $\Delta f/f$, but also on the power of the microwave generator, the power of the modulation microwave generator, the parameters of the microwave detector, the parameters of the synchronous detector circuits, including the coefficient transmission of phase-shifting circuits.

To eliminate the influence of these circuits, the formation of signals on the final measurement result, we in [5] proposed the formation of results in the form of the so-called hybrid signals. Their magnitude will be uniquely determined only by the signals of the resonator probe $\Delta Q/Q$ and $\Delta f/f$. Therefore, further in this work, only a discussion of these signals is carried out depending on the structure and properties of the probe.

Based on previous developments, we will focus on the structure of the probe shown in Fig. 2.

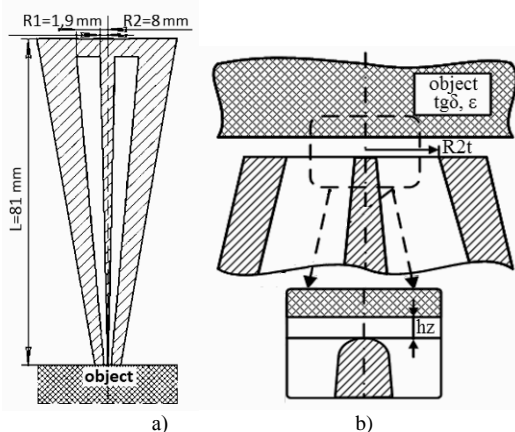


Fig. 2 - a) Schematic representation of a classic quarter-wave resonator sensor; b) schematic representation of the probe aperture assembly

Detailed theoretical and experimental studies of the electrodynamic properties of probes with a similar structure [1, 3] showed that the spatial resolution and contrast of the diagnosed properties of such probes are mutually related and determined by the geometry of the tip. Separate problems arise when studying objects with significant microwave losses, or vice versa, when registering very small manifestations of the contribution of the imaginary part of the dielectric constant [1, 3].

Let us consider the possibility of removing these problems by designing a probe with a movable variable design of the aperture-forming region. An idea of the properties of such a probe can be obtained by characterizing it at two extreme points of locality, for example, $5 \mu\text{m}$ and $50 \mu\text{m}$. To do this, you need to use a resonator measuring transducer (RMT), which is rebuilt according to the degree of interaction with the object. So far, there are no ideas about such a resonator in the literature, but the initial one can be a resonator probe (RP) based on the open end of the coaxial line, which is already quite often used in biophysical and biomedical research [2]. The design of such a RMT is shown schematically in Fig. 3.

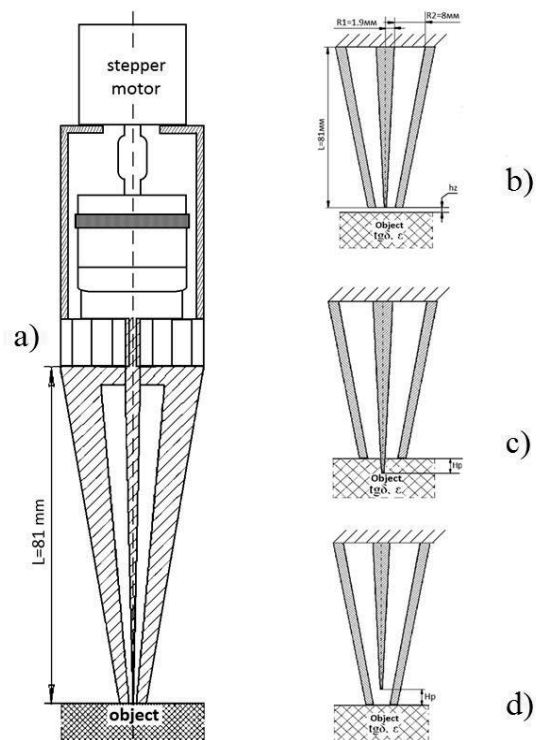


Fig. 3 - Schematic representation of a probe with a movable variable design of the aperture-forming region

As shown in Fig. 3a, it is proposed to move the tip using a system consisting of a micrometer head, a stepper motor, and a control system. This design of the sensor allows the probe tip to be positioned both coplanar with the end aperture and displaced inward or outward of the coaxial. To avoid breaking the microwave currents in the end part of the resonator, reliable contact between the resonator base and the tip is provided by means of spring-loaded brush contacts [6].

Obviously, variant 3d will be characterized by the weakest interaction of a quarter-wave resonator with an object located on the plane of the aperture. Option 2c will provide the strongest interaction with the object. Note that the location of the object with a gap relative to the original aperture in Fig. 3b weakens the interaction in all three options. These general physical concepts are illustrated in Fig. 4, which shows the results of a numerical study of the dependence of the Q-factor and resonance frequency of such a resonator probe for aperture geometry $R1t = 5$ and $50 \mu\text{m}$, $R2t = 0.6 \text{ mm}$ with a spherical tip and various parameters of the object under study in the region of 10 GHz. The numerical data of all figures in the work were obtained by solving the system of Maxwell's equations by the finite element method [7].

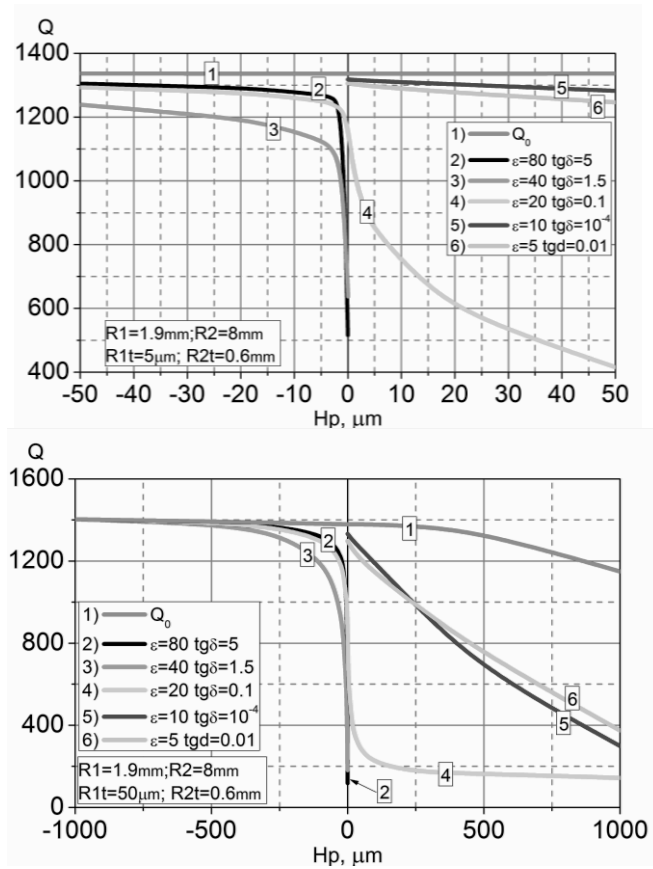


Fig. 4 - Q-factor of the RMT with axial displacement of the tip depending on the value of Hp

Shown here are the dependences of the indicated values on the axial position of the tip, characterized by its distance Hp from the point of the classical coaxial aperture. The region with negative values of Hp along the abscissa corresponds to the immersion of the tip into the aperture. The area with positive Hp values corresponds to the protrusion of the tip into the object. From the data in Fig. 4, we can draw a conclusion about the effective operating range of our resonator, depending on the properties of the objects under study. Thus, we see that it is unreasonable to immerse the tip into the aperture by $Hp > 100 \mu\text{m}$, because in this area, the RMT sensitivity is significantly reduced. In turn, the sensitivity when the tip extends into the object is limited by a decrease in the Q factor below the resonance

threshold at $Hp > 1 \text{ mm}$. When extending the tip into the object, the dimensions of the object model were selected so that the Sommerfeld condition was satisfied [7].

On the whole, these results convincingly indicate the broad possibilities of controlling the influence of an object on the Q-factor of a resonator sensor with a coaxial aperture. In fact, these dependences illustrate quantitatively the influence of the coefficient of inclusion of the object in the electromagnetic field of the resonator, which can be used to select the optimal value of the operating frequency of the sensor and its sensitivity. Separately, we note that this approach is an effective alternative to similar control using the gap between the object and the plane of the aperture [8, 9]. The advantage is the fact that this approach is separated from the diagnostic process itself and thus eliminates the systematic error, which in practice turns out to be significant [9].

The results presented in Fig. 5 are associated with the study of the sensitivity of the probe with axial displacement of the tip along the coaxial for reproducible diagnostics of various spectra of objects. The properties of such materials, which are mainly represented by ε and tgδ, can differ by an order of magnitude or more.

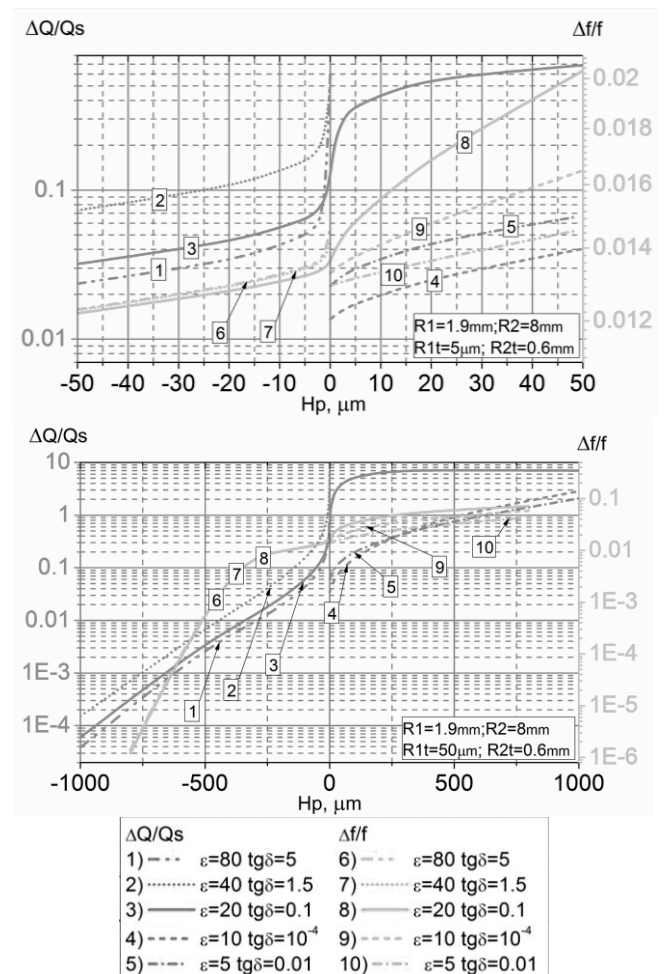


Fig. 5 - Properties of RMT with a movable probe-forming center conductor

The dependences shown in Fig. 5 clearly convince of the advisability of using a probe of this type for local

microwave diagnostics. As can be seen from the data in this figure, when the tip moves from the position $H_p=0$ to $H_p<0$, the fundamental signals, and hence inclusion factor, decrease. The behavior of the considered dependences, when the sensor operates in the range $H_p<0$, is physically interpreted by the known concepts of the dependence of the Q factor and the resonant frequency of a quarter-wave coaxial resonator with a shortening capacitance [10]. The use of a resonator of this type effectively solves the problems that arise in the study of objects with significant microwave losses. In biomedicine, these include skin and muscle tissues with $\varepsilon>40$. At the same time, when the tip moves from the position $H_p=0$ to $H_p>0$, in a similar way, both the signals and inclusion factor increase, which opens up prospects for studying objects with very small values of the imaginary part of the dielectric constant. These are often objects with a low water content. In particular, for example, in biomedicine, these are bone and adipose tissues with $\varepsilon<5$.

When using a coaxial RMT with axial displacement of the tip, in practice, in full growth, the problem of the dependence of signals on the position of the tip relative to the end of the aperture may arise. When solving such problems, the key point, like the version with the classical quarter-wave RMT, can be the use of a hybrid signal based on the fundamental ratio [5]. The behavior of such a signal with a change in the position of the tip is shown in Fig. 6.

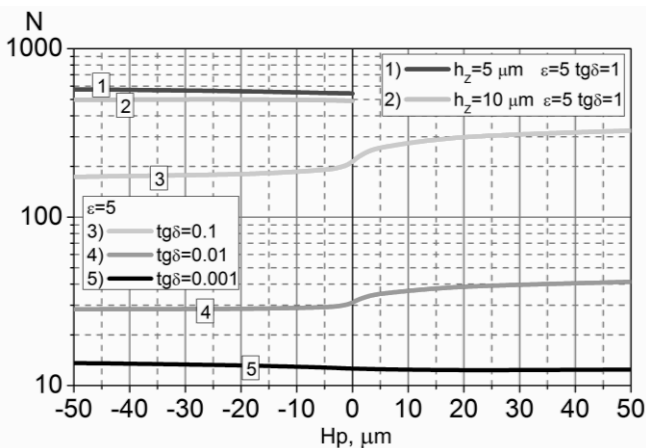


Fig. 6 - Invariance of the hybrid signal to the displacement of the tip relative to the plane of the butt

As can be seen from the data in Fig. 6, the invariance of the signal of the ratio N to the position of the tip relative to the aperture H_p takes place if we are not talking about the transition of the RMT robot mode from a "submerged tip" to a "protruding tip". Since in the vicinity of the zero position of H_p , a certain transition zone of the signal manifests itself quite noticeably. In our opinion, such transitions are associated precisely with a sharp change in the parameters of the medium at the interface between the fluoroplastic and the object under study. It is not difficult to notice that the less the parameters of the dielectric filler of the coaxial probe and the object under study differ, the less pronounced the change in the hybrid signal in the zone of their contact becomes. However, carrying out diagnostics purposefully in one of two possible modes of RMT

operation, the considered "transition zone" practically does not manifest itself. Nevertheless, the use of a hybrid signal in diagnostics opens up prospects for measurements of various materials without ultra-precise tracking of the position of the tip relative to the plane of the aperture.

Also, it should be noted that the dependences taken with a gap in this figure are in good agreement with the experimental ones [9]. As expected, there is no ideal invariance of the hybrid signal to the gap in such a resonator. This is primarily due to the complex electrodynamic structure of the RMT with a movable probe-forming central conductor. However, as can be seen from Fig. 6, the degree of influence of the gap on the hybrid signal of the form $(\Delta Q/Q)/(\Delta f/f)$ is so small that we can speak of the invariance of N to h_z in a resonator of this type.

III. CONCLUSIONS

The work theoretically and technically substantiated the possibility of changing the degree of inclusion of an object in the electromagnetic field of the aperture coaxial resonator sensor in order to expand the range of measurement of the main electrophysical parameters of the objects under study.

Particular attention is paid to the diagnosis of objects with a high value of $\text{tg}\delta$, which include biological media and tissues.

The efficiency of changing the coefficient of inclusion of the object in the electromagnetic field of the resonator is shown due to the introduction into the sensor structure of a mechanism that provides axial movement of the central conductor of the coaxial. This design allows the probe tip to be positioned both coplanar with the end aperture and displaced inward or outward of the coaxial.

A functional diagram of a microwave sensor has been developed, in which it is proposed to modulate the resonant frequency of the probe, rather than the operating frequency of the microwave generator, as in previous works. With this approach, a significant reduction in the influence of the modulating signal on the noise level in the signal extraction channels in the AFC system is achieved.

For objects with $\text{tg}\delta \ll 1$, an increased sensor sensitivity is realized by axial displacement of the tip outside the coaxial and transferring it to the monopole antenna mode.

The invariance of the combined signal $(\Delta Q/Q)/(\delta f/f)$ to the influence of interfering factors within each of the two considered modes of operation of the proposed tunable sensor has been established. At the same time, it remains possible to calibrate it theoretically, similar to the previously proposed and studied resonator sensor with a classical coaxial aperture.

REFERENCES

- [1] Gordienko Yu.Ye., Lepikh Ya.I., Dzyadevich S.V. and others. Intelligent measuring systems based on new generation microelectronic sensors. Odesa: Astroprint, 2011. – 352 p.
- [2] Boyko, V.V., Ivanov, V.K., Silin, A.O., Stadnik, A.M., Ivanova, Yu.V., Zamyatin, P.N., Gusak, I.V., Nevzorov, V.P., (2009), Radiophysical fundamentals and experience in the application of microwave electromagnetic fields in surgery, *New Word*, 1:166 (in Russian).
- [3] T. Mitch Wallis and Pavel Kabos, "Measurement Techniques for Radio Frequency Nanoelectronics", Cambridge University Press, 2017, 314 p.

- [4] A. Imtiaz and S. M. Anlage, “Effect of tip geometry on contrast and spatial resolution of the near-field microwave microscope”, *Journal of Applied Physics*, Vol. 100., 2006, pp. 1–8.
- [5] Gordienko Yu.Ye., Shcherban I.M. Hybrid signals in the local microwave diagnostics of small objects / *Telecommunication and Radio Engineering*, 2019. Vol. 78, № 19. – P. 1747–1757.
- [6] Dzhurinsky K.B. Miniature coaxial RCs for microwave microelectronics (World of electronics series) - 2006.
- [7] Bate K.-Yu., “Finite element methods”, M.: Fizmatlit, 2010, 1024 p.
- [8] Bagdad, B. A. Near-field scanning microwave microscope platform based on a coaxial cavity resonator for the characterization of semiconductor structures / Bendehiba Abadlia Bagdad, Carmen Lozano, Francisco Gamiz // *Solid State Electronics* – 2019. – Vol.159. – p. 150-156.
- [9] Gordienko Yu.Ye. Resonator aperture microwave sensors for small objects properties testing / Yu.Ye. Gordienko, A.V. Levchenko, A.V. Polishchuk, A.M. Prokaza, I.M. Shcherban, // *Telecommunications and Radio Engineering* – 2017. – Vol.76. – №18. – p. 1649-1659.
- [10] L.F. Chen, C.K. Ong, C.P. Neo, V.V. Varadan, V.k. Varadan, “Microwave Electronics: Measurement and Materials Characterization”, John Willy & Sons, Ltd, 2004. – 537 p.

Modelling the structures of polyimide composite systems and calculating their thermal conductivity coefficients

O. Listratenko
LLC «Research and Production
Enterprise «LTU»
Kharkiv, Ukraine
info@ltu.ua

I.V. Borshchov
LLC «Research and Production
Enterprise «LTU»
Kharkiv, Ukraine
info@ltu.ua

Oleksandr Kravchenko
LLC «Research and Production
Enterprise «LTU»
Institute for Scintillation Materials
National Academy of Sciences of
Ukraine
Kharkiv, Ukraine
info@ltu.ua

Abstract - The analysis is carried out, methods and recommendations for structural modeling and calculation of thermal conductivity of polyimide composite systems are summarized. Variants of structural models of heat-conducting polyimide films for theoretical and experimental studies have been developed. The program “Thermal conductivity of a polyimide composite” was developed, which made it possible to automate the calculations of the coefficients of thermal conductivity of the developed new high-thermal conductivity composite polyimide films according to the Burger model.

Keywords - structural models, polyimide composite films, thermal conductivity.

I. INTRODUCTION

Predicting the effective thermal conductivity of filled polymer systems requires knowledge of not only the thermal properties of the initial components but also a number of other factors. Of prime importance, here is the study of the structural changes taking place in the composite. The development of a model of the filled polymer as well as the modeling of the boundary layers, which have a very significant influence on the properties of the filled polymer composite system, seems very important from this point of view. It should be borne in mind that the mechanisms of influence of the matrix and filler on thermal conductivity are different at different concentrations. The control of the properties of polymer composite materials should be ensured not only by an increase in concentration but also by an increase in the modifying effect of the filler (due to dispersion and other factors).

Polymer composite materials (PCM), which are structures consisting of two or more components with different physical properties and a clear boundary between them, are currently widely used in various fields of science and technology. When using PCM in electrical insulation systems and switching elements of electronic nodes, the tasks of improving heat transfer while ensuring high dielectric characteristics are urgent. The polymer matrix (including polyimide), as a rule, has low thermal conductivity and high dielectric properties. To improve the heat transfer of PCM, it is possible to introduce micron or nanosized dielectric fillers with high thermophysical

characteristics into the polymer matrix. With this approach, one cannot exclude a decrease in the electrical insulating properties of PCM, the nature of the change in which is determined by the electrophysical properties of particles and their concentrations in PCM. Possibilities for increasing the efficiency of heat transfer in PCM will be determined by correctly selected properties, sizes, and concentration of filler particles in the polymer matrix.

Since the investigated PCM object is a two-component system, it is advisable to use analytical models to solve thermophysical problems. The most proven analytical models for the approximate calculation of the effective thermal conductivity of composites are given in [1, 2, 3].

The purpose of this work is to improve the effective thermal conductivity of polyimide (PI) composite films. In this regard, a numerical simulation of thermal conductivity should be carried out when composites of highly heat-conducting microparticles and nanoparticles of various shapes are introduced into the polyimide matrix. In this case, the volume concentration of these micro- and nanoparticles should vary. The effect of the thermal conductivity of filler particles on the effective thermal conductivity of polyimide composites should be analyzed. Specific recommendations should be offered to improve the effective thermal conductivity by changing the shape, concentration, thermal conductivity of the filler particles and increasing the thermal conductivity of the polyimide matrix. The calculation results should be in good agreement with experimental and published data.

Structural modeling and calculation of effective thermal conductivity should allow a deeper understanding of the effect of micro- and nanoparticles of high-thermal conductivity fillers on the effective thermal conductivity of polyimide composites.

II. STRUCTURAL MODELING AND CALCULATION OF EFFECTIVE THERMAL CONDUCTIVITY OF POLYIMIDE COMPOSITES

For the development of new heat-conducting polyimide composite films, it is necessary to choose such binders and fillers that provide optimal values of thermophysical,

physicomechanical, and dielectric characteristics. The most commonly used and effective are polyimide varnishes, solutions of polyamic acids in some compounds (dimethylformamide, dimethylacetamide, *N*-methylpyrrolidone). For example, varnish AD 9103 IC is intended for the production of films and foil-clad dielectrics. Имеет высокую вязкость и более высокую стойкость к кислотам, используемым при производстве печатных плат. Polyimide varnish AD-9103 IC is a solution of poly(pyromellitic acid) in dimethylformamide. The dry residue content in the varnish is 12-14% [4].

To obtain polyimide composite films with controlled physical, mechanical and thermophysical characteristics, it is necessary to add a dispersed filler to the polyimide binder.

According to the classification [5], dispersed fillers by particle size d are divided into coarse (d more than 40 μm), medium dispersed (d from 10 to 40 μm), highly dispersed (d from 1 to 10 μm) and ultrafine (d less than 1 μm). The group of nanodisperse powders (d less than 0.1 μm) has been added to this classification.

To increase the thermal conductivity of polymer materials while maintaining their necessary properties, including high electrical insulation characteristics, most often when creating polymer composites and nanocomposites, micro and nanoparticles of the following widely known and used in industrial production of dielectric heat-conducting materials are used, such as BN, AlN, TiO₂ and Al₂O₃, SiO₂, SiC (Table 1).

TABLE 1. THERMAL CONDUCTIVITY OF FILLERS

№	Filler type	Coefficient of thermal conductivity, W / m · K
1	Boron nitride	180
2	Aluminium nitride	285
3	Aluminium oxide	20
4	Titanium oxide	7-8
5	Silicon oxide	11-14
6	Silicon carbide	300-490

For structural modeling and calculation of the effective thermal conductivity of new PI composite films, the particle size of filler powders was selected, belonging to the group of highly dispersed and nanodispersed powders.

A. Structural modeling of thermally conductive polyimide composites

The theoretical description of transport phenomena (electrical conductivity, thermal conductivity, etc.) in solids, liquids, and gases is based on the similarity of the underlying equations. It is the similarity of the equations that is reflected in the theory of "generalized conductivity". "Generalized conductivity" combines the properties of compositions that are sensitive to their structure. Such properties are dielectric and magnetic permeability, thermal conductivity, shear modulus, elasticity, etc.

The value of the properties of the composition depends both on the volume fraction of the components in the PCM, and on the structure of the PCM and the orientation of the interfaces between the binder and filler.

Analyzing theoretical and experimental studies of mixtures and PCMs [5, 6, 7, 8] containing more than one phase, it is possible to put forward a number of assumptions about the properties and characteristics of functional materials.

These include:

- the geometry of solid particles is simple and correct;
- given distribution of filler particles in the binder (chaotic / ordered). This makes it possible to single out a typical unit cell characterizing the material as a whole;
- the interaction of the phases of the filler and/or binder (isolation or cohesion);
- thermal contact of filler particles (ideal or conditioned);
- presence/absence of chemical interactions between the filler and the binder;
- heat transfer is considered according to the main mechanism - heat conduction.

The task of structural modeling is the development of polyimide composite materials, in which it is possible to use fine fillers - down to nanosized particles - and to ensure a uniform distribution of the heat-conducting filler in the polyimide matrix, which guarantees a high level of heat-conducting, dielectric, and physicochemical properties of the resulting functional material.

Another task of structural modeling is also to obtain heat-conducting electrical insulating polyimide composite materials (variants) with high heat-conducting and dielectric properties while maintaining good physical and mechanical properties even at ultra-high degrees of filling.

In [9] it is reported that a decrease in the size of filler particles in a composite material down to nanoscale does not lead to a significant change in thermal conductivity compared to prototype materials using micron filler particles (at close values of the amount of filler). A decrease in the size of nanoparticles less than 20 nm leads to a significant decrease in the value of the thermal conductivity coefficient. In particular, it is reported that when a mixture of micron and nanosized particles is used as a filler, the thermal conductivity of the composites increases. At the same time, the size of micro- and nanoparticles of fillers in the mixture used does not affect the properties of the composite as noticeably as their mass ratio in the mixture. It was found that the ratio of the size of microparticles to the size of nanoparticles should not exceed 1000, but also should not be less than 100, since otherwise the optimal distribution of nanoparticles between microparticles is not achieved and a sufficient number of heat-conducting paths are not formed, as a result, the thermal conductivity of the composite material decreases.

Varying the amount of filler in the material made it possible to establish that high heat-conducting and dielectric properties are achieved when the content of filler particles in the composite is at least 55 wt. % and increase

with a further increase in the filler content. The increase in the content of the filler is more than 90 wt. % leads to a deterioration in the deformation and strength properties (the characteristics of strength and plasticity deteriorate).

Based on the positive results published in [9] for the development of structural models of variants of new highly filled heat-conducting electrical insulating polyimide composite materials, the sizes of nano and microparticles of fillers SiO₂, SiC, Al₂O₃, AlN and BN were selected in the ranges from 20 nm to 100 nm and from 10 μm up to 20 microns, respectively.

Table 2 shows the developed version of the structural model of new highly filled polyimide heat-conducting composite materials selected for theoretical and experimental studies.

TABLE 2. STRUCTURAL MODELS OF HIGHLY FILLED POLYIMIDE HEAT-CONDUCTING COMPOSITE MATERIALS BASED ON POLYIMIDE VARNISH AD 9103 IC.

№	Filler type	Thermal conductivity of the filler (powders), λ _f , W / m · K	Thermal conductivity of the binder, λ _m , W / m · K	Filler in PCM (mixture), Mass. %	Microparticles in the mixture, Mass. %	Nanoparticles in the mixture, Mass. %
1	SiC	25	0,12	60	30	70
2					50	50
3					70	30
4	AlN	50			30	70
5					50	50
6					70	30
7	αBN	55			30	70
8					50	50
9					70	30
10	Al ₂ O ₃	11			30	70
11					50	50
12					70	30
13	SiO ₂	7			30	70
14					50	50
15					70	30

B. Calculation of the effective thermal conductivity of polyimide composites.

According to [6], the initial data for the theoretical modeling of the effective thermal conductivity of the PCM are: thermal conductivity of the components, size, and shape of particles, the surface roughness of solid particles, density, particle contact area, thermal contact resistance, temperature, humidity, etc.

When calculating the effective thermal conductivity of a polyimide composite film, conditions (temperature, environment, etc.) are considered under which the main mechanism of heat transfer is thermal conductivity, and the contribution of radiation and convective heat transfer is negligible.

Consequently, the task of theoretical research is to determine the main indicator of the quality of heat-conducting polyimide films - thermal conductivity from the known values of thermal conductivity of its components (binder and filler).

In [3, 10, 11] the possibility of using linear models for approximate estimates of the effective thermal conductivity of two- and three-component mixtures for a wide range of powder filler contents was shown. This allows for practical evaluations to use simple computational models, for example, Burger's formula (1) for spherical particles.

The presence of the C coefficient in the Burger formula also makes it convenient for describing the thermal conductivity of multicomponent PCMs.

The value of this coefficient takes into account such material characteristics as the continuity/discontinuity of the phases of each of the components, the shape and size of the filler particles, and the ratio of their thermal conductivity coefficients. This is precisely its physical meaning.

The disadvantage of this formula is the need to select the value of the coefficient "C" for each specific PCM (Table 2), which reduces its versatility.

To calculate the effective thermal conductivity of new polyimide composites, the program "Thermal conductivity of polyimide composite" (NET framework, C #) was written. It made it possible to automate calculations related to the calculation of the thermal conductivity coefficient of the developed composite materials, consisting of a polyimide binder and dispersed non-metallic fillers according to the Burger model:

$$\lambda = \frac{V_m \lambda_m + CV_f \lambda_f}{V_m + CV_f} \quad (1)$$

where λ - coefficient of thermal conductivity of the composite; λ_f - thermal conductivity coefficients of the filler; λ_m - thermal conductivity coefficients of the matrix; V_f - volume fraction of filler; V_m - volume fraction of the matrix; C - calculation factor.

The program has the following features:

1. Calculation of the thermal conductivity coefficient of a composite film with a preliminary calculation of the component concentrations.
2. Plotting the dependences of the effective thermal conductivity of composite films on the values of the volume or mass concentration.
3. Calculation and selection of the coefficient "C" according to experimental data.
4. Plotting the dependences of the coefficient C on λ_f/λ_m.
5. Calculation of the volume or mass concentration of components for the manufacture of a sample (composite).
6. Comparison of experimental data (points) from theoretical plotting.

7. Calculation of the deviations of the experimentally obtained values of the thermal conductivity of the composite material from those theoretically calculated by the model.

8. Presentation of information in Russian and English.

III. CONCLUSIONS

Structural models and models for calculating the effective thermal conductivity of highly filled polyimide composite films based on highly heat-conducting microparticles and nanoparticles of various shapes and polyimide varnish AD 9103 IC are proposed for theoretical and experimental studies.

Programs have been developed and written that allow automating the processes of calculating thermal conductivity coefficients for composite materials. In particular, programs have been developed for calculating the thermal conductivity of one-component composite polyimide films (with one type of filler material). Calculations of the effective thermal conductivity of polyimide composite films were carried out according to the modified Burger formula [3].

For experimental confirmation of the applicability of the developed structural models, models and programs for calculating thermal conductivity, it is planned to manufacture and study the effective thermal conductivity of experimental samples of various types of new highly filled polyimide composite films.

REFERENCES

- [1] Stepanov V.V., Petrenya Y.K., Andreev A.M., Kostelov A.M., Mannanov E.R., Talalov V.A. "Effect of component properties on the effective thermal conductivity of polymer composites". Scientific and Technical Bulletin of SPbSPU. Physico-mathematical sciences. - 2018. - V. 11. - № 4. - P. 85-94. (in Russian)
- [2] Oliferov L.K. "Mechanochemical synthesis of functional nanostructured polymer-based composites". dis. Ph.D. Sciences. - 2016. - P. 154. (in Russian)
- [3] Mikheev V.A. "Quality assurance of new functional materials for heat-conductive coatings at development and production stages". dis. Ph.D. Sciences. - 2018. - P. 173. (in Russian)
- [4] Demina V.A. "Chemistry of dielectrics". Electronic edition. Moscow. - 2006. - P. 243. (in Russian)
- [5] Bondaletova L.I. "Polymer composite materials (part 1)": textbook - Tomsk: Publishing house of Tomsk Polytechnic University - 2013. - P. 118. (in Russian)
- [6] Dulnev G.N., Zarichnyak Y.P. "Thermal conductivity of mixtures and composite materials". Reference Book. - L. : Energy, 1974. - P. 264. (in Russian)
- [7] Chudnovsky A.F. "Thermophysical characteristics of disperse materials". - Moscow: Fizmatgiz - 1962. - P. 456. (in Russian)
- [8] Shevchenko V.G. "Fundamentals of physics of polymer composite materials": textbook. - M.: MOSCOW STATE UNIVERSITY - 2010. - P. 98. (in Russian)
- [9] Patent RU № 2600110 "A thermally conductive electrically insulating composite material (variants) and method of its production". Date of publication: 20.10.2016. (in Russian)
- [10] Mikheev V. A., Sulaberidze V. Sh., Mushenko V. D. "Linear model of heat conduction of disperse materials based on polymeric binders". Proceedings of Higher Education Institutions. Instrumentation. - 2017. - V. 60. - № 3. - P. 275-279. (in Russian)
- [11] Mikheev V. A., Sulaberidze V. Sh., Mushenko V. D. "Thermal conductivity modelling of three-component compositions". Proceedings of Higher Education Institutions. Instrumentation. - 2016. - V. 59. - № 7. - P. 584-591. (in Russian)

Atomic Force Microscopy investigation of laser-induced periodic surface structure as a perspective elements for sensors construction

Dmytro Snizhko
Biomedical Engineering dept.
Kharkiv National University of Radio
Electronics
Kharkiv, Ukraine
dmytro.snizhko@nure.ua

Yuriy Zholudov
Biomedical Engineering dept.
Kharkiv National University of Radio
Electronics
Kharkiv, Ukraine
yuriy.zholudov@nure.ua

Olena Bilash
Biomedical Engineering dept.
Kharkiv National University of Radio
Electronics
Kharkiv, Ukraine
olena.bilash@nure.ua

Kateryna Muzyka
Biomedical Engineering dept.
Kharkiv National University of Radio
Electronics
Kharkiv, Ukraine
kateryna.muzyka@nure.ua

Abstract — Morphology features of electrode materials modified by laser-induced periodic surface structures are investigated. Glassy carbon electrode explored before and after femtosecond laser treatment. The specific surface transformation after laser treatment was detected, that is microscopic and nanoscopic structures on the electrode surface with repetition period 14 μm and 765 nm correspondently. The new electrode material fabrication technology is perspective for a sensor application.

Keywords— laser, periodic structure, microscopy, glassy carbon, electrode

I. INTRODUCTION

Nanotechnological processing is a new way to obtain perspective materials. Electrode surface functionalization can be done by different methods [1-2]. One of the methods of material treatment is laser ablation. Femtosecond laser irradiation stimulates reorganization of an illuminated material and formation laser-induced periodic surface structures (LIPSS) on a surface [3-6]. This feature of laser treatment can be used for different material including enough hard as glassy carbon (GC). Last one is wide applicable in electrochemical analytics.

Determination of the laser irradiation impact on surface morphology is important to recognize relationship between LIPSS parameters and their electrochemical properties. Atomic force microscopy is helpful in investigation of material surface parameters [7-10]. This is a quite usable unique method of surface visualization and reconstruction 3-D surface gives possibilities to calculate different mechanical characteristics, control them after technological operations.

II. MATERIALES AND INSTRUMENTATION

A. Materials

The samples of electrodes was fabricated from glassy carbon material purchased from Sigma-Aldrich GmbH. Samples of electrodes had the following structure. The glassy carbon cylinder with an outer diameter of 3 mm is fixed in a plastic tube with an outer diameter of 7 mm. The end surface of the structure was prepared by grinding and polishing (fig.1a). At the other end of the electrode, a thread is made to be combined with a holder used to set up electrode in an electrochemical cell.

After glassy carbon electrode assembling, the LIPSS was fabricated by LLC NOVINANO LAB (Lviv, Ukraine) with femtosecond laser to shape LIPSS on the carbon surface (fig.1b).

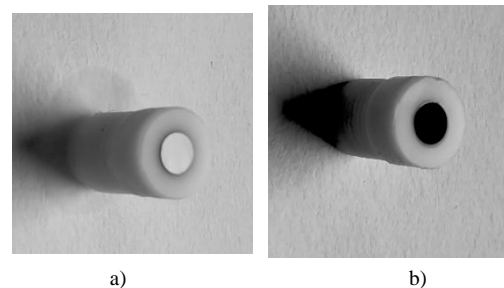


Fig. 1. Electrode with glassy carbon disk working surface: a) bare, b) with LIPSS.

B. Instrumentation and methods

Atomic force microscopy were done by NT-206 (Microtestmachines, Belarus) is used, which allows to conduct measurement in different operational modes. In this work, the topography of surface in static and dynamic mode were explored by CSC-37 and NSC-11 probes by (Micromash, USA).

III. ELECTRODS MATERIALS CHARACTERIAZATION

To obtain information on the topography and morphological features of LIPSS, the method of atomic force microscopy is used, which allows to conduct operational and large-scale studies of the structure of materials with a resolution at the level of nanometers and survey fields of tens of micrometers.

A. Contact mode

Recognition of technology parameter influence on surface features was done by a comparison of bare (fig. 2) and modified glassy carbon electrode (fig. 3) samples. To conduct measurements in contact mode was used probe CSC-37 cantilever A with spring force constant 0.3 N/m. Samples of electrodes were observed for series from 3 electrodes. Samples were observed in different places that is arbitrary selected on the electrode surface.

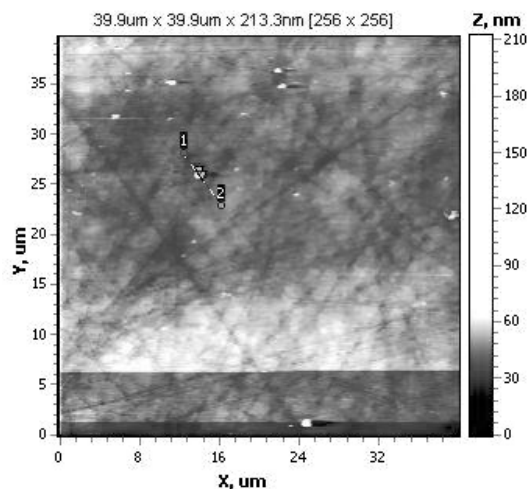


Fig. 2. Topography of electrode surface of bare glassy carbon material. Scan range is 39.9×39.9 μm.

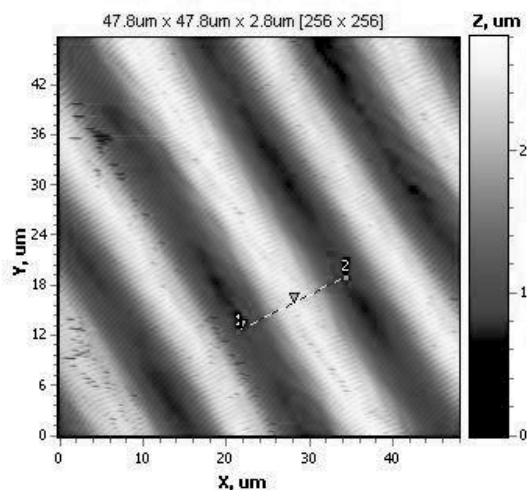


Fig. 3. Topography of electrode surface of glassy carbon with LIPSS. Scan range is 47.8×47.8 μm.

Small field sample observation shown in fig. 4 and fig. 5 for bare and LIPSS. They demonstrated nanocrystalline structure of glassy carbon.

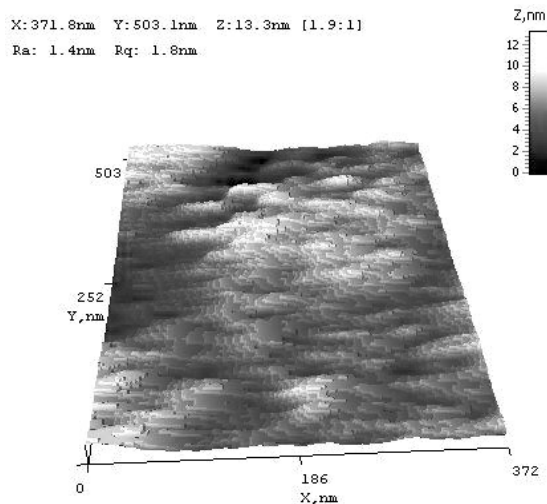


Fig. 4. Topography of electrode surface of bare glassy carbon material. Scan range is 372×503 nm.

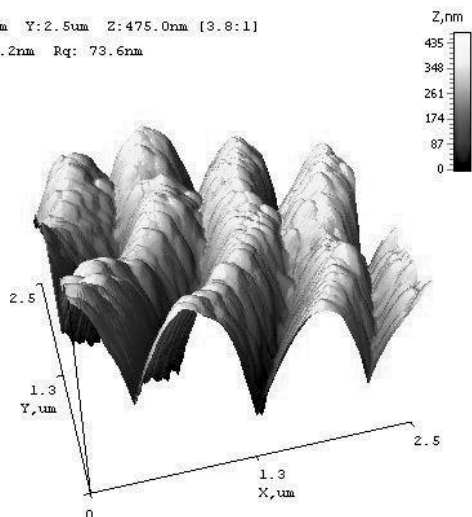


Fig. 5. Topography of electrode surface of glassy carbon with LIPSS. Scan range is 2.5×2.5 μm.

B. Typing mode

The cantilever A of NSC-11 probe was used to done electrode surface investigation. The imaging of the force of the intermittent contacts of the tip with the sample surface with lips are shown in fig. 6.

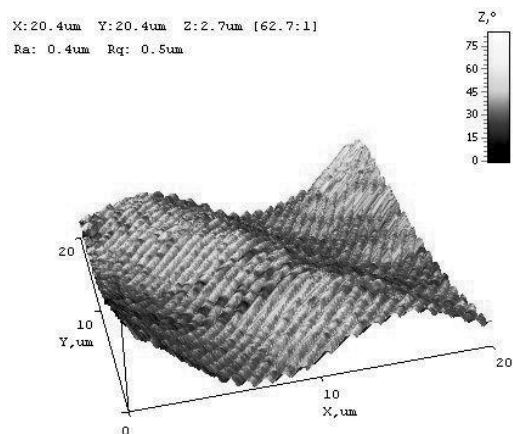


Fig. 6. Topography of electrode surface with phase contrast of cantilever oscillation of glassy carbon with LIPSS. Scan range is 20.4×20.4 μm.

IV. RESULTS AND DISCUSSION

Analysis of the surface of different samples of one series reveals their related nature of the surface elements, which are reflected in the following data. After laser treatment and LIPSS formation, it has a significant effect on the surface characteristics.

A. Microstructures

On a large field of scanning of electrode samples structures with LIPSS on GC (fig. 3) formation of ripples with a step of 14 microns is observed. The magnitude of the amplitude of the ripples is 1.8 μm (fig. 7). Significantly increased surface roughness (Fig. 8): $R_a = 569.4 \text{ nm}$, $R_q = 631.77 \text{ nm}$, and $R_{sk} = 0.03 \text{ nm}$, $R_{ku} = 1.53 \text{ nm}$, even decreased, indicating about the high reproducibility of LIPSS on the electrode surface both on the ridges and in the valleys of harrows.

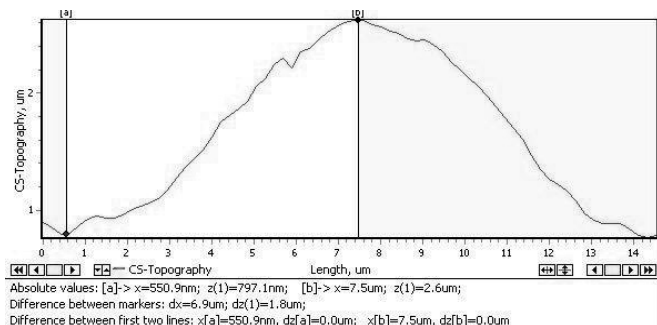


Fig. 7. The profile of the surface of the GC sample with LIPSS along line 1-2 in Fig.3.

B. Nanostructures

In studies in small fields of view (fig. 5), the characteristics of LIPSS, formed due to the interference pattern on the electrode surface, are analyzed in more detail. The magnitude of LIPSS waves is 252 nm (fig. 8). On the surface after removal of the material, the microcrystalline structure is observed, which was previously observed on the GC electrode before its processing. However, formations larger than 200 nm are not observed, which may only indicate the preservation of nanocrystallites, and the high-energy effect of laser irradiation significantly changes the topography of the surface.

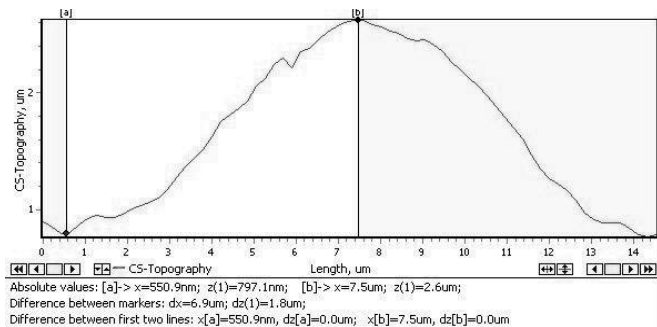


Fig. 8. The profile of the surface of the GC sample with LIPSS in Fig.5.

V. CONCLUSION

AFM studies of samples of electrode structures revealed the identity of the character for a series of 3 electrodes with the same processing conditions: pre-polished and subsequently treated with laser radiation to form LIPSS.

Samples of electrode structures with LIPSS after the polishing process are characterized by high flatness, roughness $R_a = 5.06 \text{ nm}$ and $R_q = 6.93$ indicate a high degree of surface treatment. Although in some cities there are small peaks of individual grains, which are subsequently not detected on the electrode structures with LIPSS.

Analysis of the phase contrast of the surface of the GC electrode structures confirmed the homogeneity of the initial GC material.

The LIPSS study was performed on the same samples, but after appropriate laser treatment. Characteristic dimensions of LIPSS on the GC are the ripple height of 250 nm with a period of 765 nm of structures covering the surface of the GC electrodes.

For LIPSS, the formation of microborin is observed on the LIPSS. The microprotectors have a period of 14 μm and are formed in accordance with the scanning trajectory of the laser beam on the working surface of the electrode structure.

Comparison of surface roughness indicates a significant increase for electrode structures with LIPSS, respectively $R_a = 569.4 \text{ nm}$ against $R_a = 5.06 \text{ nm}$ for polished GC.

LIPSS demonstrate high order and reproducibility on the surface, they cover both the hills and valleys of the microripples on the GC.

Investigation of morphology properties was done on different hierarchical levels of LIPSS. Modification of electrode by LIPSS is interesting for sensor application. Sufficient increasing of electrode surface area supports the rise of the density of immobilized chemicals on an electrode surface.

ACKNOWLEDGMENT

This work is supported by the National Research Fund of Ukraine project (application reg. number 2020.02/0390).

REFERENCES

- [1] Y. Zholudov, D. Snizhko, A. Kukoba, H. Bilash, and M. Rozhitskii, "Aqueous electrochemiluminescence of polycyclic aromatic hydrocarbons immobilized into Langmuir-Blodgett film at the electrode," *Electrochimica Acta*, vol. 54, no. 2, pp. 360–363, Dec. 2008.
- [2] Y. T. Zholudov and G. Xu, "Electrogenerated chemiluminescence at a 9,10-diphenylanthracene/polyvinyl butyral film modified electrode with a tetraphenylborate coreactant," *The Analyst*, vol. 143, no. 14, pp. 3425–3432, 2018.
- [3] J. Bonse, J. Krüger, S. Höhm, and A. Rosenfeld, "Femtosecond laser-induced periodic surface structures," *Journal of Laser Applications*, vol. 24, no. 4, p. 042006, Sep. 2012.
- [4] J. Bonse, A. Rosenfeld, and J. Krüger, "On the role of surface plasmon polaritons in the formation of laser-induced periodic surface structures upon irradiation of silicon by femtosecond-laser pulses," *Journal of Applied Physics*, vol. 106, no. 10, p. 104910, Nov. 2009.
- [5] J. E. Sipe, J. F. Young, J. S. Preston, and H. M. van Driel, "Laser-induced periodic surface structure. I. Theory," *Physical Review B*, vol. 27, no. 2, pp. 1141–1154, Jan. 1983.
- [6] M. Huang, F. Zhao, Y. Cheng, N. Xu, and Z. Xu, "Origin of Laser-Induced Near-Subwavelength Ripples: Interference between Surface Plasmons and Incident Laser," *ACS Nano*, vol. 3, no. 12, pp. 4062–4070, Nov. 2009.
- [7] D. V. Snizhko, Y. T. Zholudov, O. M. Bilash, A. V. Kukoba, and M. M. Rozhitskii, "Electrochemiluminescence at nitrogen doped diamond-like carbon film electrodes," *Russian Journal of Electrochemistry*, vol. 50, no. 3, pp. 260–266, Mar. 2014.
- [8] F. J. Giessibl, "Advances in atomic force microscopy," *Reviews of Modern Physics*, vol. 75, no. 3, pp. 949–983, Jul. 2003.
- [9] B. Voigtländer, "Atomic Force Microscopy," *NanoScience and Technology*, 2019.
- [10] R. Garcia, "Dynamic atomic force microscopy methods," *Surface Science Reports*, vol. 47, no. 6–8, pp. 197–301, Sep. 2002.

Automation of Mathematical Modeling of Physical and Technological Processes in the Electronic Devices Manufacture

Igor Nevliudov
Department of Computer-Integrated
Technologies, Automation
and Mechatronics
*Kharkiv National University
of Radioelectronics*
UKRAINE, Kharkiv, Nauky Ave., 14
igor.nevliudov@nure.ua

Olena Chala
Department of Computer-Integrated
Technologies, Automation
and Mechatronics
*Kharkiv National University
of Radioelectronics*
UKRAINE, Kharkiv, Nauky Ave., 14
olena.chala@nure.ua

Iryna Botsman
Department of Computer-Integrated
Technologies, Automation
and Mechatronics
*Kharkiv National University
of Radioelectronics*
UKRAINE, Kharkiv, Nauky Ave., 14
irina.botsman@nure.ua

Oleksandr Klymenko
Managing Director
Kapelou LLC
UKRAINE, Kyiv, St. Mashynobudivna,
44
kan@kapelou.com.ua

Maksym Vzhesnievskyi
R&D business partner
Kapelou LLC
UKRAINE, Kyiv, St. Mashynobudivna, 44
yvo@kapelou.com.ua

Abstract—The variant of automation of the mathematical modeling process for forecasting the technological process parameters of manufacturing nano and microelectromechanical systems is proposed in the paper. For this task realization, a number of defects were identified and the causes of their occurrence were analyzed, as well as physical and technological transformations that occur in the substrates during technological processes. The software for automation of technological parameters forecasting process is developed and described.

Keywords—production, component, nanoelectromechanical systems, microelectromechanical systems, defect, silicon substrate, software.

I. INTRODUCTION

One of the promising directions of research in electronic devices production technology is the development of nano and microelectromechanical systems (NEMS and MEMS). A special area of these systems use are telecommunications devices.

But there are contradictions between the need of further improve the quality of NEMS and MEMS components, the use of promising variants for the implementation of their production technological processes and operations and the limited known approaches to ensuring their quality and testing.

The work is aimed at solving the current scientific and applied problem of improving the quality of functional components of micro-optoelectronic systems by developing technological support for their individual production stages based on the study of physical and technological parameters and testing methods for micro-optical switches substrates.

As research object the functional components (FC) for optical signal switches of microoptoelectromechanical systems (MOEMS) were selected.

FC of MOEMS switches are usually silicon substrates with a thin film of metallization, or without it, which provides a high light beam reflectivity for redirecting it in the optical fibers [1-5]. One of the important characteristics of MOEMS FC is the defectiveness.

II. ANALYSIS OF FC SUBSTRATES DEFECTIVENESS

Assume that the FC of MOEMS-switch is already fabricated and its parameters correspond to the specified in technical documentation. However, it should be noted that the practice of MOEMS switches operation indicates that the development of defects occurring during its manufacture (operation) is one of the main causes of failures and incorrect operation of the whole device.

Currently, there are a large number of methods and tools to detect manufacturing defects, but the capabilities of these methods are limited [2, 5-10]. The testing and checkout operations included in the modern technological processes (TP) structure cannot give a full guarantee of the defects absence in the production of such components. In this regard, there is an urgent problem of developing a model for predicting MOEMS FC defects, taking into account the physical and technological features of their production TP [11].

So the purpose of this research is to develop a method for predicting production defects for substrates of MOEMS FC on the basis of physical and technological models of TP of their manufacture.

If the substrate of the FC for MOEMS switch is considered directly at the stage of its fabrication TP, then the substrate structure can be divided into four main layers, in

which defects can be displaced. Such structures are characterized by the depth of the disturbed layer, roughness and various kinds of pollutions [5, 10].

Layer 1 is the outer relief, which characterized by chaotically placed protrusions, cracks and splinters. Layer 2 is disturbed layer that has separate punctures and microcracks, which tend to spread to the depth of other layers and grow. Layer 3 is deformed and characterized by accumulation of dislocations, continuation of microcracks and zones located around them that are the centers of mechanical stresses. And layer 4 is conditionally intact structure of the FC substrate.

The most important stage at which the manufacturing defects occur in the substrates is the first stage of the optical switch production TP. At this stage, it is possible to predict defects in the structures of substrates, their layers and sublayers, that allows at the next stages to build a TP which would provide for the opportunity minimize the variety, number and size of defects.

Defectiveness of FC at the production stage is laid on the basis of defects of three groups: 1) defects of a functional component substrate Ω_s ; 2) defective spraying of thin films Ω_c ; 3) defects of technological combination of structures Ω_d .

In this view, it is possible to symbolize a generalized mathematical description of the MOEMS FC production defects set in the form (1):

$$\Omega_{md} = \Omega_s + \Omega_c + \Omega_d \quad (1)$$

If assume that a significant part of production defects occurs in particular because of the defect of the substrate plates or sublayers of MOEMS FC substrates, it was decided to consider the defects of MOEMS FC as the main and primary source of defects in the whole MOEMS-device.

The problem arises that at the stage of raw materials production, it seems unlikely to be able to track defects in structures and dependence of physical and technological parameters that directly affect the quality and compliance of initial characteristics to the required one. A special limitation on them is imposed by the kinetics of degradation processes in materials.

Based on the analysis of modern literature, physical and technological models of processes that take place in the manufacturing of MOEMS FC are developed. From the conducted research, we concluded that diffusion, corrosion and evaporation of materials are the main sources of defective structures.

The layers diffusion of the MOEMS FC substrate is expressed using Fick's second law: for one-dimensional diffusion (2) or diffusion through the film (3):

$$\frac{dV}{dt} = D \frac{d^2V}{dx^2}, \quad (2)$$

$$\frac{dV}{dt} = D \frac{\Delta V}{y}, \quad (3)$$

where D is the diffusion coefficient; V is concentration of the substance (component); y is the thickness of the FC substrate.

Thermal oxidation of silicon occurs due to the diffusion of components oxidation (O_2, H_2O) through the oxide to the phase boundary $Si-SiO_2$, where the oxidation reaction takes place. The kinetics of the oxidation process is described by a model developed by Dilom and Gurov [5, 11-13]. Oxidation is a nonequilibrium process, the driving force of which is the deviation of oxygen concentration from equilibrium. The oxidant particles flow through the oxide for any point of the oxide V -layer is described by law (4, 5). Oxidation during the production of MOEMS FC substrates is a special case of diffusion:

$$\frac{dV}{dt} = V_0 e^{-\frac{E}{RT}}, \quad (4)$$

$$\frac{dV}{dt} = \frac{k_d k_p}{k_d + k_p h_0} V_0, \quad (5)$$

where E is the activation energy of the molecules involved in the reaction; k_p is chemical reaction rate constant; V_0 is the reagent (e.g. oxygen) concentration on the outer surface at the boundary with the gas phase; h_0 is coating thickness; k_d is diffusion coefficient in the process of corrosion.

If the substrate fabrication TP involves the use of electrical corrosion, the layer of corroded material can be expressed as (6) [5]:

$$V_E = \gamma_{(-)} Q, \quad (6)$$

where $\gamma_{(-)}$ is erosion coefficient; Q is electric current.

The wear depth for the substrate layer of MOEMS FC can be determined as (7):

$$h = \frac{\gamma_{(-)} Q}{\rho S_0} = \frac{\gamma_{(-)}}{\rho S_0} \int_0^t idt = \frac{\gamma_{(-)}}{\rho S_0} I_{CP} t, \quad (7)$$

where ρ is specific density; S_0 is the area of the worn surface part; I_{CP} is average value of current strength; t is the time of current action.

If in the TP of the FC substrate production there is electro-chemical corrosion, (8) express the amount of current-transferred substance and (9) express the wear depth for the FC substrate layer:

$$V = \eta Q = \eta \int_0^t idt = \eta I_{CP} t, \quad (8)$$

$$h = \frac{\eta}{\rho S_0} I_{CP} t. \quad (9)$$

In TP there are not uncommon cases of violation of the dependence between the rate of solvents evaporation and their boiling points due to the fact that the liquid molecules are conjugated at normal temperature. This causes a decrease of the substance pressure for a given temperature range [5].

First of all, it should be noted that the rate of solvent evaporation from the film is not the main physical characteristic, it is only a technological parameter that reflects the influence of a number of basic physical properties such as pressure, evaporation and solvent vapor density. To obtain practical data on the evaporation rate it should be measured under certain conditions: temperature, relative humidity.

Increasing the evaporator concentration reduces the rate of solvent evaporation and thus promotes the formation of a dense, so-called active (selective) layer on the FC surface. Regulation of FC porosity can be carried out by changing the concentration and conditions of solutions evaporation, as well as the introduction of special substances in this process [2, 5, 10-14].

The evaporation rate of the substrate material or sublayers of MOEMS FC can be expressed as (10):

$$V' = \frac{k_p}{\sqrt{2\pi R}} \cdot p \sqrt{\frac{M}{T}}, \quad (10)$$

where M is the molecular weight of the evaporated material; p is pressure; R is gas constant; T is absolute temperature.

An important indicator of each physical and technological process is speed. Diffusion and chemical reactions can serve as a basis for determining the rate and, therefore, the description of the kinetics of the processes under consideration. Physics makes it possible to explain the kinetics of the medium thermodynamic parameters on the basis of the behavior of the particles set of which this medium consists.

The microscopic state of a particles set is completely given by the canonical variables (X). From the macroscopic point of view, the state of matter is determined by a rather limited number of parameters sufficient for the macroscopic characteristics of the environment. Macroscopic parameters, including the volume of the substance that reacted, are functions of the canonical variables: $V_k(X)$, and $k = 1, 2, \dots, n$, where $n \ll N$.

Thus, the macroscopic system is represented by setting the density of variables probability $\omega(X, t)$. This phase probability density is called the phase probability distribution, or simply the phase distribution.

Knowing $\omega(X, t)$, the statistical mean value you can be calculates using (11), as well as the root-mean-square deviation, which show itself as a fluctuation of the disturbed layers observation area (12):

$$V = \int V(X) \omega(X, t) dX, \quad (11)$$

$$\Delta V = \sqrt{(V - \bar{V})^2}. \quad (12)$$

Using the basic provisions of Gibbs's theory [5, 12], it is possible to calculate the average levels and fluctuations of any physical values that are functions of coordinates, if the dependence of the these values average levels on external constant forces acting on them is known. It is not possible to estimate these forces for specific objects. It is possible to conclude the hierarchical nature of fluctuations given by different order of relaxation time for microscopic and macroscopic parameters.

The occurrence of defects in any structure (regardless of the object physical state or the impact nature) is a random variable whose behavior can be described using fluctuation theories. That is, it is a random deviation of any value from the random variable average level that characterizes a system with a large number of chaotically interacting particles.

To display fluctuations, taking into account the impossibility of full use of the statistical physics results caused by lack of necessary quantitative information about the Hamiltonian set of interacting particles, it is possible to use methods of statistical analysis of observations results to determine and predict defects in the FC substrates for MOEMS switches.

III. SOFTWARE DEVELOPMENT

Based on obtaining mathematical models of physical and technological parameters for TP of MOEMS FC substrates production, the next step is to calculate data sets to select the optimal variant of TP for different parameters, such as minimizing defects in the structures of substrates.

In order to reduce the complexity of solving the data analysis problem, it is proposed to introduce processes visualization in the TP of the substrates production for MOEMS FC, using the developed software, the interface of which is shown in Fig.1.

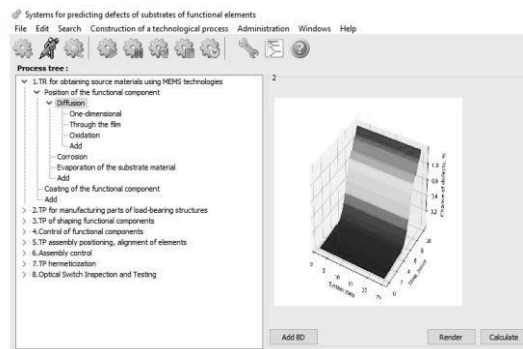


Fig. 1. The interface of the developed software

With the developed software help, it is possible to reduce labor costs of solving the problem of forecasting production defects in the substrates of MOEMS FC, to increase the accuracy and reliability of the information obtained in the development of manufacturing TP of such objects as a whole.

Using a number of initial parameters for MOEMS FC substrates, focusing on the requirements of their defects

minimizing and using data from previous experimental studies of a particular perform variant, the developer can make decision about the optimal TP use and its parameters.

At this stage of research, the base of TP input parameters was formed for the manufacture of MOEMS FC substrates made of silicon.

The software makes it possible to store material parameters, values of constant coefficients and variables, equipment parameters.

The program has the choice functions of standard equipment for the enterprise, the ability to adjust the parameters of the manufacturing TP, such tabs can be up to 50.

New projects can be created, saved and the parameters can be changed, due to adjustments, there is the possibility of changing each parameter separately or adjusting the parameters of the manufacturing TP to predict defectiveness and choose the equipment for production. The operator himself decides on the use of the existing TP, or the development of a new one, on the obtained technical conditions basis.

In this case, the basis for making such a decision can be a physical and technological model for predicting the parameters of defect formation in the substrates of MOEMS FC, proposed in this research.

According to the available theoretical and experimental data, the person who makes the final decision on the TP variant for the product manufacture can also analyze the behavior of the system for the time interval that goes beyond the experimental or calculated results, but allows analyze the product condition at its subsequent operation stage.

IV. CONCLUSIONS

On the basis of the conducted complex research of possible mechanisms of failures occurrence types of defects were systematized and the reasons of their occurrence and also the physical and technological transformations taking place in substrates during technological processes of their manufacturing were analyzed.

As a result, variables were selected for the physical and technological base formation of the defect prediction mathematical model.

Specified physicochemical processes can serve as a basis for determining the speed and, consequently, the description of the kinetics of the processes under consideration.

To reduce labor costs and ease of the obtained information analysis, according to the proposed mathematical models, the numbering of each TP is performed to embody the possibility of graphical visualization the simulation results using the developed software.

The decision maker, i.e. the technologist, can analyze the behavior of the technological system, i.e. to predict the technological process parameters, which can cause

production defects of the functional components substrates, as well as adjust the technological processes of their manufacture.

References

- [1] L. Guo, K. Kamei, K. Momose and H. Osawa, "Evaluation and reduction of epitaxial wafer defects resulting from carbon-inclusion defects in 4H-SiC substrate," *2016 European Conference on Silicon Carbide & Related Materials (ECSCRM)*, 2016, pp. 1-1, doi: 10.4028/www.scientific.net/MSF.897.39.
- [2] Stanley Wolf, Richard Tauber, "Silicon Processing for the for VLSI era". Sunset Beach (CA), Lattice Press, 1986, Volume I.
- [3] Y. Zhu, G. Coletti and Z. Hameiri, "Injection Dependent Lifetime Spectroscopy for Two-Level Defects in Silicon," *2019 IEEE 46th Photovoltaic Specialists Conference (PVSC)*, 2019, pp. 0829-0832, doi: 10.1109/PVSC40753.2019.8981261.
- [4] J. H. Lau, "Evolution challenge and outlook of TSV 3D IC integration and 3D silicon integration", *Proc. Int. Symp. Adv. Packag. Mater. (APM)*, pp. 462-488, Oct. 2011.
- [5] İ. Nevludov , M. Omarov and O. Chala , "Mathematical Model Of The Development Of Manufacturing Defects In The Surface Layer Of Substrates Of Moems' Functional Components", *Eskişehir Technical University Journal of Science and Technology A - Applied Sciences and Engineering*, vol. 21, pp. 113-127, Nov. 2020, doi:10.18038/estubtda.823088
- [6] T. J. Brosnihan *et al.*, "Optical IMEMS/sup /spl reg//a fabrication process for MEMS optical switches with integrated on-chip electronics," *TRANSDUCERS '03. 12th International Conference on Solid-State Sensors, Actuators and Microsystems. Digest of Technical Papers (Cat. No.03TH8664)*, 2003, pp. 1638-1642 vol.2, doi: 10.1109/SENSOR.2003.1217096.
- [7] Wang, Cong, et al. "Tin selenide: a promising black-phosphorus-analogue nonlinear optical material and its application as all-optical switcher and all-optical logic gate." *Materials Today Physics* (2021): 100500.
- [8] O. Filipenko, O. Chala, V. Bortnikova, O. Sychova and I. Botsman, "Impact of Technological Operations Parameters on MOEMS Components Formation," *2019 IEEE 8th International Conference on Advanced Optoelectronics and Lasers (CAOL)*, 2019, pp. 371-374, doi: 10.1109/CAOL46282.2019.9019570.
- [9] D. Li and J. Su, "Nondestructive Defect Detection and Localization of Defects in Annular Through Silicon Via(TSV)," *2019 Cross Strait Quad-Regional Radio Science and Wireless Technology Conference (CSQRWC)*, 2019, pp. 1-3, doi: 10.1109/CSQRWC.2019.8799141.
- [10] I. Nevludov, N. Demska, V. Palagin, V. Nevludova, I. Botsman and K. Kolesnyk, "Stiffness Matrix of MEMS on the Stress-Strain Method Basis," *2020 IEEE XVth International Conference on the Perspective Technologies and Methods in MEMS Design (MEMSTECH)*, 2020, pp. 142-145, doi: 10.1109/MEMSTECH49584.2020.9109509.
- [11] M. Herms, M. Wagner, J. De Messemaeker and I. De Wolf, "Study of stress in through silicon via structures", *Proc. GADEST*, Oct. 2017.
- [12] .C Schmidt, K. Wadhwa, A. Reverdy et al., "Localization of electrical active defects caused by reliability-related failure mechanism by the application of lock-in thermography[C]", *Proc. IEEE Int. Rel. Phys. Symp. (IRPS)*, pp. 5B. 4. 1-5B.4.6, 2013.
- [13] B. Malyk, O. Tokarieva and S. Malyk-Zamorii, "Optical fiber structures performance enhancement under the conditions of ionizing radiation high power levels", *Problems of Atomic Science and Technology*, vol. 2, no. 114, pp. 13-18, 2018.
- [14] G. Margutti et al., "Silicon defects characterization for low temperature ion implantation and spike anneal processes," *2014 20th International Conference on Ion Implantation Technology (IIT)*, 2014, pp. 1-4, doi: 10.1109/IIT.2014.6940014.

Using High-Voltage Converters in Hybrid Photovoltaic Systems

Mykhailo Kirichenko

*Materials for electronics
and solar cells department*

National Technical University

“Kharkiv Polytechnic Institute”

Kharkiv, Ukraine

mykhailo.kirichenko@khp.edu.ua

Roman Zaitsev

Materials for electronics

and solar cells department

National Technical University

“Kharkiv Polytechnic Institute”

Kharkiv, Ukraine

roman.zaitsev@khp.edu.ua

Anton Drozdov

Materials for electronics

and solar cells department

National Technical University

“Kharkiv Polytechnic Institute”

Kharkiv, Ukraine

anton.drozdov@khp.edu.ua

Gennadiy Khrypunov

Materials for electronics

and solar cells department

National Technical University

“Kharkiv Polytechnic Institute”

Kharkiv, Ukraine

khrip@ukr.net

Eugene Sokol

Industrial and Biomedical

Equipment Department

National Technical University

“Kharkiv Polytechnic Institute”

Kharkiv, Ukraine

yevgen.sokol@khp.edu.ua

Liliia Zaitseva

Materials for electronics

and solar cells department

National Technical University

“Kharkiv Polytechnic Institute”

Kharkiv, Ukraine

liliia.zaitseva@khp.edu.ua

Abstract—In the article analytical and field test of the experimental photovoltaic station equipped with hybrid photovoltaic module equipped and innovative power take-off system with DC-DC converters was carried out. It was established that the power take-off system with DC-DC converters working with hybrid photovoltaic modules has an efficiency up to 92.5 % in a wide range of solar radiation intensity, and was confirmed reliability and effective working of hybrid photovoltaic modules innovative components. It has been shown that experimental sample of the optimized photovoltaic station with a low concentration of solar radiation can generate in stable mode values of electric power on a level of 14 kW.

Keywords—*photovoltaic module, solar energy, solar station, circuit design, power take-off system*

I. INTRODUCTION

Previously, based on experimental results, it has been proposed a concept and on its base was developed hybrid photovoltaic module equipped with a mirror solar radiation concentrator and solar cells cooling system in order to build up a high-efficiency photovoltaic station [1, 2]. The solar concentrator provides 1.7-time increase of standard module electrical power up to 450 W, and the water-cooling system reduces the equilibrium module temperature on 10 degrees and as a result provides decreasing on 50% the efficiency losses from overheating [3]. Implementation of the proposed concept will allow reducing the number of modules required to build up a photovoltaic station.

Also, earlier it has been proposed a circuit solution and, on its base, was developed a DC-DC converter with adjustable resonant circuit for using with hybrid photovoltaic modules [4, 5]. Using computer simulation based on the multiple iteration's algorithm, the optimal resonant circuit parameters were determined in order to build DC-DC converters for working in a wide range of electrical power nominals [6]. The implementation of microprocessor control in the converters design allowed to

increase the device reliability and increase the conversion efficiency to 96-97% [4, 7].

The aim of this article was carried out of analytical and field test of the experimental low-power photovoltaic station in order establish the efficiency of above-mentioned innovative components.

II. ANALYSIS OF THE PHOTOVOLTAIC STATION POWER TAKE-OFF SYSTEM

A. Power take-off system without DC-DC converters

To estimate the feasibility of DC-DC converters using, the calculation of the power losses and power take-off system (PTOF) of the photovoltaic station (PS) efficiency without the DC-DC converters P_{lossNoDC} was carried out for 12 kW power PS (based on data obtained during the development of photovoltaic modules with increased power [1, 8, 9]). The PS selected for calculation consists from 12 generator units with four photovoltaic modules on each. The calculation was performed using the developed software, the results are shown in table 1, and graphs of the dependences are presented on Figures 1.

As can be seen from the presented dependences, with the growth of the modules output current (I_{PM}), which characterizes the lighting conditions (P_i) and using of a low concentrating system, the power losses values in the PTOF (P_{lossNoDC}) increases significantly in proportion to the square of the current. The value of power losses at 1700 W/m² is 6.2 kW at PS generating power up to 21.3 kW. This circumstance, as a consequence, leads to a significant, up to 71 %, reduction of PTOS efficiency [10-12], which is much less than the expected value. Losses on a level of 30 % are unacceptable. Thus, the considered design of PTOS cannot be used in PS built on the basis of previously developed photovoltaic modules.

TABLE II. PARAMETERS OF POWER LOSS AND EFFICIENCY CALCULATED FOR PS WITHOUT DC-DC CONVERTERS

P_i , W/m ²	I_{PM} , A	P_{PS} , W	$P_{lossNoDC}$, W	Eff_{NoDC} , %
1000	7.93	12275.64	2283.13	81.40
1100	8.73	13551.75	2727.24	79.88
1200	9.52	14828.35	3204.58	78.39
1300	10.31	16113.29	3720.13	76.91
1400	11.11	17438.26	4281.68	75.45
1500	11.90	18735.36	4874.12	73.98
1600	12.70	20043.65	5512.63	72.50
1700	13.49	21316.36	6180.82	71.00
1800	14.28	22455.01	6883.01	69.35
1900	15.08	23474.13	7628.82	67.50
2000	15.87	24414.41	8401.52	65.59

B. Power take-off system with DC-DC converters

The use of previously developed DC-DC converters [4], which will reduce the currents in main part of PTOS and, accordingly, reduce the power losses in proportion to the square of the current, can lead to a significant reduction of power losses in the power take-off system.

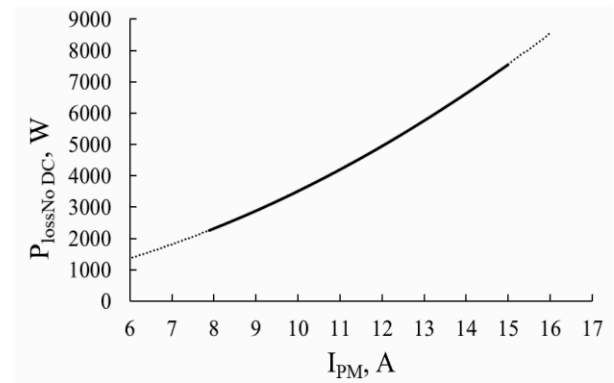
In case of PTOS design using DC-DC converters, the system will be divided into the following sections, where there will be losses in PTOS:

- Section of the cable network between module and DC-DC converter ($P_{LossPM-DC}$);
- DC-DC converter itself (P_{LossDC});
- Section of the cable network from DC-DC converter to inverter through the ($P_{LossDC-Inv}$);
- Inverter ($P_{LossInv}$).

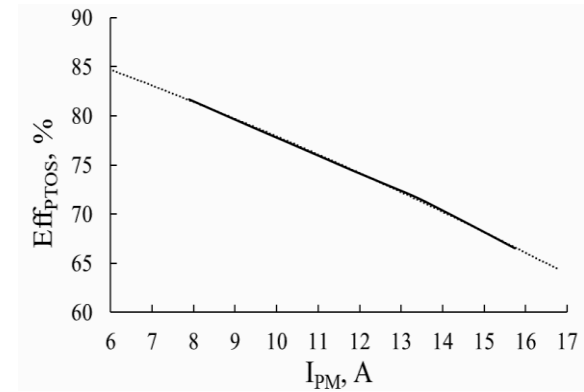
The calculated losses for each of the above-mentioned sections depending on the photovoltaic module current are presented in table 2 and on figures 2 and 3.

TABLE III. POWER LOSS PARAMETERS AND EFFICIENCY, CALCULATED FOR PS PTOS WITH DC-DC CONVERTERS

P_i , W/m ²	I_{PM} , A	$P_{LossPM-DC}$, W	P_{LossDC} , W	$P_{LossDC-Inv}$, W	$P_{LossInv}$, W	$P_{Loss\Sigma}$, W	Eff_{DC} , %
1000	7.68	0.56	10.83	21.43	266.13	697.60	92.50
1100	8.45	0.68	11.95	26.61	293.70	774.99	92.45
1200	9.21	0.81	13.08	32.35	321.24	853.63	92.41
1300	9.98	0.95	14.21	37.02	348.94	931.72	92.37
1400	10.76	1.10	15.37	43.74	377.23	1013.89	92.33
1500	11.54	1.27	16.53	51.02	405.65	1097.47	92.28
1600	12.29	1.44	17.67	58.86	433.45	1180.27	92.23
1700	13.03	1.61	18.77	65.10	460.42	1259.2	92.2
1800	13.83	1.82	19.57	71.66	485.25	1334.87	92.16
1900	14.60	2.02	20.45	78.54	507.51	1403.97	92.12
2000	15.33	2.23	21.27	85.73	528.30	1470.11	92.08

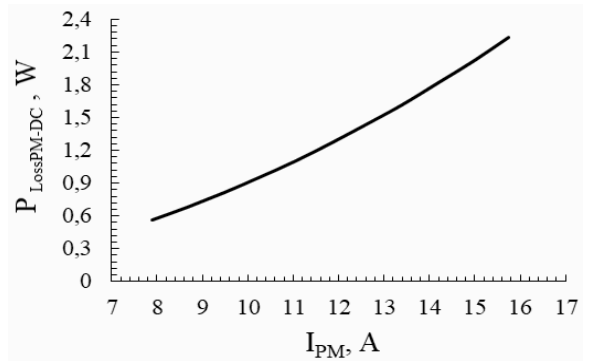


a)

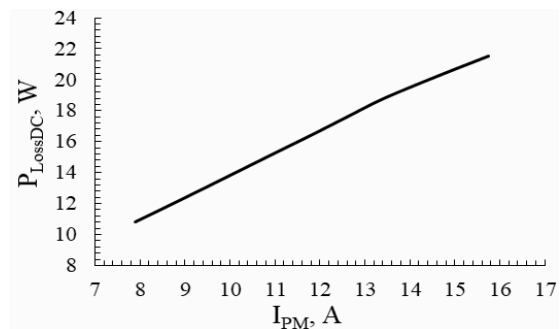


b)

Fig. 1. Calculated values of power losses in PS PTOS without DC-DC converters (a) and calculated values of the PS PTOS without DC-DC converters efficiency of PTOS without the use of DC-DC converters (b) in dependence from photovoltaic module current



a)



b)

Fig. 2. Calculated values of power losses on sections FEM - DC-DC converter (a) and DC-DC converter (b) in dependence from photovoltaic module current

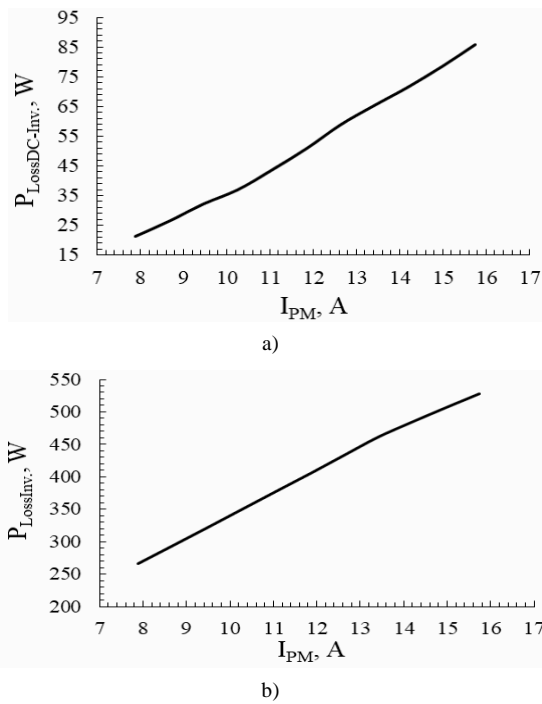


Fig. 3. Calculated values of power losses on sections DC-DC converter-inverter (a) and on the inverter (b) in dependence from photovoltaic module current

Losses in DC-DC converters were calculated based on the experimental device efficiency, which was established as 95.8% [3]. As can be seen from the dependences, the losses on the PTOS sections will increase with the photovoltaic module current [13, 14], but the losses values is much smaller due to the smaller currents values on the sections after the DC-DC converter [15, 16]. The total power loss and efficiency of PTOS using step-up DC-DC converters are shown in Figure 4 in comparison with similar parameters obtained for PTOS without DC-DC converters.

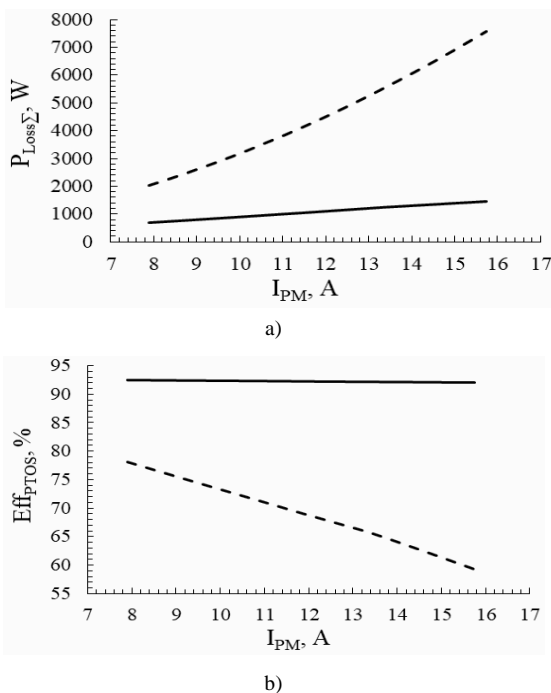


Fig. 4. Calculated values of power losses (a) and efficiency (b) for PTOS with DC-DC converters (solid line) in comparison with PTOS without DC-DC converters (dotted line)

without DC-DC converters (dotted line) in dependence from photovoltaic module current

Based on the results of the PTOS calculations, it can be concluded that the use of DC-DC converters in such system can significantly reduce power losses in the PTOS and, consequently, increase the efficiency of the whole system [17-19]. This will lead to an additional increase of useful power delivered to the consumer through the inverter. According to Figure 4, a, the total power loss in such PTOS at 1700 W/m² illumination power, will be 644.6 W, which is practically in a ten time less than 6180.8 W, which typical for PTOS without DC-DC converters. This will increase the PTOS efficiency, which will increase from 71.0 % to 92.5 %. It is also should note that the efficiency remains almost unchanged in a wide range of illumination powers, which will vary depending on weather and seasonal conditions.

III. EXPERIMENTAL RESULTS OF THE PHOTOVOLTAIC STATION TESTING

A. Research methods

Using the developed and manufactured test bench [4] for the experimental PS parameters investigation, the PS research tests were carried out during five days of working week.

The method of carried out and collecting experimental data, according to the test program, was as follows. At the beginning of daylight, at 6:20AM, the power supply of the test bench was turned on into the data transfer mode onto in-built personal computer. During daylight hours, the operation of measuring instruments and the correctness of experimental data transfer to the PC were monitored. At the end of daylight, the test bench was turned off and obtained data: voltage at the inverter input, the electric power produced by the experimental photovoltaic station and the solar radiation power was saved onto external storage for subsequent analysis and analytical processing [20, 21]. The tests were repeated during 5 working days.

The values of the mentioned parameters received as a result of experimental data analytical processing are presented in table 3.

TABLE IV. PHOTOVOLTAIC STATION TEST RESULTS

Parameter	Date					Average parameter value
	25.04	26.04	27.04	28.04	29.04	
Voltage values on the inverter input, V	624.6-675.0	625.5-675.1	626.7-674.8	625.2-675.0	627.3-675.5	625.8-675.0
Maximal electric power, generated by PS, W	15322.1	14952.8	13195.8	13909.2	14064.7	14065.2
Eff _{PS} , %	18.1-18.4	18.2-18.4	18.1-18.4	18.1-18.4	18.2-18.4	18.29

B. Analysis of the results obtained during photovoltaic station experimental tests

The carrying out of photovoltaic station experimental tests allows not only to confirm the compliance of the main operating parameters, but also to carry out a complex

verification of the efficiency and design completeness for the main PS components.

During the PS research tests the operation of photovoltaic modules cooling system, the PTOS high-voltage part operation and the accuracy of modules installation angles were monitored.

Module cooling system, was built on the principle of thermosyphon coolant circulation, was demonstrate its high efficiency [3, 22]. Due to the design features, the cooling system is fully autonomous and coolant circulation is provided only when module photoreceiving surface is really heating. The absence of temperature sensors and circulating pumps in the system design increases its reliability and minimizes energy costs for its maintenance.

Periodic measurements of module surface temperature carried out during research tests showed that, depending from the incident solar light intensity and the ambient temperature, it was kept at a level of 20-25 °C [23]. This value confirms the presence of cooling system performance margin in order to compensate ambient temperature increase during summer [10].

The power take-off system based on high-voltage DC-DC converters has demonstrated high reliability during research tests [24, 25]. Also, the fact that during the research tests were obtained the calculated efficiency values, confirms the previously achieved high efficiency parameters of power take-off and transfer system, as well as the fact that during DC-DC converters manufacturing did not have place deviate from the developed design solution.

Equipping of PTOS by high-voltage (up to 700 V DC) DC-DC converters requires special demands from insulation quality of high-voltage cables connecting DC-DC converters to the inverter. Therefore, in the process of experimental tests carried out, periodic monitoring of high-voltage connecting cables insulation condition was performed. During the tests, it has not been found any faults or breakdowns of the high-voltage cable insulation and the laying of connecting cables in cable boxes raised above ground level provided good protection of cables from weather and other external factors.

It should also be noted that the decision to use parallel switching of individual generator sets when connecting them to the inverter in addition to increasing the PS reliability (with this type of connection failure of one generator set does not lead to interruptions of entire PS operation) provided the possibility of technological and preventive PS maintenance directly during its work. At parallel switching of generator installations shutdown for carrying out scheduled maintenance or emergency repair of any necessary quantity of generator installations will allow to continue PS operation in stable mode. This feature significantly increases the performance of the developed photovoltaic station design.

Photovoltaic station experimental tests were carried out using test bench. The tests were performed during a summer day, in clear weather conditions, in order to avoid the influence of weather conditions on the specified dependence of the relative power distribution generated by the PS depending on the daytime. The experimentally established power distribution, generated during the day, is shown in Figure 5. Analysis of the above-mentioned dependence for one day allows to exclude the influence of data averaging,

which was carried out at the stage of PS testing. Also, from the data, presented on Figure 5 clearly shown that PS power decreases in inconsistency with sun position that can be explained by a little inaccuracy of a vertical latitude angle installation.

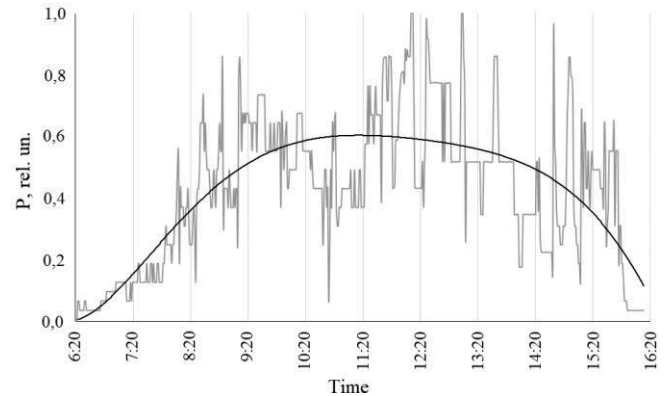


Fig. 5. The relative distribution of power generated by PS depending on daytime of day

IV. CONCLUSION

A power take-off system has been developed for photovoltaic modules, operating under low concentrated solar radiation, which provides the possibility of their use as part of a photovoltaic station. It is established that the power take-off system with adjustable resonant LLC converter in case of using developed photovoltaic modules has an efficiency up to 92.5 % in a wide range of solar radiation intensity, while for classic power take-off system efficiency values no more than 71.0 %. Carrying out the experimental tests of the photovoltaic station allows to confirm the reliable and efficient operation of innovative components, such as the module cooling system, solar concentrators and high-voltage power take-off system. The calculations based on the results of the optimized photovoltaic station experimental tests proved that the experimental sample of the optimized photovoltaic station with a low concentration of solar radiation allows to obtain stable values of electric power on a level of 14 kW.

REFERENCES

- [1] R.V. Zaitsev, M.V. Kirichenko, G.S. Khrypunov, D.S. Prokopenko, L.V. Zaitseva, "Hybrid solar generating module development for high-efficiency solar energy station", *Journal of nano- and electronic physics*, vol. 10, no. 6, pp. 06017, 2018.
- [2] M. Ghadiri, M. Sardarabadi, M. Pasandideh-fard, A.J. Moghadam, "Experimental investigation of a PVT system performance using nanofluids", *Energy Conversion and Management*, vol. 103, pp. 468-476, 2015.
- [3] R.V. Zaitsev, M.V. Kirichenko, G.S. Khrypunov, R.P. Migushchenko, L.V. Zaitseva, "Hybrid solar generating module", *2017 IEEE International Young Scientists Forum on Applied Physics and Engineering*, pp. 112-115, December 2017.
- [4] Y. Sokol, V. Ivakhno, V. Zamaruev, B. Styslo, "Full Soft Switching Dual DC/DC Converter with Four-Quadrant Switch for Systems with Battery Energy Storage System", *2018 IEEE 3rd International Conference on Intelligent Energy and Power Systems*, pp. 155-160, September 2020.
- [5] M.V. Kirichenko, R.V. Zaitsev, A.L. Ivanov, D.S. Lobotenko, "Pulsed LED illuminator for carrier lifetime investigation", *International Young Scientists Forum on Applied Physics*, pp. PECCS-5, October 2015.
- [6] V.P. Nerubatskyi, O.A. Plakhtii, D.V. Tugay, D.A. Hordiienko, "Method for optimization of switching frequency in frequency

- converters”, *Scientific bulletin of National mining university*, vol. 177, no. 1, pp. 61-68, 2021.
- [7] R. Martínez, Y. Bolea, A. Grau, H. Martínez, “Fractional DC/DC converter in solar-powered electrical generation systems”, *2009 IEEE Conference on Emerging Technologies & Factory Automation*, pp. 1-6, September 2009.
- [8] G. Dileep, S.N. Singh, “Selection of non-isolated DC-DC converters for solar photovoltaic system”, *Renewable and Sustainable Energy Reviews*, vol. 76, pp. 1230-1247, 2017.
- [9] M.V. Kirichenko, R.V. Zaitsev, V.R. Kirichenko, “Advanced methods of increasing and monitoring the lifetime of nonequilibrium minority charge carriers in master dies for high-performance silicon solar cells”, *Telecommunications and Radio Engineering*, vol. 69, no. 5, pp. 441-450, 2010.
- [10] R.V. Zaitsev, M.V. Kirichenko, G.S. Khrypunov, *et. al.*, “Operating temperature effect on the thin film solar cell efficiency”, *Journal of nano- and electronic physics*, vol. 11, no. 4, pp. 04029, 2019.
- [11] A. Tetu, “Power Take-Off Systems for WECs”, *Handbook of Ocean Wave Energy*, Springer, pp. 203-220, 2016.
- [12] D.A. Kudii, M.G. Khrypunov, R.V. Zaitsev, A.L. Khrypunova, “Physical and technological foundations of the «Chloride» treatment of cadmium telluride layers for thin-film photoelectric converters”, *Journal of Nano- and Electronic Physics*, vol. 10, no. 3, pp. 03007, 2018.
- [13] I.A. Gospodarev, V.I. Grishaev, E.V. Manzhelii, E.S. Syrkin, S.B. Feodosyev, “Phonon heat capacity of graphene nanofilms and nanotubes”, *Low Temp. Phys.*, vol. 43, no. 3, pp. 264-273, 2017.
- [14] O. Plakhtii, V. Nerubatskyi, “Analyses of energy efficiency of interleaving in active voltage-source rectifier”, *2018 IEEE 3rd International Conference on Intelligent Energy and Power Systems*, pp. 253-258, September 2018.
- [15] M. Shapovalova, O. Vodka, “Image microstructure estimation algorithm of heterogeneous materials for identification their chemical composition”, *2019 IEEE 2nd Ukraine Conference on Electrical and Computer Engineering*, pp. 975-979, July 2017.
- [16] O. Vodka, “Analysis of quantitative characteristics of microstructures that are generated by the probabilistic cellular automata method”, *2019 IEEE 2nd Ukraine Conference on Electrical and Computer Engineering*, pp. 990-994, July 2017.
- [17] V. Nerubatskyi, O. Plakhtii, D. Hordiienko, S. Mykhalkiv, V. Ravlyuk, “A method for calculating the parameters of the sine filter of the frequency converter, taking into account the criterion of starting current limitation and pulse-width modulation frequency”, *Eastern-European Journal of Enterprise Technologies*, vol. 1, no. 8, pp. 46-55, 2021.
- [18] P.C. Pasc, C.D. Dumitru, “SCADA system for solar MPPT controller monitoring”, *Procedia Technology*, vol. 22, pp. 803-807, 2016.
- [19] V. Zamaruev, V. Ivakhno, B. Styslo, “Anti-Aliasing Filter in Digital Control System for Converter with Active Power Filter Function”, *2019 IEEE 39th International Conference on Electronics and Nanotechnology*, pp. 797-801, April 2019.
- [20] L. Yan, S. Jianwei, “Monitoring and fault diagnosis system of wind-solar hybrid power station based on ZigBee and BP neural network”, *Australian Journal of Mechanical Engineering*, vol. 16, pp. 54-60, 2018.
- [21] Ya.V. Scherback, O.A. Plakhtiy, V.P. Nerubatskiy, “Control characteristics of active four-quadrant converter in rectifier and recovery mode”, *Technical Electrodynamics*, no. 6, pp. 26-31, 2017.
- [22] Y.A. Sheikh, A.D. Butt, K.N. Paracha, *et. al.*, “An improved cooling system design to enhance energy efficiency of floating photovoltaic systems”, *J. Renewable Sustainable Energy*, no. 12, p. 053502, 2020.
- [23] K.A. Minakova, R.V. Zaitsev, “Improving the Solar Collector Base Model for PVT System”, *Journal of nano- and electronic physics*, vol. 12, no. 4, p. 04028, 2020.
- [24] S. Nagaraj, R. Ranihemamalini, L. Rajaji, “Design and analysis of control ERS for high voltage gain DC-DC converter for PV panel”, *International Journal of Power Electronics and Drive System*, vol. 11, no. 2, pp. 594-604, 2020.
- [25] O.A. Plakhtii, V.P. Nerubatskyi, D.A. Hordiienko, H.A. Khoruzhevskiy, “Calculation of static and dynamic losses in power IGBT-transistors by polynomial approximation of basic energy characteristics”, *Scientific bulletin of National mining university*, vol. 176, no. 2, pp. 82-88, 2020.
- [26] O. Plakhtii, V. Nerubatskyi, Ya. Scherbak, A. Mashura, I. Khomenko, “Energy efficiency criterion of power active filter in a three-phase network”, *2020 IEEE KhPI Week on Advanced Technology*, pp. 165-170, October 2020.

Electronic Load based on FET-transistor

Roman Zaitsev
Materials for electronics
and solar cells department
National Technical University
“Kharkiv Polytechnic Institute”
Kharkiv, Ukraine
roman.zaitsev@khp.edu.ua

Mykhailo Kirichenko
Materials for electronics
and solar cells department
National Technical University
“Kharkiv Polytechnic Institute”
Kharkiv, Ukraine
mykhailo.kirichenko@khp.edu.ua

Kseniia Minakova
Physics Department
National Technical University
“Kharkiv Polytechnic Institute”
Kharkiv, Ukraine
kсениia.minakova@khp.edu.ua

Abstract—The introduction of electronic load for testing high-accurate low-voltage sources (solar cells) requires thorough reviewing not only the circuit construction, but also thermal and mechanical constructions. Adherence to the indications and principles, which are set out in this article, will provide the load with the ability to work at high power, and in the same time maintain good characteristics and reliability.

Keywords—*electronic load, MOSFET, transistor, testing device, components*

I. INTRODUCTION

The electronic loads, which are available on the market, combine excellent accuracy with complex control interfaces and, as a rule, capable of operating at very high currents at high power [1]. Different models are usually available, each of them is corresponding to a different voltage, power and current range (eg. Chroma examples, Fig. 1) [2]. The figure shows that the lowest achievable resistance is about 5 mOhm, and the current can reach 80 A.

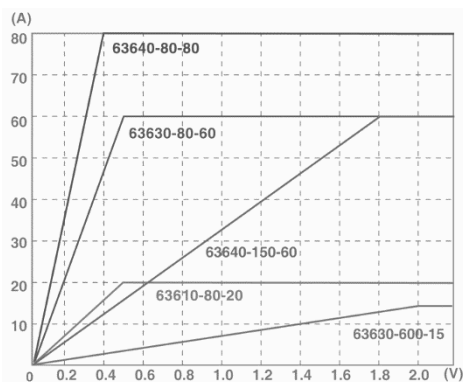


Fig. 1. Voltage and load current characteristics of the Chroma 63600 series [2]

However, despite these technical characteristics, the overall efficiency of the load array is fundamentally limited by its electrical connection to the tested power supply source. Copper and aluminum conductors with a cross section of 40 cm² or more are used for the connection requirements and this connection length imposes significant resistive losses between the tested power supply source and the load modules. This additional resistance affects the load voltage, and the parasitic inductance L_p in the conductors limits the maximum speed of transients (dI/dt) [3]:

$$\frac{dI}{dt_{max}} \leq \frac{Vd}{L_p} \quad (1)$$

Also, for testing more powerful power supply sources, it is possible to combine several of these load modules in

parallel (it is possible to achieve an effective resistance below 2.7 mOhm). Moreover, when more and more individual loads that are connected in parallel, the installation becomes larger, and, accordingly, the more resistance busbars and inductive losses on the connection busbar. Obviously, to achieve the highest speed of transients and the lowest total resistance requires a more specialized solution of electronic load.

II. SCHEME OF ELECTRONIC LOAD REALIZATION

To simulate the behavior of a powered semiconductor device [4, 5], we need an electronic load with the following characteristics:

- the highest possible rate of load current increase (dI/dt) (at best the rate of increase is also regulated);
- regulated load current;
- high scattering power, both peak and continuous;
- ability to control the load current with high accuracy and wide bandwidth.

To test low voltage power supply sources at very high current levels (eg. solar modules), the electronic load must have an ultra-low minimum resistance. Finally, the electronic load must be designed for connecting to the test source with minimal resistance and inductance [6], otherwise the overall efficiency will be limited by the connection itself [7].

The simplest load that can be offered is a power resistor. If its size and cooling are correct, it can meet the requirement for high power dissipation, and the current can be controlled directly (by measuring the voltage on a known resistor). Sequentially adding a switch allows you to generate a transient load. However, the load will be either fully on or off, and the current will depend on the voltage being tested. The velocity of current change is not controlled or regulated [8, 9]. Obviously, this is not a flexible solution that can be adapted to a wide range of testing requirements.

For providing changeable load and adjustable current reduction velocity (velocity which impact on the load current increases and decreases), it is necessary to build an active circuit based on an operational amplifier. The topology of this circuit is shown in Figure 2. The operational amplifier activates the gate of the power MOSFET transistor to set the controlled voltage on the sensor resistor. It results in a controlled load current flowing from the outlet to the MOSFET source and through the sensor resistor to ground. The power of the MOSFET adds current amplification, but does not add voltage amplification

because it works as a current amplifier (source - follower) [10].

This circuit can be implemented with an n-channel MOSFET with a sensor resistor on the lower side or with a p-channel MOSFET with a sensor resistor on the upper side. Anyway, the sensor resistor adds negative reverse connection because it is plugged to a MOSFET source, subtracting the voltage from the gate voltage as the current increases [11, 12], and vice versa by adding the gate voltage as the current decreases, which promotes stability.

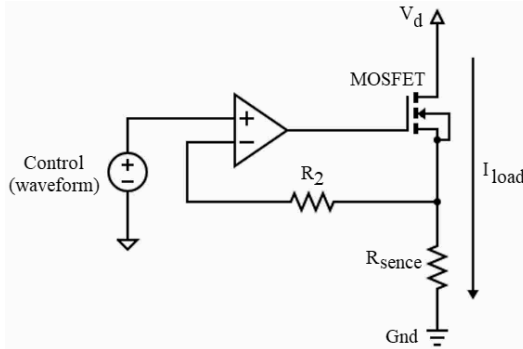


Fig. 2. Basic circuit of controlled electronic load

The practical implementation of an active electronic load circuit with an n-channel MOSFET is shown in Figure 3. This circuit is a combination of a simple load from Fig. 2 and a differential amplifier. This topology improves accuracy by taking into account the dynamic and static differences in ground potential between the input signal (SGND) and the underside of the sensor resistor (GND).

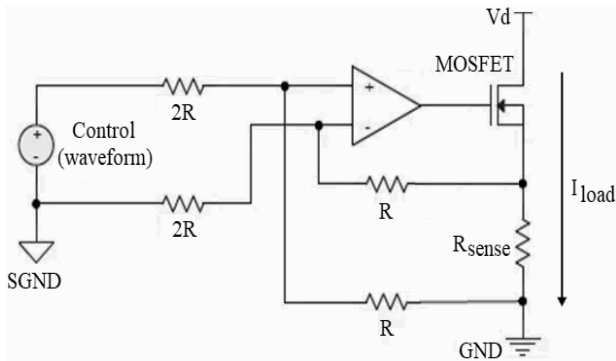


Fig. 3. Detailed circuit of the electronic load

The load current, according to the proposed scheme, is proportional to the voltage and the shape of the control signal [13], while the coefficient of amplification is set by ratio input resistances and reverse connection of resistances.

An active electronic load circuit has many advantages over a simple switching resistor. Unlike simple resistance, active resistance can generate alternating load current from zero to maximum current. Besides, when the load current is controlled by an operational amplifier in a closed loop, the current accurately tracks the control signal [14]. Therefore, the active electronic load can control the rate of decrease of current. Finally, since the circuit has a resistive element with a fixed value, accurate measurement of the load current of the high bandwidth is relatively simple.

Figure 4 presents one of the options for adding a second amplifier to accurately measure the load current. In this case, it is configured as a conduction amplifier, which

allows you to easily sum up the current measurement signals from several electronic load circuits.

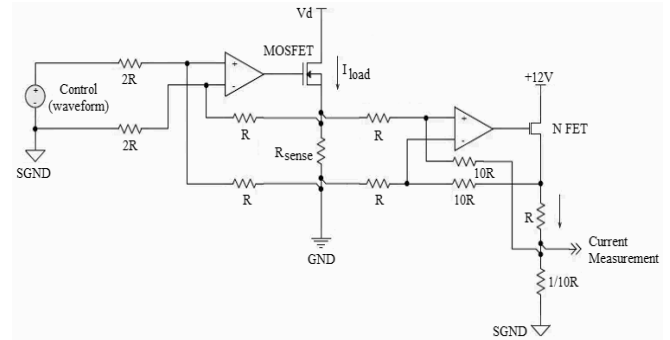


Fig. 4. Measurement of the current with the additional amplifier

III. SELECTION OF COMPONENTS AND THEIR CALCULATION

A. Selection of MOSFET-transistor

The power transistor must be selected to provide a fast response while maintaining high power dissipation. It is necessary to consider several electrical and thermal characteristics.

Shutter charge. To modulate the current flowing through the MOSFET with high stability and high bandwidth, the operational amplifier must be able to quickly change the voltage from the gate to the source. A high-capacity gate-source and gate-drain MOSFET (C_{GS} and C_{GD} , respectively) will require more control current to achieve the desired rise rate. Therefore, it is important to choose a transistor with a low FOM and, accordingly, low parasitic capacitance. For many MOSFETs, the total charge Q_G is a good metric, and comparisons between MOSFETs can be made quickly using only this parameter.

Voltage drain source. The drain source voltage (V_{DS}) must be high enough to withstand the voltage of the power supply under test, including any transient surges or overvoltages. Most MOSFET transistors are designed for 12 V, 25 V, 30 V or even higher, so choosing a transistor suitable for testing low and medium voltage sources is not difficult. In general, the MOSFET should be selected with a voltage of V_{DS} that is at least 125% of the measured voltage. A higher V_{DS} in a transistor of the same size will adversely affect other performance, so choose the device with the lowest allowable V_{DS} value.

Drain current. The rated current of the drain source I_D must be sufficient to transmit the required load current. If it is necessary to operate with high currents, it is possible to use an array of parallel load circuits, which facilitates power dissipation and increases the maximum I_D . In other words, if an array of N equal active load loads is used, the current through each MOSFET transistor is the total load current divided by N . In this case, one operational amplifier can control several MOSFETs in parallel, provided that each MOSFET is connected to an independent sensor resistor on the output terminal. This circuit ensures that the total current is distributed evenly between the MOSFET transistors through the previously described negative reverse connection characteristic of the source-follower.

While controlling two or more MOSFET transistors, it is usually necessary to add small supports in series with the MOSFET gates to prevent oscillations. The configuration

of the operational amplifier is further expanded, including summation by duplicating the reverse connection and resistance of the input divider in each input of the circuit.

B. Thermal power of the load

The most important characteristic of the MOSFET used in electronic loading is its ability to dissipate processed heat. The total load power (P_L) is obviously the product of the load current and the test voltage:

$$P_L = I_{load} \times V_d$$

If several load chains operate in parallel, each chain conducts current I_{load}/N [15, 16], and the total load power is distributed more or less evenly between the transistors.

Part of this power is dissipated in the sensor resistors (P_R) and this part varies as the square of the load current:

$$P_R = (I_{load}/N)^2 \times R_{sense}$$

The power remnant is dissipated in the MOSFET-transistor (P_M):

$$P_L = (P_M + P_R) \times N$$

$$P_M = P_L/N - P_R$$

$$P_M = (I_{load} \times V_d)/N - (I_{load}/N)^2 \times R_{sense}$$

The ability of the MOSFET to dissipate heat is summarized by two key parameters: the thermal resistance of the transition to the Θ_{JC} barrel and the stationary power dissipation P_D . Of these two values, Θ_{JC} is the most useful because it indicates the lowest possible increase in the MOSFET transition temperature as a function of power, excluding all environmental influences [15, 17, 18].

Although the MOSFET characteristics provided by the manufacturer also provide the values of the thermal resistance to the environment Θ_{CA} , this value is determined by the standard PCB size and design. High power electronic loads are typically designed for maximum heat dissipation with significantly lower thermal resistance than the typical open air thermal resistance values Θ_{JA} contained in the MOSFET characteristics provided by the manufacturer. In other words, because a high-power electronic load requires a heatsink that is significantly different from the standard test board Θ_{JA} , the value of Θ_{JC} is the most useful.

In addition to the thermal resistance characteristics of the transistor package, the maximum p-n transition temperature of the silicon T_{Jmax} should also be taken into account. Most high-power MOSFETs are rated at T_{Jmax} from 150°C to 175°C [19]. The electronic load must be designed so that the multiplication of the MOSFET P_M power and the thermal resistance of the transistor package in combination with the maximum temperature T_{MB} of the package does not exceed T_{Jmax} [20]:

$$P_M = (T_{jmax} - T_{MB})/Q_{JC}$$

Depending on the choice of parameters, this correlation gives either the maximum allowable stable power for the MOSFET, or the maximum allowable radiator temperature at the desired maximum power.

C. Safe range of MOSFET operating parameters

The MOSFET power table usually includes a safe-operating-area (SOA) graph. This graph shows the constant

pulse power of the MOSFET. The SOA graph, for example, for PSM2R0 is shown in Figure 5.

The SOA graph is formed for a fixed temperature, additional curves present an increase in peak power for a shorter pulse duration. It is worth noting that the curves on the SOA graph are usually constant power lines (constant product of $I_{DS} \times V_{DS}$). The ability of the MOSFET to process much more power at short pulses is very useful for electronic load, which is designed to test transients.

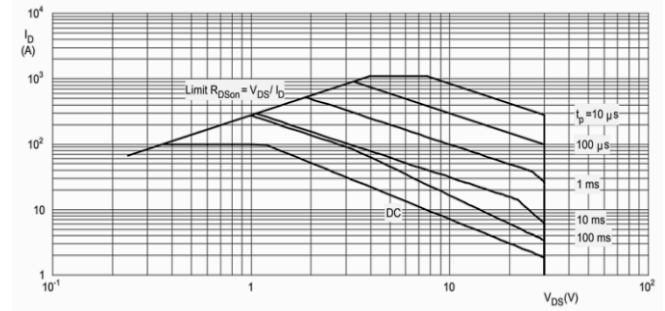


Fig. 5. Graph of the safe operating area for the MOSFET-transistor PSMN2R0, $T_c = 25^\circ\text{C}$

It is important to design the electronic load so that the MOSFET does not operate above its SOA curve for any predicted pulse width [21, 22]. Operating points must be located on the SOA section to ensure safe operation of the structure. Some MOSFETs are optimized for linear operation and are specifically designed to have a larger area under the SOA curve, there are also MOSFETs optimized for fast transitive processes.

D. Transitive thermal resistance

The pulsed transient thermal impedance of the MOSFET is much lower than the stationary thermal impedance due to the heat capacity of the device package, lead base and package materials.

Unlike the SOA graph, the thermal impedance graph is not a function of a specific T_{MB} value. This makes it very useful to determine the increase in MOSFET transition temperature above T_{MB} for any given current pulse width and duty cycle. When the operative cycle is close to 100% and the pulse width is close to DC, the graph of the transient thermal impedance coincides with the value of the steady state thermal impedance of the transition to the barrel Θ_{JC} . For example, using Figure 4, we can see that the MOSFET will pass a pulse of 200 W, which lasts no more than 100 μs at an operative cycle of 10% (in other words, a pulse of 100 μs , repeated at a frequency of 1 kHz), the effective thermal impedance at this transition process is only 0.075 $^\circ\text{C}/\text{W}$, compared with a stable value of $\Theta_{JC} = 0.45^\circ\text{C}/\text{W}$. The product of this transient thermal impedance and the pulse value of 200 W gives the predicted increase in T_j by approximately $200\text{ W} \times 0.075^\circ\text{C}/\text{W} = 15^\circ\text{C}$.

E. Selection of sensor resistor

Heat sink. Like a power MOSFET, a sensor resistor in an active electronic load circuit also dissipates a significant part of the total load power. It is important to choose a sensitive resistor that can not only conduct the load current of each parallel branch, but also quickly transfer the processed heat to the printed circuit board and radiator.

Such a resistor must have the following mechanical characteristics:

- large area of contact with the printed circuit board for heat sink;
- barrel with low thermal resistance, which can be joined with cooling (radiator);
- resistive element and barrel materials that can withstand high operating temperatures.

The first characteristic favors components for surface mounting because the resistor conductors are electrically connected to the PCB at only two through holes. The conductors also have a significant resistive and inductive resistance for the load current. Also, most enclosures are difficult to thermally connect to the PCB and heatsink for efficient cooling. SMD resistors have two key advantages: they are soldered to the wide plates on the PCB and usually have a thin flat housing, which allows you to easily establish an effective thermal connection with the radiator.

Housing materials are also important for thermal performance. The resistor, made of plastic, has the advantage that it is electrically isolated from the radiator [23]. However, the encapsulation usually has a higher thermal resistance than the element itself, so non-encapsulated devices can achieve a lower total thermal resistance.

Low parasitic inductance. The parasitic inductance in the sensor element directly limits the maximum current rise rate that can be achieved with an electronic load (1), because the current cannot grow faster than the inductance allows [24]. In addition, at high current growth rates, the parasitic inductance reduces the voltage on the sensor element, which leads to a deviation from the actual load current. Instead, the transient voltage across the resistor is the sum of the resistive voltage and the inductive voltage:

$$I_{sense} = (V_{sense}/R_{sense}) \times (1 - e^{-t/t})$$

$$V_{sense} = (I_{sense} \times R_{sense}) / (1 - e^{-t/t})$$

$$t = L_{sense}/R_{sense}$$

The circuit of the electronic load amplifier cannot distinguish the inductive part of the signal from the resistive part, so the actual load current increases more slowly than the voltage signal on the sensor resistor (Fig. 6).

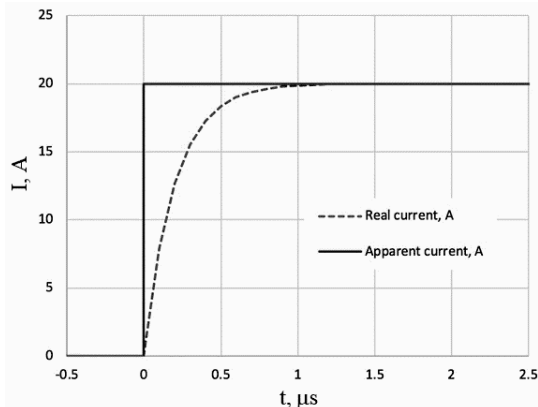


Fig. 6. Transient characteristic of the resistor (5 mOhm with an inductance of 1 nH)

In Figure 6, the ideal current is the voltage across the sensor resistor, which is regulated to a constant value by the operational amplifier in the load circuit, responding to the step of the input control voltage. The real current lags behind the voltage of the sensor resistor with a time constant $\tau \approx 200$ ns. The actual current agrees with the control signal only after approximately $5\tau = 1$ μ s, which makes the circuit inefficient for generating fast load transients.

This lag is a problem for both electronic load and current measurement circuits - both must be compensated by the value of this time constant. The inductive signal can be leveled by applying a single-pole low-pass filter to the signal. The filter can be implemented as an RC filter on a touch resistor. The filter should be chosen so that the time constant corresponds to the sensor resistor:

$$t = R_{filter} \times C_{filter} = L_{sense}/R_{sense}$$

If the filter is added through a sensor resistor, care must be taken to ensure that the DC ratio of the operational amplifier does not change.

To alleviate the problem before it occurs, choose a sensitive resistor with low inductance. A short, wide and thin resistive element will have a lower inductance than a long and thin or spiral one.

Accuracy of sensor resistor. Although this is not critical for load transient tests, the absolute accuracy of the electronic load is extremely important if the measured current is to be used to calculate the efficiency of the power supply being tested [25, 26]. The electronic load can never be more accurate than the sensor resistor itself, so it is important to choose a sensor resistor with high accuracy.

Because the sensor resistor will also dissipate power, the temperature coefficient of resistance (TCR) plays a significant role in load accuracy over a wide power range. As the resistor heats up, its resistance R_T also increases, usually in direct proportion to the temperature T :

$$R_T = R_{nom} \times (1 + (T - 25^\circ C) \times TCR)$$

Many industrial sensor resistors have a TCR value of 50 ppm/ $^\circ$ C or lower. This is equivalent to a change in resistance of only 0.5% with increasing temperature by 100 $^\circ$ C [27]. If greater accuracy is required, a temperature measurement circuit can be added to the electronic load. Then the current measurements can be adjusted after data collection based on the TCR value and the temperature of the element at the time of measurement.

A sensor resistor with a separate special power connection and sensor also helps increase accuracy. Separation of the connection into a high current circuit and a low current circuit eliminates the need to add current to the current due to the measuring circuit. This connection is commonly referred to as a Kelvin connection, or a four-probe connection. Many sensor resistors are made in this way, especially when the resistor is designed for high current and low resistance.

Maximum current. The maximum current of the electronic load is a simple function of the voltage of the test power supply and the combined resistance of all MOSFETs and sensor resistors, with the MOSFET fully open. To prevent saturation of the amplifier at the highest load current, the structure must have a total series resistance,

which is significantly below the test voltage divided by the maximum current:

$$R_{load,min} = (R_{DS} + R_{sense})/N$$

$$R_{load,min} = V_{d,min}/I_{load,max}$$

This allows the operational amplifier to hold the MOSFET in the linear region at the maximum controlled current. If the current rises above $I_{load,max}$, the load circuit enters saturation, fully opening the MOSFET, but can no longer support load current control.

Package design. Because the active circuit controls the load current by holding the MOSFET in the saturation region [28], the MOSFET dissipates most of the power in the electronic load. The sensor resistor also dissipates power proportional to the square of the load current. Because the resistor and MOSFET dissipate significant power under load, they should be chosen carefully. Thermal construction is very important, it will avoid damage caused by excessive heating.

Even distribution of full power. If both the MOSFET and the sensor resistors have the same power, the design of the electronic load can be approximately optimized by distributing the power between the transistor and the sensor element at maximum current. This is achieved by setting the value of the sensitive resistor approximately equal to the R_{DS} of the open MOSFET. This method also minimizes peak power in both sensor resistors and MOSFETs, but requires cooling of the resistor resistors.

The graph in Figure 7 shows how power is dissipated in the MOSFET and sensor resistors depending on the load. If the transistors or sensor resistors are a limiting factor for the total power dissipation, the resistance balance $R_{load,min}$ can be shifted to reduce the power in the transistor or sensor resistor, due to the higher peak power in the opposite component.

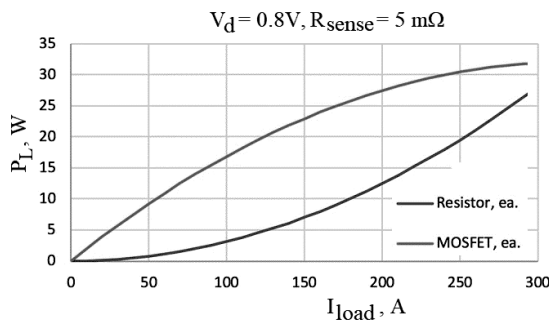


Fig. 7. Power output in MOSFET and sensor resistor, depending on load current

Using this circuit at current levels below the maximum, the MOSFET always dissipates more power than the sensor resistor, because most of the voltage drop occurs on the MOSFET. The power dissipation balance also varies greatly depending on the voltage of the power supply under test.

F. Selection of operational amplifiers

The operational amplifier must have sufficient output power to control the MOSFET, which is a capacitive load on the operational amplifier. The strength of the control current and the rate of voltage drop are also important parameters when choosing an operational amplifier,

especially when a high rate of load current reduction is required.

Unipolar power supply. Since the electron load must have a linear response from zero to full load, a unipolar supply is sufficient. Bipolar power is not required because the MOSFET stops conducting current when the output voltage of the amplifier is less than the threshold voltage of the V_{GS} gate. However, the operational amplifier and its power supply must be selected so that the voltage on the MOSFET gate is high enough to achieve the maximum desired load current. This means that the output voltage of the operational amplifier must exceed $I_{load,max} \times R_{sense} + V_{GS}$. This criterion significantly narrows the range of operational amplifiers, as many devices with unipolar power supply are limited to +5 V. There are significantly fewer operational amplifiers with a supply voltage of +12 V or higher.

Amplifier accuracy. Precise operational amplifier provides better accuracy of load current setting depending on the input control signal. This makes the load easier to use and more stable. Low input bias voltages can reduce or eliminate the load current bias, especially when the control signal is 0 V. Low bias input currents allow you to use more input and feedback resistance in the differential amplifier circuit, which in turn improves the input resistance.

Current measurement. In addition to providing a fast and accurate load current value, the circuit should also include load current monitoring means. This is usually an output signal that can be connected to the input of the measuring device (Fig. 4) to provide a graphical indication of the shape of the load current in real time. If a separate amplifier is used to measure the load current, its accuracy can reduce or eliminate the need for calibration. This is especially useful for very high current loads, in which case it may not be possible to find a precision shunt, making it difficult or impossible to calibrate to an external reference. The simplest current control circuit is a summing amplifier that generates an output voltage proportional to the load current [29].

One of the possible improvements is the conversion of the output signal of the amplifier into a current source (Fig. 4). This provides an output current proportional to the load current. This approach has some advantages over the voltage signal. The individual outputs of the current source can be easily summed by applying them to a single resistor, which allows multiple load devices to report the total load current without the need for additional summing amplifier. The outputs of the current source are also less sensitive to noise caused by earth potential shifts between the load device and the measuring equipment, especially if the summing resistor is located on the measuring equipment.

The current or monitoring circuit can be optimized for accuracy or for speed and bandwidth. The first is important if the electronic load is to be used to measure efficiency, where the direct load current must be accurately known. The latter is important for the analysis of the transient reaction, where the shape of the load current signal is critical to accurately represent the rate of increase of the load current. In many cases, a good compromise between speed and accuracy can be reached. Amplifiers with higher accuracy typically support a lower bandwidth, whereas faster amplifiers typically have higher input bias voltages and bias currents.

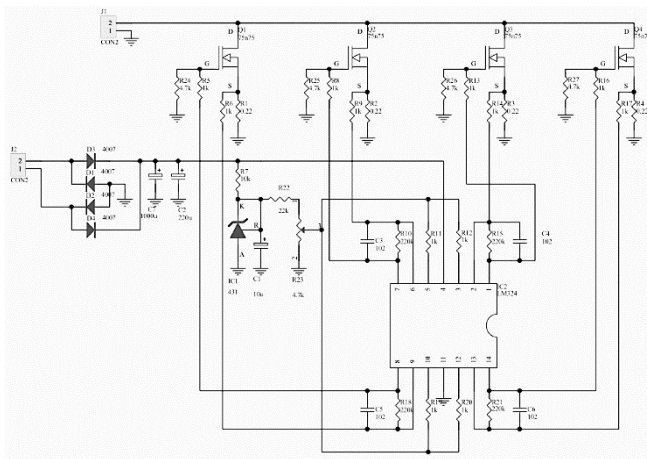


Fig. 8. Electrical diagram of the electronic load unit

IV. CONCLUSION

Based on the considered physical and circuit solutions for the implementation of the electronic load unit, the electrical circuit shown in Figure 8 was developed. These transistors are controlled by four unipolar operational amplifiers integrated in the LM324 chip. The control of the electronic load unit is realized by controlling the voltage at the positive feedback terminals, which is additionally stabilized by the TL431 chip. The unit is powered by a source of direct stabilized current with a voltage of 12 V (provides additional filtering from voltage fluctuations).

REFERENCES

[1] G.C. Mazumder, P.R. Biswas, N. Shams, *et al.*, "Development Of A Computerized I-V-Tracing System For Solar PV Module Testing", *International Journal of Scientific & Technology Research*, vol. 5, no. 6, pp. 328-333, 2016.

[2] <https://idm-instrumentos.es/>

[3] M.L. Beye, T. Wickramasinghe, J.F. Mognotte, *et al.*, "Active Gate Driver and Management of the Switching Speed of GaN Transistors during Turn-On and Turn-Off", *Electronics*, vol. 10, no. 2, pp. 106-119, 2021.

[4] M.V. Kirichenko, R.V. Zaitsev, A.L. Ivanov, *et al.*, "Pulsed LED illuminator for carrier lifetime investigation", *International Young Scientists Forum on Applied Physics*, pp. PECCS-5, October 2015.

[5] G. Nel, W. Doorsamy, "Development of an Intelligent Electronic Load Controller for Stand-Alone Micro-Hydropower Systems", *2018 IEEE PES/IAS PowerAfrica*, pp. 18202117, November 2018.

[6] O.A. Plakhtii, V.P. Nerubatskyi, D.A. Hordiienko, *et al.*, "Calculation of static and dynamic losses in power IGBT-transistors by polynomial approximation of basic energy characteristics", *Scientific bulletin of National mining university*, vol. 176, no. 2, pp. 82-88, 2020.

[7] V. Nerubatskyi, O. Plakhtii, D. Hordiienko, *et al.*, "A method for calculating the parameters of the sine filter of the frequency converter, taking into account the criterion of starting current limitation and pulse-width modulation frequency", *Eastern-European Journal of Enterprise Technologies*, vol. 1, no. 8, pp. 46-55, 2021.

[8] Y. Sokol, V. Ivakhno, V. Zamaruev, *et al.*, "Full Soft Switching Dual DC/DC Converter with Four-Quadrant Switch for Systems with Battery Energy Storage System", *2018 IEEE 3rd International Conference on Intelligent Energy and Power Systems*, pp. 155-160, September 2020.

[9] V. Zamaruev, V. Ivakhno, B. Stylo, "Anti-Aliasing Filter in Digital Control System for Converter with Active Power Filter Function", *2019 IEEE 39th International Conference on Electronics and Nanotechnology*, pp. 797-801, April 2019.

[10] S. Ichino, T. Mawaki, A. Teramoto, *et al.*, "Analysis of Random Telegraph Noise Behaviors toward Changes of Source Follower

Transistor Operation Conditions using High Accuracy Array Test Circuit", *IEICE Tech. Rep.*, vol. 117, no. 260, pp. 57-62, 2017.

[11] O. Plakhtii, V. Nerubatskyi, "Analyses of energy efficiency of interleaving-source rectifier", *2018 IEEE 3rd International Conference on Intelligent Energy and Power Systems*, pp. 253-258, September 2018.

[12] R.V. Zaitsev, M.V. Kirichenko, G.S. Khrypunov, D.S. Prokopenko, L.V. Zaitseva, "Development of hybrid solar generating module for high-efficiency solar energy station", *First Ukraine Conference on Electrical and Computer Engineering*, Kiyv, Ukraine, pp. 360-364, June 2017.

[13] O. Miroshnyk, S. Kovalyshyn, A. Tomporowski, *et al.*, "Research of probability characteristics of current and voltage unbalance based on using graphs of load for the duration at the substation", *Journal of Physics: Conference Series*, vol. 1426, no. 1, pp. 012036, 2020.

[14] S. Sergey, D. Dmitriy, "Experimental studies of current voltage characteristics of the arrester leakage currents in the area", *2015 International Young Scientists Forum on Applied Physics*, pp. 15617754, September 2015.

[15] V.P. Nerubatskyi, O.A. Plakhtii, D.V. Tugay, *et al.*, "Method for optimization of switching frequency in frequency converters", *Scientific bulletin of National mining university*, vol. 177, no. 1, pp. 61-68, 2021.

[16] A. Kelin, O. Larin, R. Naryzhna, *et al.*, "Mathematical Modelling of Residual Lifetime of Pumping Units of Electric Power Stations", *Advances in Intelligent Systems and Computing*, vol. 1113, pp. 271-288, 2020.

[17] Ya.V. Scherback, O.A. Plakhtii, V.P. Nerubatskyi, "Control characteristics of active four-quadrant converter in rectifier and recovery mode", *Technical Electrodynamics*, no. 6, pp. 26-31, 2017.

[18] A. Tsbizov, I. Kovačević-Badstübner, B. Kakarla, *et al.*, "Accurate Temperature Estimation of SiC Power mosfets Under Extreme Operating Conditions", *IEEE Transactions on Power Electronics*, vol. 35, no. 2, pp. 1855-1865, 2020.

[19] V.V. Eremenko, V.A. Sirenko, I.A. Gospodarev, *et al.*, "Role of acoustic phonons in the negative thermal expansion of the layered structures and nanotubes based on them", *Low Temp. Phys.*, vol. 42, no. 5, pp. 401-410, 2016.

[20] O. Plakhtii, V. Nerubatskyi, Ya. Scherbak, *et al.*, "Energy efficiency criterion of power active filter in a three-phase network", *2020 IEEE KhPI Week on Advanced Technology*, pp. 165-170, October 2020.

[21] V.V. Eremenko, V.A. Sirenko, I.A. Gospodarev, "Electron and phonon states localized near the graphene boundary", *Low Temp. Phys.*, vol. 43, No. 11, pp. 1323-1331, 2017.

[22] R.V. Zaitsev, V.R. Kopach, M.V. Kirichenko, *et al.*, "Single-crystal silicon solar cell efficiency increase in magnetic field", *Functional Materials*, vol. 17, no. 4, pp. 554-557, 2010.

[23] O. Rubanenko, O. Yanovych, O. Miroshnyk, *et al.*, "Hydroelectric Power Generation for Compensation Instability of Non-guaranteed Power Plants", *2020 IEEE 4th International Conference on Intelligent Energy and Power Systems*, pp. 52-56, September 2020.

[24] V.V. Eremenko, V.A. Sirenko, I.A. Gospodarev, *et al.*, "Electron spectra of graphene with local and extended defects", *Journal of Physics: Conference Series*, vol. 969, no. 1, pp. 012021, 2018.

[25] M.V. Kirichenko, R.V. Zaitsev, A.I. Dobrozhan, *et al.*, "Adopting of DC magnetron sputtering method for preparing semiconductor films", *2017 IEEE International Young Scientists Forum on Applied Physics and Engineering*, pp. 108-111, December 2017.

[26] O. Avdieieva, O. Usatyi, O. Vodka, "Development of the Typical Design of the High-Pressure Stage of a Steam Turbine", *Lecture Notes in Mechanical Engineering*, pp. 271-281, 2020.

[27] G.S. Khrypunov, G.I. Kopach, R.V. Zaitsev, *et al.*, "Flexible solar cells are based on underlying layers of cdte obtained by magnetron sputtering", *Journal of Nano- and Electronic Physics*, vol. 9, no. 2, pp. 02008-1-02008-5, June 2017.

[28] Y. Taur, H.-H. Lin, "Modeling of DG MOSFET I - V Characteristics in the Saturation Region", *IEEE Transactions on Electron Devices*, vol. 65, no. 5, pp. 1714-1720, 2018.

[29] M.A. Bin Mohd Yusof, N. Tsukiji, Y. Kobori, *et al.*, "A Study on Loop Gain Measurement Method Using Output Impedances in Operational Amplifier", *J. Tech. Soc. Sci.*, vol. 2, no. 3, pp. 19-28, 2018.

Increasing Efficiency of Photovoltaic Thermal Systems

Kseniia Minakova
 Physics Department
 National Technical University
 “Kharkiv Polytechnic Institute”
 Kharkiv, Ukraine
[ksenii.minakova@kmpi.edu.ua](mailto:kseniia.minakova@kmpi.edu.ua)

Roman Zaitsev
 Materials for electronics
 and solar cells department
 National Technical University
 “Kharkiv Polytechnic Institute”
 Kharkiv, Ukraine
roman.zaitsev@kmpi.edu.ua

Mykhailo Kirichenko
 Materials for electronics
 and solar cells department
 National Technical University
 “Kharkiv Polytechnic Institute”
 Kharkiv, Ukraine
mykhailo.kirichenko@kmpi.edu.ua

Abstract— The main aim of proposed research is to consider a method for increasing the efficiency and the lifetime of photovoltaic systems. This article briefly presents theoretical methods for increasing the efficiency of such systems, as well as increasing the service life, by simulating the cooling parameters of the absorber surface of such systems and tracking the maximum power. Modeling and the obtained theoretical model will allow in the future selecting the most suitable technical solutions to maximize the energy output of photovoltaic systems for various design solutions.

Keywords—photovoltaic systems, solar energy, PV/T panels, thermal conductivity, temperature gradient, solar thermal collector, heat transfer

I. INTRODUCTION

Photovoltaic systems (PV), which convert solar energy into electricity, are promising systems among renewable energy sources. The electricity produced by photovoltaic panels has great potential, but at present, there are technological shortcomings that prevent them from increasing their efficiency. Moreover, eliminating these shortcomings can increase the service life of photovoltaic systems and the total amount of electricity produced.

The efficiency of modern photovoltaic cells currently ranges from 10% to 38% under standard conditions. The efficiency of photovoltaic panels is less than the photovoltaic cells used to create them. Thus, one way to increase efficiency is to find new suitable design solutions. An example of photovoltaic panels optimization is creating of PV/T panels [1, 2]. This can be achieved by improving processes and models of heat balance [3, 4], the results of optimization research and methods are given in this article.

In earlier works [5-7] were examined only heat removal options from the tube along its surface without losses in passing through the heat absorber plate that is a kind of heat absorber (an absorber on which has the tube) and the heat loss of the adsorbing surface.

II. ADVANCED MODEL

The heat sink absorber usually consists of round tubes connected to a flat absorber plate. The plate absorbs the heat that enters the solar cell when it is irradiated with sunlight, and transfers it to the coolant circulating in the tubes [8]. The absorber and tubes are made of materials with high thermal conductivity (copper, aluminum) to optimize heat

transfer to the liquid and reduce losses. Figure 1 shows a cross section of the absorber.

The minimum temperature (T_p) in the absorber is observed over the cooling tube. The maximum temperature is observed in the middle between the tubes ($x = 0$), that is, at the same distance from the tubes. The temperature gradient at this point is zero, and the temperature profile is symmetrical. If the gradient is zero, then according to Fourier's law, there is no heat transfer at this point. Based on this, we can assume that the absorber plate is a normal edge of the radiator at $x = 0$ and length $(W-D)/2$ (fig. 2).

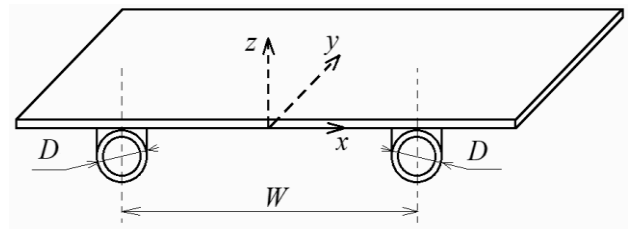


Fig. 1. Absorber of a solar thermal collector

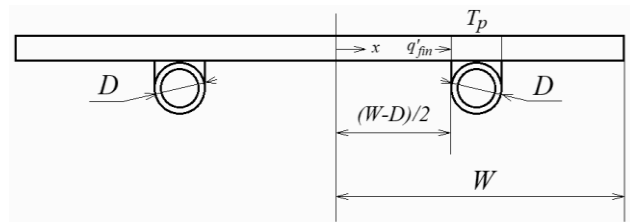


Fig. 2. Temperature distribution in the absorber along the axis x

Assume that the material of the absorber plate is thin and has a high thermal conductivity, and then the temperature above the tube can be considered as homogeneous at T_p . To simplify the analysis and evaluate the heat transfer only by direction x [9- 12], suppose that in the direction y (along the tube) there is no temperature gradient.

Under these conditions, the absorbent section between the middle ($x = 0$) and the surface above the tube ($x = (W-D)/2$) can be considered as a classic problem (fig. 3).

To analyze the configuration-reduced areas, the law applicable to the heat balance [13, 14] of the unit area (steady state energy balance of an element) and get the following equation:

$$\Delta x I - \Delta x U_L (T_x - T_a) + \left(-k_{abs} H \frac{dT}{dx} \Big|_x \right) - \left(-k_{abs} H \frac{dT}{dx} \Big|_{x+\Delta x} \right) = 0 \quad (1)$$

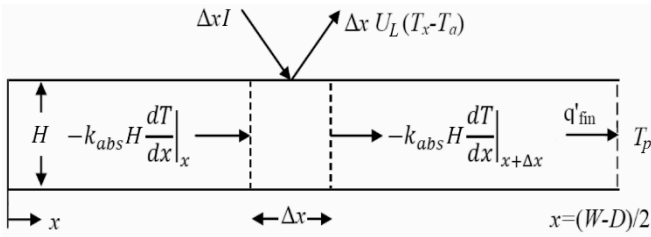


Fig. 3. Heat balance in any part of the absorber

where I – absorbed thermal energy (W/m^2); H – collector plate thickness (m); U_L – loss factor ($W/m^2 \cdot K$); k_{abs} – thermal conductivity of the absorber material ($W/m \cdot K$); T_a – ambient temperature; T_x – the temperature of the absorber at the point x ; q'_{fin} – heat transfer in the direction x at $x = (W-D)/2$ per unit length of tube (W/m).

Calculating the above equation with respect to Δx and finding the limit when approaching Δx to 0 [15, 16], equation (1) can be reduced to the following form:

$$\frac{d^2 T}{dx^2} = \frac{U_L}{k_{abs} H} \left(T_x - T_a - \frac{I}{U_L} \right) \quad (2)$$

As discussed earlier, if we do not take into account heat transfer at $x = 0$, and temperature T_p above the tubes is constant [17], the following boundary conditions can be specified:

$$\frac{dT}{dx} \Big|_{x=0} = 0, T \Big|_{x=(W-D)/2} = T_p \quad (3)$$

$$m^2 = \frac{U_L}{k_{abs} H} \quad (4)$$

$$\Psi = \left(T_x - T_a - \frac{I}{U_L} \right) \quad (5)$$

Equation (2) is simplified:

$$\frac{d^2 \Psi}{dx^2} - m^2 \Psi = 0 \quad (6)$$

The marginal requirements of expression (3) are transformed:

$$\frac{d\Psi}{dx} \Big|_{x=0} = 0, \Psi \Big|_{x=(W-D)/2} = T_p - T_a - \frac{I}{U_L} \quad (7)$$

Expression (5) is a linear differential equation of the second order. His overall decision:

$$\Psi = C_1 \operatorname{sh} mx + C_2 \operatorname{ch} mx \quad (8)$$

Applying the first boundary condition:

$$\frac{d\Psi}{dx} \Big|_{x=0} = C_1 \operatorname{sh} mx + C_2 \operatorname{ch} mx \Big|_{x=0} = C_1 m = 0 \quad (9)$$

From the first boundary condition $m \neq 0$, that is why $C_1 = 0$. Given the second boundary condition, we obtain

$$\Psi \Big|_{x=(W-D)/2} = T_p - T_a - \frac{I}{U_L} = C_2 \operatorname{ch} (m(W-D)/2) \quad (10)$$

$$C_2 = \frac{T_p - T_a - \frac{I}{U_L}}{\operatorname{ch} (m(W-D)/2)} \quad (11)$$

From relations (5) and (8) we obtain

$$\frac{T_x - T_a - \frac{I}{U_L}}{T_p - T_a - \frac{I}{U_L}} = \frac{\operatorname{ch}(mx)}{\operatorname{ch}(m(W-D)/2)} \quad (12)$$

$$T_x = T_a + \frac{I}{U_L} + \left(T_p - T_a - \frac{I}{U_L} \right) \frac{\operatorname{ch}(mx)}{\operatorname{ch}(m(W-D)/2)} \quad (13)$$

Equation (13) allows us to calculate the temperature distribution in the absorber plate (fig. 2) [18].

Heat q'_{fin} , which is transferred to the collector area above the tube at $x = (W-D)/2$, can be calculated from equation (13) using Fourier's law [19]:

$$\begin{aligned} q'_{fin} &= -k_{abs} H \frac{dT}{dx} \Big|_{x=\frac{W-D}{2}} = \\ &= -k_{abs} H \left(T_p - T_a - \frac{I}{U_L} \right) m \frac{\operatorname{sh}(mx)}{\operatorname{ch} \left(\frac{m(W-D)}{2} \right)} \Big|_{x=\frac{W-D}{2}} = \\ &= -k_{abs} H \left(T_p - T_a - \frac{I}{U_L} \right) m \frac{\operatorname{sh} \left(\frac{m(W-D)}{2} \right)}{\operatorname{ch} \left(\frac{m(W-D)}{2} \right)} \end{aligned} \quad (14)$$

$$q'_{fin} = \frac{k_{abs} H}{U_L} m \left(I - U_L (T_p - T_a) \right) \operatorname{th} (m(W-D)/2) \quad (15)$$

Assuming that $m^2 = \frac{U_L}{k_{abs} H}$, that

$$q'_{fin} = \frac{(W-D)}{2} \left(I - U_L (T_p - T_a) \right) \frac{\operatorname{th} (m(W-D)/2)}{(m(W-D)/2)} \quad (16)$$

Relation (16) can be used to calculate the heat transferred to the area of the collector above the tube, when $x = (W-D)/2$, on one side of the tube [20].

Let us define F as the efficiency of the edge, i.e.:

$$F = \frac{\text{th}(m(W-D)/2)}{(m(W-D)/2)} \quad (17)$$

and substituting F to (16)

$$q'_{fin} = \frac{(W-D)}{2} (I - U_L(T_p - T_a)) F \quad (18)$$

Equation (18) is the equation of the efficiency of the edge (F). The efficiency of the edge is the ratio of heat coming to the area above the tube (q'_{fin}), to the heat obtained at a constant temperature T_p . This ratio simplifies calculations and allows you to calculate the useful energy using a single temperature T_p .

If the heat transferred from the adsorber is known, it is possible to calculate the heat transferred to the coolant from both edges of the adsorber.

Useful heat q'_u – this heat is transferred from the adsorber plate to the liquid inside the tube. q'_u can be obtained from the energy balance for the element shown in the figure 4 [20].

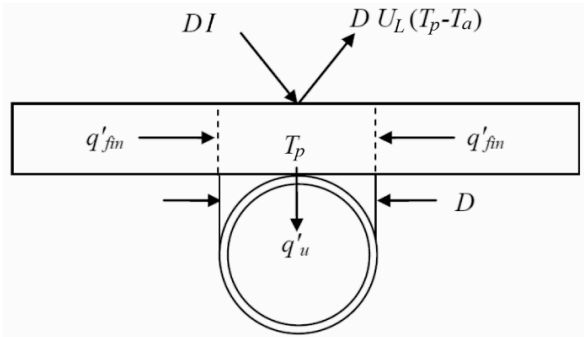


Fig. 4. Heat balance for the area of the absorber above the tube with the coolant

$$2 q'_{fin} + DI - D (I - U_L(T_p - T_a)) - q'_u = 0$$

$$q'_u = ((W - D)F + D) (I - U_L(T_p - T_a)) \quad (19)$$

In real conditions, the temperature T_p is unknown; therefore, it is necessary to calculate the efficiency depending on the temperature of the liquid, which is known. Heat efficiency is the ratio of heat transferred from the area above the tube to the liquid coolant. If the communication resistance is known R_p , then q'_u can be written relative to the temperature of the liquid T_f .

$$q'_u = \frac{(T_p - T_a)}{R_p}$$

$$T_p = q'_u R_p + T_f$$

Communication resistance R_p , is the thermal resistance between the absorber plate on the tube and the liquid (associated with the technological type of connection of the tube with the absorber) [21]. The first term takes into account the heat transfer between the inner side of the tube and the liquid and takes into account the inner diameter of the tube, the second term takes into account the heat transfer from the plate above the tube (the size of the contact is equal to the outer diameter of the tube). It can be written in the form (is inverted to heat transfer):

$$R_p = \frac{1}{h_w \pi (D-2B)} + \frac{H}{k_w D} \quad (20)$$

where h_w – the heat transfer coefficient between the inside of the tube and the liquid ($W/m^2 \cdot K$); H - the thickness of the layer on the tube (m); k_w – thermal conductivity of the site ($W/m \cdot K$); B – tube wall thickness (m).

Substituting (20) into equation (19) we obtain:

$$q'_u = \frac{1}{\frac{1}{U_L((W-D)F+D)} + R_p} (I - U_L(T_f - T_a)) \quad (21)$$

and

$$F' = \frac{1/U_L}{W \left[\frac{1}{U_L((W-D)F+D)} + R_p \right]} \quad (22)$$

Given the expressions above, us get:

$$q'_u = W F' (I - U_L(T_f - T_a)) \quad (23)$$

Relation (22) is the collector efficiency equation (F'). The efficiency of the collector is the ratio of the actual energy transferred to the liquid (q'_u), to the energy obtained at a constant temperature of the absorber and the temperature of the liquid T_f . This ratio simplifies the calculations and allows you to calculate the useful energy using one unknown temperature T_f . Coefficient F' similar to the efficiency factor of the edge F, because it connects the heat transfer characteristics with the coolant temperature.

Equation (23) can be used to calculate the useful energy collected per unit length of tube in the direction y.

III. MODEL TESTING

Simulation has been carried out for a model of a solar collector consisting of an absorber plate ($S_c = 2m^2$ - total area of the solar collector (m^2)), 8 tubes through which the coolant passes with a length of $D = 1,2 \cdot 10^{-2}m$, placed every 12,5 sm ($W = 12,5 sm$).

On fig. 5, 6 shows the results of simulation of changes in the surface temperature of the plate between adjacent tubes and the temperature dependence of the surface of the

plate with increasing distance from the tube with the flowing coolant.

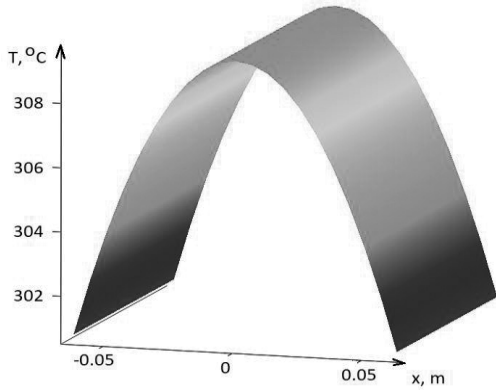


Fig. 5. The results of modeling the temperature distribution between two adjacent tubes

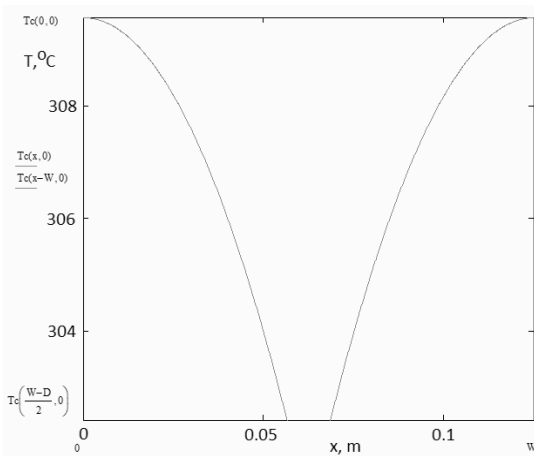


Fig. 6. The dependence of temperature around the tube of the classical plate of the collector

IV. CONCLUSIONS

The improved model of thermal processes in PV/T systems offered in the article will allow to calculate optimal constructive decisions of such systems at a design stage. This model takes into account all the key parameters of PV/T systems within the main coordinate and has the flexibility for further improvement on other axes, which will allow to develop a universal calculation mechanism for such systems.

The solutions of the basic equations of the proposed model have a fairly simple form and can be quite simple to use for writing modeling algorithms in the relevant software products.

The conducted testing of the proposed model confirmed its correct solution and adequacy, and the obtained modeling results are fully correlated with experimental studies.

REFERENCES

[1] X. Yang, L. Sun, Y. Yuan, *et al.*, "Experimental investigation on performance comparison of PV/T-PCM system and PV/T system", *Renewable Energy*, vol. 119, pp. 152-159, 2018.
[2] D. Das, P. Kalita, O. Roy, "Flat plate hybrid photovoltaic-thermal (PV/T) system: A review on design and development", *Renewable and Sustainable Energy Reviews*, vol. 84, pp. 111-130, 2018.

[3] N. Khordeghah, A. Żabnieńska-Góra, H. Jouhara, "Energy Performance Analysis of a PV/T System Coupled with Domestic Hot Water System", *ChemEngineering*, vol. 4, no. 2, pp. 22-35, 2020.
[4] R.V. Zaitsev, M.V. Kirichenko, G.S. Khrypunov, *et al.*, "Operating temperature effect on the thin film solar cell efficiency", *Journal of nano- and electronic physics*, vol. 11, no. 4, pp. 04029, 2019.
[5] K. Minakova, R. Zaitsev, "Optimization of a basic solar collector model for combined photo-energy systems", *Energy: Series Modern problem of power engineering and ways of solving them*, vol. 96, no. 4, pp. 114-119, 2020.
[6] K.A. Minakova, R.V. Zaitsev, "Improving the Solar Collector Base Model for PVT System", *Journal of nano- and electronic physics*, vol. 12, no. 4, p. 04028, 2020.
[7] M.V. Kirichenko, A.N. Drozdov, R.V. Zaitsev, *et al.*, "Design of Electronic Devices Stress Testing System with Charging Line Based Impulse Generator", 2020 IEEE KhPI Week on Advanced Technology, pp. 38-42, October 2020.
[8] M. Ghadiri, M. Sardarabadi, M. Pasandideh-fard, *et al.*, "Experimental investigation of a PVT system performance using nanofluids", *Energy Conversion and Management*, vol. 103, pp. 468-476, 2015.
[9] O. Vodka, "Analysis of quantitative characteristics of microstructures that are generated by the probabilistic cellular automata method", 2019 IEEE 2nd Ukraine Conference on Electrical and Computer Engineering, pp. 990-994, July 2017.
[10] V. Nerubatskyi, O. Plakhtii, D. Hordiienko, *et al.*, "A method for calculating the parameters of the sine filter of the frequency converter, taking into account the criterion of starting current limitation and pulse-width modulation frequency", *Eastern-European Journal of Enterprise Technologies*, vol. 1, no. 8, pp. 46-55, 2021.
[11] V.V. Eremenko, V.A. Sirenko, I.A. Gospodarev, *et al.*, "Electron spectra of graphene with local and extended defects", *Journal of Physics: Conference Series*, vol. 969, no. 1, P. 012021, 2018.
[12] I.A. Gospodarev, E.V. Manzhelii, V.I. Grishaev, *et al.*, "Phonon heat capacity of graphene nanofilms and nanotubes", *Low Temp. Phys.*, vol. 43, no. 2, pp. 264-273, 2017.
[13] V.V. Eremenko, V.A. Sirenko, I.A. Gospodarev, *et al.*, "Role of acoustic phonons in the negative thermal expansion of the layered structures and nanotubes based on them", *Low Temp. Phys.*, vol. 42, no. 5, pp. 401-410, 2016.
[14] H. Liang, F. Wang, L. Yang, *et al.*, "Progress in full spectrum solar energy utilization by spectral beam splitting PV/T system", *Renewable and Sustainable Energy Reviews*, vol. 141, pp. 110785, 2021.
[15] M.G. Khrypunov, R.V. Zaitsev, D.A. Kudii, *et al.*, "Amplitude-time characteristics of switching in thin films of cadmium telluride", *Journal of Nano- and Electronic Physics*, vol. 10, no. 1, pp. 01016, 2018.
[16] V.P. Nerubatskyi, O.A. Plakhtii, D.V. Tugay, *et al.*, "Method for optimization of switching frequency in converters", *Scientific bulletin of National mining university*, vol. 177, no. 1, pp. 61-68, 2021.
[17] O. Plakhtii, V. Nerubatskyi, Ya. Scherbak, A. Mashura, I. Khomenko, "Energy efficiency criterion of power active filter in a three-phase network", 2020 IEEE KhPI Week on Advanced Technology, pp. 165-170, October 2020.
[18] M.R. Saffarian, M. Moravej, M.H. Doranehgard, "Heat transfer enhancement in a flat plate solar collector with different flow path shapes using nanofluid", *Renewable Energy*, vol. 146, pp. 2316, 2020.
[19] M. Simoncelli, N. Marzari, A. Cepellotti, "Generalization of Fourier's Law into Viscous Heat Equations", *Phys. Rev. X*, vol. 10, pp. 011019, 2020.
[20] H.P. Singh, A. Jain, A. Singh, *et al.*, "Influence of absorber plate shape factor and mass flow rate on the performance of the PVT system", *Applied Thermal Engineering*, vol. 156, pp. 692-701, 2019.
[21] D. Zhang, H. Tao, M. Wang, *et al.*, "Numerical simulation investigation on thermal performance of heat pipe flat-plate solar collector", *Applied Thermal Engineering*, vol. 118, pp. 113-126, 2017.

Investigations of interconnection approach for novel ultralight vertex detectors based on curved pixel sensors

V. Borshchov
LLC «Research and Production
Enterprise «LTU»
Kharkiv, Ukraine
info@ltu.ua

I. Tymchuk
LLC «Research and Production
Enterprise «LTU»
Kharkiv, Ukraine
info@ltu.ua

M. Protsenko
LLC «Research and Production
Enterprise «LTU»
Kharkiv, Ukraine
info@ltu.ua

O. Listratenko
LLC «Research and Production
Enterprise «LTU»
Kharkiv, Ukraine
info@ltu.ua

O. Suddia
LLC «Research and Production
Enterprise «LTU»
Kharkiv, Ukraine
info@ltu.ua

Abstract - Interconnection approach for curved pixel sensors for novel vertex detectors for physics experiments is suggested. Key features of the approach are using ultralight aluminium-polyimide interconnection elements, possibility to curve a sensor after connecting interconnection elements and acceptance of using approach for both options of curving (when interconnection elements are above or under a sensor). Suggested approach allowed to perform testing MAPS sensor in four different curving options for defining possible changing parameters of the sensor depending on bending option and possible failures. Bending tests of thin (50um) MAPS sensors have been performed and any sensor or interconnection failures have not been observed. At the same time changes of some parameters (Ia) up to 10% were observed. Obtained results can be used for further realization of large-scale curved silicon pixel sensors MAPS-type for creating novel ultralight vertex detectors.

Keywords - MAPS, SpTAB, adhesiveless aluminium-polyimide dielectric, ultrasonic welding, ribbon leads, curving.

I. INTRODUCTION

Recent innovations in the field of silicon imaging technology for consumer applications open extraordinary opportunities for new detector concepts, and hence offer strongly improved physics scope. One of possible implementation of these innovations is vertex detector for upgraded Inner Tracking System (ITS) of ALICE (A Large Ion Collider Experiment) Experiment at Large Hadron Collider (LHC) at CERN [1]. Such novel vertex detector consisting of curved wafer-scale ultra-thin (30-50um) silicon sensors arranged in perfectly cylindrical layers, featuring an unprecedented low material budget of 0.05%X₀ per layer, with the innermost layer positioned at only 18mm radial distance from the interaction point [1]. It will provide a large reduction of the material budget in the region close to the interaction point and a large improvement of the tracking precision and efficiency at low transverse momentum.

The combination of these two improvements will lead to a significant advancement in the measurement of low momentum charm and beauty hadrons and low-mass

dielectrons in heavy-ion collisions at the LHC, which are among the main objectives of the ALICE physics programme in the next decade. An experiment aimed at studying quark - gluon plasma (QGP) in a super hot and super dense state of aggregation of matter. Physicists assume that it was in this state that the Universe was in the very first microseconds of its existence.

One of key point of the improvements is development of stitched wafer-scale sensors based on approaches and results obtained for ALPIDE (ALice Pixel DEtector) Monolithic Active Pixel Sensor (MAPS) for improved ALICE ITS (ITS2) [2].

Meanwhile, for successful realization of the detector reliable and robust interconnection technique and low budget materials for realization of interconnection elements also need to be investigated and chosen. Taking into account features of existing technologies, materials and approaches one of possible option is using single- and multilayered flexible microcables and boards based on adhesiveless aluminium-polyimide foiled dielectrics. As an interconnection techniques ultrasonic welding of aluminium ribbon leads can be used. Abovementioned materials and approaches based on Single-point TAB (SpTAB) technique already have been successfully used and verified in physics experiments ALICE [3], CBM [4], NICA-MPD [5], Mu3e [6], PANDA [7] and also for creating pixel probes [8] and Digital Tracking Calorimeter for proton computer tomography [9] and demonstrated well results and reliable operating of prototypes, detector modules and their components.

However, in spite of well worked-off technological approaches, assembly technique for single- and multilayered microcables and boards, detector modules and their components, realized for abovementioned experiments, for using in new ITS vertex detector need to be developed and investigated new/modified technological approach for realization of vertex detector with curved silicon sensors.

At R&D and production stages of realizing detector layers of ITS2 lot of investigations and tests of ALPIDE MAPS sensors have been done but all of them were

performed in flat (noncurved) shape of the sensors. Meanwhile, as it is known, during curving silicon devices (including silicon pixel sensors) changing electrical parameters of such devices might be observed. Therefore, additional important point needs to be investigated is possible difference in electrical parameters of MAPS for flat and curved shape of it for further implementation at realization of wafer-scale large MAPS for novel vertex detectors as well as possible failures during curving sensors.

II. INITIAL DATA FOR DEVELOPMENT AND INVESTIGATIONS

ALPIDE MAPS is the result of an intensive R&D effort carried out by ALICE collaboration in the past about ten years which has led to a quantum leap in the field of MAPS for single-particle detection, reaching unprecedented performance in terms of signal/noise ratio, spatial resolution, material budget and readout speed. ALPIDE type MAPS chips manufactured by Tower Jazz Company (USA) based on radiation resistive 0,18 μm CMOS technology were chosen as the main sensitive element for all pixel layers of upgraded ITS2 [10]. This semiconductor device is silicon chip (15x30) mm^2 size. In it formed high-resistance silicon epitaxial layer (active sensor volume), array of diodes (pixels) for charge collecting with pitch about 30 micrometers, and electronics, which performs amplification and digitization of the selection of the useful signals to noise background. In this case is reading information on passing particles through the pixels.

To minimize material budget of a tracking system integrated pixel array sensor must be made as thin as possible. Its minimum thickness is determined by the thickness of the epitaxial layer (nominal thickness - 18 μm) plus the thickness of layers of CMOS structure (about 10 micrometers) (Fig. 1a). Manufacture of such sensor is performing by thinning the base wafer from the back side to required safe thickness what is about 50 μm or 100 μm [10]. Appearance of ALPIDE pixel sensor is shown on Fig.1 b and main parameters are given below.

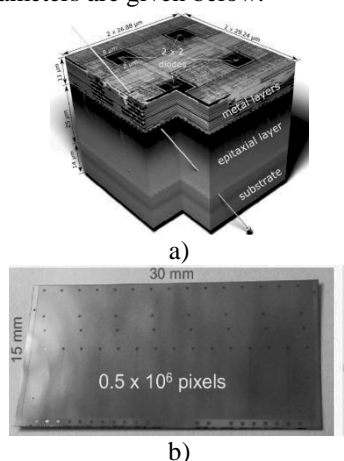


Fig.1. MAPS ALPIDE sensor: a) schematic cross section with dimensions of the layers; b) appearance of ALPIDE pixel sensor

Main parameters of ALPIDE chip are: chip size 30×15 mm^2 , pixels 1024×512, in-pixel amplification, shaping, discrimination and multi-event buffer, on-chip high speed data link (1.2 Gb/s), power consumption 40 mW/cm^2 .

Yet, there is still a lot that can be done to further improve MAPS for high energy physics detectors by fully exploiting the rapid progress that this technology is making in the field of imaging for consumer applications. One of the features offered recently by CMOS imaging sensor technologies, called stitching, will allow developing a new generation of large size MAPS with an area of up to 21 $\text{cm} \times 21 \text{ cm}$ using wafers that are 300mm in diameter. Moreover, the reduction of the sensor thickness to values of about 20–40 μm will open the possibility of exploiting the flexible nature of silicon to implement large-area curved sensors. In this way, it will become possible to build a cylindrical layer of silicon-only sensors, with a further significant reduction of the material thickness [1].

The baseline technology for the development of mentioned new MAPS stitched sensor is the 65 nm CMOS process of Tower Semiconductor, which offers a number of advantages with respect to the 180 nm process used for the development of ALPIDE [1]:

- the process, which uses wafers that are 300mm in diameter, allows the realization of the entire half-cylinder as a single chip.

- owing to the smaller feature size of the transistors, the pixel pitch can be reduced by a factor larger than two. This allows a significant reduction of the charge collection time and also a better position resolution.

As further improvement of ALICE ITS2 by ALICE collaboration is considering possibility of constructing a new vertex detector consisting of three cylindrical layers based on curved wafer-scale stitched sensors, featuring a material budget of 0,05% X_0 per layer, with the first layer positioned at a radial distance from the interaction point of 18 mm. This new vertex detector ITS3 will be installed to replace the three innermost layers of the ITS2. With the first detection layer closer to the interaction point (from 23mm to 18 mm) and a reduction of the material budget close to the interaction point by a factor of six (0.35% \rightarrow 0.05% per layer), the new vertex detector will significantly improve the tracking precision and efficiency. The improvement of the vertexing performance and the reduction of material budget will have a dramatic impact on the measurement of charm and beauty hadrons at low transverse momentum as well as on the measurement of low-mass and low p_T dielectrons [1].

A completely new Inner Barrel for ALICE ITS3, consisting of the three innermost layers and will consist of two halves, named half-barrels, to allow the detector to be mounted around the beampipe. Each half-barrel will consist of three half-layers. The half-layers are arranged inside the half-barrel as shown in Fig. 2 [1]. They have a truly (half-) cylindrical shape, with each half-layer consisting of a single large pixel chip, which is curved/bent to a cylindrical shape.

However, for successful creating new Inner Barrel for new ITS3, in addition to significant efforts for MAPS development, other important direction is to define and to investigate reliable interconnection method and materials for ensuring functionality of curved/bent stitched MAPS in the ITS.

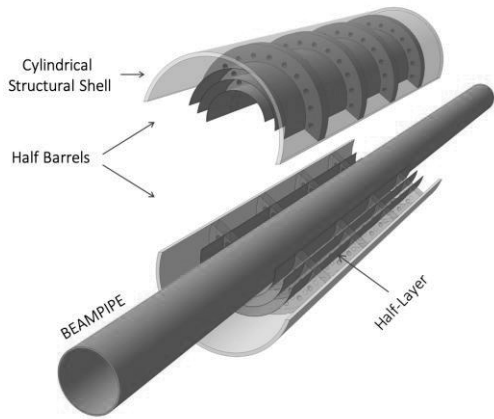


Fig. 2. Mechanical layout of the new Inner Barrel [1]

Based on overview and analyze of features and details of proposal on possible realization of a new vertex detector for ALICE ITS can be noted one extraordinary feature, namely using curved (bent) silicon MAPS stitched structures as key sensitive part. Taking into account this feature and topics need to be investigated for realization of the vertex detector, following goals for performing investigations were defined:

- developing concept of possible realization of curved detector layers (sensor and interconnection elements) based on SpTAB technique and low budget materials;
- developing concept for realization of SpTAB interconnection prototype;
- creating SpTAB interconnection prototype;
- performing bending (curving) tests of SpTAB interconnection prototype based on single MAPS ALPIDE.

As one of possible base line for interconnection of bent MAPS wire bonding can be considered. Possible reasons for such choice are enough popularity of wire bonding in industry and its successful using at e.g. creating detector modules based on ALPIDE chips at creating ITS2.

Meanwhile, wire bonding has following key features and possible complications in case of using for curved/bent sensors:

- sensor need to be glued to Flexible Printed Circuit (FPC) (or FPC-to-sensor) - possible complication at further handling and bending;
- wire bonding on bent sensor- special complicated jig agreed/tuned with/to wire bonder;
- encapsulating of wires for flat sensor- complications at further bending;
- encapsulating of wires for bent sensor- complicated process (liquid glues).

For excluding abovementioned features and complications concept of realization of curved vertex detector layers based on Single-point TAB (SpTAB) technique based on ultrasonic welding of aluminium ribbon leads has been developed. Key features of the developed concept are followings:

- for connecting sensor-to-FPC chipcable (single layered ultralight interconnection element) is using;
- connecting chipcable to sensor and to FPC is performing in flat (noncurved) shape;
- bending of functional assembly (sensor + chipcable + FPC) is foreseen;

- chipcable is bonding to the sensor first, then to FPC what allows to test chipcable assembly;
- interconnection technique: SpTAB- ultrasonic welding ribbon aluminium leads of chipcable (to sensor and to FPC);
- chipcable (single layered) and FPC (multilayered) are made of adhesiveless aluminium-polyimide dielectrics;
- protecting bond joints chipcable-to sensor - by dots of glue;
- functional electrical testing after each technological step;
- functional testing MAPS with welded chipcable before mounting on multilayered flex and exclude possible using bad/defected sensors for creating half-layers;
- approach compatible with standard wedge wire bonding equipment (e.g. Delvotec, K&S etc.).

Taking into account overview and analyze of features and details of possible realization of a new vertex detector for ALICE ITS3, defined goals of the work and tasks need to be solved, following key initial data for investigations are defined:

- sensitive structure for investigations –ALPIDE MAPS chips;
- interconnection technique for test prototypes – SpTAB;
- bending/curing tests need to be carried in smaller radius of new ITS inner layer – 18mm;
- during bending tests functional tests need to be performed for flat/unbent and curved/bent MAPS chips;
- bending tests are intended for investigations absence of failures of MAPS, interconnections and possible changing parameters of the MAPS.

III. EXPERIMENTAL

Taking into account abovementioned features and suggested approach for investigations SpTAB ALPIDE chipcable assembly was developed, designed and few samples of it have been manufactured and investigated (Fig.3).

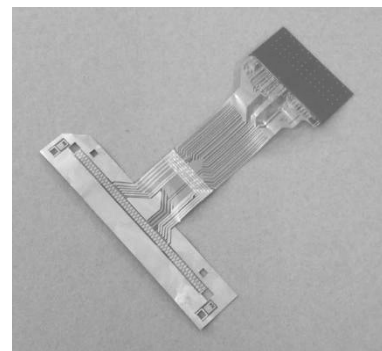


Fig.3. Flat/unbent SpTAB ALPIDE chipcable assembly

For investigations of SpTAB ALPIDE prototypes following tests were chosen:

1. preliminary mechanical tests of bent/unbent assembled chipcable with MAPS for defining possibility to bend ALPIDE at required minimal radius (18mm);
2. bending tests of SpTAB chipcable assembly in different positions for defining possible influence of bending ALPIDE on its electrical parameters and defining

possible failures (MAPS or interconnection) – 11 bent/unbent steps for each position/direction of the sensor.

Based on features of the chip, possible connecting chipcable to it and possible bending such assembly (depending on location of epitaxial layers at bending MAPS) following test options for bending tests of SpTAB chipcable assembly have been chosen (schematically oh Fig.4):

- bending along 30mm side Face Up (matrix from a core) - 30 FU option;
- bending along 30mm side Face Down (matrix to a core) - 30 FD option;
- bending along 15mm side Face Up (matrix from a core) - 15 FU option;
- bending along 15mm side Face Down (matrix to a core) - 15 FD option.

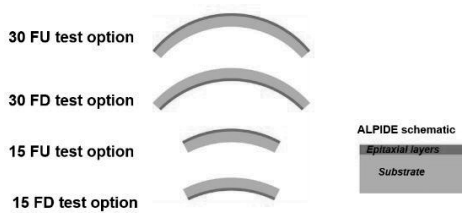


Fig.4. Location of epitaxial layers at bending MAPS for different options of bending tests

Bending tests of SpTAB chipcable assembly is performing on plexiglass (for excluding shorts between conductive traces for FD bending options) core 18mm radius

Curved ALPIDE MAPS chipcable assemblies in different bending options are shown on Fig.5.

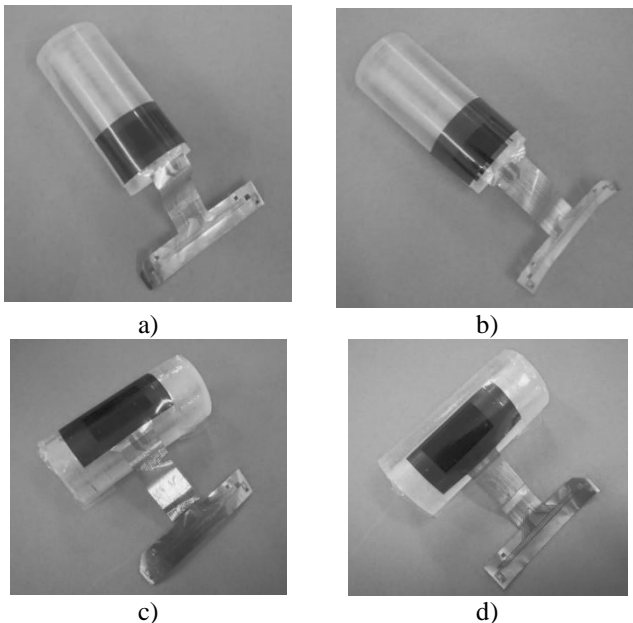


Fig.5. SpTAB ALPIDE chipcable assembly in different bending options: a)30FU; b)30FD; c) 15FU; d)15FD

For performing testing SpTABed ALPIDEs for pCT, ALICE ITS and ALICE FoCal projects special test set-up (so-called “Production Test Box”, PTB) has been

developed and created by scientists from University of Bergen in cooperation with experts from CERN, University of Utrecht and RPE LTU. Such equipment is considered as base hardware for testing MAPS chipcable assemblies during bending tests. Need to be noted that the PTB is not developed for analog testing pixel matrix.

All ALPIDE MAPS chips are passing QA testing during production and classification at CERN and other laboratories. Result of qualification of ALPIDE is conclusion about its quality. Typical conclusion is GOOD or BAD but based on obtained results for GOOD chips they, depending on values of analog and digital current, are classifying on three categories namely Gold, Bronze and Silver. Testing ALPIDE MAPS by the PTB includes Power Test, Register Test; FIFO test and High-Speed Link Test.

Based on features of testing ALPIDEs using PTB and preliminary bending test were observed that difference in I_a value for bent/unbent shape of the ALPIDE is present. At the same time any significant difference for I_d value has not been observed. Therefore, for each bent/unbent step obtained results must include:

- quality of ALPIDE (OK/BAD);
- classification of ALPIDE (GOLD/SILVER/BRONZE);
- value of I_a in mA.

IV. OBTAINED RESULTS

According to developed test approach and abovementioned chosen bending options bending tests of SpTAB chipcable assemblies have been performed.

Preliminary mechanical tests of bent/unbent assembled chipcable with MAPS confirmed possibility to bend ALPIDE at required minimal radius (18mm) without any visual damages (Fig.6).

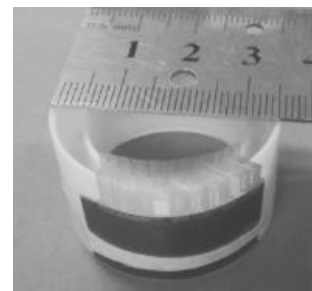


Fig.6. Bent (R=18mm) SpTAB chipcable assembly at preliminary mechanical test

Taking into account positive results at preliminary mechanical tests 11 flat/bent steps for each bending option have been performed with functional tests at flat/bent position.

During bending tests any changes in quality of ALPIDE MAPS chips have not been observed and classification of chips has not been changed.

Key observed repeatable difference in parameters of MAPS chips was in value of analog current (I_a) for flat and bent shape (significant repeatable difference in digital current I_d was not observed). Typical results of investigations of I_a value for different bending options are given on Fig.7.

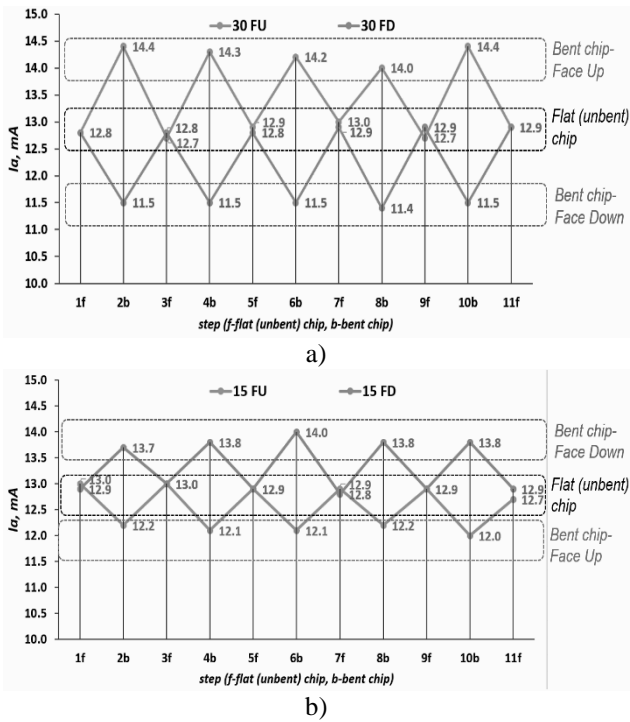


Fig. 7. Obtained test results, namely difference in I_a value for bending ALPIDEs, a) 30 FU and 30 FD options; b) 15 FU and 15 FD options.

Based on results of bending tests of SpTAB ALPIDE chipcable assembly prototypes following outcomes and conclusion can be done:

- 50um thick ALPIDE with connected chipcable by SpTAB technique can be bent at minimal radius ($R=18\text{mm}$) corresponding to minimal radius of L0 curved sensor in new ITS3 vertex detector without any damages or cracks on chip and on chipcable or weld joints;

- any significant quality differences have not been observed during multiple bending tests for bending ALPIDE along two directions (along 30 mm and 15mm) and at two directions of location of epitaxial layers (from and to a core);

- changes of I_a value in range of ~5-10% for bent chip comparing to flat chip have been observed, possible reason of this effect might be piezo-resistive effect;

- ALPIDE chip is passed about 50 bending steps without any failures and is still functional.

V. CONCLUSIONS

Interconnection SpTAB approach for further realization of novel ultralight vertex detectors based on curved thin silicon pixel sensors MAPS -type (e.g. for creating new vertex detector for ALICE ITS3 project at LHC at CERN) is suggested in the paper.

Bending tests of SpTAB interconnection assembly prototypes allowed to observe changes of I_a value in range of ~5-10% for bent chip comparing to flat chip, possible reason of this effect might be piezo-resistive effect.

Multiple bending thin MAPS chip not leads to any failures or significant changes in quality or classification of sensor (tested sensors passed about 50 bending test steps and is still functional).

SpTAB interconnection technique and ultralight interconnection element made of adhesiveless aluminium-polyimide dielectrics have advantages and allow to exclude complications present for wire bonding and can be considered as a base approach for creating curved detector layers of new vertex detectors (e.g. new ALICE ITS3).

ACKNOWLEDGMENTS

We would like to thank the University of Bergen team and Bergen pCT collaboration (Prof. Dr. Dieter Røhrich, Prof. Dr. Kjetil Ullaland, Ola Grøttvik, Viljar Eikeland) for support this activity, participating in discussions about realization of prototypes and assemblies, providing hardware and software for testing MAPS-based assemblies and the CERN ALICE ITS3 team (Prof. Stefania Beolè, Dr. Giacomo Contin, Dr. Magnus Mager) for suggestion ideas on creating SpTAB ALPIDE interconnection prototypes and to all abovementioned experts together for fruitful and successful cooperation.

REFERENCES

- [1] Letter of Intent for an ALICE ITS Upgrade in LS3/ ALICE Collaboration, CERN, Geneva, Switzerland, October 22, 2019 - ALICE-PUBLIC-2018-013
- [2] ALICE Collaboration, G. Aglieri Rinella, "The ALPIDE pixel sensor chip for the upgrade of the ALICE Inner Tracking System", Nucl. Instrum. Meth. A845 (2017) 583-587.
- [3] ALICE Collaboration, K. Aamodt et al., "The ALICE experiment at the CERN LHC", JINST 3 (2008) S08002.
- [4] Technical Design Report for the CBM. Silicon Tracking System (STS) / T. Balog, V. Borshchov, M. Protsenko, I. Tymchuk and the CBM Collaboration // GSI Report 2013-4 - GSI Darmstadt, Germany, October 2013 - 167 p.
- [5] The MPD detector at the NICA heavy-ion collider at JINR / Kh. U. Abraamyan, V. N. Borshchov, M. A. Protsenko, I. T. Tymchuk, et al. // Nuclear Instruments and Methods in Physics Research. - 2011. - A 628. - P. 99-102.
- [6] Ultra-low material pixel layers for the Mu3e experiment - Berger, N. *et al.* / JINST 11 (2016) no.12, C12006 arXiv:1610.02021
- [7] Tracking Detector for Luminosity Measurement at PANDA /C.Motzko/ 12th International Conference "Instrumentation for Colliding Beam Physics" INSTR-2017 February, 27 - March, 3, 2017 Budker Institute of Nuclear Physics SB RAS, Novosibirsk - Book of Abstract, p.10
- [8] Development and test of TAB bonded silicon PAD detectors and micro-cables for the construction of silicon probes for imaging / V. Linhart, V. Borshchov, M. Protsenko, I. Tymchuk, P. Weillhammer et al. // Nuclear Science Symposium Conference Record, - Orlando, FL, 2009 IEEE NSS-MIC. - 24 October - 1 November 2009. - P. 2423-2426.
- [9] A High-Granularity Digital Tracking Calorimeter Optimized for Proton CT/ Alme J, Borshchov V, Protsenko M, Tymchuk I. at al// Front. Phys. 8:568243. doi: 10.3389/fphy.2020.568243
- [10] ALICE collaboration, Technical Design Report for the Upgrade of the ALICE Inner Tracking System, J. Phys. G 41 (2014) 087002 [CERN-LHCC-2013-024, ALICE-TDR-017] - 189 p

Calculation Of The Absorption Capacity Of Multi-Junction Solar Photoconverters

Aleksandr Galat

Department of Microelectronics,
Electronic Devices and Appliances
Kharkiv National University of Radio
Electronics
Kharkiv/Ukraine
oleksandr.galat@nure.ua

Liudmila Sviderska

Department of Microelectronics,
Electronic Devices and Appliances
Kharkiv National University of Radio
Electronics
Kharkiv/Ukraine
liudmyla.sviderska@nure.ua

Aleksandr Sliusarenko

Department of Microelectronics,
Electronic Devices and Appliances
Kharkiv National University of Radio
Electronics
Kharkiv/Ukraine
oleksandr.sliusarenko@nure.ua

Abstract— The efficiency of solar cell depends on the operation of its several basic elements: focusing system, positioning device, photoconverter and power conversion system. This paper considers the possibility of evaluating the efficiency of the solar battery (photoconverter) by calculating its absorbing capacity. A technique for calculating absorption by a multi-junction structure is considered. We have to optimize light absorption of the structure by choosing proper material and its thickness. On the other hand, it is necessary to match the short-circuit currents of each layer. We have a multiparameter problem, the complexity of which increases sharply with the number of layers. The currently existing programs for calculating photoconverters (SCAPS, gpdm, AMPS) face difficulties in entering material parameters, restrictions on the size of layers, etc.

The light absorption efficiency of some multi-junction light transformers calculated in this work using analytical method. The calculations take into account the spectrum of sunlight AM1.5, the dependence of the conversion rate and absorption coefficients from light quantum energy.

Keywords— solar cell, efficiency, multi-junction, absorption, structure

I. INTRODUCTION

Solar cells are manufactured in the form of structures based on crystalline (c-Si) and hydrogenated amorphous silicon (a-Si: H), cadmium telluride (CdTe), indium diselenide (CuInSe₂ - CIS), gallium diselenide (CuGaSe₂ - CGS), solid solutions CuIn_{1-x}Ga_xSe₂ - CIGS and other materials. In special applications (for example, in spacecraft), the high efficiency of the solar cell per unit area and mass is very important. In this case, expensive materials and complex design solutions are used, in particular, multi-junction (2 ... 6 layers) structures of photoconverters.

Development of multilayer structures of photoconverters requires high costs and at the modeling stage they can be significantly reduced. The increase in the efficiency of photoconverters depends primarily on their absorption capacity and the coefficient of conversion of solar energy into electrical energy. The absorption capacity is determined by the dependence of the absorption coefficient of the material on the wavelength in the range of solar radiation. Calculations of the absorption capacity of solar cells made on the basis of various materials [1,2] are based on the known spectral distributions of the absorption coefficients of materials in the range of the main solar radiation flux [3].

Experimentally investigated the structures of multijunction solar photoconverters [4,5], which have a high efficiency (35 ... 50%). The results of measurements of the conversion efficiency of the most common semiconductor materials show that for each there are wavelength ranges with maximum efficiency [6]. Based on this, it is possible to select a sequence of layers of a multi-junction photoconverter. A similar structure of 4 transition elements was used to test the proposed technique.

To adequately compare the efficiency of light absorption by different materials, one should take into account their absorption coefficient in the range of at least 0.3 ... 2.5 microns, which contains more than 99% of solar energy reaching the Earth's surface. Therefore, the efficiency of the photoconverter should be calculated taking into account the ratio of the values of the absorbed to the incident power in the specified spectral region. Obviously, such a wide range requires the use of several active layers (tandem photoconverters) for the maximum absorption effect [6].

The paper presents the results of calculating the absorption capacity of the Ge / InAs / GaAs / InP structure. The calculations are carried out on the basis of the technique [1, 2], modified as applied to multi-junction structures, and make it possible to compare the absorption efficiency of the 0.3 ... 2.5 μm spectrum for multilayer thin-film structures.

II. METHOD FOR CALCULATING THE ABSORPTION CAPACITY OF A MULTILAYER SOLAR CELL

The solar radiation spectrum has been studied in sufficient detail and presented in publications. This work uses the distribution obtained by the American Society for Testing and Materials (ASTM) [3] for certain atmospheric conditions and geographic location. This distribution is used for calculations in this work (Fig. 1). The top graph is the solar power spectral density outside the atmosphere (AM0). The average is actually the dependence AM1.5 used in this work, taking into account the radiation scattered by the atmosphere (according to Rayleigh's law). The bottom graph is the AM1.5 direct solar radiation. Taking into account the radiation scattered by the atmosphere, as can be seen from the graphs, adds power mainly in the visible part of the spectrum. In general, this additive is about 10%.

The distribution is presented in the range 0.25 ... 4.0 μm (Fig. 1), however, it is obvious that most of the AM1.5 Global power flux of interest to us is in the range 0,3 ... 2.5

microns. Therefore, for all investigated materials, the same solar spectrum range of 0.3 ... 2.5 μm was used.

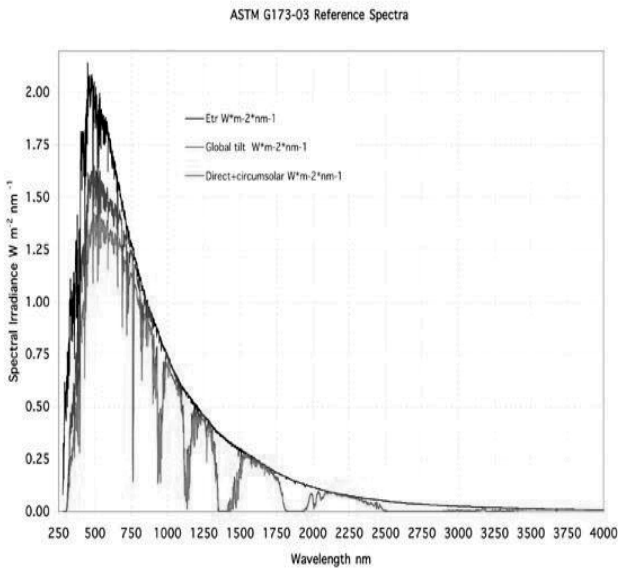


Fig. 1. Distribution of the solar radiation spectrum AM0 (Etr), AM1.5 taking into account light scattering (+ 10%) (Global), direct AM1.5 (Direct +)

For confirmation, calculations of the radiation power density of the AM1.5 Global spectrum of the Sun, cut from the top along the wavelength [4], were performed. Calculations show that in the range of 0.3 ... 2.5 microns, 99.1% of the total power of solar radiation falls on the Earth. Literature data on solar power density measurements give 0.846 kW / m² for AM1.5 Direct + and 0.93 kW / m² for AM1.5 Global, which is in good agreement with the calculation. Since the spectrum of solar radiation is represented by a discrete function [5], these data can be used directly in the calculations of the absorption capacity. Spectral dependences of the absorption coefficients of materials are presented by experimental data or calculated on the basis of empirical formulas [7, 8], with sufficient accuracy for our calculations.

Taking into account the above, the processing of the indicated dependences was carried out, the spectrum range of interest to us was divided into subranges with a size of 10 ... 50 nm (the size is dictated by the required accuracy of calculations). To calculate the absorption capacity, we used the relation [1], which, as applied to a four-junction structure, has the form

$$AA(dd1, dd2) := \frac{\sum_{k=0}^{n1} \left[FY_k \cdot \lambda_k \cdot \left[1 - \left(e^{-A1_k \cdot dd1 \cdot 100} \cdot e^{-A2_k \cdot dd2 \cdot 100} \cdot e^{-A3_k \cdot dd3 \cdot 100} \cdot e^{-A4_k \cdot dd4 \cdot 100} \right) \right] \right]}{\sum_{k=0}^{n1} (FY_k \cdot \lambda_k)} \quad (1)$$

where FY_k is the power density of solar radiation AM1.5 Global, averaged over the k -th subband of the spectrum;
 λ_k is the wavelength corresponding to the middle of the k -th subband of the spectrum;
 A_{mk} is the absorption coefficient of the material m -th layer, averaged over the k -th subband of the spectrum;

dd_m is the thickness of the material of the m -th layer;
 k is the number of the subband of the spectrum;
 $n1$ is the number of subbands of the spectrum into which main radiation range;

1... 4 - number of the layer of the corresponding material in the structure of the photoconverter.

In each subrange, we determine the average value of the functions FY_k , A_{mk} , λ_k . These data arrays are used in the program for direct calculations.

III. CALCULATION OF THE ABSORBANCE OF THE PHOTOCONVERTER

Calculations of the absorbance are presented for the four-junction structure of the Ge / InAs / GaAs / InP photoconverter. The calculations provide for the determination of absorption by each layer separately and by the entire structure as a whole. During the simulation, the thicknesses of the layers of the corresponding materials were changed. The calculations were performed for the wavelength range of 300 ... 1800 nm.

Fig. 2 shows the calculations of the absorbance of the structure with a change in the thickness of layer 1 (Ge) from 1 to 1,000,000 nm. With a thickness of 1 ... 50 nm, the material practically does not affect the absorption of the entire structure. In the range of 50 ... 3000 nm, the material significantly affects the absorption of the photoconverter.

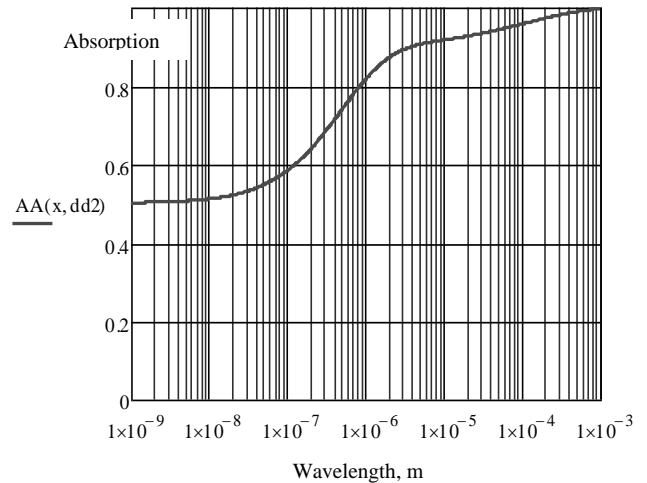


Fig. 2. Absorption of the structure with a change in the thickness of the first layer $d1$ ($d2, d3, d4 = 100$ nm)

A further increase in thickness leads to a significant waste of material and does not give an adequate increase in efficiency. Figures 3, 4 and 5 show similar dependences taking into account the change in the thickness of layers 2, 3, 4, respectively.

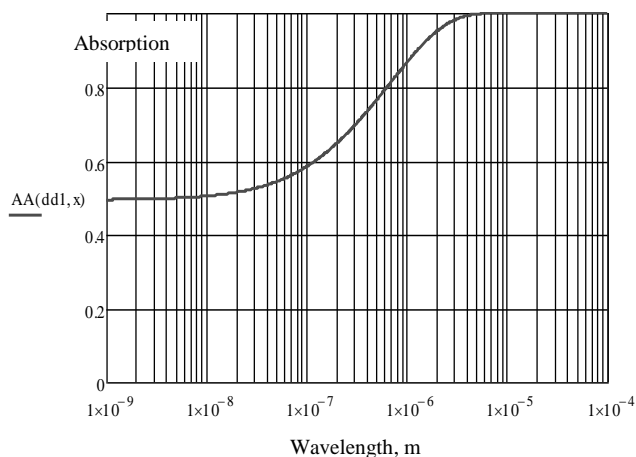


Fig. 3. Absorption of the structure with a change in the thickness of the second layer d_2 ($d_1, d_3, d_4 = 100$ nm)

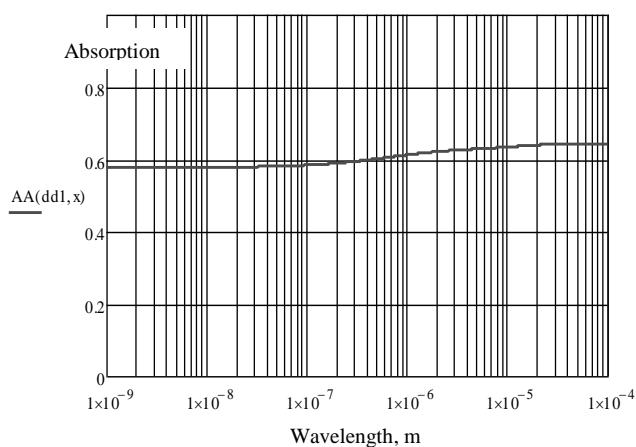


Fig. 4. Absorption of the structure with a change in the thickness of the third layer d_3 ($d_1, d_2, d_4 = 100$ nm)

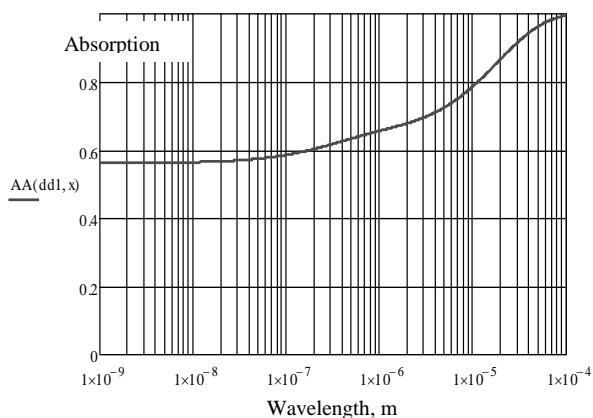


Fig. 5. Absorption of the structure with a change in the thickness of the fourth layer d_4 ($d_1, d_2, d_3 = 100$ nm)

As can be seen from the above calculations, the dependences of absorption for a multi-junction structure differ significantly with a change in the thickness of one layer or another. The absorption curves have rather sharp breaks. This indicates a complex dependence of absorption on geometric parameters. The rapid increase in the absorption capacity indicates a significant effect of this material on the properties of the structure. A slight change in absorption indicates excess material thickness.

IV. CONCLUSIONS

The paper proposes to use analytical calculations of the absorptivity of multilayer solar cells to determine the optimal structure of the photoconverter. Analytical estimates of the absorption of radiation by various materials make it possible to choose the thickness of the layers in the first approximation, and the energy characteristics calculated, for example, by the SCAPS program, make it possible to refine all the parameters of the structure of a solar cell.

REFERENCES

- [1] Галат А.Б. Расчет поглощательной способности солнечных фотопреобразователей // 9-я Международная научная конференция «Функциональная база нанoeлектроники». Сб. науч. трудов. – Харьков: ХНУРЭ, 2017. – С.103–106.
- [2] Galat, A.B. Calculation of the absorbing capacity of a solar $\text{CuIn}_{1-x}\text{Ga}_x\text{Se}_2$ photovoltaic converter//Telecommunications and Radio Engineering, Volume 77, Issue 1, 2018, Pages 61-67
- [3] <http://ust.su/solar/media/section-inner12/637/>
- [4] В.М. Емельянов ¶, Н.А. Каложный, С.А. Минтаиров, М.З. Шварц, В.М. Лантратов Многопереходные солнечные элементы с брэгговскими отражателями на основе структур $\text{GaInP}/\text{GaInAs}/\text{Ge}$ //Физика и техника полупроводников, 2010, том 44, вып. 12. – С. 1649-1654.
- [5] Aho A, Isoaho R, Raappana M, et al. Wide spectral coverage (0.7–2.2 eV) lattice-matched multijunction solar cells based on AlGaInP , AlGaAs and GaInNASb materials. Prog Photovolt Res Appl. 2021;29: 869–875. <https://doi.org/10.1002/pip.3412>
- [6] Kuznicki Z.T., Multiinterfase Solar Cells I. Limits, Modeling, Desing//First Polish-Ukrainian Symposium "New Photovoltaic Materials for Solar Cells", E-MRS, Krakow (Poland). –1996. – P. 58–78.
- [7] K. Papatryfonos, T. Angelova, A. Brimont, B. Reid, S. Guldin, P. R. Smith, M. Tang, K. Li, A. J. Seeds, H. Liu, D. R. Selviah. Refractive indices of MBE-grown $\text{Al}_x\text{Ga}_{1-x}\text{As}$ ternary alloys in the transparent wavelength region, AIP Adv. **11**, 025327 (2021)
- [8] S. Adachi. Optical dispersion relations for GaP , GaAs , GaSb , InP , InAs , InSb , $\text{Al}_x\text{Ga}_{1-x}\text{As}$, and $\text{In}_{1-x}\text{Ga}_x\text{As}_y\text{P}_{1-y}$, J. Appl. Phys. **66**, 6030-6040 (1989)

Simulation of the temperature mode of a solar photoconverter

Aleksandr Sliusarenko
Department of Microelectronics,
Electronic Devices and Appliances
Kharkiv National University of Radio
Electronics
Kharkiv / Ukraine
oleksandr.sliusarenko@nure.ua

Aleksandr Galat
Department of Microelectronics,
Electronic Devices and Appliances
Kharkiv National University of Radio
Electronics
Kharkiv / Ukraine
oleksandr.galat@nure.ua

Abstract—One of the main tasks of researchers is to find ways to increase the solar cells efficiency. In this paper we propose an original structure of a thin-film solar cell based on a tandem connection of a photoelectric converter and a thermoelectric layer based on CuInSe_2 . The photoelectric converter consists of CuInSe_2 and CdS layers. A 3D model of the proposed thin-film solar cell was implemented in the COMSOL Multiphysics environment with using the Heat Transfer module. The simulation was carried out taking into account the diurnal and seasonal variations of both the ambient temperature and the power density of the AM1.5 solar spectrum for the geographical coordinates of Kharkiv. The temperature pattern and temperature gradients are calculated in each layer of the solar cell without and with the temperature stabilization of the substrate back side as well as without and with the thermal insulation of the substrate ends. Graphs of the temperature gradients of the thermoelectric layer and the temperature variations of the photoelectric converter of the solar cell are given. As a result of the simulation, it is shown how the uneven heating of both the surface of a thin-film solar cell and its layers occur under conditions of diurnal and seasonal variations of both the ambient temperature and the solar radiation power density. This made it possible to achieve an increase in the output power of the solar cell both by summing the photo- and thermoelectric output voltages and by the concentration of solar radiation.

Keywords— thin-film solar cell, interface stability, multilayer structure, COMSOL Multiphysics, temperature gradient

I. INTRODUCTION

Development and study of the properties of thin-film solar cells is one of the topical problems of modern semiconductor power industry [1]. Copper indium selenide (CuInSe_2) has recently been used as a material of such elements [2]. It most fully meets the requirements for use in terrestrial conditions, owing to its narrow band gap (1.04 eV at 300 K), presence of homo- and heterojunctions, flexibility [3], high radiation resistance, environmental safety and cost.

Experimental studies show that long-term operation of solar cells leads to a decrease in their operational efficiency and a service life [4] due to their heating above ambient temperatures (up to 50–55 °C and more). Therefore, it is of interest to search for efficient ways of reducing the operating temperature of the solar cell and increasing the solar photovoltaic conversion efficiency [5].

The purpose of this paper is to develop methods for increasing the solar photovoltaic conversion efficiency of a thin-film semiconductor cell based on CuInSe_2 by using both the thermal energy released in this cell and the infrared radiation of the sun and the environment.

II. CONSTRUCTION OF THE THIN-FILM SOLAR CELL

The structure of the proposed thin-film solar cell based on CuInSe_2 is shown in the fig. 1 [6], where the first electrode layer 2, the thermoelectric layer 3 based on CuInSe_2 , the second electrode layer 4, the photoelectric converter 5 and 6 consisting of CuInSe_2 and CdS layers respectively, as well as a transparent electrode 7 are electrically connected and sequentially arranged on the polished face surface of the substrate 1 made of stainless steel and with rounded edges.

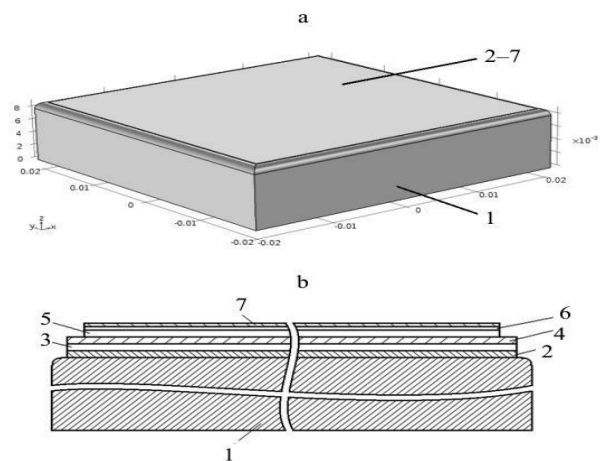


Fig. 1. The thin-film solar cell structure (a) and its cross-section (b): 1 – substrate; 2 – first electrode layer; 3 – thermoelectric layer based on CuInSe_2 ; 4 – second electrode layer; 5, 6 – photoelectric converter consisting of CuInSe_2 and CdS layers respectively; 7 – transparent electrode

III. OPERATION ALGORITHM OF THE THIN-FILM SOLAR CELL

The material of the transparent electrode 7 is zinc oxide with a band gap of 3.3 eV and a visible light transmittance of more than 80 %. This electrode passes input solar radiation, the visible part of which is absorbed in the layers 5 and 6 of the photoelectric converter that generates electric charges. The infrared part of input solar

radiation heats the layers 5 and 6 of the photoelectric converter.

One fraction of the charges generated in the layer 5 is separated by the electric field of the p-n junction of the photoelectric converter, which generates photoelectromotive-force (photo-emf) between the transparent electrode 7 and the second electrode layer 4. The remaining fraction of the photogenerated charges recombine and thereby contribute to the heating of the photoelectric converter. Therefore, a temperature gradient is generated between the first 2 and the second 4 electrode layers. This gradient induces thermo-electromotive-force (thermo-emf) between the upper and lower sides of the thermoelectric layer 3. As a result of this, the solar cell output voltage consisting of photo- and thermoemf between the first electrode layer 2, electrically connected to the lower side of the thermoelectric layer 3, and the transparent electrode 7 is produced. Since the solar cell efficiency depends on the temperature, it is necessary to stabilize the photoelectric converter temperature, maintaining its efficiency at a constant level.

IV. COMPUTER SIMULATION

Computer-aided design is an essential tool for construction of modern technical facilities. This is due to several factors. It makes it possible to significantly reduce the financial costs of developing the hardware components of photovoltaic devices and moreover to optimize the production processes in order to reduce the energy and resource intensity of output products, to improve its consumer qualities, and ultimately to increase its competitiveness.

The simulation was carried out using the COMSOL Multiphysics software package, which served to solve most scientific and engineering problems (starting from the geometric parameters definition and the physics description and ending with the visualization and preservation of the results) based on the system of nonlinear partial differential equations by the finite element method. The Heat Transfer Module of this software package was used to quantify the increase in the power produced by the proposed thin-film solar cell based on CuInSe_2 . This module is a specialized tool for modeling thermal processes in electronics components and power engineering, which include solar cells working under real operating conditions. Predefined settings are available for solar and ambient radiation, where the surface absorptivity for short wave-lengths (the solar spectral band) may differ from the surface emissivity for the longer wavelengths (the ambient spectral band). Further, the sun radiation direction can be easily defined from the geographical position and time. The view factors are computed by using the hemicube or direct integration area method. For computationally effective simulations, it is possible to define planes or sectors of symmetry [7].

In the developed numerical three-dimensional model of a thin-film solar cell, the various conditions of its operation were considered in the presence and absence of the thermal insulation of the substrate ends as well as in the presence and absence of the temperature stabilization of the substrate back side.

The calculations were carried out taking into account the diurnal and seasonal variations of both the ambient temperature and the power density of the AM1.5 solar

spectrum for the geographical coordinates of Kharkiv (fig. 2). The maximum value of the solar radiation power density was equal to 500kW/m^2 . In climatology, the diurnal variation of the ambient temperature is averaged over many years, moreover, nonperiodic temperature changes offset each other and the ambient temperature follows a simple 24 hour periodic sinusoidal distribution around an average temperature [8]:

$$T_{amb} = T_{avg} + \Delta T \cos\left(2\pi \frac{t-14}{24}\right) \quad (1)$$

Here T_{avg} and ΔT are two customizable parameters corresponding to the average temperature and half diurnal temperature variation, respectively. The time variable t is expressed in hours. In the simulation we used above-mentioned function and average minimum ($T_{avg} - \Delta T$) and average maximum ($T_{avg} + \Delta T$) monthly ambient temperatures. The substrate temperature was set taking into account both the change in the ambient temperature and the stabilization at 1 and 10°C .

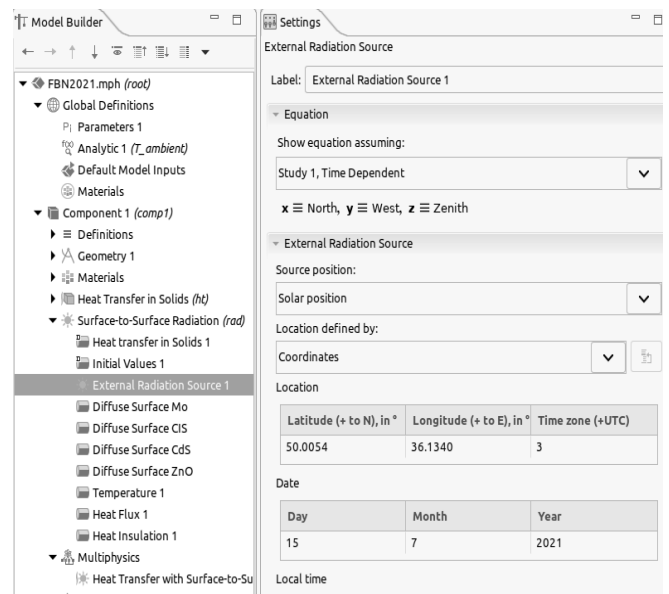


Fig. 2. Screenshot of the setting window in the COMSOL Multiphysics when defining an external radiation source using the Solar Position option.

The thin-film solar cell was divided into finite tetrahedral elements in the simulation (fig. 3). At calculations, the grid density for each layer of the solar cell was adjusted taking into account its geometrical configuration by selecting one of nine preset modes: from extremely fine to extremely rough. If it is necessary to use a finer grid in any area, for example for 50 nm thick layers 6 and 7, the partition operation was performed manually. The problem solving was carried out taking into account the change in the ambient temperature. The program facilities made it possible to visualize and process calculated numerical data for all the concerned operating regimes of the thin-film solar cell.

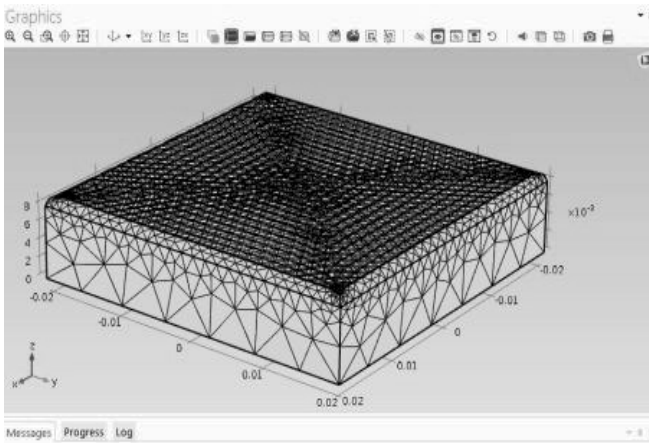


Fig. 3. Screenshot of the mesh operation of the thin-film solar cell in the COMSOL Multiphysics

V. ANALYSIS OF THE RESULTS

As calculations have shown, the uneven heating of both the surface of a thin-film solar cell and its layers occur under conditions of diurnal and seasonal variations of both the ambient temperature and the solar radiation power density. Under the above conditions, the surface of a proposed CuInSe₂ thin-film solar cell without both its cooling and thermal insulation of the substrate ends can be heated up to the temperature (T_s) of about 700 °C (fig. 4a), which leads to permanently damages. The temperature stabilization of the substrate back side at the ambient (air) temperature ($T_0 = T_{amb}$) makes it possible to reduce the surface temperature of CuInSe₂ solar cell up to $T_s \approx 55$ °C (fig. 4b). When the temperature of the substrate back side is stabilized ($T_0 = 10^\circ\text{C}$), the temperature (T_s) on the surface of CuInSe₂ solar cell reaches a maximum value of about 44 °C (fig. 4c). By thermal insulation of the substrate ends and temperature stabilization of the substrate back side at $T_0 = 10^\circ\text{C}$, it was possible to reduce the surface temperature of CuInSe₂ thin-film solar cell up to values $T_s \approx 14.2^\circ\text{C}$ (fig. 4d).

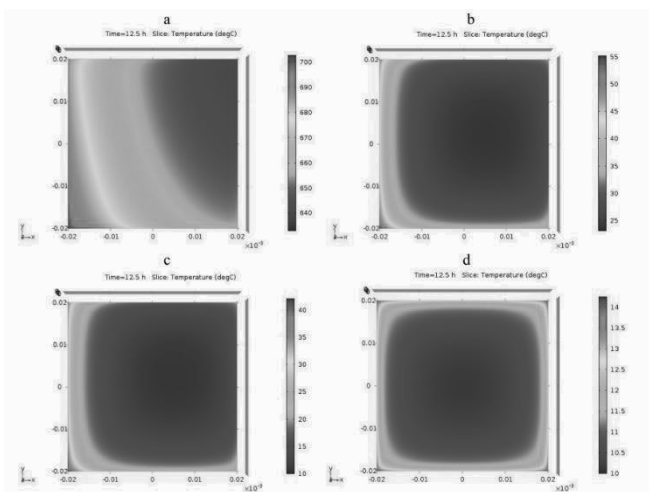


Fig. 4. The surface temperature pattern of CuInSe₂ thin-film solar cell without (a) and with ($T_0 = T_{amb}$ (b) and $T_0 = 10^\circ\text{C}$ (c, d) the temperature stabilization of the substrate back side as well as without (a, b, c) and with (d) the thermal insulation of the substrate ends at 12.30 hours in the middle of July.

According to the calculations, the temperature gradient of the thermoelectric layer varies within a year from about $1.7 \cdot 10^5$ to about $0.5 \cdot 10^5$ K/m (fig. 5).

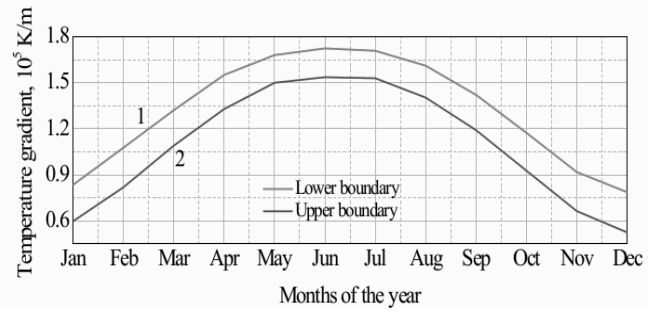


Fig. 5. The temperature gradients of CuInSe₂ solar cell with the thermal insulation of the substrate ends at the lower (curve 1) and upper (curve 2) boundaries of the thermoelectric layer on the southeast side during the year

VI. CONCLUSIONS

The performed simulation shows that the amplitude of the output voltage which generated by the thermoelectric layer of CuInSe₂ thin-film solar cell varies from 2.1 mV (in December) to 5.23 mV (in June and July). This means that by selecting an operating point on the current-voltage characteristic of the proposed solar cell and by using a thermoelectric layer, its output power can be increased up to 5 %. Moreover, a more significant increase in the output power of the concerned solar cell can be achieved even by means of substrate temperature stabilization. It should be noted that the cooling inertia of a thin-film solar cell stabilizes the output voltage in some degree under partly cloudy conditions.

REFERENCES

- [1] Novikov G. F., Gapanovich M. V. Third Generation Cu-In-Ga-(S, Se)-Based SolarInverters. *Physics-Uspeshki*, 60 (2), 2017, pp. 161–178.
- [2] Dottermusch S., Quintilla A., Gomard G., Rösler A., Voggu V. R., Simonsen B. A., Park J. S., Pernik D. R., Korgel B. A., Paetzold U. W., Richards B. S. Infiltrated Photonic Crystals for Light-Trapping in CuInSe₂ Nanocrystal-Based Solar Cells. 2017
- [3] Voggu V. R., Sham J., Preffer S., Pate J., Phillip L., Harvey T. B., Brown R. M. Jr., Korgel B. A. Flexible CuInSe₂ Nanocrystal Solar Cells on Paper. *ACS Energy Letters*, 2 (3), 2017, pp. 574–581.
- [4] Galat A., Sliusarenko A. Problems of solar cell simulation. XI International Scientific Conference "Functional Basis of Nanoelectronics", Kharkiv-Odesa, Ukraine, 2020, pp. 102-104.
- [5] Patel Ch., Shah P., Pandey A. I. Performance Improvement of Solar PV Cells using Various Cooling Methods: a Review. *International Journal on Recent Trends in Computing and Communication*, 5 (11), 2017, pp. 194–198.
- [6] Esman A. K., Kuleshov V. K., Zykov G. L., Zalesski V. B., Leonova T. R. Method for Manufacturing Thin-Film Solar Cell: Patent of the Republic of Belarus No 20481 (in Russian). 2016
- [7] Analyze Thermal Effects with the Heat Transfer Module. Available at: <https://www.comsol.com/heat-transfer-module> (Accessed: 15 May 2021).
- [8] Parasol and Solar Irradiation. Created in COMSOL Multiphysics 5.3a. Available at: https://www.comsol.com/model/download/466231/applications.parasol_and_solar_irradiation.pdf (Accessed: 15 May 2021)

Application of multilayer reflective masks for one-dimensional image compression

Yu.P. Pershyn

*Metal and Semiconductor Physics
Department, Institute of Education and
Science in Engineering and Physics,
National Technical University
"Kharkiv Polytechnic Institute"
Kharkiv, Ukraine
persh@kpi.kharkov.ua*

V.S. Chumak

*Metal and Semiconductor Physics
Department, Institute of Education and
Science in Engineering and Physics,
National Technical University
"Kharkiv Polytechnic Institute"
Kharkiv, Ukraine
vitalik_93@meta.ua*

A.Yu. Devizenko

*Metal and Semiconductor Physics
Department, Institute of Education and
Science in Engineering and Physics,
National Technical University
"Kharkiv Polytechnic Institute"
Kharkiv, Ukraine
devizenko@kpi.kharkov.ua*

V.V. Kondratenko

*Metal and Semiconductor Physics
Department, Institute of Education and
Science in Engineering and Physics,
National Technical University
"Kharkiv Polytechnic Institute"
Kharkiv, Ukraine
kondratenko@kpi.kharkov.ua*

Abstract—This work is a part of experiments to study the possibility of realization the one-dimensional image compression using multilayer reflective masks. The purpose of this work is to manufacture and test these masks.

Keywords— nanomaterials, X-Ray mirrors,

I. INTRODUCTION

The use of X-rays for submicron imaging offers greater potential over ultraviolet radiation due to its shorter wavelengths. For this purpose, multilayer reflective masks were previously used, which were multilayer Mo/Si coatings with partial removal of this coating from the substrate surface in accordance with a given pattern [1]. The X-ray source was a synchrotron (wavelength 14 nm [2]). With an average distance between the reflective mask and the photoresist of 7 mm, images of structural elements larger than 8 μm were obtained.

In this work, for the same purpose, we applied shorter wavelength X-rays (0.154 nm) using standard X-ray equipment (X-ray diffractometer), in contrast to expensive synchrotron equipment. The illumination of the photosensitive element was carried out in air without using a vacuum chamber required for experiments with soft X-ray radiation.

II. METHODS

The reflective masks were WC/Si multilayer mirrors deposited on a glass substrate (surface roughness less than 0.3 nm) by direct current magnetron sputtering. The ratio of the thicknesses of the WC and Si layers in the period was 1:1 in order to suppress the second order of reflection. The pattern on the surface of the mask was created by a W absorbing layer.

The research was carried out on a DRON-3M X-ray diffractometer with a (110) Si monochromator crystal.

AGFA photographic film for electron microscopy was used as a photosensitive element.

III. EXPERIMENTAL

A. Theoretical introduction

The idea of application of a multilayer reflecting mask (MRM) is based on the fact that visible dimension of any flat element is smaller than its origin by factor of $\sin\theta$, with θ - a grazing angle of the incidence to the surface of the flat element. So if we direct X-rays to a reflecting area at an oblique angle, we'll always receive a pattern shrunk in one dimension at a plane perpendicular to the reflected beam.

Schematic drawing of the MRM and the scheme of its application are shown in fig. 1. Reflecting mask represents a multilayer (ML) coating on a substrate (for example, Si-wafer or float glass), part of which is covered by an absorbing mask to make a pattern according to a designed picture. Just for illustration, a mask in fig. 1 has streaky or grating-like structure. During illumination (fig. 1a), X-ray beam (for example, from synchrotron) is directed onto reflecting elements of dimension t_m .

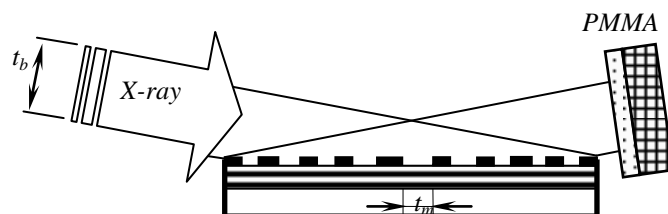


Fig. 1. Schematic drawing of the multilayer reflecting mask and the schemes of its application according to a normal exposure of photoresist.

The reflected beams have dimensions t_b in a perpendicular plane. Thus demagnification, D , of the mask structure in this plane will be equal to:

$$D=t_b/t_m = \sin\theta \quad (1)$$

To estimate real dimension of imprints from different reflecting elements of *MRM* at the photoresist plane we should include diffraction effects. For this purpose we'll use an expression for the slit dimension for the case of Fresnel diffraction. Final formula for the imprint dimension, t_b , as a function of a mask element dimension, t_m , looks:

$$t_b=t_m \times \sin\theta + 2L\lambda/\sin\theta \quad (2a)$$

$$t_b=\lambda \times t_m/2d + 2Ld/t_m, \quad (2b)$$

here L is a distance from mask element to the photoresist plane; λ is central wavelength of bandwidth reflected from the ML X-rays; d is a period of ML. Formula (2a) was converted to formula (2b) using Bragg's law not corrected for a refraction ($2d\sin\theta=\lambda$).

B. Test of MRMs with X-ray tube and photographic film

For successful application of multilayer reflecting masks, it is necessary to fulfil two requirements: to have comparatively large dimensions of a transferred pattern; and to provide an acceptable image resolution. As these requirements are interdependent, we will specify the former and then evaluate the latter. Silicon wafers with diameter of ~76 mm and more are used in lithographic technology. According to the scheme of fig. 1 the distance between mask elements and photoresist is changed across the reflected beam, and for the above mentioned Si-wafers can amount 20-86 mm for a single pattern on the photoresist (we took the distance between the mask and a photoresist plane 10 mm and consider only reflecting elements disposed 10 mm off the wafer edge). So we can fix 20-40 mm as a lower dimension limit for the distance till reflecting masks. Under inclined or multiple inclined irradiation geometry, the distance from the mask till the resist should be increased, and we can take 200 mm as reasonable upper limit for the distance.

As an input data we took a grazing angle of the incidence $\theta=1.76^\circ$ that corresponded to the angle position of Bragg maximum for a ML coating with a period $d\sim 2,5$ nm at wavelength $\lambda=0,154$ nm. So we should get a demagnification $1/\sin(1.76^\circ)\approx 33$.

We used WC/Si MLs to prepare MRMs. Periods of MLs were 2,5 nm, and the number of bilayers was 200 to obtain moderate width of the first Bragg peak. Ratio of layer thicknesses was taken close to 1 to suppress the second ML harmonic.

Figure 2 shows successive stages illustrating different steps in fabrication of MRM and getting a shrunk pattern on the photographic film (AGFA for electron microscopy) with $\text{CuK}\alpha_1$ radiation at standard X-ray diffractometer. Figure 2a shows SEM image of the prepared MRM on the base of WC/Si ML (dark) with W-absorber layer (bright).

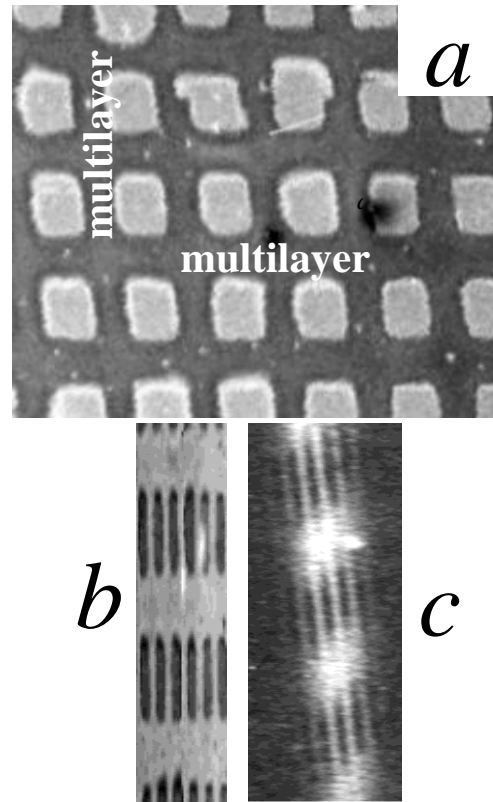


Fig. 2. Scanning electron microscopy images of (a) multilayer reflecting mask with W-absorber, (b) computer compression of the MRM image of fig. 2a, (c) imprint of the X-ray beam reflected from MRM on a photographic film.

For comparison with an imprint of the X-rays on the photo-film (fig. 2b), we made a computer compression of the image represented in fig. 2a which is placed in fig. 2c. Mean dimension of the mask pattern to be compressed is ~300 μ (vertical dark stripes in fig. 2b). As it can be visible figs. 2b and 2c are very similar indicating that one-dimensional compression of the mask pattern was received. For 2.5-nm-WC/Si ML and the distance from *MRM* till photo-film of 10 mm clear periodicity of 10-11 μ in the striped regions of fig. 2c can be evidenced. This roughly corresponds to the compressed 330- μ -mask element at demagnification of ~32.

Alteration of the imprints with increasing distance till the photo-film is shown in fig. 3. This figure demonstrates that a shrunk pattern can be visible even for as long distance as 140 mm. Degradation of the picture quality with distance is connected with diffraction effect and with a divergence of X-ray beam, especially in vertical direction.

C. The merits of such MRMs

- Small distortions caused by X-ray absorption and corresponding heating.
- Easy cooling of irradiated field.
- Adjustable scaling within the certain range by simple change of incidence angle.
- Simplicity and low cost of the mask fabrication.
- Possible preliminary Si-wafer processing (instead of coating processing) to fabricate a mask pattern before multilayer deposition.
- Availability to apply MRM as filters.

- Possibility to use Si wafers as substrates to be deposited with a multilayer for all wavelength ranges.

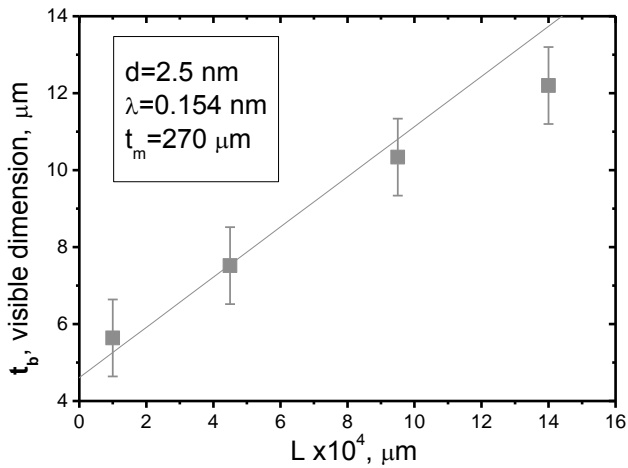


Fig. 3. Dependence of the photoresist element dimension, t_b from the reflective mask-photoresist distance L .

IV. CONCLUSIONS

It was experimentally shown a possibility to fabricate the reflecting multilayer masks on the base of WC/Si multilayer X-ray mirror with a pattern of absorber layer. Applicability of ML masks for one-dimensional scaling of a surface pattern is demonstrated in grazing geometry using 0,154 nm. One-dimensional shrinkage of the pattern up to ~40 times is received. The photoresist picture with elements of as low dimension as ~12 μm is obtained.

REFERENCES

- [1] S. Rahn, A. Kloidt, J. Hormes et al., "Large area soft X-ray projection lithography using multilayers structured by RIE", Proc. SPIE Vol. 1742, p. 585-592 January 1993.
- [2] S. Mardix and A. R. Lang, "Image reduction to submicrometer dimensions by asymmetric crystal reflection of x rays", Review of Scientific Instruments 50, 510, 1979.

FPGA Nano Structures For Vehicle Electronics

Vladimir Karnaushenko
Dept. of Microelectronics, electronic
devices and appliances
Kharkiv National University of
Radioelectronics
Kharkiv, Ukraine
vladimir.karnaushenko@nure.ua
[ORCID 0000-0001-7744-2569](https://orcid.org/0000-0001-7744-2569)

Alexander Borodin
Dept. of Microelectronics, electronic
devices and appliances
Kharkiv National University of
Radioelectronics
Kharkiv, Ukraine
alexander.borodin@nure.ua

Yuriy Vasilyev
Dept. of Microelectronics, electronic
devices and appliances
Kharkiv National University of
Radioelectronics
Kharkiv, Ukraine
yurii.vasiliev@nure.ua

Abstract— As microelectronics becomes increasingly important in automotive systems, transport electronics developers are increasingly relying on FPGA programmable structures to create applications with better performance and flexible architectures.

Keywords— electronic control units, transport applications, programmable logic blocks, automotive information technology

I. IMPROVING COMPUTING PERFORMANCE FOR TRANSPORT.

Although cars have a long and rich history, electronics have been used extensively in transport applications relatively recently, becoming an integral part of the automotive world only in recent decades. Today, car companies compete fiercely not only with each other, but also with the latest and most modern technologies [1].

Currently, manufactured cars rely on many sensors to measure many internal and external variables that could affect the car's driving behavior, as well as additional parameters such as visibility and passenger comfort. Depending on their level of sophistication, sensors can be classified from simple sensors that directly measure individual physical parameters (eg ambient light sensors and temperature sensors) to complex intelligent sensors that determine environmental parameters using broad-spectrum signals (eg radio frequency, radars and light, video); in addition to measurements, they perform data processing and have the ability to perform drives [2].

Using processor-based electronic control units (ECUs), it is difficult to keep up with consumer electronics due to the long cycles of chip development and strict standards of reliability and quality applied to the automotive industry. The automotive industry uses increasingly sophisticated electronic systems to offer the driver better safety and efficiency. Programmable arrays of valves (FPGAs) can play an important role in filling this gap, providing up-to-date performance and high flexibility to system architects to customize projects through a flexible (programmable) electronic circuit structure.

The main goal in automotive design is to reduce the total number of ECUs, as they increase the overall cost of the vehicle and reduce reliability. Thanks to the latest advances in FPGA structures, it is now possible to combine electronic components inside the car more intelligently.

For example, the implementation of a purely hardware processor architecture is a problem that needs to be

addressed urgently. However, one possible solution to these interferences is a hybrid approach that combines processors and ECUs with FPGA-based chip systems (SoC), Fig.

FPGAs contain an array of programmable logic blocks, such as built-in memory, digital signal processing units (DSPs), and high-speed receivers. With FPGAs, the automotive system becomes easily scalable with minimal hardware changes.

In this way, FPGAs create opportunities for automotive original manufacturers and suppliers to more effectively build innovative safety programs, such as adaptive cruise control, driver assistance, collision avoidance and blind spot warning.

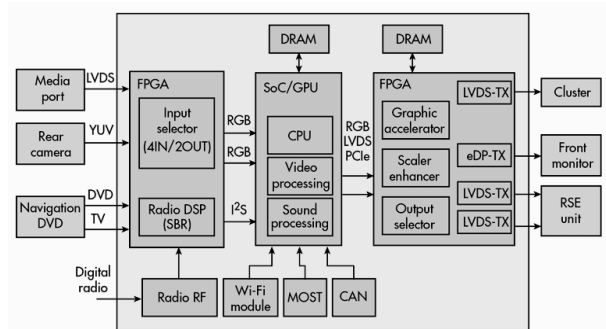


Fig.1. Hardware processor architecture

As the name implies, driver assistance includes features such as reversing cameras, three-dimensional surveillance cameras, lane departure warning systems, pedestrian detection and more [3].

II. HARDWARE AND SOFTWARE

FPGA is a nanodevice based on a matrix of programmable logic blocks, which are determined by their functionality. This feature distinguishes FPGAs from specialized integrated circuits (ASICs) designed for applications designed for specific design tasks. ASICs and FPGAs have a number of key benefits that need to be carefully evaluated before making a decision. With the development of unmatched logic density and many other features such as digital signal processing, clock speed and high-speed serial bus, FPGAs become a reliable helper for almost any type of design.

For example, automotive infotainment systems are of great importance in modern vehicle design and have a

significant impact on the sale of global vehicles. In these systems, it is important to choose the right main system processor to differentiate the user interface with the latest graphics. With several models to support, you may have to choose different SoCs due to system variations and the emergence of new interoperability technologies.

Thanks to FPGA, the system becomes easily scalable, which allows you to update the firmware remotely to support more manufacturers, regions and models with minimal hardware modifications. You can use the FPGA to support any combination of I / O interfaces [4].

The most important design factor of FPGAs is that they are programmable logic devices. Of course, CPU software can be upgraded, but the same cannot be said for computer architecture. On the other hand, FPGAs can be configured or reprogrammed to perform various functions an infinite number of times. In many recent cars, the software tracks many functions during operation. For example, Tesla models already support software updates remotely.

Thanks to this feature, FPGAs are able to constantly support the original software of manufacturers with the latest versions of programmable or customized hardware architecture systems. Such software updates can be applied to various car features, which may include more FPGA-oriented structures as they become more powerful, smaller and cheaper [5].

Connected vehicles are able to analyze information in real time to provide new information to car users, optimizing their experience. Meanwhile, IoT connectivity can help develop new development models for the automotive market by transforming the relationship between automakers and drivers.

III. AUTOMOTIVE INFORMATION TECHNOLOGY

As more IoT technologies are implemented in automotive applications, this is a prerequisite for the convergence of innovations - especially in the electronics industry. However, experienced engineers know that there is a learning curve when using something new that comes into direct conflict with less development time. In turn, this increases the project risk.

For this reason, designers tend to reuse technologies that are already well known or have been used before. Over time, this philosophy transforms some architecture into widely used industry standards, while most others are used only in narrow market niches.

IoT engineers will have to deal with significant issues such as energy efficiency and management of incompatible interfaces. The FPGA-based design approach can help solve these problems by offering a fully functional hardware platform for very low-power IoT applications.

When researching which 32-bit processor will best serve customers, many companies realize that the standard

industry architecture offers significant benefits to the owner. Standard industry processors, as a rule, have a wide range of development tools, a large number of available software codes and designers who have the knowledge and experience to use them. Such benefits accelerate project development time (and therefore time to market) and also reduce a project risk, which in turn provides users with higher value-added solutions [6].

On this front, the ARM Cortex – M1 processor, designed from scratch for use in FPGAs, stands out. One of the main functions - it helps to minimize the amount of resources needed to meet the requirements of the developer. For example, debugging functions can be enabled or removed. Operating system extensions for system timers and software interrupts are not required. Cortex-M1 works with most basic FPGAs, which means that switching from one FPGA device to another requires minimal effort.

IV. CONCLUSIONS

FPGAs are now implemented separately or together with processors in many automotive systems, as they provide more efficient and faster solutions for hundreds of ECUs in a vehicle. They provide higher performance without consuming more energy, and improve customization and scaling capabilities.

FPGAs can also help reduce overall car ownership costs by integrating and / or reducing the number of external components, speeding up time to market, and consolidating accelerated project development.

In addition, thanks to innovative and cost-effective imaging solutions, FPGAs support the implementation of even more automotive features. Finally, they often offer a more cost-effective option in programs such as traffic control systems or engines. At present, it is expected that the design needs of the growing hybrid and electric vehicle industry will also focus on expanding the FPGA market.

REFERENCES

- [1] FPGA Considerations for Automotive Applications. Rick Nicholson, Michael Gabrick, Frank Winters. Conference: SAE World Congress & Exhibition. DOI 10.4271/2006-01-0368
- [2] M. Maurer, "Forward Collision Warning and Avoidance." In: A. Eskandarian (Ed.), Handbook of Intelligent Vehicles, Springer London, 2012..
- [3] Deep multi-modal object detection and semantic segmentation for autonomous driving: Datasets, methods, and challenges, – D Feng, C Haase-Schuetz, L Rosenbaum, H Hertlein – IEEE Transactions on Intelligent Transportation Systems, 2020.
- [4] A parallel implementation of sequential minimal optimization on FPGA. DH Noronha, MF Torquato, MAC Fernandes, – Microprocessors and Microsystems 69, 138-151
- [5] Markvollrath; Schleicher, S.; Gelau, C. The influence of Cruise Control and Adaptive Cruise Control on driving behaviour—A driving simulator study. *Accid. Anal. Prev.* 2011, 43, 1134–1139.
- [6] Field Programmable Counter Arrays Integration with Field Programmable Gates Arrays. Vladimir Karnaushenko, Alexander Borodin. – Theoretical and Applied Aspects of Device Development on Microcontrollers and FPGAs, MC&FPGA. – 2019. – P. 14-16.

TABLE OF CONTENTS

Yuriy Zholudov, Boris Chichkov, Kateryna Muzyka, Mykola Slipchenko, Olena Slipchenko, Volodymyr Vasylovskyi LASER ASSISTED GENERATION OF NANOPARTICLES FOR ELECTROCHEMICAL AND ELECTROCHEMILUMINESCENT APPLICATIONS	5
Kateryna Muzyka, Yuriy Zholudov, Iaroslav Gnilitskyi, Dmytro Snizhko, Volodymyr Vasylovskyi, Olena Slipchenko LASER-BASED NANOSTRUCTURING OF CARBON MATERIALS	10
Volodymyr Vasylovskyi, Yuriy Zholudov, Iryna Beshpalova, Mykola Slipchenko, Alexander Sorokin, Olena Slipchenko RESEARCH OF ELECTROCHEMILUMINESCENCE OF CESIUM LEAD HALIDE PEROVSKITE NANOCRYSTALS	13
Yevgen Sokol, Andrii Dobrozhan, Andrey Meriuts, Alina Khrypunova DC MAGNETRON SPUTTERING METHOD FOR OBTAINING NANOSCALE SEMICONDUCTOR FILMS	16
Sergey Berdnik, Oleksandr Dumin, Victor Katrich, Mikhail Nesterenko, Svetlana Pshenichnaya, Sergey Shulga DETERMINATION OF LONGITUDINAL SIZES OF CARBON NANOTUBES AT THE FUNDAMENTAL RESONANT FREQUENCY	20
Andrey Boyarintsev, Alexandr Kolesnikov, Sergii Kovalchuk, Tatiana Nepokupnaya, Igor Nevliudov, Vladimir Tarasov HIGH-SENSITIVE COMBINED GAMMA DETECTOR	23
Viktor Vlasiuk, Roman Korkishko, Vitaliy Kostylyov, Oleg Olikh IRON-IMPURITIES-ACTIVATED KINETICS OF THE LIGHT-INDUCED PROCESSES IN SILICON SOLAR CELLS	27
Mykola Kulish, Vitaliy Kostylyov, Anatoly Sachenko, Anatoly Shkrebtii, Igor Sokolovskyi LUMINESCENT SOLAR CONCENTRATOR WITH NANO-SCALE ABSORBER: THE FORM-FACTOR	32
V. Borshechov, O. Listratenko, Oleksandr Kravchenko, O. Suddia, Mykola Slipchenko, Boris Chichkov DISPERSION OF NANOPARTICLES IN OPTICALLY TRANSPARENT POLYMER MATRICES	36
M.A. Mehrabova, N.H. Hasanov, S.N. Huseynli AB INITIO ELECTRONIC-STRUCTURE CALCULATIONS FOR Cd_{1-x}Fe_xS SEMIMAGNETIC SEMICONDUCTORS	41
Yan Karandas, Andrii Korotun THE SURFACE PLASMONIC RESONANCE IN THE METALLIC 1D-STRUCTURES WITH THE ELLIPTIC CROSS-SECTION	44
Andrii Korotun THE SIZE THERMAL EFFECTS IN THE NEIGHBORHOOD OF THE PLASMONIC BIMETALLIC NANOPARTICLE	49
Nazar Pavlysheche, Andrii Korotun, Vitalii Reva, Igor Titov THE SPECTRAL Q-FACTOR OF THE METALLIC NANODISCS	54

V.M. Skobeeva, V.A. Smyntyna, M.I. Kiose, N.V. Malushin EFFECT OF ZINC ON CdS QD SURFACE MODIFICATION	59
Yu.Ye. Gordienko, I.M. Shcherban ELECTRODYNAMIC FUNDAMENTALS OF DESIGNING A HIGHLY LOCALIZED RESONATOR PROBE WITH ADJUSTABLE SENSITIVITY FOR MICROWAVE DIAGNOSTICS OF NANOELECTRONIC OBJECTS	62
O. Listratenko, V. Borshchov, Oleksandr Kravchenko MODELLING THE STRUCTURES OF POLYIMIDE COMPOSITE SYSTEMS AND CALCULATING THEIR THERMAL CONDUCTIVITY COEFFICIENTS	67
Dmytro Snizhko, Yuriy Zholudov, Olena Bilash, Kateryna Muzyka ATOMIC FORCE MICROSCOPY INVESTIGATION OF LASER-INDUCED PERIODIC SURFACE STRUCTURE AS A PERSPECTIVE ELEMENTS FOR SENSORS CONSTRUCTION	71
Igor Nevliudov, Olena Chala, Iryna Botsman, Oleksandr Klymenko, Maksym Vzhesnievskyi AUTOMATION OF MATHEMATICAL MODELING OF PHYSICAL AND TECHNOLOGICAL PROCESSES IN THE ELECTRONIC DEVICES MANUFACTURE	74
Mykhailo Kirichenko, Roman Zaitsev, Anton Drozdov, Gennadiy Khrypunov, Eugene Sokol, Liliia Zaitseva USING HIGH-VOLTAGE CONVERTERS IN HYBRID PHOTOVOLTAIC SYSTEMS	78
Roman Zaitsev, Mykhailo Kirichenko, Kseniia Minakova ELECTRONIC LOAD BASED ON FET-TRANSISTOR	83
Kseniia Minakova, Roman Zaitsev, Mykhailo Kirichenko INCREASING EFFICIENCY OF PHOTOVOLTAIC THERMAL SYSTEMS	89
V. Borshchov, I. Tymchuk, M. Protsenko, O. Listratenko, O. Suddia INVESTIGATIONS OF INTERCONNECTION APPROACH FOR NOVEL ULTRALIGHT VERTEX DETECTORS BASED ON CURVED PIXEL SENSORS	93
Aleksandr Galat, Liudmila Sviderska, Aleksandr Sliusarenko CALCULATION OF THE ABSORPTION CAPACITY OF MULTI-JUNCTION SOLAR PHOTOCONVERTERS	98
Aleksandr Sliusarenko, Aleksandr Galat SIMULATION OF THE TEMPERATURE MODE OF A SOLAR PHOTOCONVERTER	101
Yu.P. Pershyn, V.S. Chumak, A.Yu. Devizenko, V.V. Kondratenko APPLICATION OF MULTILAYER REFLECTIVE MASKS FOR ONE-DIMENSIONAL IMAGE COMPRESSION	104
Vladimir Karnaushenko, Alexander Borodin, Yuriy Vasilyev FPGA NANO STRUCTURES FOR VEHICLE ELECTRONICS	107

Collection of scientific works

XII INTERNATIONAL SCIENTIFIC CONFERENCE

Functional Basis of Nanoelectronics

Responsible for the release of materials: Mykola Slipchenko, Volodymyr Vasylykovskiy

Collection materials are published in the author's version without editing

Format 60x84/8. A paper is offset. Garniture of Times New.
Conditionally printed sheets 13,02. Drawing 50 things. Order 0915/3-21.

It is printed from prepared original iv in the printing-house of FOP Azamaev V. R.
Testifying to state registration of V02 № 229278 from 25.11.1998.
Testifying is to bringing of subject of publishing business in the state register of publishers,
manufacturers and spreaders of publishing products. Series of HK № 135 from 23.02.05.
City Kharkiv, street Poznanska 6, k. 84, tel. +7 (057) 778-60-34 e-mail:bookfabrik@mail.ua